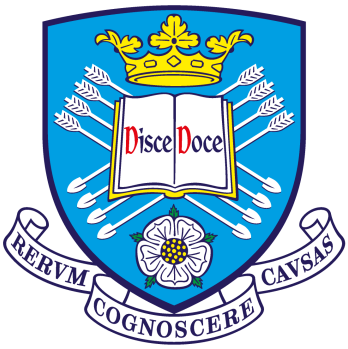
Arc Damage Identification and Its Effects on Fatigue Life of Contact Wires in Railway Overhead Lines



Özgün Sunar

Department of Mechanical Engineering
University of Sheffield

This dissertation is submitted for the degree of
Doctor of Philosophy

January 2021

I would like to dedicate this thesis to
Nilgün and my loving parents ...

Declaration

I hereby declare that except where specific reference is made to the work of others, the contents of this dissertation are original and have not been submitted in whole or in part for consideration for any other degree or qualification in this, or any other university. This dissertation is my own work and contains nothing which is the outcome of work done in collaboration with others, except as specified in the text and Acknowledgements. This dissertation contains fewer than 65,000 words including appendices, bibliography, footnotes, tables and equations and has fewer than 150 figures.

Özgün Sunar
January 2021

Acknowledgements

The completion of this thesis could not have been possible without the participation and assistance of a number of people and organisation whose names may not all be enumerated.

I would like to express my sincere gratitude to;

- my sponsor, **Turkish Ministry of National Education**,
- my supervisor, **Prof David Fletcher**, for his continuous support, motivation and immerse encouragement,
- my advisory supervisors, **Dr Adam Beagles** and **Prof Roger Lewis**, for their assistance and valuable contributions to my research ,
- **Partic Mac and colleagues at Network Rail** for their important support for accessing site observations and valuable OLE mainline data
- team members of **Furrer+Frey**; particularly, **Katherine Chan, Rob Daffern** and **Noel Dolphin** for their unforgettable support to my research and career,
- **Chris Bryan now at HS2** who has always shared his expertise in OLE system,
- **MERail research colleagues** for all the fun and experience we have had together in the last four years,
- **Hakan Doğan** for his valuable guidance to post-processing in Matlab,
- **Friends in Sheffield** who always offered me a family welcoming,

Last but not least

- **My Mother** for teaching me how to be a hard-working person,
- **My Father** for being the best teacher in my life,
- **Nilgün**, the strong woman who has been always encouraging me with her faith and warm smile.

Abstract

Electrified trains are considered one of the most efficient ways of passenger and freight transportation. Recently, railway electrification has received particular attention due to its low carbon emissions. Around 40 % of the UK rail network is electrified and by 2050, it is expected that the share of electrified trains in total railway lines in the world will grow from 30 % to 50 %. Although the installation cost of electrification is expensive, in 2019 UK Railway Industry Association reports that electrified lines are cost-effective systems in the long term when compared to the whole-life costs of diesel services. Therefore, the maintenance cost plays a vital role in the long term efficiency of the electrification. In electrified railway systems, overhead line equipment (OLE) is widely used for providing energy to electrified trains. In these systems, the pantograph collects current from the contact wire. The pantograph and contact wire are in both mechanical and electrical interaction, with the pantograph carbon current collector sliding over the contact wire during the train journey. Therefore, mainly wear was considered for determining the design life of the contact wire, which was in a range between 30 and 50 years. However, reports from World Congress on Railway Research (WCRR) mentioned that this interaction brings several problems together with the increase in train speed, and those are expected to be significant for determining the design life of the OLE wires. Arcing can be shown as one of the most critical interaction problems. The momentary loss of contact or flashover due to low clearance between OLE cables and civil structures (bridges, overpass) can generate arcs in the contact wire. Additionally, the increase in the train speed leads the contact wire to be more vulnerable to fatigue problems as well as the arcing problem. This PhD study aims to answer the question of whether arcing is a cause of damage, and then whether arc damage can be the potential to shorten long term fatigue life of the contact wires. For this purpose, initially, both real-world data and contact wire samples from an existing electrified mainline were analysed. Following the inspection of the data, contact forces driving stress fluctuations in the contact wire were determined using finite element method. A novel fatigue test configuration was developed to establish the fatigue life of unmodified contact wires under real boundary conditions. This experimental configuration also helped to investigate the fatigue life of contact wires after arcing, which would not be possible to test with standard fatigue tension tests.

Arc-affected contact wire samples were prepared with an overhead line arc machine (SOLARC) which was designed and built for this research purpose. This machine is capable of investigating the parameters of current, voltage type and the number of arcs affecting arc damage to the contact wire. The interior damage to wires after arcing was revealed with optical microscopy, metallography, surface mapping and microhardness tests. A thermal finite element model was also developed from the findings of arc experiments to gain an in-depth understanding of temperature distribution in the contact wire during arcing. Experimental studies were completed by testing fatigue life of arc-affected contact wire samples. This enabled comparison of the fatigue life of arc affected contact wire samples with those of arc-free contact wire samples. Particularly, the variables of the current magnitude and the number of arcs were the key parameters to help to explore what was causing the damage. Severe arc damage, grain modification and void formation existed in the range between 100 and 200 A for direct current and 200 A for alternating current. For the same testing parameters, DC had a more substantial effect on the change in metallurgical and mechanical properties of the contact wire rather than AC. Higher currents caused the softening to spread deeper into the contact wire, but the effect of the increasing number of arcs at a single location was not significant. The fatigue tests of arc-affected contact wires showed that arcs could lead to the acceleration of the crack initiation stage and significantly shorten the fatigue life of the contact wire.

As for the void (internal defect) formation in the material after arcing, it was recognised this could be hydrogen embrittlement which could be mitigated by the use of low oxygen content material. Thus, arc experiments were repeated with low oxygen-content copper material (OFC 0.00005 % vs 0.04 % for the conventional material). The insights gained from using OFC material shows that large voids after arcing may be restricted by using a low oxygen content contact wire. This research successfully identifies the potential consequences of arcs to the contact wire mechanical and metallurgical properties and predicts the fatigue life of the contact wire before and after the arc exposure. Strain-fatigue life curves developed from the experimental results can be used for extrapolating a trend for further high cycle fatigue problems of the contact wire. The methods developed for determining fatigue life of the copper-silver contact wire considered in this work can also be applied to other types of contact wires elsewhere in the world. This study helps us to understand the role of avoiding arcing in achieving more reliable OLE systems. Also using OFC material shows important opportunities for the mitigation of the severity of the arc damage, and this could minimise the maintenance cost that plays an essential role in long-term efficiency of the overhead line electrification.

Table of contents

List of figures **xi**

List of tables **xvi**

Symbols **xviii**

1 Introduction **1**

1.1 Aim and Objectives 2

1.2 Thesis Outlines 3

1.2.1 Literature Review (Chapter 2) 3

1.2.2 Fatigue Life of Overhead Contact Wires (Chapter 3) 3

1.2.3 Effects of Arcing on Contact Wires (Chapter 4) 3

1.2.4 Modelling Thermal Damage Due to Arcing with Finite Element Method (Chapter 5) 4

1.2.5 Effects of Arcing on Fatigue Properties of Overhead Contact Wires (Chapter 6) 4

1.3 Contributions to Knowledge 5

2 Literature Review **6**

2.1 Background 6

2.2 Overhead Line Equipment 10

2.2.1 General Features 11

2.2.2 Components of OLE 11

2.2.3 The Pantograph 13

2.2.4 Contact Wires in OLE 14

2.3 Pantograph and Contact Wire Interaction Problems 21

2.3.1 Pantograph Bending Effects on Contact Wire 22

2.3.2 Mechanical Wear 23

2.3.3 Fatigue in Contact Wires 27

2.3.4 Fatigue Fracture in Contact Wires . . . 41
2.3.5 Arcing Problem . . . 49
2.4 Identification of Current Research Gaps . . . 54
2.5 Summary . . . 55

3 Fatigue Life of Overhead Line Contact Wires 56
3.1 Introduction . . . 56
3.2 Materials and Methods . . . 56
3.2.1 OLE Inspection Data Analysis . . . 58
3.2.2 Modelling of Overhead Contact Lines . . . 62
3.2.3 Tensile Testing . . . 70
3.2.4 The Design of OLE Fatigue Rig . . . 73
3.2.5 Specimen Preparation . . . 76
3.3 Fatigue Testing . . . 79
3.3.1 Appropriate Test Load Selection . . . 79
3.3.2 Loading Conditions . . . 81
3.4 Results . . . 82
3.5 Discussion . . . 85
3.6 Conclusions . . . 86

4 Effects of Arcing on the Contact Wires 87
4.1 Arcing in Overhead Line Electrification . . . 87
4.1.1 Pantograph Arcing . . . 88
4.1.2 Flashover . . . 89
4.2 Materials and Methods . . . 91
4.2.1 Arc Investigation in Real OLE Contact Wire . . . 93
4.2.2 Overhead Line Arc Machine . . . 94
4.2.3 Sample Preparation for Experiments . . . 98
4.2.4 Arc Experiments . . . 99
4.2.5 Specimen Preparation for Metallography . . . 100
4.2.6 Metallurgical and Mechanical Investigations . . . 105
4.3 Results . . . 106
4.3.1 Arc Damage and Microstructure . . . 106
4.3.2 Voltage-Current Measurements . . . 119
4.3.3 Temperature Measurements . . . 123
4.3.4 Hardness . . . 124
4.3.5 Hardness Map with Microstructure . . . 127

4.3.6 Tempering Effects of Arcing . . . 130
4.4 Discussion . . . 132
4.5 Conclusions . . . 135

5 Thermal Modelling of Arc Affected Contact Wire 136
5.1 Hypotheses Used in the Model . . . 136
5.2 Understanding the Mechanism of Arcing . . . 138
5.3 Thermal Effects of Arcing between the Pantograph and Contact Wire . . . 139
5.3.1 Properties of Contact Wire in the Thermal Model . . . 139
5.3.2 The Quality of Finite Element Models and Meshes . . . 142
5.3.3 Boundary Conditions . . . 144
5.4 Results . . . 145
5.4.1 Comparing Temperature Results with Experimental Measurements . 146
5.4.2 Thermal Distribution in OLE Contact Wire . . . 148
5.5 Discussion . . . 153
5.6 Conclusions . . . 154

6 Effects of Arcing on the Fatigue Life of Contact Wires 157
6.1 Introduction . . . 157
6.2 Materials and Methods . . . 157
6.2.1 Arc Exposure . . . 158
6.2.2 Fatigue Testing . . . 159
6.3 Results . . . 162
6.3.1 Fatigue Results . . . 162
6.3.2 Fracture Analysis . . . 165
6.4 Discussion . . . 168
6.5 Conclusions . . . 170

7 Conclusions and Future Work 171
7.1 Conclusions . . . 171
7.2 Future Work . . . 174
7.2.1 Academic Next Steps . . . 174
7.2.2 Application Next Steps . . . 175

References 177

Appendix A Fatigue Properties of OLE Contact Wires **193**
A.1 UK Electrification History 193
A.2 OLE Circuit Breaker Components 197
A.2.1 Neutral Section 197
A.2.2 Section Insulator 197

Appendix B Chapter 4 **199**
B.1 SOLARC Machine Configuration 199
B.1.1 High Speed Camera Measurement 199

Appendix C Parameters Used in Thermal Modelling **201**
C.1 Hypothesis for Developing the Model 201
C.1.1 Thermal Cooling due to Radiation 201
C.2 FE Model Parameters 201
C.2.1 Specific Heat and Thermal Conductivity 201

List of figures

1.1 Schematic of the overhead contact line 2

2.1 Length of electrified rail network (route km) in European countries 7
2.2 Electrification systems in Europe 8
2.3 Contact systems in railway electrification 9
2.4 Overhead line contact line components 12
2.5 Schematic of the pantograph 13
2.6 Schematic of the pantograph 14
2.7 A contact wire cut from OLE main line 15
2.8 Silver-copper phase diagram 16
2.9 Identification grooves on the top surface of the copper-silver contact wire . 16
2.10 Contact wire manufacturing process 18
2.11 Schematic of grain size and grain boundaries 19
2.12 Pantograph bending effects on contact wire 22
2.13 Schematic of a sliding wear 24
2.14 Comparison of contact wire wear against copper and graphite pantograph strips 25
2.15 Effects of electric current on sliding friction of contact wire-pantograph pair 26
2.16 Stress and cycles to failure graphs of different materials 28
2.17 Dynamic stress loading over time 29
2.18 Log-log scale strain and reversals to failure 31
2.19 General design criteria for axial fatigue testing by ASTM E466 34
2.20 Schematics of types of machines used in fatige testing of ASTM specimens 36
2.21 Schematic of the contact wire fatigue rig in previous studies 37
2.22 Surface defects in contact wire 38
2.23 Fatigue crack near a junction claw of a contact wire 39
2.24 Standard mean stress emprical curves 40
2.25 Fractured surface of Cu-Mg contact wire after fatigue bending 41
2.26 Schematic of the contact wire fatigue rig in previous studies 42

2.27 Schematic of failure modes 43
2.28 Schematic of a finite width centre cracked sample 44
2.29 Schematic of a finite width edge cracked sample 45
2.30 Standard fracture toughness testing specimens by ASTM 46
2.31 Schematic of crack branching 47
2.32 Schematic of crack branching 48
2.33 Void forms in ETP copper sample due to hydrogen embrittlement reaction . 52
2.34 CFD analysis of temperature distribution when the current is 200 A 53
2.35 Schematic of the rotating disc experimental setup 54

3.1 Methods used in testing the fatigue life of the contact wire 57
3.2 Electrification map of Great Britain 59
3.3 Peak force in GWML 61
3.4 Stiffness profiles of standard overhead contact lines 62
3.5 General features of OLE designs in Europe and the UK 63
3.6 Schematic of boundary conditions of a span length of contact wire 64
3.7 Finite element model with the mesh and beam connections 65
3.8 Convergence analysis of the simplified FE model 66
3.9 The maximum stress in the middle section of the contact wire at 350 N contact force 68
3.10 Relationship between contact force and maximum stress for different overhead line designs 69
3.11 Relationship between contact force and maximum strain for different overhead line designs 70
3.12 Tensile test 71
3.13 Stress-strain behaviours of copper silver contact wire 72
3.14 Comparison of stress-strain curves of tested copper-silver contact wire and different grade wires in the literature 73
3.15 The four-point bending mechanism used in the experimental design 74
3.16 Schematic of movement of the components 75
3.17 Components of OLE fatigue apparatus 76
3.18 Tensioning mechanism of OLE fatigue apparatus 77
3.19 Monitoring of the fatigue experiments 77
3.20 Clamps and the contact wire used in fatigue experiments 78
3.21 Clamps and the contact wire used in fatigue experiments 79
3.22 Convergence analysis of FE model in log scale 80
3.23 The effect of the contact wire tension on the fatigue loading condition . . . 81

3.24 Strain-life curve of the tested contact wire samples 83
3.25 Fracture surface and crack directions of the samples in Test 5 and Test 9 . . 84

4.1 Pantograph arcing 88
4.2 Flashover between structures and OLE live wires 90
4.3 Methods used for investigation of the arc damage to the contact wire 92
4.4 Flashover arc exposed contact wire samples 93
4.5 Schematic of OLE arc rig 94
4.6 Configuration of SOLARC Machine 95
4.7 Actuator position recorded with the highspeed camera measurement 96
4.8 Equipment used in voltage-current measurements 97
4.9 Contact wire samples in arc experiments 98
4.10 Longitudinal sectioning of the contact wire 101
4.11 Mounted specimens for optical metallurgy 101
4.12 Surface improvement of specimens with grinding and polishing 103
4.13 Etching process of contact wire samples 104
4.14 Optical microscope used in microstructural investigations 105
4.15 Schematic of micro hardness indentation of sectioned contact wire samples 106
4.16 Microstructure of a control sample with no arc damage 107
4.17 Microstructure of flashover samples 108
4.18 Hardness analysis of arc spots extracted from OLE main line 109
4.19 DC Arc presence during the experiments 110
4.20 Burn marks on the surface of contact wire samples 110
4.21 Microstructure of the contact wire before and after arcing 112
4.22 Microstructures of the contact wire samples 113
4.23 Microstructure of T5 (double arcing) 113
4.24 AC Arc presence during the experiments 114
4.25 Microstructures of the contact wire samples tested with AC 115
4.26 Voids in the microstructure after arcing with 200A and repeated arc 116
4.27 3D surface mapping of void forms 117
4.28 Arc damage in oxygen free copper with different magnifications 118
4.29 Hardness survey of arc affected OFC 119
4.30 Current and voltage measurements with corresponding carbon collector position during the arc experiment 120
4.31 Power generated by arcing 122
4.32 Setup used to measure temperature variations of contact wires during the experiments 123

4.33 Maximum temperature of measured points over the time 124
4.34 Hardness reduction of the sample of T4 (200 A- Multiple arc) 125
4.35 Hardness variation of tested samples 126
4.36 Hardness map of the samples from experiments with microstructure 129
4.37 Hardness map of the samples from OLE main lines with microstructure . . 130
4.38 Grain sizes after tempering and arcing of the copper samples 131

5.1 Geometry and model of pantograph-contact wire system 138
5.2 Burn marks measured after the experiments with AC and DC 140
5.3 Sensitivity analysis of the burn mark diameter 141
5.4 Mesh sizing regions used in finite element models 143
5.5 Convergence analysis of FE models of DC and AC 144
5.6 Boundary conditions of the FE model 145
5.7 Verification of FEM results by comparing the temperature variation of selected points 147
5.8 The difference in the maximum temperature between FE model solutions and experimental findings 147
5.9 Maximum temperature distribution in the cross section of the contact wire model 148
5.10 Maximum temperature distribution at bottom surface of the contact wire . . 149
5.11 Temperature distribution from A to B across the cross section of the contact wire 150
5.12 Cooling stages of contact wire from A to B after reaching at maximum temperature with 200 AC 151
5.13 Cooling stages of contact wire from A to B after reaching at maximum temperature with 200 DC 152
5.14 Combination of the optical microstructure images and FE temperature solutions 154

6.1 Flow chart of the methods applied for assessing effects of arcing on fatigue life of OLE contact wires 158
6.2 SOLARC machine setup used in arc exposure of contact wire samples . . . 159
6.3 Fatigue testing of arc affected contact wire samples 160
6.4 Arc-affected contact wire sample loading with bending 160
6.5 Arc-affected contact wire sample loading with reverse bending 161
6.6 Strain-life curves of the contact wire with arc-free bending, arc-affected bending and arc-affected reverse bending conditions. 165

6.7 Fracture surface and crack initiation locations of contact wire samples in the fatigue tests loaded with plastic strain 166
6.8 A typical fatigue fracture after testing the arc-affected contact wire with fully elastic reverse bending condition 167

A.1 The design of Arthur Flury neutral section 197
A.2 A typical section insulator used in OLE main lines 198

B.1 Highspeed camera unit used in measuring movement of current collector . . 199
B.2 Configuration of highspeed camera equipment 200

C.1 Thermal conductivity of copper from 1 K to the melting point 203
C.2 Thermal conductivity of copper from the melting point to 1900 K 204
C.3 Temperature depended specific heat of copper material 204

List of tables

2.1 Current values in OLE main lines 11
2.2 Contact wire configurations 14
2.3 Composition of AC120 contact wire 17
2.4 Material properties of Copper-Silver contact wire 17
2.5 Contact force limits for different current types and train speeds 23
2.6 ASTM standards for testing the fatigue behaviours of specimens 34
2.7 Pantograph-contact wire polarity 51

3.1 System parameters of Great Western Series 1 58
3.2 Maximum contact forces measured in GWML 60
3.3 Mesh parameters used in convergence analysis 66
3.4 Varying parameters in finite element model 67
3.5 Increase in stress and strain values in OLE main lines between 100 N and 300 N contact force. 69
3.6 Copper-silver contact wire tensile test results 71
3.7 Mechanical properties of CuAg contact wire and comparison with other grades in literature 72
3.8 Element quality assessments of the FE model developed to determine fatigue test loads 80
3.9 Load selection for fatigue testing 81
3.10 Fatigue test results 82

4.1 Parameters used in the arc experiments 99
4.2 Traditional grinding and polishing parameters for copper alloys 102
4.3 Hardness reduction and input energy due to arcing 127
4.4 The maximum grain size of samples after arcing and tempering 132

5.1 Material properties used in FE modelling 142

5.2 Element sizes and corresponded number of elements used in convergence analysis 143
5.3 Measures of element quality 144
5.4 Heat input converted from voltage-current measurements 146

6.1 Fatigue testing parameters in bending condition 161
6.2 Fatigue testing parameters in reverse bending condition 162
6.3 Fatigue life results of arc free and arc affected contact wire samples 164

C.1 The energy lost per unit time due to radiation depending on maximum temperature at the ambient temperature of 18 degrees. 202
C.2 Average specific heat of copper in the forms of solid and liquid 202

Symbols

Roman Symbols

a	Crack length
b	Fatigue strength exponent
c	Fatigue ductility exponent
d	Grain size
E	Young's modulus
E_a	Accumulated energy
F_M	Mean force
F_N	Perpendicular force
G	ASTM grain size
H	Hardness
h	Height
I	Electric current
I_{peak}	Peak current
K_y	Hall-Petch slope
K_{ad}	Wear coefficient for adhesive wear
K_{I_c}	Fracture toughness
K_i	Stress intensity factor

L Specimen Length

m_1 Mass of the lover arm of the pantograph

m_2 Mass of the upper arm of the pantograph

m_3 Mass of the pantograph head

N Cycles to failure

N_{AE} Number of grains per square inch

Q Volume of material loss

q Heat transfer per unit time

R Stress ratio of the system

$R_{p0.01}$ Proof elastic limit

$R_{T=300K}$ Electrical resistance of a metal at room temperature

$R_{T=4.2K}$ Electrical resistance of a metal at liquid helium temperature

s Sliding distance

t Time

T_0 Ambient temperature

T_i Object temperature

T_{RE} Recrystallisation temperature

U Voltage drop

v Speed

V_{peak} Peak voltage

V_{RMS} Root mean square of voltage

w Specimen width for fracture analysis

Greek Symbols

α Stephan-Boltzmann constant

ε Strain

ε_a Strain amplitude

ε_e Elastic strain

$\varepsilon_f^{'}$ Fatigue ductility coefficient

ε_p Plastic strain

$\varepsilon_{p0.01}$ Proof elastic strain

λ Emissivity coefficient of ojject

π $\simeq 3.14\ldots$

σ Normal stress

$\sigma_f^{'}$ Fatigue strength coefficient

σ_s Standard deviation of contact force

σ_a Stress amplitude

σ_e Fatigue limit under zero mean stress

σ_i Friction stress

σ_{max} Maximum stress

σ_{min} Minimum stress

σ_m Mean stress

σ_r Stress range

σ_y Yield strength

σ_{TS} Tensile strength

Acronyms / Abbreviations

AC Alternating Current

ASTM American Society for Testing and Materials

BS British Standards

CFD Computational Fluid Dynamics

DC Direct Current

DOF Degree of freedom

EN European Norm

fcc Face centered cubic

FE Finite Element

HAZ Heat affected zone

HRE Hydrogen Reaction Embrittlement

IMS Industrial methylated spirit

OFC Oxygen-free copper

OCS Overhead Catenary System

OLE Overhead Line Equipment

ROCS Rigid Overhead Conductor Rail System

RMS Root Mean Squared

RRR Residual resistivity ratio

SOLARC Sheffield Overhead Line Arc Machine

UK United Kingdom

Chapter 1

Introduction

The railway is considered one of the most efficient ways of passenger and freight transportation in the world. The demand in passenger and freight activity is expected to be more than double by 2050, and it has been already known that the transport sector is responsible for more than half of global oil demand and around one-quarter of global CO_2 emissions from fuel combustion [1]. Reports showed that emissions from transports could be reduced up to 60 % by electrification [2]. Therefore, recently, railway electrification has been paid particular attention. Just over a quarter of railway lines (344000 km of 1.3 million km) are electrified in the world, but it is expected to grow in the order of 50 % by 2050 [3]. Mainly Overhead Line Equipment (OLE) systems are used for rail mainlines as well as public transportation. These systems are complex structures that contain a number of elements along with mechanical, electrical and electronic equipment. Many challenges are affecting the quality of transmitting power from OLE cables to the trains and reliability of the system. Pantograph-contact wire interaction (Fig. 1.1) is considered one of the most critical research areas to enhance the reliability and efficiency of the OLE systems. In particular, the contact wire is the vital component which does not have a backup wire, when it fails, the train will stop, and serious incidents or disruptions are expected. Therefore, failures in the contact wires need to be predicted and prevented.

In this thesis, research identifying the effects of arcs on mechanical and metallurgical properties, and the fatigue life of contact wires are conducted, and results from experimental tests are discussed. The findings from arc experiments are extended by a finite element (FE) thermal model about temperature distribution in the contact wire during arcing.

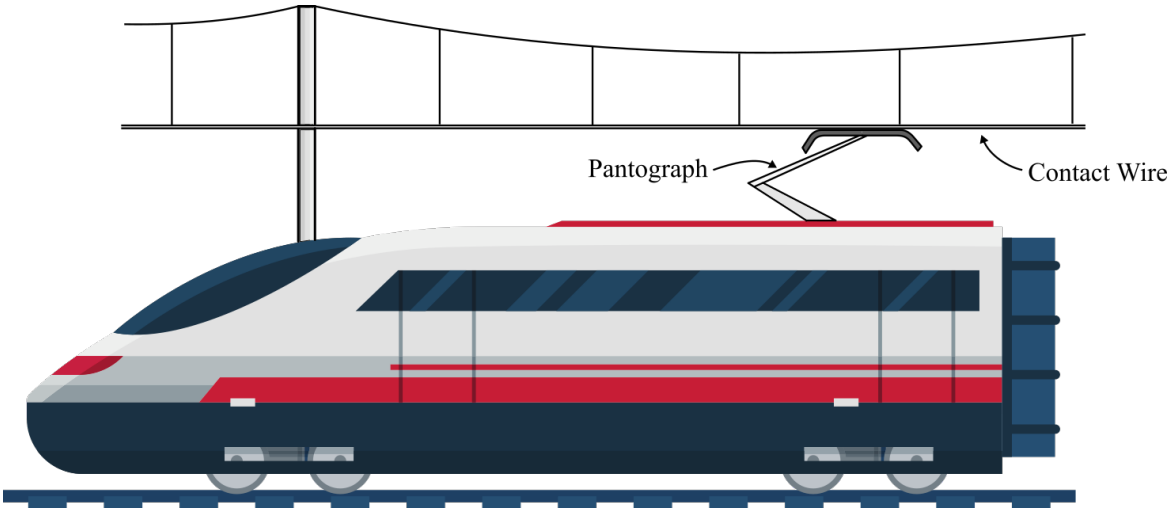


Fig. 1.1 Schematic of the overhead contact line

1.1 Aim and Objectives

This study aimed to answer the question of whether arcing is a cause of damage, and then also the potential fatigue mechanism by which it creates that damage and a possible way to mitigate it. Therefore, existing OLE contact wires were analysed for fatigue and arcing problems, and contact wire samples were tested in laboratory conditions and to understand the contribution of arc damage to the reduction of fatigue life of contact wires.

The following objectives provided as the steps of this aim;

- Understanding the stress in OLE driving the contact wire fatigue
- Building an experimental set-up for testing the fatigue life of the contact wire with pretension
- Testing the contact wires experimentally to estimate the fatigue life
- Investigating arc cases in contact wires extracted from a real OLE mainline
- Designing experimental configuration to test arcing in laboratory
- Conducting experiments to find out the arc damage to the contact wire and its contribution to the reduction of fatigue life of contact wires
- Developing a thermal model with FE for an in-depth study on the thermal distribution of the contact wire during the arcing process using experimental outputs
- Draw conclusions on the consequences of arcing to the OLE reliability and maintenance

1.2 Thesis Outlines

This thesis is divided into five main chapters.

1.2.1 Literature Review (Chapter 2)

In this chapter, existing studies about OLE fatigue and arcing was investigated. Experimental and theoretical approaches to the contact wire and pantograph interaction problems were studied, and current research gaps in the literature were identified.

1.2.2 Fatigue Life of Overhead Contact Wires (Chapter 3)

Contact wires are subjected to repeated bending strain caused by uplifting force from the pantograph. In particular, these dynamic stresses increase due to the growth of train speed. It is combined with the pretension in the wires that is designed to prevent sagging in the lines.

In this chapter, the fundamentals of the fatigue phenomenon in OLE contact wires are explained, and the relationship between the contact force and stress magnitude in the contact wire is established. UK Series 1 mainline electrification is analysed by using test inspection train data, and cycling peak force values are determined at specific locations. These results are used for developing a test scheme. A machine is designed to test the fatigue life of OLE contact wires with realistic boundary conditions. In this machine, repeating bending force and pretension in the wire are applied. Different loading conditions and parameters are tested in the experiments to explore a range of conditions representative of service loading on the components. The loading parameters were selected based on the findings from the OLE mainline inspection, which was carried out initially in this chapter.

1.2.3 Effects of Arcing on Contact Wires (Chapter 4)

The heat transferred by arcing between the contact wire and pantograph causes defects on the surface of the contact wire. Material loss during arcing also contributes to the wear of overhead catenary systems. However, the interior modification of the contact wire due to arcing is less visible but potentially severe defect produced.

This chapter investigates metallurgical and mechanical modifications after arcing in the contact wire. Before reporting arcing, the Sheffield Overhead Arc (SOLARC) machine that replicates the arcing in OLE is described. SOLARC allows us to control the parameters of current flowing in the circuit, the type of the current AC or DC and the number of arcs.

Grain modifications, voids and hardness survey of the sectioned area of the contact wire are examined at the microscopic scale. Additionally, the material of low oxygen content

copper is tested to explore if this offers a way to reduce voiding after arc exposure. Voltage and current during the experiments are recorded and analysed. Differences between AC and DC arcs are explored and correlated with energy input. This voltage and current data provide essential input for the finite element model designed in Chapter 5 in order to investigate thermal distribution in the contact wire.

The results of the experiments are also compared with contact wire samples that are extracted from UK OLE mainlines. The same metallurgical and mechanical investigations are conducted for the extracted contact wires and validate the findings of the lab investigation.

The samples to test the effects of arcing on fatigue properties of contact wire in Chapter 6 were exposed to arcs during the work described here by using the SOLARC machine.

1.2.4 Modelling Thermal Damage Due to Arcing with Finite Element Method (Chapter 5)

The thermal path, which is taken from the sample during and after arcing, plays an essential role in understanding the modification of grain sizes and shapes in the contact wire. Although the duration of arcing is in milliseconds, results in Chapter 4 show that it can reform the microstructure of the contact wire and leave defects in the material.

Due to the limitations of temperature measurement possible in an arc spot, a detailed model is needed to understand how the temperature changes over time in the material. Therefore, a finite element model is developed by using the voltage-current data from Chapter 4.

In order to verify the finite element model, temperatures of selected points on the models are compared with those of locations measured in experiments in Chapter 4.

This study provides insights into understanding the maximum temperature of different layers of material, arc damage, grain growth, recrystallisation, and the transition occurred after arcing in the contact wire.

1.2.5 Effects of Arcing on Fatigue Properties of Overhead Contact Wires (Chapter 6)

The evidence from Chapter 4 shows that arcing generates damage to contact wires even in cases of a brief single arc exposure. OLE contact wires are subjected to combined pretension and bending, and it is essential where the arc spots are located relative to peak stress in the wire.

In this chapter, the upper and lower surfaces of the contact wire are subjected to arcing with SOLARC machine, and contact wire samples are tested with the equipment designed in Chapter 3. The damage due to heat influences the fatigue characteristics of contact wires; therefore, the fatigue life of the contact wire with different loading parameters are tested and compared with those without arc damage tested in Chapter 3.

The data generated here provides evidence of how important it would be to prevent arcing or enhance the metallurgical properties and extend the fatigue life of the contact wire at specific locations in which is likely to observe arcing.

1.3 Contributions to Knowledge

This thesis intends to determine whether arcing causes damage in the contact wire and then its potential to initiate the fatigue and a possible way to mitigate it. The study builds a new understanding of OLE contact wire reliability and safety related to arcing and fatigue life. Experimental results and the analysis of extracted OLE mainline contact wires confirmed that local heating during arcing modified microstructure of the contact wire. The arcing damaged the material surface and microstructure regardless of the current system of DC or AC. Investigation of real OLE contact wires also showed that arcs could occur not only between the contact wire and the pantograph but also between civil structures (bridges, overpasses) and the contact wire. This type of arcs was usually placed on the upper and side surfaces of the contact wire and named "flashover arcs". Examination of arc exposed contact wire's fatigue properties showed that arc damage on the upper surface of the contact wire represents a crack initiation point and reduce the fatigue life. However, the arcing spot that was on the lower surface of the contact wire did not contribute to the fatigue fracture due to being on the compression surface. Therefore, it is essential to note that arcing problem due to flashovers between contact wire and civil, structural components can play an important role in fatigue life of OLE contact wires.

Chapter 2

Literature Review

The literature chapter of this thesis has been included for an understanding of OLE contact systems and, the pantograph and contact wire interaction problems. The pantograph and contact wire interaction is a fast-growing research area that holds a number of different research purposes. In this thesis, this interaction was investigated to understand the effects of electrical arc discharge on the fatigue properties of OLE contact wires. However, because this research idea has not been studied with arc problem and fatigue together thus far, studies in the past were needed to be reviewed separately as arc and fatigue problem in OLE contact wires. The theories used in conducting this research and the literature of material and metallurgical properties of the contact wire containing copper-silver were also reviewed in the context.

2.1 Background

The primary purpose of OLE is not only supplying electrical energy to trains without storing energy onboard but also is ensuring uninterrupted traction to the railway vehicles.

Electrical power demand on the railway continues to increase as a result of expanding electrification and longer, more frequent and more power-intensive trains. Transmission of power is done by either an overhead wire or by rails at ground level. AC systems often use overhead wires, and DC systems can use either an overhead wire or a third rail [4]. Approximately 40% of the British railway network is electrified, comprising 25 kV AC (two-thirds) and 750 DC (one-third) systems supplying traction power to trains [5, 6].

The railway electrification network also extends significantly across Europe due to low carbon emissions and 35 % cheaper operating costs compared to diesel trains [7]. Fig. 2.1 shows the total length of electrification in the rail network of European countries.

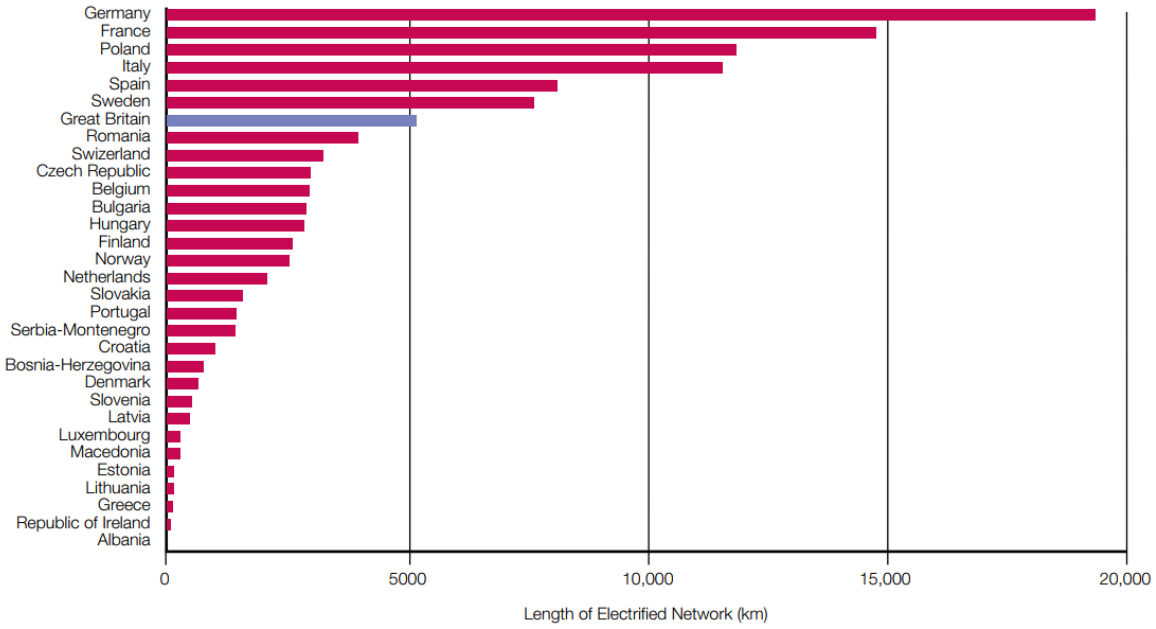


Fig. 2.1 Length of electrified rail network (route km) in European countries [8]

Electrified lines are classified differently due to the area of use, power systems and types of contact types. In this chapter, mainly, the overhead line type electrification system is explained, which is consistent with the content of the PhD study.

Due to the problems of human safety and energy efficiency, contact lines design was considered problematic over history. First attempts to use insulated rail systems to ensure power to electric trains were ineffective and unsuccessful. After the idea of building underground and overground systems, trains running on wires or rails have been used for passenger and freight transportation.

There are several approaches to classify the contact lines used in rail electrification. However, generally, it can be gathered under three main categories by;

- Voltage (Low voltage 750 V, high voltage 25kV)
- Current (AC, DC)
- Contact Systems

Electric trains can be running with different voltage, current and contact systems. However, AC type structures are preferred more in high-voltage mainline railways due to the flexibility to transmit power long distances with altering voltage-current values. Fig. 2.2 shows the variation of railway electrification in Europe.

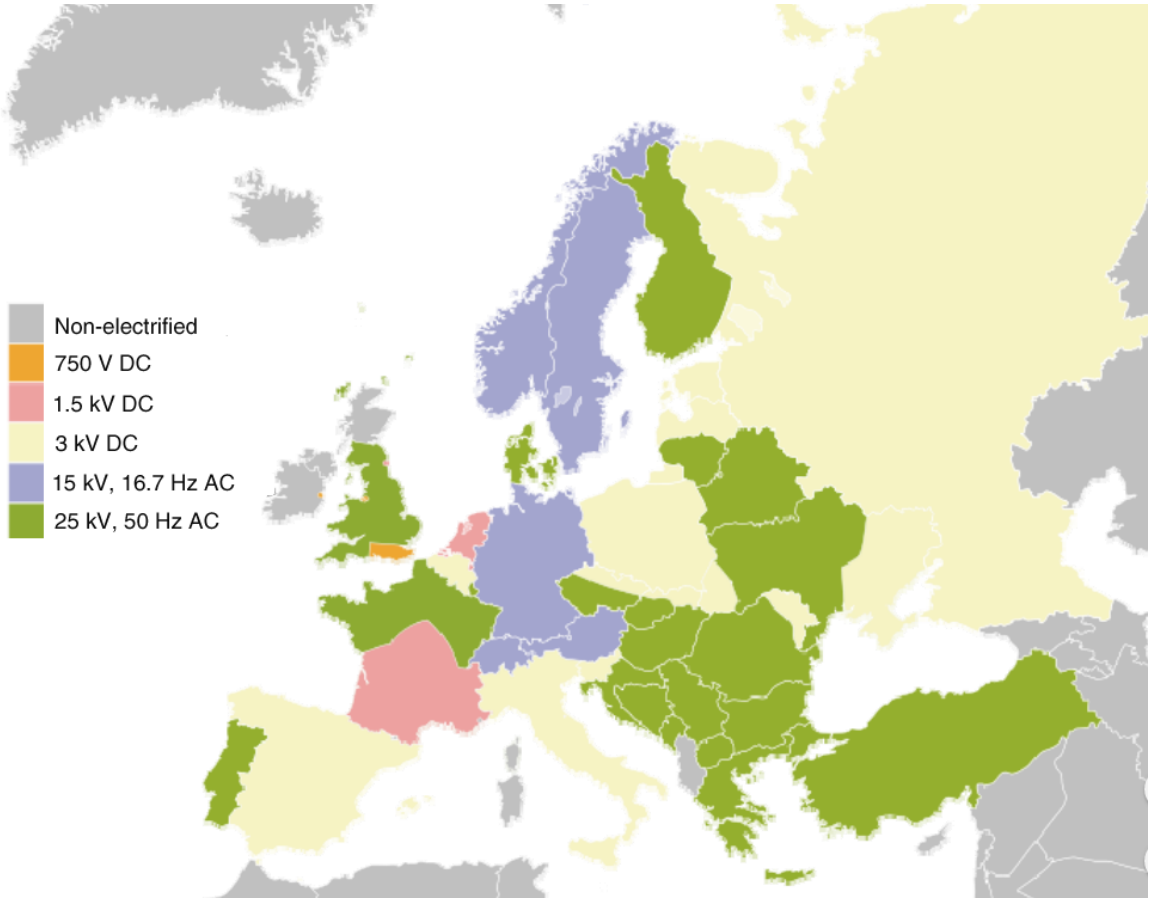


Fig. 2.2 Electrification systems in Europe [9]

In order to study and investigate dynamics and mechanical interactions in energy collecting systems, it is useful to categorise power traction depending on contact systems rather than classifying current and voltage type of the contact line.

Contact systems are classified by the location where the electrical contact occurs between train and power lines. In conductor rail systems, the electrical energy is provided for trains by semiconductors placed side of railways while in OLE, it is transmitted by the pantograph. Fig. 2.3 shows the classification of the contact line systems used in railway electrification [10].

Metros and trams are one of the most common rail transportation methods that are operated in city centres. Many measures have been taken to minimise the potential risks of electricity. One of the main regulations is that low-voltage systems are usually used in tram and metro electrifications. Secondly, on-ground systems, such as; trams, are designed to work with overhead line cables. Besides, third rail systems have been preferred in underground transportation because narrow tunnel structures are unable to accommodate large-scale OLE components.

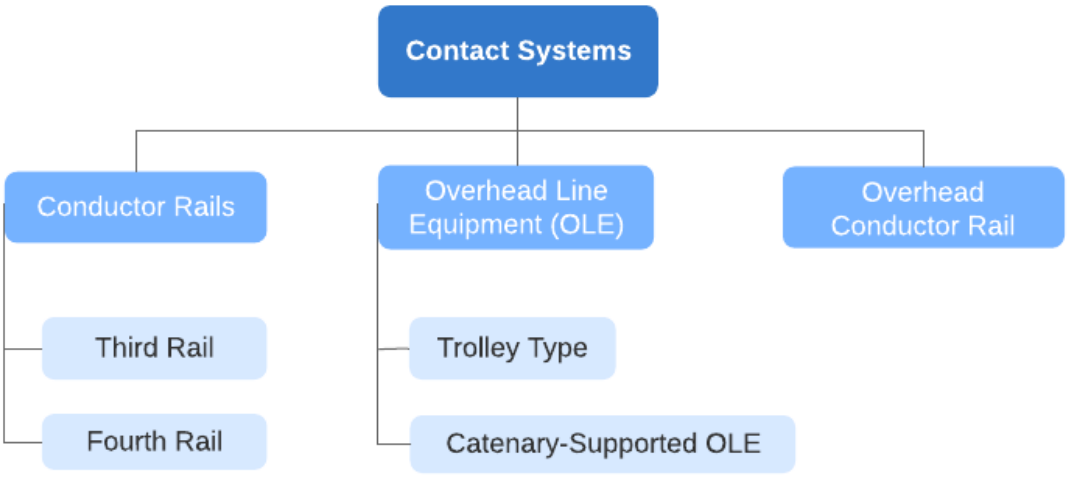


Fig. 2.3 Contact systems in railway electrification

Developments in conductor rail systems are solving some difficulties, such as; limited height for installation of OLE in tunnel structures. A rigid conductor system called Rigid Overhead Conductor Rail System (ROCS) has been providing solutions for tunnel electrifications since the 1980s. The ROCS makes it possible to transfer energy from conductor rails mounted the top of tunnel roof to pantographs which are above vehicles. In contrast to conventional overhead lines, clipped-in contact wire works without any mechanical tension

in ROCS. These new developing systems allow designers to build more reliable systems in tunnel structures thanks to the absence of tensioning in the contact wire, a small number of components and high fire resistance.

Recently, developments in the field of electrified railways have led to renewed interest in high-speed transportation across the world. The maximum speed of electrified trains has surpassed over 300 km/h in countries like Japan (405 km/h), Germany (403.7 km/h), South Korea (430 km/h), France (574.8 km/h), and China (483 km/h) [11]. In light of recent events in high-speed train technology, safety precautions and requirements are becoming more and more important day by day. Both DC and AC feeding systems may cause catastrophic incidents in railway electrification due to carrying a great amount of voltage. Therefore, mechanical and electrical interaction of the pantograph with the contact wire has a vital role in the reliability and efficiency of overhead train lines.

2.2 Overhead Line Equipment

The development of electric motors in the late 1800s marked a significant step forward in subway development, allowing trains to run on electric power transmitted through an overhead line or a third rail on the track [12]. Particularly, after the mid-twentieth century, electrification systems started to take place widely in the railway industry. When looking at principles of OLE, it has been used as a power transmitting system to provide uninterrupted electrical energy to running trains. It is also named as Overhead Catenary System (OCS) in Europe and the US. Design parameters of OLE can be varied for AC and DC units. It must be remembered that the OLE is a sort of electro-mechanical system and whereas contact wire is transmitting energy, it is also exposed to tensioning, uplifting and frictional contact with pantograph strips.

Geographic conditions, environmental effects, climate conditions and the route of the tracks can be considered one of the most critical challenges during the planning stage. Providing constant electric energy to the vehicle is the main aim of OLE systems. Hence, contact wires, messenger wires, catenary masts, registration arms, frames and other equipment should be arranged to ensure electric supply safely.

Many considerations are taken into account not only in the design stage but also in installation. Because of carrying high voltage on the system, every single minor fault can cause high impact failures. Maintenance of OLE components is vital as well as the installation. In case of any faults happened on catenary systems, the contact wire and the pantograph can be damaged initially and lead to catastrophic failures and significant disruptions as a result.

2.2.1 General Features

Due to the safety regulations, only overhead lines are allowed to operate at voltages above AC 1000V and DC 1500V [10]. Continuous energy demand becomes more important to improve the current collection efficiency of OLE systems with the increase of speed of electrified trains. Mainly, components, such as; contact wire, messenger wire, droppers, registration arms and stitch wire, play a crucial role in the dynamic behaviours of OLE. However, different from other components, the contact wire is directly subjected to mechanical and electrical contact with the current collector device pantograph that is placed on the roof of the trains. The supply current can vary based on train characteristics and the number of running trains in a section at any one time. Table. 2.1 shows current values used 25 kV AC main lines.

Table 2.1 Current values in OLE main lines [13]

Train Type	**Train Current Draw**
25kV AC passenger train	200 A
25kV Double headed freight train	500 A

2.2.2 Components of OLE

OLE comprises overhead contact lines, cantilevers, poles, foundations and return conductors to ensure current to be used by electrified railways. Contact lines consist of contact wire, messenger wire, droppers, stitch wires, fixed points and tensioning devices. Depending upon OLE design, other components can vary, however fundamental parts of the system can be listed as seen in Fig. 2.4.

Contact wire and the pantograph head are designed to be in contact over the train journey. Therefore, the contact wire is an essential element of the OLE to ensure continuous current flow by sliding contact with the pantograph. Messenger wire is required to support contact wire along its length and to withstand mechanical stresses exerted by pantograph and side winds. The connection of messenger wire and contact wire is held by droppers. They play an essential role to keep the contact wire in the correct position. Masts are structures carrying all of the OLE components, and associated insulators separate the live system electrically from earthed parts. The contact wire is connected to masts with registration arms. The distance in between masts is named span length and varies from 20 m to 80 m depending on track radii, train speed limits and wind effects [10]. In the UK max span length is limited by 65 m [14].

A tensioning device maintains the tensions in the contact and catenary wires to prevent any sagging that can cause discontinuous pantograph contact and irregular pantograph-wire

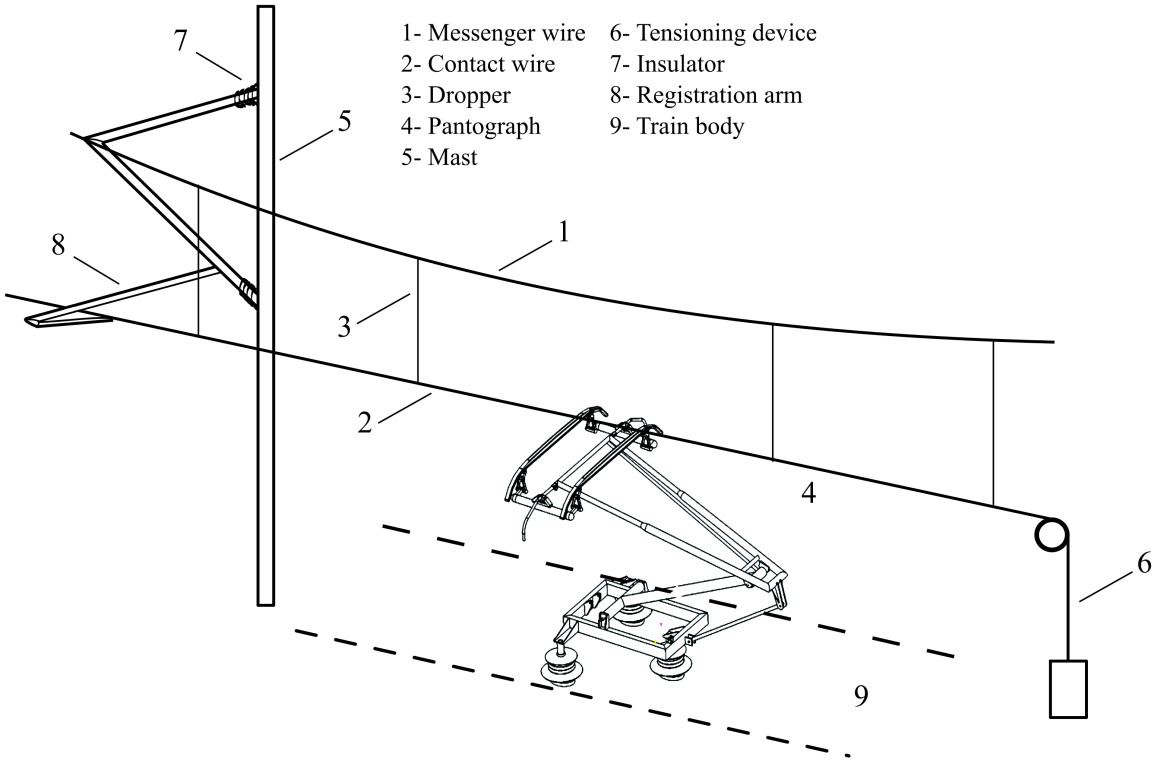


Fig. 2.4 Overhead line contact line components

sliding contact. Contact wire tensions can vary from 8 kN to 40 kN depending on the speed of train lines and climate conditions. Mainlines usually run between 10 kN and 20 kN [15].

The effect of pretension on the contact wire is also significant. Since constant tension in the OLE line creates uniaxial tension in the contact wire, it increases the mean stress. The increasing mean stress causes the systems more vulnerable to fatigue oriented failures.

2.2.3 The Pantograph

The pantograph is a device on the top of the train that collects electrical energy from mainlines and transmits into the train. Fig. 2.5 shows a schematic view of the pantograph. For good current collection, loss of contact between pantograph and contact wire is required to be minimum. Therefore, the pantograph controlled by an actuator provides a continuous uplifting force to the contact wire. In general, the pantograph is divided into four parts, namely; *collector head, upper arm, lower arm and base frame*. The collector's head consists of a carbon-grade strip that is in sliding contact with the contact wire. This interaction causes the strips to be replaced after a while due to the wear [16]. The vertical movement of the pantograph is driven by a spring load. The pantograph is placed to train's roof by a base frame and electrically insulated from the train body with insulators.

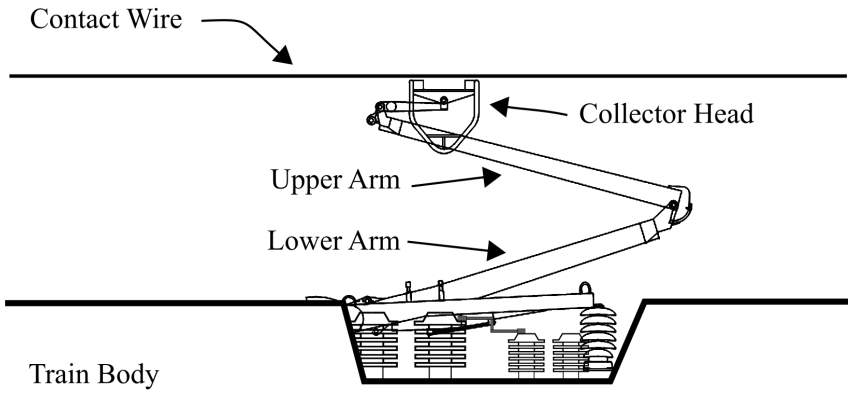


Fig. 2.5 Schematic of the pantograph

Considering the detailed dynamic characteristics of the pantograph, it is modelled as a mass-spring-damper system specified by the standard of BS EN 5318 [17] (Fig. 2.6). It is often represented with 3 lumped masses, namely; m_1 is the lower arm, m_2 is the upper arm and m_3 is the pan head [18, 19].

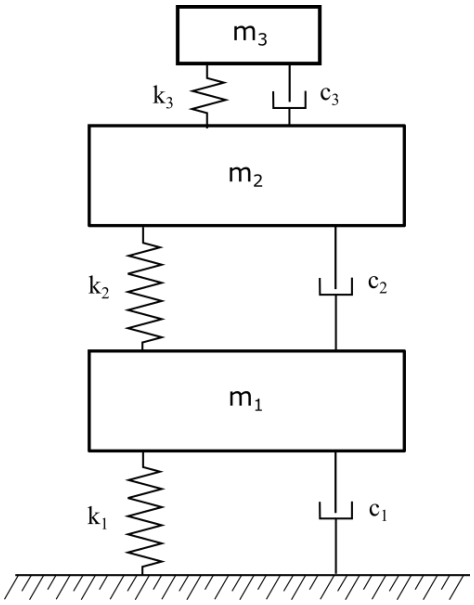


Fig. 2.6 Schematic of mass-spring-damper model of the pantograph

2.2.4 Contact Wires in OLE

Contact wires with circular shape and grooves on the side of the top section are manufactured from copper as a base material. The composition of contact wire alloys can be forms of copper-silver, copper-magnesium, copper-tin and copper-cadmium. Silver (0.1 %) is used as an additive to enhance the thermal and mechanical properties of contact wires. Design parameters, mechanical and electrical properties and chemical compositions of contact wires were standardised under BS EN 50149:2012. Contact wires are named with nominal cross-sectional areas. Table 2.2 shows contact wire standard sizes and configurations which are based on BS EN standards [20].

Table 2.2 Contact wire configurations [20]

Type	Nominal Cross Sections [mm^2]	Max Diameter [mm]
AC-80	80	10.52-10.72
AC-100	100	11.84-12.08
AC-107	107	12.27-12.52
AC-120	120	12.99-13.26
AC-150	150	14.53-14.85

Contact wires wear away over repeated train passes due to mechanical sliding contact with pantograph head. Hence, they need to be replaced after a certain period depending on

the traffic density of the train line and geographical conditions. Since contact lines work under pre-tensioning, worn contact wires are subjected to higher tensile stress due to reduced cross-sectional area. Therefore, wear of contact wires is limited between 20% and 30% of the original cross-sectional area [10], [21].

Different from flat bottom contact wires in trolley lines, circular shape grooved contact wires are used in mainline electrification systems. Grooves on the top sides of contact wire enable to connect OLE fittings, such as; droppers, connection clamps. Fig. 2.7 shows cross-sectional geometry of AC 120 type OLE contact wire.

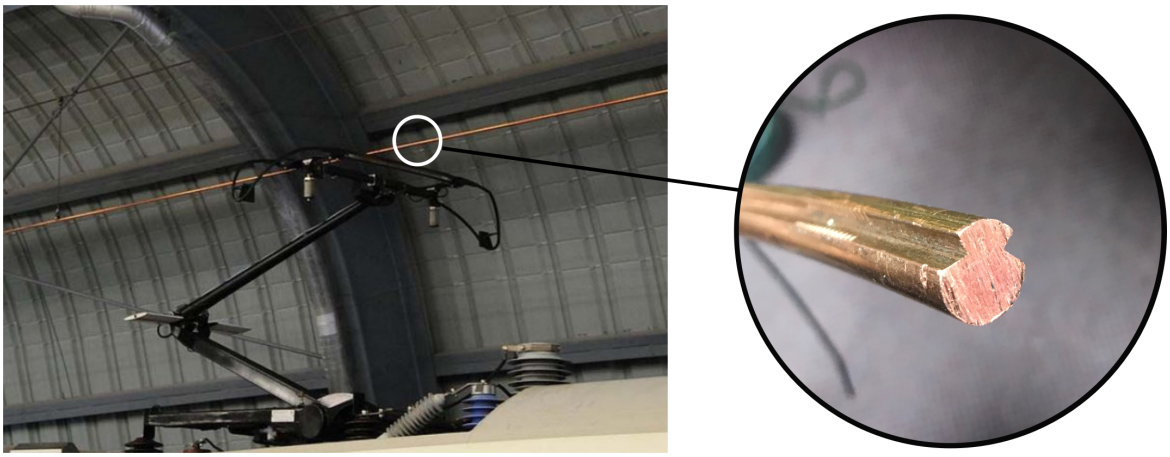


Fig. 2.7 A contact wire cut from OLE main line

Copper Silver Systems

Copper is one of the most used elements in electricity and it provides high electrical and thermal conductivity. However, due to that fact that copper element has poor mechanical properties, (tensile strength limited to 225 MPa), it needs to be strengthened with reinforcing elements [22]. Different alloying elements, such as; Ag, Cr, Fe, Nb, Zr and Be are used to enhance the mechanical properties of the material of copper. Additionally, hardening of the copper is also done by increasing dislocation density in the grains, such as; forming the material [23].

A copper-alloy with silver manufactured by drawing process is widely used in rail overhead line electrification. Copper-silver system is a eutectic equilibrium that is shown in Fig. 2.8. The equilibrium phases of the copper-silver system are liquid, silver-rich phase, face centred cubic (fcc) solid solution, with a maximum solubility of 8.8 wt. % Cu and copper-rich phase, fcc solid solution with maximum solid solubility of 8 wt. % Ag. The maximum solubility of Ag in Cu, in lower temperatures, below 200 $^{\circ}$ C is smaller than 0.1 % [25].

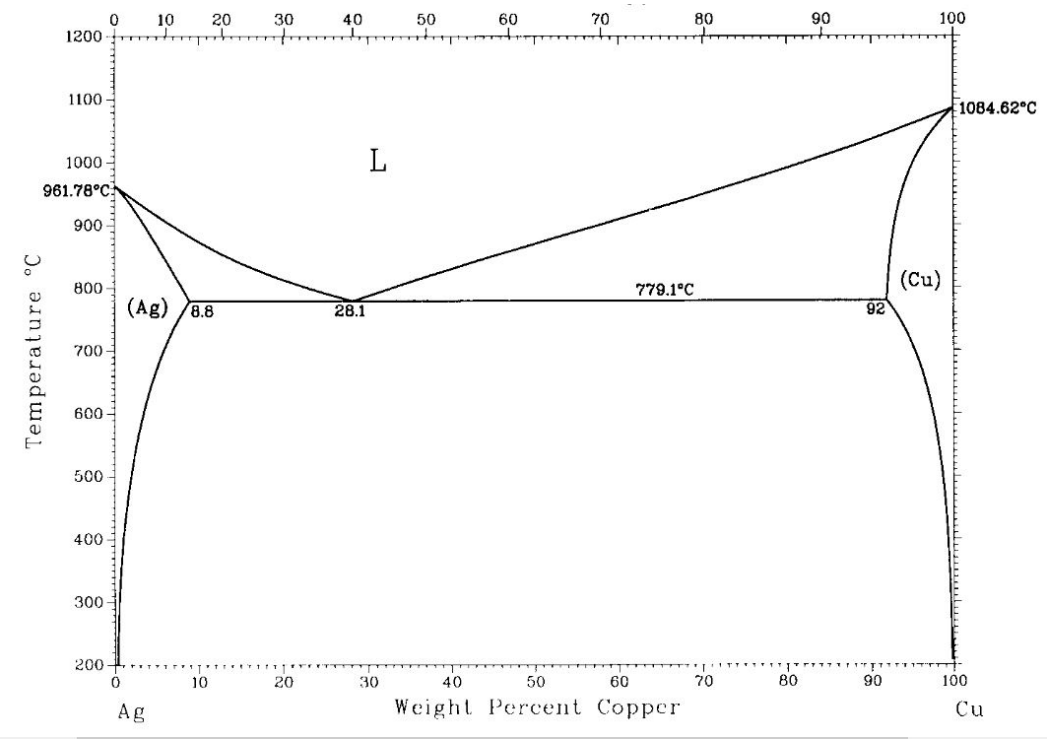


Fig. 2.8 Silver copper phase diagram [24]

Copper-Silver Contact Wires

Copper silver alloys are widely used in OLE rail electrification and manufactured by drawing process. According to BS EN 50149 [20], wires of copper alloy with silver contain two identification grooves on the top surface of the contact wire. Fig. 2.9 shows the identification grooves on the top surface and the geometry of cross-section of the contact wire.

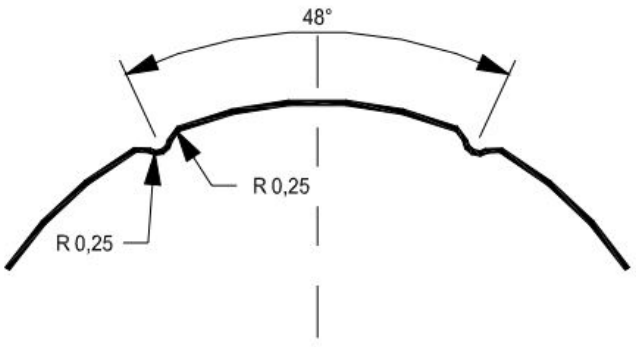


Fig. 2.9 Identification grooves on the top surface of the copper-silver contact wire

Copper alloy contact wires containing 0.1 % silver are used with the application name of AC120. Due to the low content of silver, this alloy maintains its Cu rich phase and fcc lattice structure within the range from room temperature and to the melting temperature. According to BS EN 50149, Table 2.3 and Table 2.4 show chemical composition and material properties of copper-silver contact wire.

Table 2.3 Composition of AC120 contact wire

			Composition in %				
Symbol	**Name**		**Cu**	**Bi**	**O**	**Ag**	**Other**
CuAg0.1	AC120	Min	Rest	-	-	0.08	-
		Max	-	0.0005	0.04	0.12	0.03

Table 2.4 Material properties of Copper-Silver contact wire

Material	**CuAg0.1**
Tensile Strength	375 MPa
Electrical Resistance	0.122 Ω/km
Hardness	120 HV
Density	8890 kg/m^3
Wear Rate*	0.0257 mm^3/m

*carbon strip-contact wire sliding contact with the force value of 170 N [26]

The residual resistivity ratio (RRR) is commonly used for defining the level of purity of conductor materials [27]. RRR value of copper with silver alloy up to 0.2 wt % is determined to be an average of 300 [28]. RRR is expressed as the ratio of a metal's electrical resistance at room temperature to that at 0 K, which is usually replaced by liquid helium temperature (4.20K) and calculated as follows [29];

$$RRR = \frac{R_{T=300K}}{R_{T=4.2K}} \tag{2.1}$$

Contact Wire Manufacturing

Mechanical properties of copper and copper alloy OLE contact wires are regulated by BS EN 50149 and ASTM B47-95a [30]. The copper contact wire is manufactured using the following processes [31];

- casting a copper rod with appropriate composition
- hot working or "conforming" the cast rod to reduce its diameter
- cold working to form the desired wire by drawing

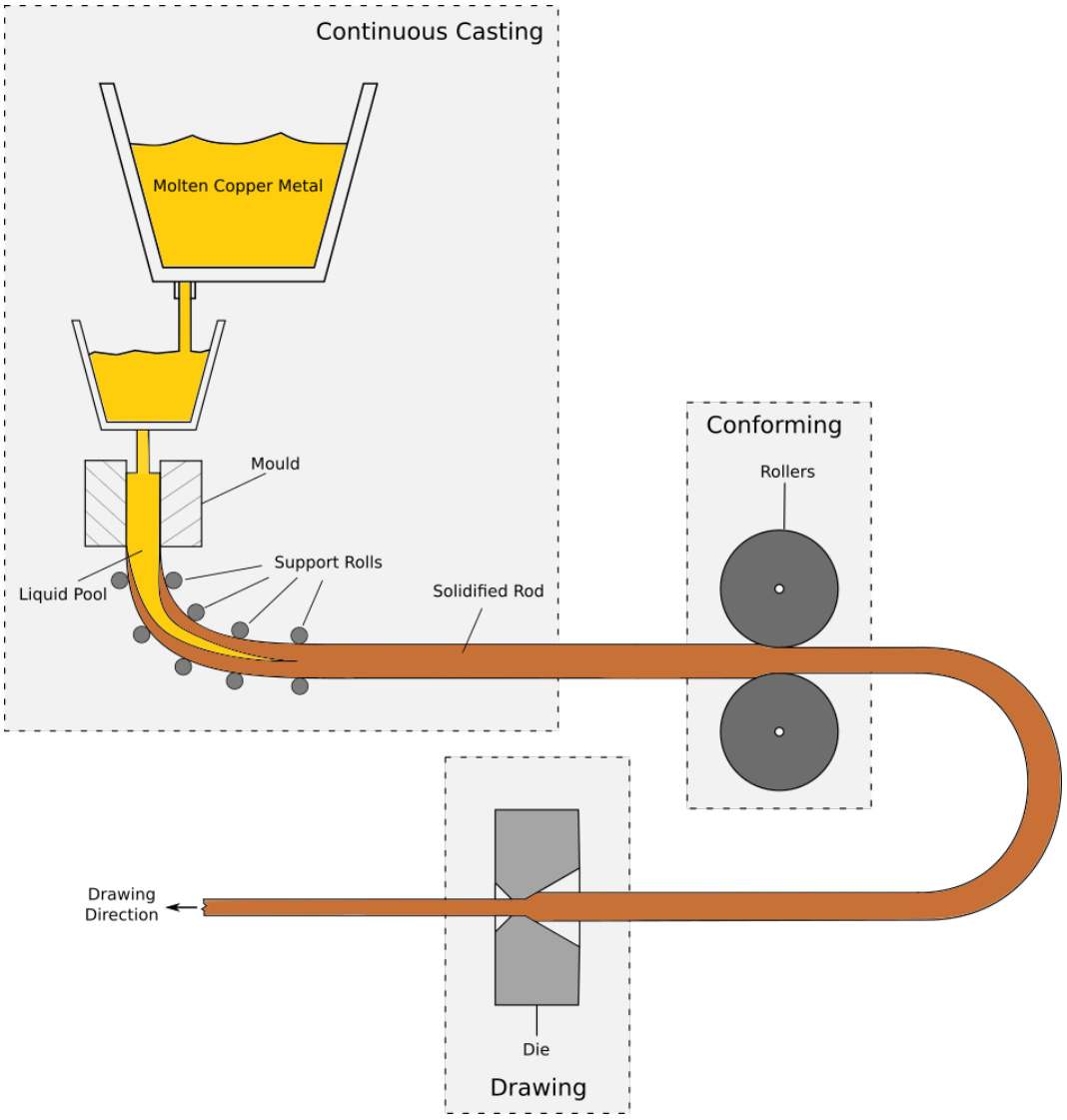


Fig. 2.10 Contact wire manufacturing process

Fig. 2.10 shows the processes of continuous casting schematically, conforming and drawing of contact wire manufacturing. Contact wires are produced from rods. These rods are often manufactured by continuous casting method. In this method, molten metal is poured into a mould and solidified while it is passing through mould and support rolls. This process is continuously sustained to obtain considerably long slabs or rods. After this stage, the rod

is passed through a rollers-pair to reduce its diameter. This process is named conforming. Lastly, in order to give the final shape (grooves and grips) to the contact wire, it is drawn through a die. The drawing is occasionally done cold to increase the strength of the contact wire.

Microstructure of Contact Wires

The microstructure is a general term used for covering a variety of material features such as; grain size, grain boundary or particle sizes. Different techniques and standards are followed for microstructural investigations. One of the most common techniques used to visualise the grain properties of the materials is "metallography".

In this section, the general properties of grain sizes and its effects on mechanical properties of the materials, and fundamental principles of sample preparation for metallography are explained.

Grain Size

Most of the engineering materials are polycrystalline that consists of three-dimensional individual grains [32]. Due to the different orientation of these individual grains, an interface named "grain boundary" occurs [33]. Fig. 2.11 shows a schematic of grains and grain boundaries under a microstructural inspection. Size and shapes of grains are the principal instruments to determine the mechanical properties of a material. Grain size quantifying is done by measuring grains per unit area/volume, average diameter or grain size number [34].

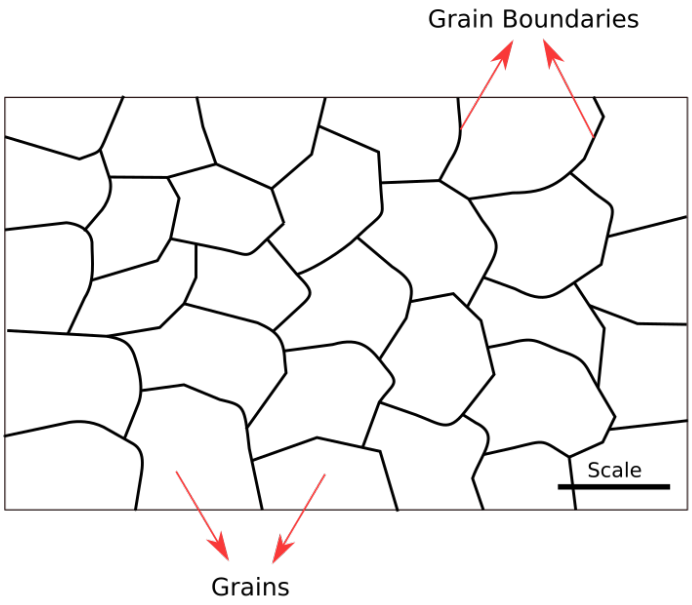


Fig. 2.11 Schematic of grain size and grain boundaries

One of the most important effects of grain sizes has been known that increased average grain size decreases the mechanical properties of polycrystalline metals [35]. This phenomenon is called Hall-Petch relationship and expressed as follows [36];

$$\sigma_y = \sigma_i + K_y \times d^{-(1/2)} \tag{2.2}$$

where σ_y is yield strength, σ_i is friction stress, K_y is Hall-Petch slope and d is grain size.

According to the Hall-Petch relationship the smaller grain size in the material, the more grain boundaries will be observed, and because grain boundaries behave as impediments as dislocations, the strength of the material will be increased. Further studies with copper materials also supported that yield strength of copper alloys increased with decreasing grain size [37–39].

Annealing of Coppers

Heat is generally seen as a factor strongly affecting the grain size of the material. This phenomenon is called annealing. Annealing can be either a process to modify the grain sizes of the material intentionally or a problem that occurs due to external factors. For instance, while annealing is used to give more workability to cold-formed materials, it can cause softening in electrical and electronic application materials due to Joule heating [40].

Three individual stages can be observed in annealing [41];

- Recovery relieves the energy in the dislocations without changing the shape and orientation of grains
- Recrystallisation replaces the highly formed grains with new-strain free grains
- Grain growth happens after the recrystallisation when the material is held at elevated temperatures for a longer period.

Yu et al. [42] investigated the mechanical properties of pure copper after the heat generated by cutting tool in machining. During their annealing experiments, they found that the grain size of pure copper varied from 100 μm to 200 μm and also the hardness of pure copper decreased from 107 HV to 57 HV due to annealing.

It was also understood from the studies by Reiss [43] et al. and Ma et al. [44] that electrical resistance of the copper increased gradually due to the decrease in the grain size. It was mentioned that grain boundaries and dislocations could increase the scattering of conducting electrons which results in an increase of electrical resistivity.

Specimen preparation is an essential step for optical metallography. This process needs to be completed correctly to avoid examination surface from being unable to visualise due to

scratches. Main characteristics that samples for metallography should contain, can be listed as below [45];

- Examination area should be free of scratches
- Surface should be kept flat, particularly edges of the samples otherwise, portions of the image under microscopic inspection will be out of focus
- Between different surface improvement processes, specimens should be adequately cleaned
- Deformations due to sectioning should be removed

The preparation stages for metallography can be named as, sectioning, mounting, grinding-polishing and etching.

2.3 Pantograph and Contact Wire Interaction Problems

OLE mainlines rely on the cables and supporting structure that carry high-voltage electricity (25kV). These structures and equipment are susceptible to mechanical or electrical problems. The pantograph exerts uplifting force to contact wire to maintain continuous sliding contact. Thanks to this contact, electrical current is transmitted to train through pantograph head. However, when sliding contact with electrical current is considered, this mechanism can create interaction problems on both pantograph and contact wire surfaces. Potential problems in the contact wire due to the effect of the contact force can be classified under two major headings, mechanical and electrical problems.

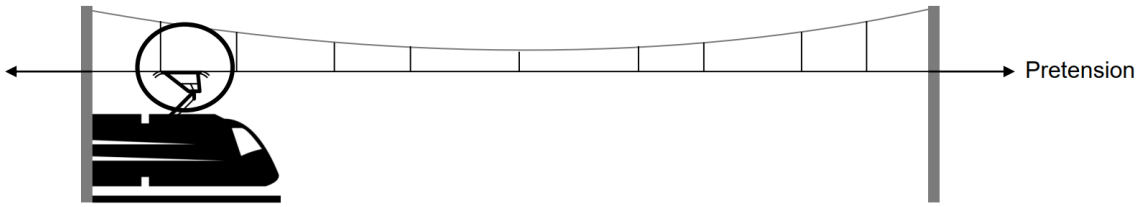
Speaking about the mechanical faults in the contact wire, exerting repetitive contact force by a pantograph and bending stress can be shown one of the most significant issues that needs to be taken into account and may result in mechanical failure of the contact wire. Another common mechanical issue seen in the contact wires is the wear due to sliding of the pantograph over the surface of the contact wire. Because this mechanical wear reduces the cross-sectional area of the contact wire, it has the potential to shorten the service life of the contact wire. Furthermore, the worn contact wire becomes vulnerable to the higher stress fluctuations because the reduced cross-section decreases the strength of the contact wire.

Not only the mechanical factors but also electrical problems play an essential role in the service life of OLE contact wires. Particularly, arcing is considered one of the biggest problems with the increase in the speed of trains. One of the main reasons for the arcing is shown to be contact loss between the pantograph and the contact wire.

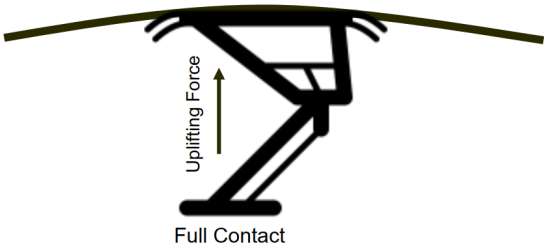
Although the problems in OLE were classified as to be mechanical and electrical, they are interconnected, and both mechanical and electrical problems can affect each other. Therefore, this research aimed to investigate the arcing problem and its effects on the fatigue life of the contact wire. In this research, firstly, the mechanical contact wire problems were reviewed, and the theoretical backgrounds used in the literature were explained. However, it was essential to review other mechanical issues that may influence the fatigue life of the OLE contact wire. Therefore, also literature review about wear and fracture of the contact wire were studied. Subsequently, the literature review of the arcing problem in the contact wire was done, and research gaps were identified together with findings from the past studies about arcing and fatigue problem in the contact wire.

2.3.1 Pantograph Bending Effects on Contact Wire

In order to sustain a continuous current flow from OLE to the pantograph, a static uplifting contact force, which is at least 60 N depending upon the configuration of the overhead line system and type of pantograph [46], is applied by pantograph. However, due to the contact wire profiles, OLE fitting structures (section insulators, neutral sections, clamps), higher contact forces can be experienced during the journey of the train. This contact force generates bending in the contact wire. Fig. 2.12 shows the bending effect of the contact force on overhead contact wire.



(a) Overhead Line System



(b) Bending due to contact force

Fig. 2.12 Pantograph bending effects on contact wire

Table 2.5 Contact force limits for different current types and train speeds

System	**Speed**	**Contact Force**	
		Maximum	**Minimum**
	km/h	**N**	**N**
AC	≤ 200	300	>0
AC	>200	350	>0
DC	≤ 200	300	>0
DC	>200	400	>0

The allowable range of the contact force is specified in standard BS EN 50119:2009 [47]. Mean value (F_M) and standard deviation of contact force (σ_s) are key parameters in current collection quality. According to BS EN 50119:2009, statical minimum and maximum of contact forces are expressed in Eq. 2.3 and Eq. 2.4 (based on three-sigma rule), respectively. The maximum and minimum limits of contact forces can also be seen in Table 2.5.

$$F_M - 3\sigma_s \tag{2.3}$$

$$F_M + 3\sigma_s \tag{2.4}$$

The static contact force is vertical exerted upward by the collector's head on the overhead contact line and caused by the pantograph raising while the vehicle is at a standstill. However, contact forces measured during the train journey are dynamic and generally higher than the static contact force.

2.3.2 Mechanical Wear

In the late 90s, the wear problem of contact wire that because pantograph slides along the contact wire over the train journey was addressed as one of the main problems that affected to efficiency of current collection and contact wire electrical properties by Hai He et al. [48]. They proposed to use solid lubricants in contact materials.

In general, wear is expressed in volume with loss of the material. Some of the common wear mechanisms can be listed as [49];

- Abrasion
- Adhesion
- Oxidation

- Surface fatigue

The basic concept of adhesion and abrasion is that when two material come into contact, they adhere to one other at localised sites [50]. However, in the abrasive wear, hard particles are the key instruments. Machining operation can be shown as an excellent example of abrasive wear. Concerning adhesive wear, surface roughness is the critical parameter that affects the wear between the materials in contact. Oxidation wear contains corrosive and chemical surface wear. Also, surface deformations due to repeated-cycle are studied in surface fatigue topic. Historically, the mechanism of adhesive wear is described by the theory of Archard.

If the contact between the materials distributes to a larger area, it is named sliding contact. However, if they roll one over the other, this results in rolling contact. In this thesis, because contact wire and pantograph is in mechanical sliding contact, sliding wear is explained in details.

Archard's Law

When the material in sliding contact over each other, one or both will be exposed to wear with a height of h (mm) [51]. Fig. 2.13 shows schematic of sliding wear of a block moving with the speed of v (mm/s) after sliding distance of s (mm).

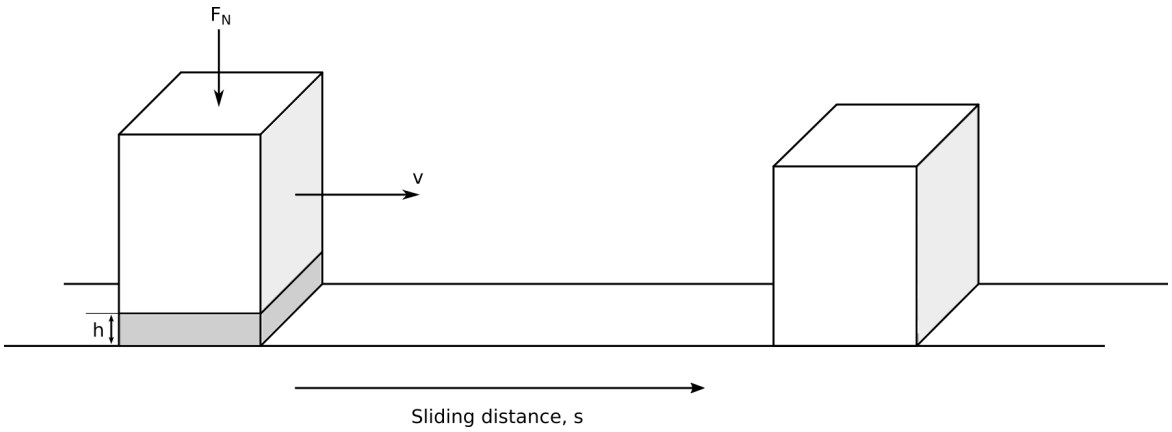


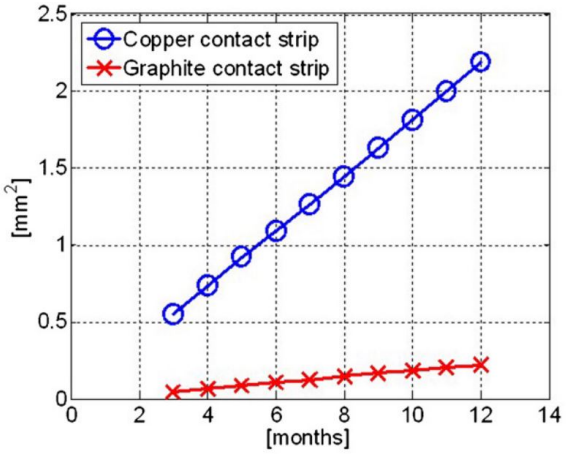
Fig. 2.13 Schematic of a sliding wear

Under the perpendicular force of F_N (N) to the wear surface, the volume of material loss, Q (mm^3) can be calculated according to a theoretical approach proposed by Archard [52] as follows;

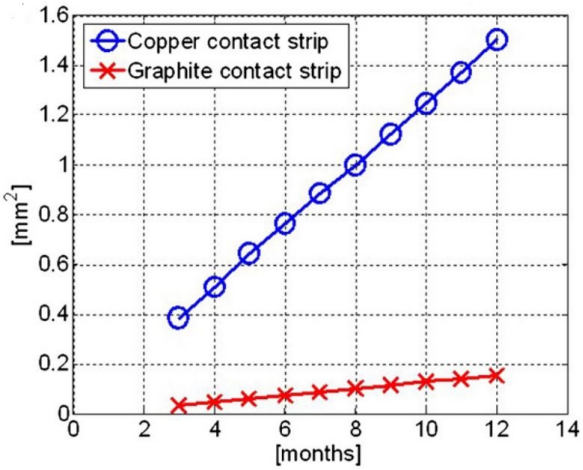
$$Q = \frac{K_{ad} \cdot F_N \cdot s}{H} \tag{2.5}$$

If two materials in contact have different hardness values, H (MPa) is to be chosen that of the softer material [53]. According to Archard's law constant of K_{ad} is named wear coefficient for adhesive wear.

Contact wires are also subjected to mechanical wear due to sliding against pantograph strips. The wear is often measured by a reduction in the cross-sectional area of the contact wire. Fig. 2.14 shows a study by Bucca et al. [54] about the wear of the contact wire at locations of under suspension and midspan against the use of copper and graphite pantograph strips over months. It can be seen from the results that because graphite was a softer material compared to copper, almost ten times less wear was observed in the cross-section of contact wire when graphite carbon strip was used against copper contact wire.



(a) Worn area of contact wire under suspension



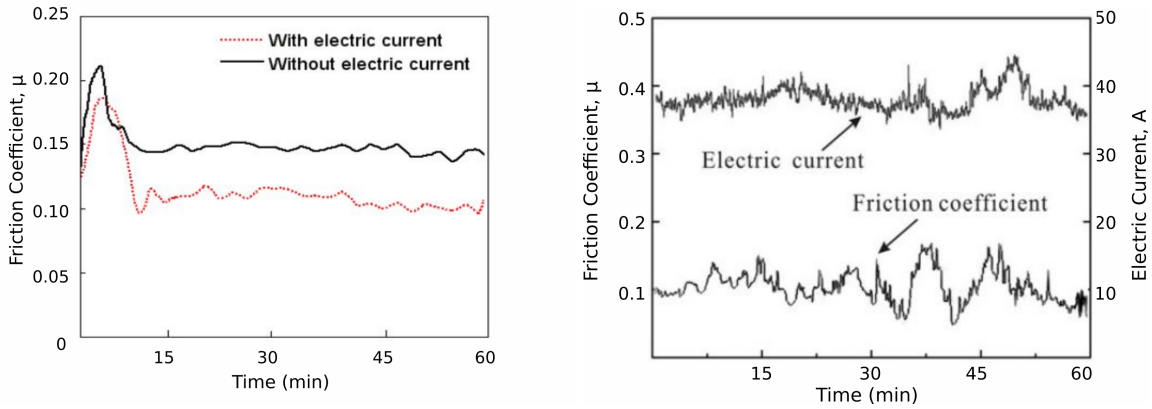
(b) Worn area of contact wire at midspan

Fig. 2.14 Comparison of contact wire wear against copper and graphite pantograph strips [54].

Wear Under Electrical Current

Contact wire and pantograph systems are in physical sliding contact with electrical current. The wear process of these is studied using parameters of sliding speed and electrical current. Bouchoucha et at. [55] mentioned in their study that in a condition of good contact between pantograph and contact wire, the electrical current has no significant influence on the friction coefficient and wear rate of the contact wire. With the increase of sliding speed, contact breaks occur and result in electrical discharges. Thus, electrical current indirectly contributes to wear of contact wire and pantograph friction pair throughout the loss of contact, which leads to arcing.

Conversely, a study by Ding et al. [56] showed that electric current has a positive contribution to decrease in sliding friction between contact wire and pantograph. This study also suggested that electric plays a lubrication role in the sliding contact at the steady stage. Fig. 2.15 shows the variation of friction coefficient with electric current and without electric current and the relationship between friction coefficient and electric current according to this study.



(a) Friction variation with electric current and without electric current

(b) Electric current and friction coefficient relationship

Fig. 2.15 Effects of electric current on sliding friction of contact wire-pantograph pair [56].

A broader perspective has been adopted by Zhang et al. [57], who suggested that the effects of electric current on friction coefficient should be investigated with different sliding speeds. According to their study, it was found that when the sliding speed is less than 20 m/s, the friction coefficient showed a decreasing trend with the increase in the current.

Another study, Ocolenau et al. [58] investigated the temperature rise in contact wire due to the flowing electric current. The results showed that although contact wire is subjected to 200 A AC, the temperature rise is limited to just below 20 °C.

Detailed examination of temperature rise and wear of contact wire-pantograph system by Yang et al. [59] showed that contact surface temperature rises with the increase of the sliding speed. This increase in sliding speed makes arc discharges stronger, which results in arc erosion on the surface of the strip.

2.3.3 Fatigue in Contact Wires

A growing body of literature has been investigated in the subject of dynamic load effects on overhead contact wires with the increase of speed and development in electrified trains [60–66] . In particular, in the last decade, studies have pointed out that fatigue is becoming an important factor which needs to be taken into account while designing and maintaining electrified train lines with the reason of dynamic loadings.

Fatigue is often defined as a term that results in cracks or failure in materials due to the repeated applications of loads. It can occur in different forms; namely, mechanical fatigue, creep-fatigue (repeating forces in conjunction with high-temperature) and thermomechanical fatigue (the combination of temperature fluctuation and mechanical fatigue) [67]. Different approaches were proposed over history, but stress life (S-N) and strain life methods are the most accepted theories used for determining the fatigue life cycles of materials [68].

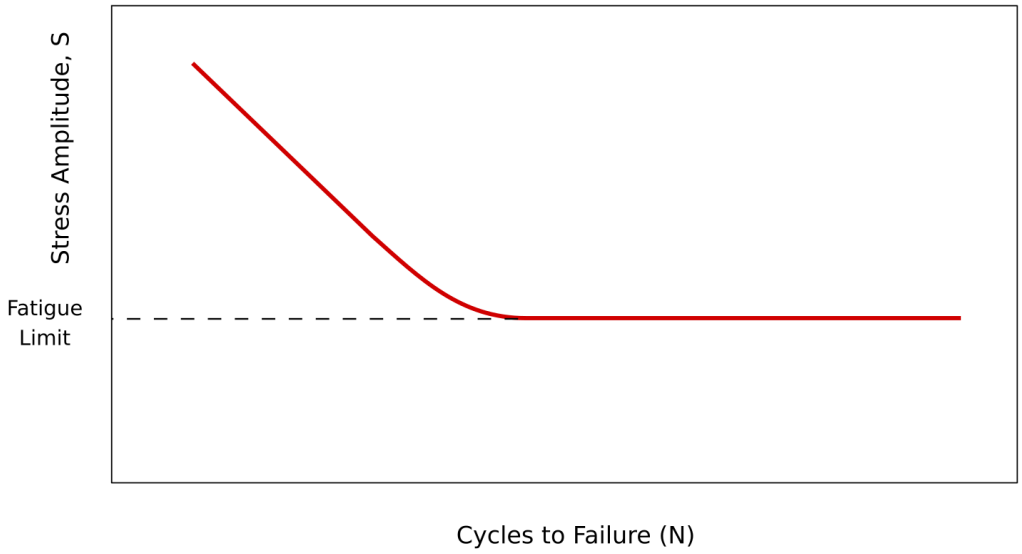
Wöhler completed the first systematic investigations about fatigue between 1852 and 1869 [69–71]. He published a final report in 1870 and conclusions defining the existence of the phenomena of fatigue as follows [72],

- Materials can be subjected to failure by repeating stress that is lower than static strength
- Stress amplitude is critical to determine the fatigue characteristics
- The higher maximum stress the system has, the lower the stress amplitudes lead to fatigue.

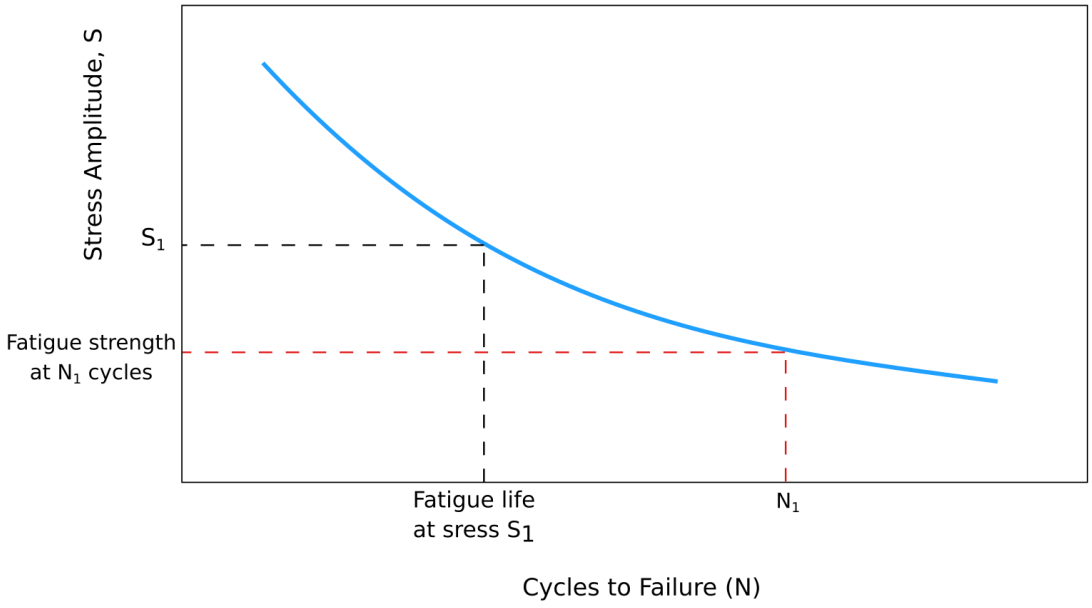
In the 1900s, metal fatigue earned particular attention by the scientists and explained that fatigue damage starts on the surface of the material by slip lines formed on the surface of grains. The slip lines eventually develop cracks [73]. Once a crack reaches to a considerable depth, this crack propagates across the material until the section is reduced and static failure takes place [74].

Wöhler represented the fatigue test results in tables; however, Spangenberg [75] plotted these results in stress and life axis. This method is known as SN curves and called "Wöhler Curves" since 1936 [76]. Because failure time or cycles to failure takes longer a period, this technique is also called *high cycle fatigue.* Primarily elastic deformation is predominant in

low-stress fatigue, and therefore, this stress life approach is traditionally characterised by stress range.



(a) A material with a fatigue limit



(b) A material does not display fatigue limit

Fig. 2.16 Stress and cycles to failure graphs of different materials

Two different types of SN curves are discovered and schematically shown in Fig. 2.16. The graphs show that the stress life curve differs depending on the material properties. Fig. 2.16a illustrates some ferrous and titanium alloys that represent a fatigue limit (endurance

limit). For these materials, the S-N curve becomes horizontal at higher cycles; below this line, no fatigue failure is seen for the infinite number of cycles [77]. However, most of the non-ferrous metals show a declining trend over the cycle to failure and does not have a fatigue limit, as seen in Fig. 2.16b. Fatigue failure is conclusively placed, although stress amplitude diminishes. This region is defined as Giga scale fatigue and was first investigated by Shabalin [78]. For this sort of materials, the fatigue strength is defined as a stress level which failure will occur for a specified number of cycles. Thus, fatigue strength estimation plays a vital role in practical engineering [79].

Fig.2.17 shows the variation of stress with dynamic loading condition. In this schematic figure, maximum stress, minimum stress, mean stress, stress amplitude and stress range are indicated with $\sigma_{max}, \sigma_{min}, \sigma_m, \sigma_a$ and σ_r, respectively.

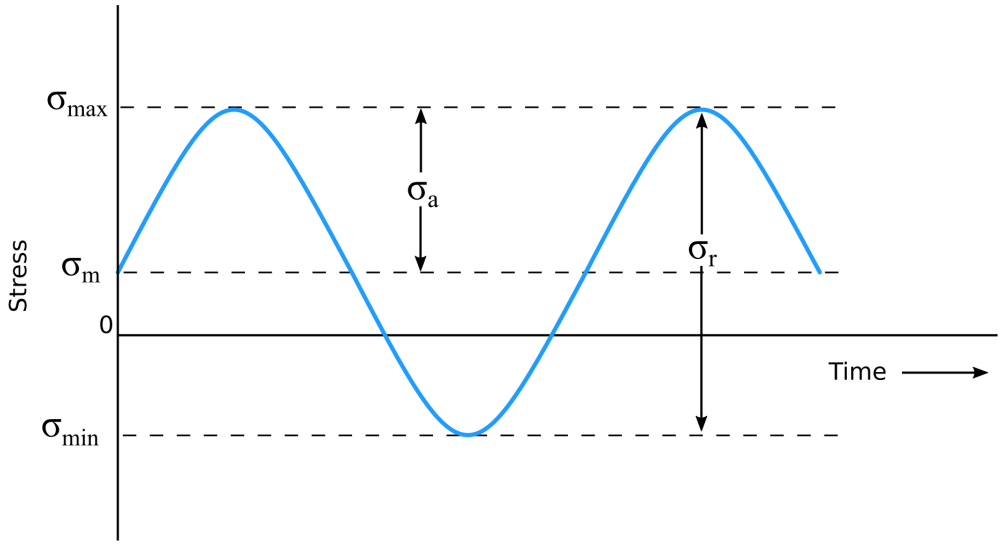


Fig. 2.17 Dynamic stress loading over time

Mean stress (σ_m) that is the average of maximum and minimum stress, is defined as follows;

$$\sigma_m = \frac{\sigma_{max} + \sigma_{min}}{2} \tag{2.6}$$

Moreover, the difference between the maximum and minimum stress gives the stress range (σ_r);

$$\sigma_r = \sigma_{max} - \sigma_{min} \tag{2.7}$$

Stress amplitude (σ_a) can also be defined either the one-half of this stress range (σ_r);

$$\sigma_a = \frac{\sigma_r}{2} = \frac{\sigma_{max} - \sigma_{min}}{2} \tag{2.8}$$

Lastly, stress ratio (R) is a rate of minimum stress (σ_{min}) and maximum stress (σ_{max});

$$R = \frac{\sigma_{min}}{\sigma_{max}} \tag{2.9}$$

Fatigue loading condition is named depending upon the stress ratio of the system.

R=-1: Fully reversed loading
R=1: Static loading
R=0: Zero based loading
0<R<1 : Alternating loading

Another approach to fatigue life estimation is strain life. Since the failures occur in a relatively small number of cycles, it is also named *low cycle fatigue* [80]. This technique is used for circumstances where fatigue loading is associated with plastic deformation (stress above the yield point). In this method, fatigue life is characterised by the strain range [67].

In 1900, Basquin [81] studied that stress amplitude and logN_f plot could be linearised with full log coordinates. When the true stress is used instead of the engineering stress, stress amplitude can be written as;

$$\sigma_a = \sigma_f^{'}(2N_f)^b \tag{2.10}$$

where σ_a is equal to $\Delta\sigma/2$ and σ_a is true stress amplitude, $2N_f$ is the number of reversals to failure (1 cycle= reversals), $\sigma_f^{'}$ is the fatigue strength coefficient; and b is the fatigue strength exponent (Basquin's exponent).

In 1953 and 1954, Manson [82] and Coffin [83] while independently studying thermal fatigue problem, they established an equation based for plastic strain amplitude as follows;

$$\frac{\Delta\varepsilon_p}{2} = \varepsilon_f^{'}(2N_f)^c \tag{2.11}$$

In strain life approach, total strain has two components namely, elastic and plastic, $\varepsilon = \varepsilon_e + \varepsilon_p$. Thus, strain amplitude is described below;

$$\frac{\varepsilon}{2} = \frac{\varepsilon_e}{2} + \frac{\varepsilon_p}{2} \tag{2.12}$$

when Eq.2.10 is divided by Young's modulus;

$$\frac{\varepsilon_e}{2} = \frac{\varepsilon_f^{'}}{2}(2N_f)^c \tag{2.13}$$

Combining Eq.2.11, Eq.2.12 and Eq.2.13:

$$\frac{\Delta\varepsilon}{2} = \Delta\varepsilon_a = \underbrace{\frac{\sigma_f^{'}}{E}(2N_f)^b}_{elastic} + \underbrace{\varepsilon_f^{'}(2N_f)^c}_{plastic} \tag{2.14}$$

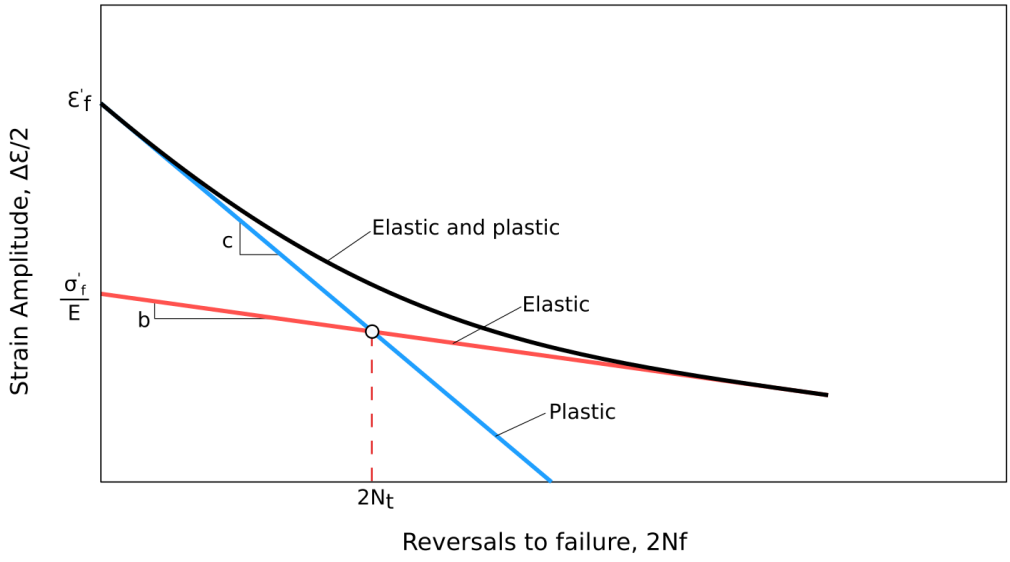


Fig. 2.18 Log-log scale strain and reversals to failure

Fig. 2.18 shows a total strain-life curve. According to the plot of total strain-life, the coefficients can be listed below [84];

- $\sigma_f^{'}$, fatigue strength coefficient
- $\varepsilon_f^{'}$, fatigue ductility coefficient
- b, fatigue strength exponent
- c, fatigue ductility exponent

One of the earliest studies in 1964 was made by Sell et al. to investigate the problems which were coming with increasing train speed and noted that further studies needed to be done with to aim to increase safety, particularly, the cases of damage to the overhead line equipment by pantographs [85].

In addition to the problem of wear in contact wires, also numerical and analytical investigations were made to understand better the dynamics of OLE in the same years. An FE model was used by Wu [86] to study current collection problems. Manabe [87] provided an in-depth analysis of the dynamic response of the overhead wire and the energy propagation in the wire by using a model of a stable load travelling along an infinite wire supported by springs. Also, an analytical approach was suggested to calculate both displacement and contact force between the pantograph head and the overhead contact wire by Wu et al. [88].

In the past, only the problem of wear was taken into account because failures due to wear was overwhelming the other prospective mechanisms which might trigger to break OLE wires. However, in recent years the increase in train speed results in higher contact force fluctuations. A growing number of studies have pointed that bending fatigue of contact wire has become a significant issue to be taken into account for OLE safety [89–98]. Zhen et al. [93] investigated the bending fatigue life of cold drawn contact wires combining experimental and finite element analysis and suggested that S-N curve estimation method can be used for predicting the fatigue life of contact wires.

Similarly, Sugahara et at. [91] also carried out several experiments into fatigue life estimation of overhead contact wire with a servo motor configured to apply oscillating force to contact wire. They highlighted the applicability of the Miner's law with fatigue tests as the premise of applying of the rain flow method. An alternative experimental approach to fatigue life estimation of contact wires by Yamashita et al. [94] studied the bending of hard drawn copper contact wire by an adjusting crank and motor. This showed that fatigue damage of worn contact wire and allowable bending stress amplitude could be estimated by S-N curves and modified Miner's rule. Also, it has been suggested that the equivalent stress approach by

Smith [99] can be used by determining a single stress-strain parameter governing fatigue life as follows;

$$\sigma_e = \sqrt{\sigma_m + \sigma_a) \times \varepsilon \times E} \tag{2.15}$$

where σ_e is equivalent stress, σ_m is mean stress, σ_a is stress amplitude, ε is strain and E is Young's modulus.

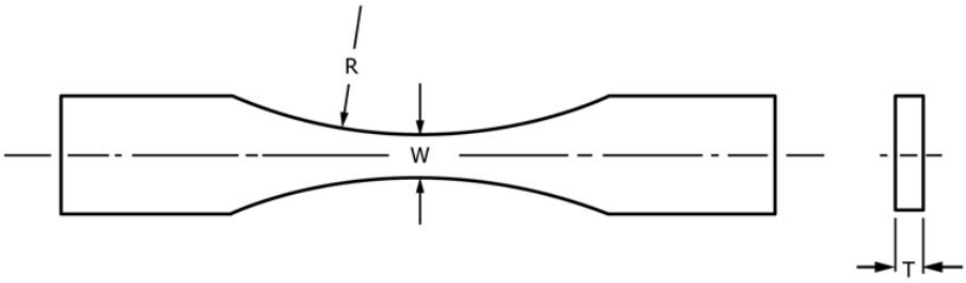
One of the most accepted fatigue life estimation methods is experimental testing. Several experimental techniques have been used in the literature to determine the fatigue life of OLE contact wires. These can be listed under standard fatigue testing and special-purpose fatigue testing. In this section, initially, the standard fatigue testing methods and the application to the contact wire in the literature are explained. Subsequently, experimental facilities designed for special purpose of testing the fatigue of OLE contact wires are shown with examples from the literature.

Standard Fatigue Testing

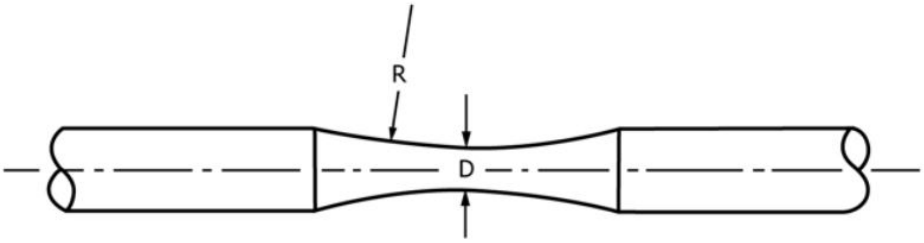
The fatigue life of a specimen means the number of cycles that causes failure. This number is depended on variables, such as; stress level, waveform, test environment, material properties of the specimen and surface parameters. Considering millions of cycles fatigue life, small changes in these parameters can significantly affect the fatigue behaviours. Therefore, laboratory experiments are essential to describe fatigue characteristics of materials. Fatigue test specimens are primarily described by the mode of loading[100]:

- Axial stress
- Plane bending
- Rotating beam
- Alternating torsion
- Combined stress

The type of specimen in fatigue testing varies depending on the purpose of the test programme. However, the design of the specimen should meet the criteria of the standards. Middle section of the specimen is reduced comparing to the two ends of the sections. This process avoids specimen from being break at gripped and threaded sections due to stress concentration. Specimens can have either circular or rectangular cross-sections. Fig. 2.19



(a) Specimen with rectangular cross section



(b) Specimen with circular cross section

Fig. 2.19 General design criteria for axial fatigue testing by ASTM E466 [101]

shows the general design criteria for specimens of circular and rectangular cross-sections outlined in ASTM standard E466.

Testing of fatigue properties of metals is often regulated by standards. Table 2.6 shows the standards used to determine fatigue properties of specimens according to ASTM [101–107].

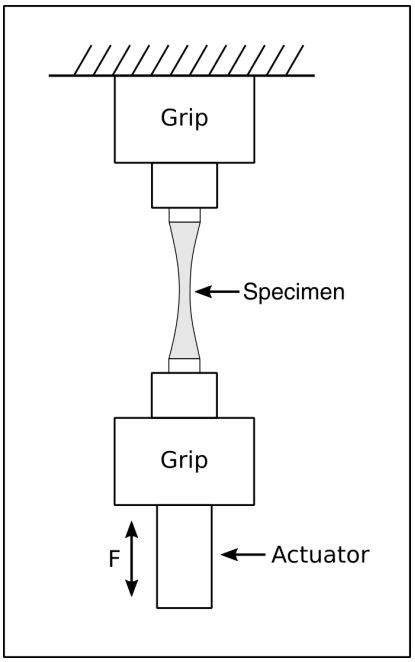
Table 2.6 ASTM standards for testing the fatigue behaviours of specimens

ASTM Number	**Description**
E466	Conducting Force Controlled Constant Amplitude Axial Fatigue Tests of Metallic Materials
E467	Verification of Constant Amplitude Dynamic Forces in an Axial Fatigue Testing System.
E468	Presentation of Constant Amplitude Fatigue Test Results for Metallic Materials
E606	Strain-Controlled Fatigue Testing
E647	Measurement of Fatigue Crack Growth Rates
E739	Statistical Analysis of Linear or Linearized Stress-Life (S-N) and Strain-Life Fatigue Data
E1049	Cycle Counting in Fatigue Analysis
E1823	Standard Terminology Relating to Fatigue and Fracture Testing

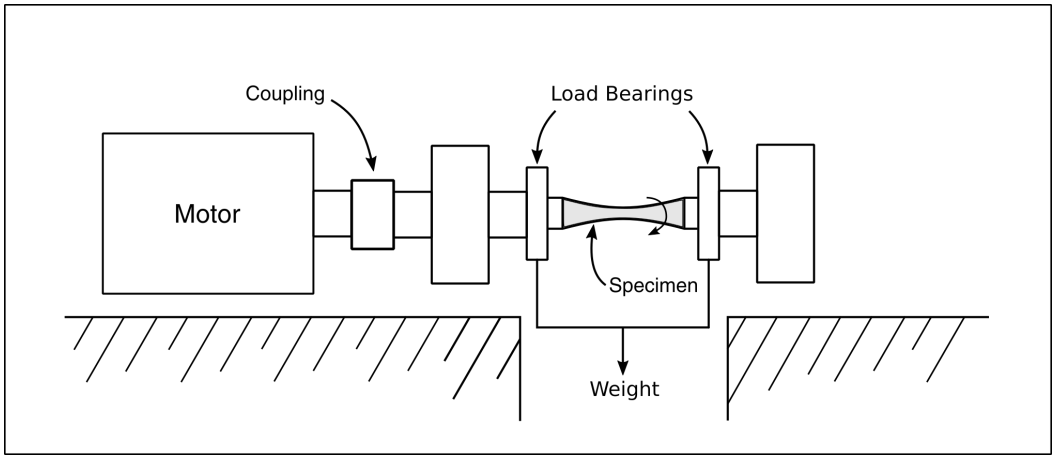
The type of machines used in testing the fatigue behaviours of samples can be divided into four groups, namely;

- Axial fatigue testing machines
- Bending fatigue testing machines
- Torsional fatigue testing machines
- Special-purpose fatigue testing machines

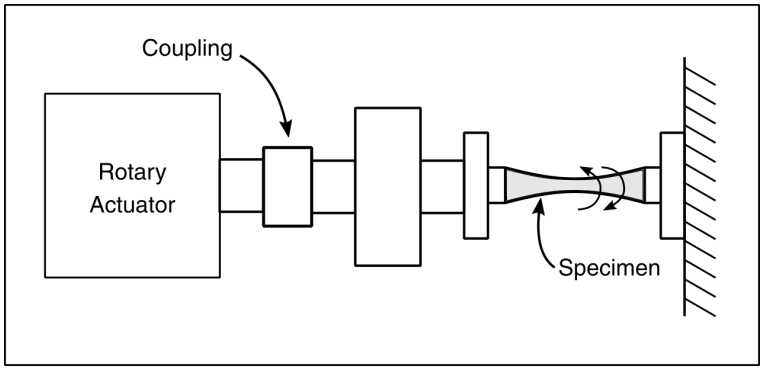
Fig. 2.20 shows schematics of the machines used in testing the fatigue properties of specimens. The axial fatigue testing machine in Fig. 2.20a applies uniform stress or strain to the cross-section of the specimen. These machines are capable of tension and compression loading fatigue tests [108]. Bending fatigue machines shown in Fig. 2.20b are considered one of the most common types of machines used in fatigue testing. The test specimen is simultaneously subjected to bending and rotating by an apparatus connected to bearings. Therefore, it has an advantage that bending moment between loading locations is uniform, and it is free of shear stress [109]. In order to determine the shearing strength of a specimen under cycling loading, tensional fatigue testing machines in Fig. 2.20c are used. In this machine, one end of the specimen is fixed by a chuck and the other end is connected to a rotary actuator. Besides, special-purpose fatigue testing machines are also developed for components, such as; gears, bearings, wires etc. [100].



(a) Schematic of axial loading fatigue testing machine



(b) Schematic of rotating bending fatigue testing machine



(c) Schematic of torsional fatigue testing machine

Fig. 2.20 Schematics of types of machines used in fatige testing of ASTM specimens

Special Purpose Fatigue Testing

It has been seen that the experimental designs used in the studies to investigate the fatigue properties of OLE contact wire show similarities in terms of geometries and boundary conditions of the rig design. Fig. 2.21 shows a common design of the contact wire fatigue test facility used in previous studies [11, 89, 91, 93, 94, 110].

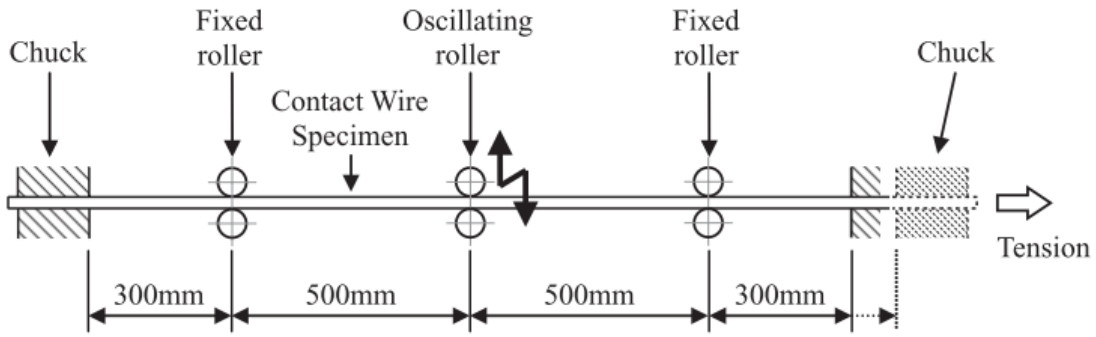


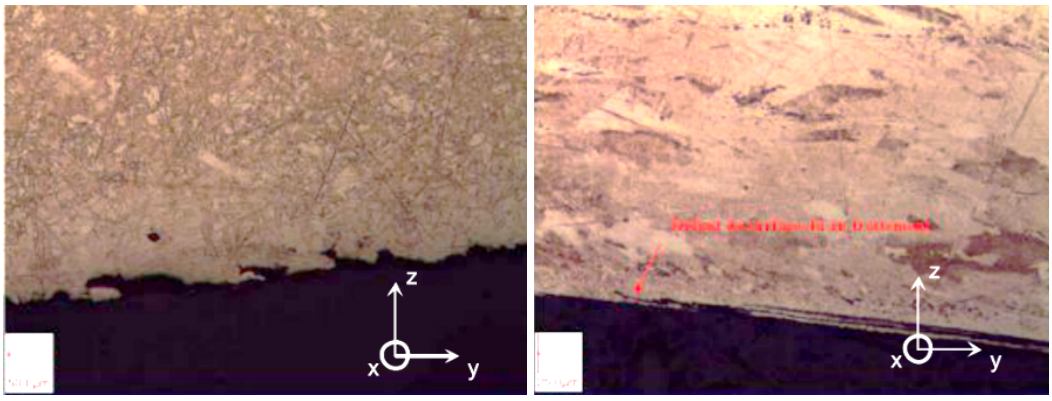
Fig. 2.21 Schematic of the contact wire fatigue rig in previous studies [11, 89, 91, 93, 94, 110]

In this design, the contact wire was fixed on both sides with chucks and tensioned with weights. It was held in place by fixed rollers. An oscillating roller in the middle of the span provided contact wire sample for bending. Since these three rollers involved single point contact, the contact wire was bent based on as three-point bending principles. These experimental configurations required 2-3 metre-length contact wire specimen. The only difference in the designs in the literature was the mechanism triggering the vertical oscillation. For instance, Yamashita et al. [94] used a crank-motor to oscillate the contact wire while Sugahara et al. [91] and Zhen et al. [93] equipped their designs with linear-servo motor and hydraulic actuator, respectively.

Findings from Past Studies

In a study investigating uplifting force which is exerted by the pantograph, Kim et al. [110] highlighted that the uplifting amount was directly related to the bending strain of the contact wire and was the most important factor in determining the fatigue life of the contact wire. Therefore, they suggested the development of a more straightforward method that was the maximum local stress at the top of the contact wire to evaluate the fatigue life of contact wires.

A small scale study by Massat et al. [111] identified that defects on the surface of the contact wire due to pantograph friction, electrical arcs and corrosion can cause crack



(a) specks due to electrical arc (b) surface defects due to friction

Fig. 2.22 Surface defects in contact wire [111]

initiation and increase the risk of fatigue failure. Fig. 2.22 shows the defects addressed in their study.

After the investigations showing the importance of fatigue problem in overhead contact wires, some studies have been done to improve to fatigue capability of contact wires. Yamashita C et al. [112] developed a new cross-section shape to reduce the bending strain effects and improve the anti-fatigue property of contact wires. Ten per cent of bending stress improvement has been obtained after the new cross-section shape. In contrast, Zhen et al. [93] were much more concerned with material selection rather than using a different cross-sectional shape. In their study, it has been pointed out that Cu-Mg alloy contact wires showed more excellent fatigue damage resistibility rather than pure copper contact wires at same working conditions.

Another problem leading to fatigue damage in the contact wire is OLE fittings. Nguyen et al. [21] investigated a fatigue associated crack observed near a junction claw (Fig. 2.23). In this failure, the crack initiated from the bottom (worn surface) of the contact wire and propagated through the section and resulted in failure at the top surface of the contact wire. In the same vein, another fatigue failure of the contact wire at the entry splice was reported by Network Rail [113]. The fatigue failure of the contact wire has been determined with the initiation point being on the top of the contact wire at the entry splice. Therefore, OLE fittings, in particular junction claws, can be a potential for fatigue mechanism and initiate the cracks either on the top or bottom surface of the contact wire. In Nguyen's study, it was mentioned that the heavyweight and high stiffness of junction claws could lead to important dynamic loads and arcing thus encouraging fatigue damage.

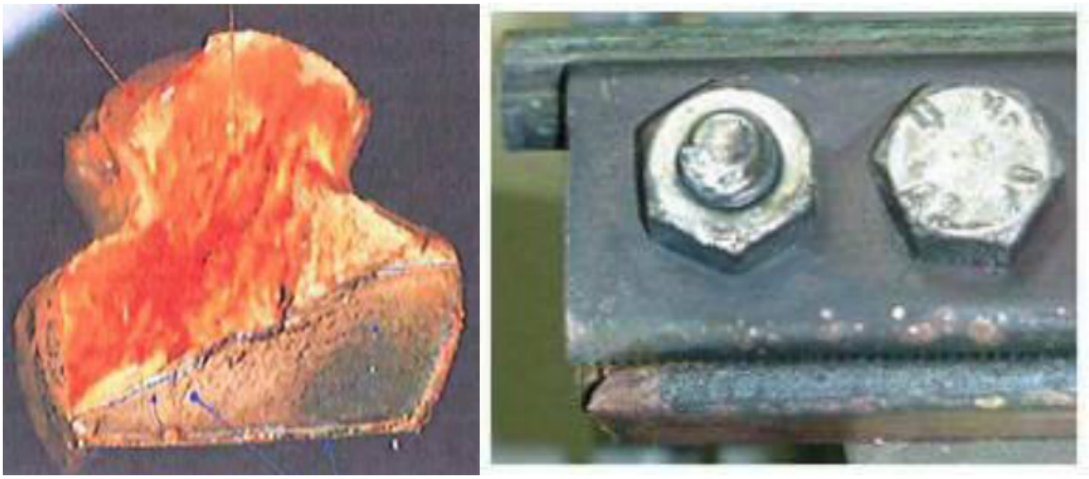


Fig. 2.23 Fatigue crack near a junction claw of a contact wire [21]

Together these studies reviewed here provide important insights that fatigue can play an important role in the reliability and safety of OLE contact wires. Particularly, the fatigue problems gather around bending stress, pantograph force and OLE fittings.

Mean Stress Effect

The contact wire works under constant tension to prevent its sag. Although this constant tension is often between 10 kN and 20 kN, it can increase up to 31.5 kN depending on the speed of the line. This pulling force generates constant tension stress and plays a vital role in the fatigue durability of the contact wire. Particularly, the mean stress can increase in time due to the wear of the contact wire.

There are a number of approaches in the literature explaining the effect of mean stress on fatigue life of materials. The empirical descriptions about fatigue life estimations are concerned about fully reversed loading conditions where mean stress is zero. However, zero mean stress and fully reversed stress cycles are not always a case for many applications [67]. Mean stress effect on fatigue life of materials has been studied over a century. Several methods have been proposed for the calculation of allowable stress amplitudes and fatigue lives. The most accepted methods can be listed as; Goodman, Gerber and Soderberg [114]. Fig.2.24 shows empirical curves according to Goodman, Gerber and Soderberg.

Goodman developed a straight relationship between fatigue limit and tensile strength, while Gerber's is parabolic, in general form of this relationship can be expressed as follows [108];

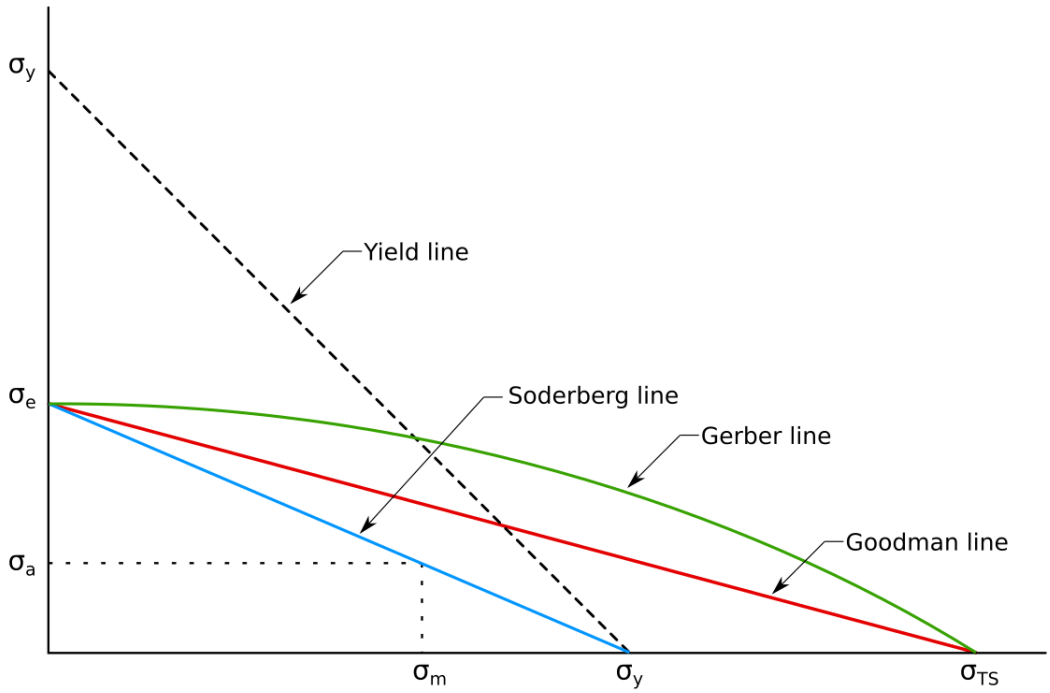


Fig. 2.24 Standard mean stress emprical curves

$$\sigma_a = \sigma_e(1 - (\frac{\sigma_m}{\sigma_{TS}})^x) \tag{2.16}$$

x=1 for the Goodman line, x=2 for the Gerber line.

where σ_e is fatigue limit under zero mean stress, σ_a is fatigue stress amplitude for (maximum allowable stress for endurance cycle) under the mean stress of σ_m, σ_{TS} is tensile strength and σ_y is yield strength.

Soderberg expressed allowable stress amplitude under mean stress using fatigue limit and yield strength as shown below;

$$\sigma_a = \sigma_e(1 - (\frac{\sigma_m}{\sigma_y})) \tag{2.17}$$

These approaches are essential for determining stress amplitude under non-zero mean stress conditions. Because the higher mean stress the system is subjected to, the less stress amplitude can be tolerated. Even small stress amplitudes can trigger fatigue failure at elevated mean stresses.

Yamashita et al. [94] investigated the effect of mean stress increase on contact wire fatigue. Their study showed that the fatigue life of the contact wire was subjected to decrease approximately three times when the diameter of the contact wire reduced from 12.3 mm to 7.5 mm.

2.3.4 Fatigue Fracture in Contact Wires

As mentioned in Section 2.3.3, due to the repetitive contact force, the contact wire can result in fatigue fracture. This type of fracture often initiates with surface cracks and causes serious OLE faults. The macroscopic fracture surface of the contact wire after the fatigue failure was investigated by a number of studies [111, 21, 93]. Thus far, previous studies have indicated that macroscopic fracture surface of the contact wire after failure shows three stages of the fracture, namely; crack initiation, crack propagation and failure. A typical fracture surface of the contact wire is shown in Fig. 2.25 after fatigue testing.

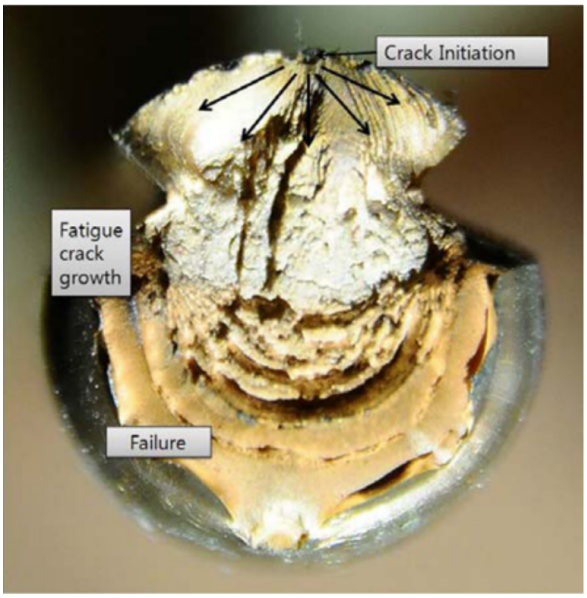


Fig. 2.25 Fractured surface of Cu-Mg contact wire after fatigue bending [93]

The relationship between fatigue and failure of the materials is occasionally explained with Paris-Erdogan crack growth law. However, before this, some fracture mechanics theories involves the fundamentals of the crack growth theory of Paris-Erdogan law are described below.

Increase in the use of metal rose in the nineteenth century with the Industrial Revolution. However, many accidents and failures followed this industrialisation. It was understood that some of the failures were due to poor design and material problems. Avoiding these problems,

some extend solved the issue; however, with World War II, larger structures, bridges and liberty ships were constructed. Unfortunately, out of 2500 Liberty ships during the war, 145 broke in two, and almost 700 significant failures occurred [115].

Until towards the end of the 1950s, failures occurred under very low stresses, and temperatures were little known. Fortunately, advances in fracture mechanics paved the way to overcome potential flaws that lead to failures in materials. Particularly, fracture mechanics mainly focus on single crack theories. However, different theoretical approaches and experimental techniques have been developed to identify the properties of crack types.

The Stress Intensity Approach

A constant called the stress intensity factor K_i is used for characterizing the stress distribution at a crack tip. Fig. 2.26 depicts a schematic of a single crack used to describe the stress intensity approach. The stress intensity of an element near the tip of a crack in an elastic material with plane stress is shown as follows [116];

$$K_i = \sigma\sqrt{\pi a} \tag{2.18}$$

where K_i is stress intensity factor, σ is normal stress of the plane and a is crack length. K_i is linearly depended on stress and the root square of crack length.

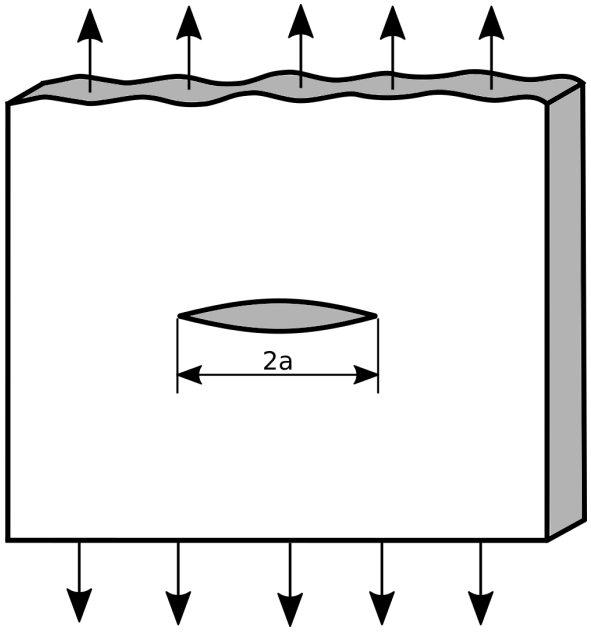


Fig. 2.26 Schematic of a single centred crack

Some studies were conducted about behaviours of cracks. Irwin [117] completed one of the first studies introducing three loading modes. Fig. 2.27 shows three standard loading modes of a crack.

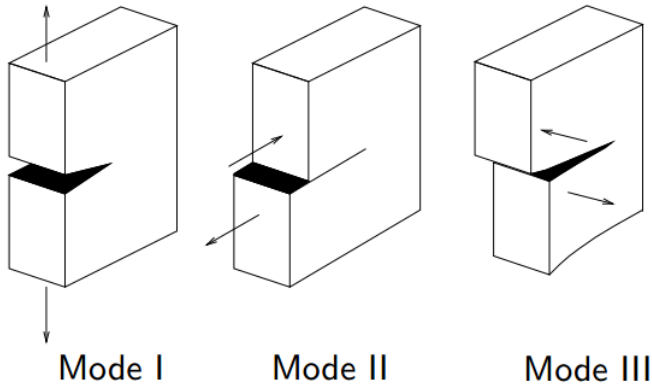


Fig. 2.27 Schematic of failure modes

Mode I is named opening crack mode that is occasionally predominant in bending problems. Different types of calculations are explained in the literature for determining Mode I stress intensity of a specimen with finite width. A general form of the stress intensity is expressed depending on geometry as follows [115];

$$K_1 = C\sigma\sqrt{\pi a} f(a/w) \tag{2.19}$$

where w is width of the specimen, a is crack size and C and $f(a/w)$ are constants determined by stress analysis. The geometry of a centre cracked finite width sample is schematically shown in Fig. 2.28.

For the stress intensity of this finite width specimen, several approaches were suggested in the literature. Irwin [118] suggested a solution with accuracy of 5 % for $a/w \leq 0.25$;

$$K_1 = \sigma\sqrt{\pi a}\sqrt{\frac{w}{\pi a} tan\frac{\pi a}{w}} \tag{2.20}$$

Brown [119] found another approximation with 0.5 % accuracy for $a/w \leq 0.35$;

$$K_1 = f(a/w)\sigma\sqrt{\pi a} \tag{2.21}$$

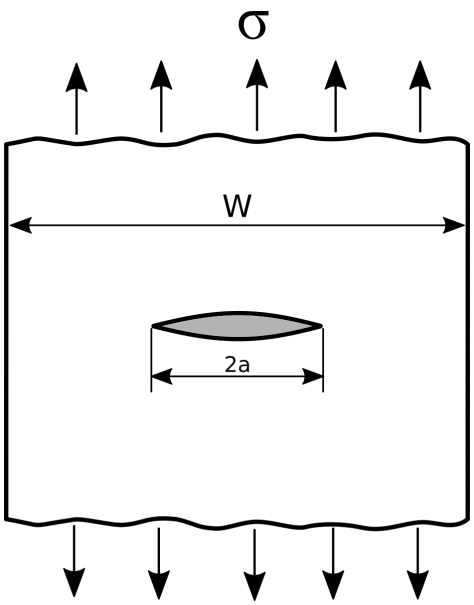


Fig. 2.28 Schematic of a finite width centre cracked sample

$$f(a/w) = 1 + 0.256\frac{a}{w} - 1.152(\frac{a}{w})^2 + 12.200(\frac{a}{w})^3 \tag{2.22}$$

However, a simpler and more accurate expression was suggested by Feddersen [120] with accuracy of 0.3 % for $a/w \leq 0.35$;

$$K_1 = \sigma\sqrt{\pi a}\sqrt{sec\frac{\pi a}{w}} \tag{2.23}$$

Stress intensity approaches are also applied to single or double edge cracked samples. The geometry of single and double edge crack is shown in Fig. 2.29.

For single and double notched edge cracks, following expressions were proposed [115];

Single edge notched crack:

$$K_1 = \sigma\sqrt{\pi a}(1.122 - 0.231(\frac{a}{w}) + 10.550(\frac{a}{w})^2 - 21.710(\frac{a}{w})^3 + 30.382(\frac{a}{w})^4) \tag{2.24}$$

Double edge notched crack:

$$K_1 = \sigma\sqrt{\pi a}\frac{(1.122 - 1.122(\frac{a}{w}) - 820(\frac{a}{w})^2 + 3.768(\frac{a}{w})^3 - 3.040(\frac{a}{w})^4)}{\sqrt{1 - \frac{2a}{w}}} \tag{2.25}$$

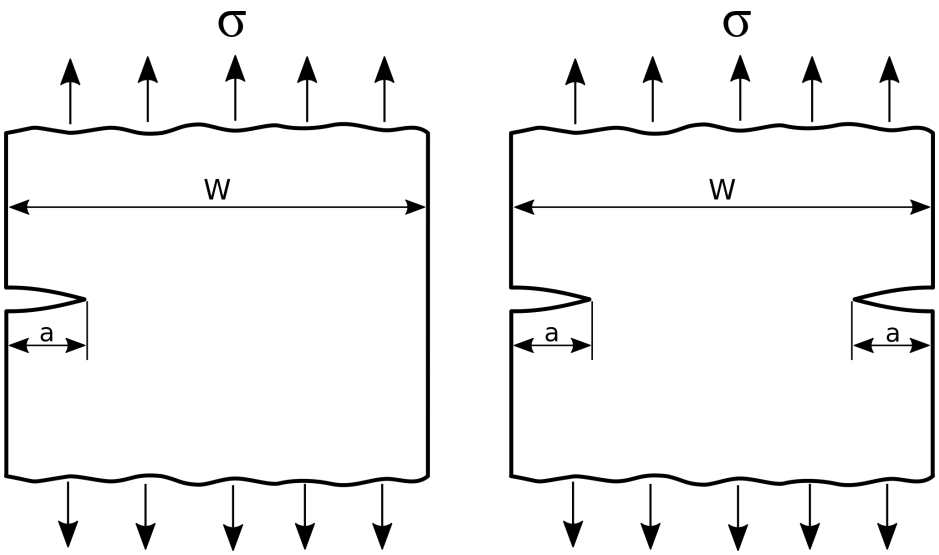


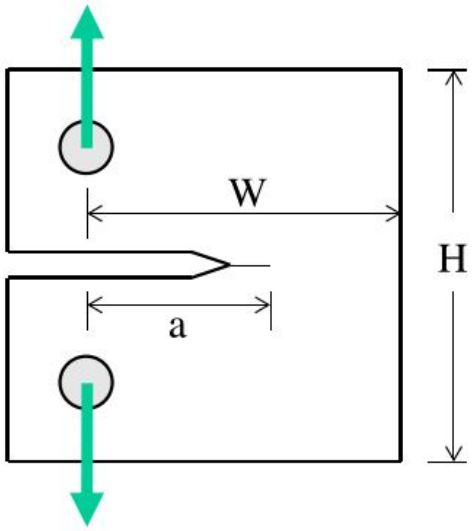
Fig. 2.29 Schematic of edge cracked specimens

Fracture Toughness

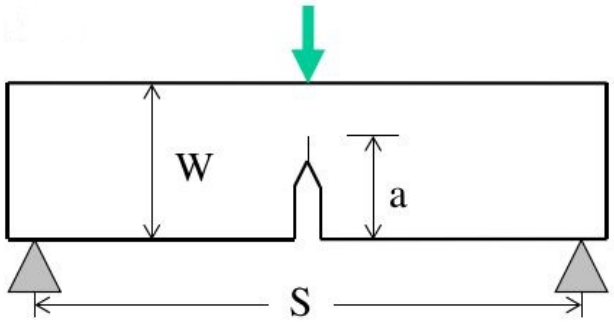
A critical stress intensity for a crack that determines the resistance to the crack in the plane strain is named "Fracture Toughness" K_{I_c}. Cracks grow when the stress intensity value exceeds K_{I_c} [121]. It can also be understood that a material with a higher fracture toughness allows a longer crack at a given stress [115].

Fracture toughness is considered a material property and determined by experimental tests [116, 122]. The first fracture toughness test was standardised with E399 [123] by American Society for Testing and Materials (ASTM) in the United States. Later, the standard terminology of fracture testing was defined in ASTM E1823 [107], and the standard test method for measurement of fracture toughness was enlarged in ASTM E1820 [124]. According to ASTM E1823, the fracture toughness of a material is determined for the opening mode (Mode I).

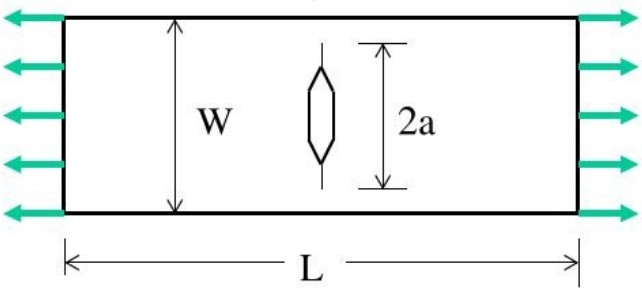
Three types of testing samples by ASTM are shown in Fig. 2.30. This includes compact tension specimen (Fig. 2.30a), single edge-notched bend (Fig. 2.30b) and middle crack tension (Fig. 2.30c) [125]. H is the height of the specimen in Fig. 2.30a, S is the span in Fig. 2.30b, L is length of specimen in Fig. 2.30c, a is the crack length of the two specimens and $2a$ is the crack length of the tensile specimen.



(a) Compact tension



(b) Single edge-notched bend specimen in three point bending



(c) Middle-cracked tension specimen

Fig. 2.30 Standard fracture toughness testing specimens by ASTM

Crack Branching

Different theories exist in the literature regarding the behaviours of cracks. Particularly, the phenomenon of dynamically growing cracks that split into multiple cracks has been paid attention after observing crack branching in crystalline as well as amorphous materials. A crack branching is shown schematically in Fig. 2.31.

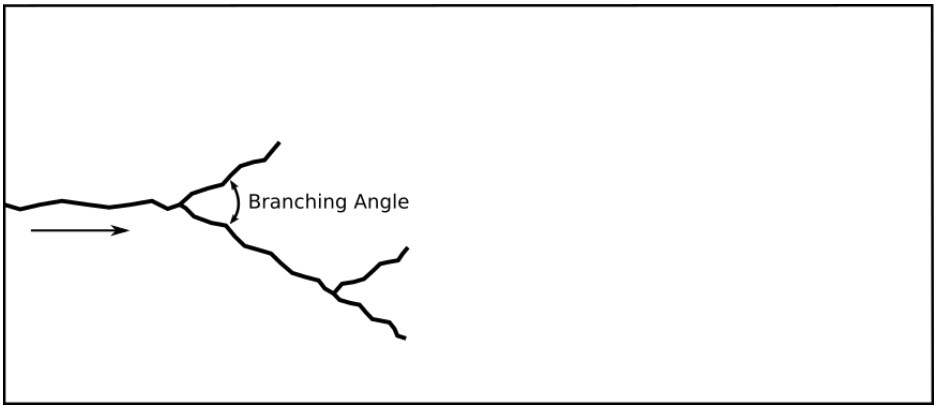


Fig. 2.31 Schematic of crack branching

Historically, research investigating the factors associated with crack branching has focused on stress intensity factors and crack propagation speed. One of the earliest studies about this has been done by Kobayashi et al. [126]. Their study showed that the critical stress intensity factor varied between 2.4 and 3 times the crack initiation stress intensity factor when the crack branching occurred. In contrast, Yoffe [127] studied on the explanation of crack branching from the perspective of the velocity of crack propagation. From their study, it was found that when the crack speed surpassed $0.60C_s$, C_s*:shear wave speed*, the maximum of the hoop stress acted normal to lines make an angle of 60 $^\circ$ with the direction of crack propagation. They also noted that rearranged stress fields would trigger crack branching. However, Ravi-Chandar [128] showed in their study that cracks hardly reach this speed and stress field rearrangement was not likely to clarify crack branching. Hull [129] proposed an explanation that stress vectors on the crack front, caused by mixed-mode loading, can result in crack branching. On the other hand, it was proposed that crack path and crack branching did not only occur in mixed modes, but also in single mode. Based on this idea, a criterion introduced by Erdogan [130] explained that crack growth direction is normal to the maximum circumferential-stress. In the same vein, Ramulu et al. [131] extended this idea and proposed a criterion of *a dynamic* crack curving. This method can predict the crack angle in both pure Mode I and mixed Mode I and II conditions. According to them, crack branching occurs when the characteristic distance of a crack is less than equal to a critical distance. Besides, Ravi-Chandar [128] pointed out that the crack branching occurs when a

crack reaches a critical stage identified macroscopically by its stress intensity factor, it splits into two or more branches, each propagating with the same speed as the parent crack.

Considering all of this evidence in the literature, it seems that studies about crack branching have revealed the emergence of several contrasting themes.

Fatigue Crack Growth

Fatigue crack growth can occur although the stress intensity K levels far less than the material's fracture toughness when a metallic alloy is subjected to cycling loading [132]. This fatigue failure is described with three regimes, namely; crack initiation, crack growth (crack propagation) and failure.

These regimes of fatigue failure in metallic materials are schematically shown in Fig. 2.32. K_{th} is a threshold value of stress intensity which determines whether cracks propagate. K_c is fracture toughness and crack growth is a regime in which the crack propagation rate continues linearly. The crack growth rate (metre per cycle) is expressed with $\frac{da}{dN}$ where a is crack length, and N is the number of cycles corresponding to the crack length.

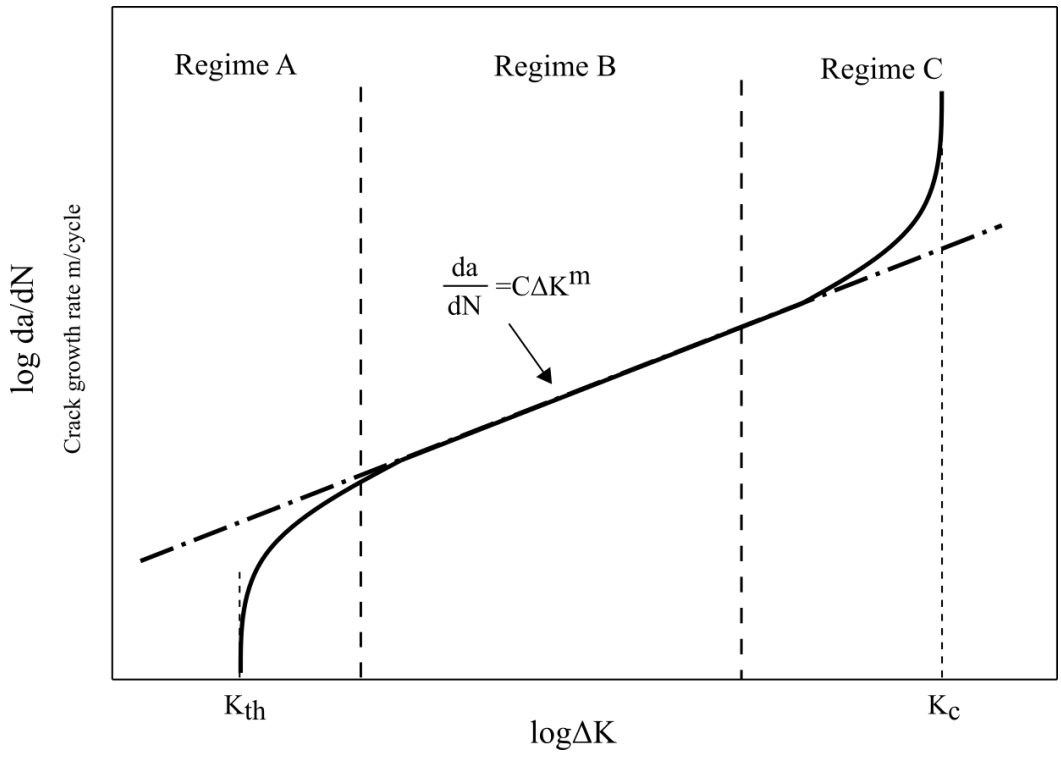


Fig. 2.32 Schematic of crack branching

It can be seen that there is a linear relationship between crack growth rate and stress intensity in the Regime B. This growth rate is often calculated by a power law. Paris-Erdogan

law is one of the most used power laws in the literature and expressed as following in Eq. 2.26 [133];

$$\frac{da}{dN} = C\Delta K^m \tag{2.26}$$

where m and C are material constants obtained by experimental tests.

2.3.5 Arcing Problem

Arcs in OLE mainlines are usually momentary faults that last shorter than seconds. Although the duration of the arcing is limited, this problem can result in excessive heat exposures on the surface of the contact wire. Arcing can be due to either the loss of contact between contact wire and pantograph or low clearance and ionising the air between structures (bridges, bridge arms, overpass) and OLE live wires.

When the arcing occurs during a loss of contact between pantograph and contact wire, it leads to damage both contact wire and pantograph surface. However, arcing caused by low clearance (flashover) is considered a type of short circuit fault. This arcing can last longer comparing to pantograph arcing; also, it is more likely to repeat at the same location.

Arc issue is considered one of the most important interaction problem. This problem may cause severe damages both on the surface of pantograph and contact wire. Particularly, there is growing attention to investigate the effects of arcs with the increase of speed in train lines [134–140]. Since arc damages become more obvious and dominant with the developments in the speed of trains and shorten the service life of the components used in OLE. [141–143].

Weather conditions also influence the current collection quality. Although moisture in the air presents a thin lubrication layer between the contact wire and collector strip, in the wintertime, this moisture layer becomes frozen and can be a form of ice or snow [144]. The presence of the icing layer is more towards the bottom of the contact wire due to the gravity. Therefore, this leads to a loss of smoothness of the sliding contact and severe pantograph arc occurrence although the train speed is low [134, 145].

Much of the research in the literature about arc damage in OLE has focused on identifying and demonstrating the problem using experimental measurements. Firstly, this problem was highlighted during the wear investigation of pantograph carbon strips. Kubo et al. [146] mentioned that electrical arc discharges mainly governed due to contact break between pantograph strip and contact wire. It was also noted that the thermal effects of discharge could be a form of melting and evaporation. He et al. [48] defined the arc issue between contact wire and pantograph surface as "electrical welding". Similarly, hot spots due to arcing

were identified by Gonzalez et al. [147] as micro-welding that significantly deteriorates the contact wire surface.

Bucca et al. [148] discussed the three main contributions to the wear rate of pantograph and contact wire: mechanical, due to frictional power dissipation; electrical, due to power dissipation related to the current flow at the contact wire (Joule effect); and electrical arcs, due to power dissipation generated by the electrical arcs that occur when the contact dynamics cause a loss of contact. Chen et al. [149] also mentioned that arc discharge becomes heavier due to fast worn pantograph surface in high-speed train lines.

Several studies have used experimental setups to examine the air-gap between pantograph and contact wire that causes electrical discharge. The varying gap between electrodes due to mechanical vibration was identified as the main reason for the pantograph arcing by Wang et al. [150]. They also highlighted that pantograph arcing could cause ablations in the contact wire and shorten the life of the contact wires. A study done by Shimanovsky et al. [151] showed that poor mechanical contact triggers the arcing phenomenon and wear of the contact wire as a result. According to a study by Wang [152], the main cause of the air gap was linked to the result of poor mechanical contact, irregularity of the contact wire and influence of the high-speed airflow.

Wei [153] presented significant analysis and discussion on the subject of arcing mechanism from the perspective of current and voltage waveforms. In their case study, arc presence was classified as approaching and drawn arc, and it has been found that the intensity of the drawn arc is much stronger than that of the approaching arc. Besides observing four times longer lasting drawn arc, maximum arc diameter was determined to be about 3.3 mm.

Jia et al. [154] explored the relationship between Joule heating and the current which was drawn by pantograph during the arc process and showed that joule heating from arc discharge made a significant contribution to the wear rate of the contact wire. Yang et al. [155] and Kubo et al. [156] studied that the accumulated arc discharge energy can be calculated as follows in Joule heating law [157];

$$E_a = \int UIdt \tag{2.27}$$

where E_a is the accumulated arc energy (Joules), U is the arc voltage drop between the contact strip and contact wire (Volts), I is the electric current flowing through the friction pair (Amperes), and t is time (seconds).

Additionally, the importance of the polarity of OLE contact systems, shown in Table. 2.7, was investigated by Midya et al. [158]. They set up a series of experiments in order to understand the effects of pantograph-contact wire polarity to the arc mechanism and found

that when the polarity of supply voltage at the contact wire is negative, there could be more interruption for short intervals due to increased air gap. However, because arcs can be seen in both polarities, He et al. [159], found that it is inevitable to loose hardness on the contact wire surface due to arcing regardless of the polarity of contact wire-pantograph systems.

Table 2.7 Pantograph-contact wire polarity

Positive Polarity	
Contact wire	**Pantograph**
Cathode	Anode
Negative Polarity	
Contact wire	**Pantograph**
Anode	Cathode

Data from several studies suggested that arc mechanism occurs in the stages of attaching to a particular point, called anode or cathode, and elongation due to electrode movement and extinguishing [160–164]. Likewise, Midya et al. [165] highlighted that noticeable burn marks and craters exist on the carbon and the aluminium frame of the pantograph, and copper contact wire indicating arc roots.

Besides the surface melting of the copper, void forms and defects were also found in the heat affected area during the studies about weldability of copper materials. This phenomenon was first introduced as "Hydrogen Sickness" by Butomo et al. in 1968 [166]. It was urged that copper alloys containing up to 0.01 % oxygen in the form of Cu_2O were subjected to heat treatment under the condition of a hydrogen-containing atmosphere. There was a danger of so-called "hydrogen sickness" that was a reaction of Cu_2O and H_2 producing Cu and H_2O. Then, Belkin et al. [167] investigated this issue under the topic of "hydrogen embrittlement", and it was mentioned in this study that this type of hydrogen embrittlement resulted in an oxide depletion or holes at the sites of cuprous oxide particles and above 375 ° C (critical temperature of water), only steam form of water existed, and pressure could reach up to 552 MPa.

Similarly, the same phenomenon was described as "hydrogen attack" in a study from Louthan [169]. It was manifested that producing copper and water reaction, took place at a temperature above the critical temperature of the water, and this reaction resulted in steam pocket or bubbles in the microstructure of the material. This problem was also mentioned in a report from Lutava [168] that the resulting water vapour had a high enough pressure to form pores in the copper (Fig. 2.33).

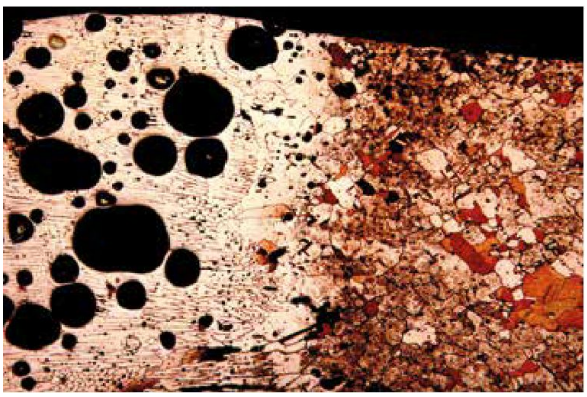


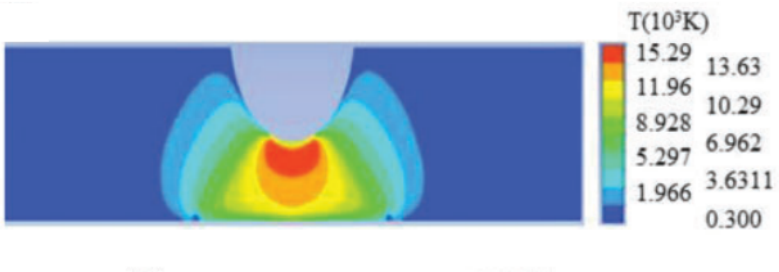
Fig. 2.33 Void forms in ETP copper sample due to hydrogen embrittlement reaction [168]

On the other hand, several lines of evidence suggest that the current type has significant effects on arcing damage. Due to existing zero voltage-current points in alternating current systems, arc plasma is exposed to more interruptions than those of direct current systems. Therefore, arc plasma can reach larger elevating temperatures and is extinguished in a larger period in direct current systems [170–172].

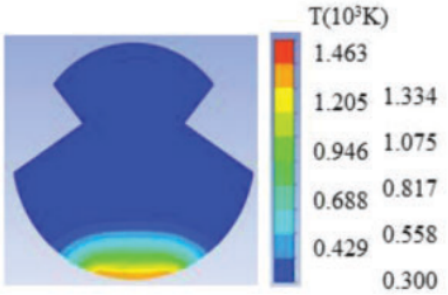
The generalisability of much-published research on this issue is problematic. Since most of the studies gather around wear mechanism of pantograph surface. Therefore, there is a relatively small amount of literature that is concerned with arc damage effects in the contact wire. One study by Zhu et al. [173] examined temperature distribution of arc discharge over pantograph and contact wire surface with the current values between 100-300 A. The results show that during the burning process, copper on the surface melts and turns into vapour due to the high temperature. Fig. 2.34 shows "Computational Fluid Dynamics" (CFD) analysis of the temperature distribution in the arc, the contact wire and pantograph strip when the current reaches to 200 A.

Similarly, Yang et al. [137] and Ding et al. [174] supported the phenomenon of extensive temperature rise due to arcing and define that the heat generated by arc discharge is enormous compared to that generated by friction. They also pointed out that the process can be resulted in arc erosion, melting wear, oxidative wear and adhesive wear.

In order to determine the effects of arc discharge intensity, an experimental study was carried out by Ding et al. [175]. The results showed that when the intensity of the arc discharge increases, the damage on the materials of pantograph and contact wire becomes more severe. The experimental setup used in this study consisted of a rotating disc, where the contact wire coiled, driven by an electric actuator, carbon strip container that has lateral movement allowance and sliding contact with the contact wire. Fig. 2.35 shows schematic of the experimental setup.



(a) arc temperature



(b) contact wire temperature



(c) pantograph strip temperature

Fig. 2.34 CFD analysis of temperature distribution when the current is 200 A [173]

The rotating disc setup is widely used with the aim to investigate wear rate of pantograph carbon strips, contact wire-pantograph frictions and current-voltage characteristics of arc discharge [137, 149, 153, 155, 156, 176–181].

Some research has been carried out to find the relationship between train speed and arc duration. Studies in Korean and Italian railways showed that there is a negative correlation between train speed and arc duration [182, 183]. Also, Gao et al. [184] have revealed calculation results of arc duration for CRH2 high-speed line in China and shown that arc duration decreases from more than 200 to 50 ms while the train speed increases from 150 to 250 km/h.

The studies presented thus far provide evidence that arcing mechanism plays an important role in the reliability and safety of OLE components. Particularly, it becomes more evident with the increase of the speed in train lines. However, most of the studies mentioned, are gathered around arc effects on the wear of pantograph carbon surface, voltage-current variation during the arc issue and damages of different current values and durations to pantograph carbon strips. It is also clearly understood that the effects of arc discharge on the contact wire can be as severe as that on the carbon strip surface. Therefore, the electrical arc discharge and results in OLE contact wires become a significant issue which is little known and needs in-depth studies to understand the effects on the contact wire strength and metallurgy.

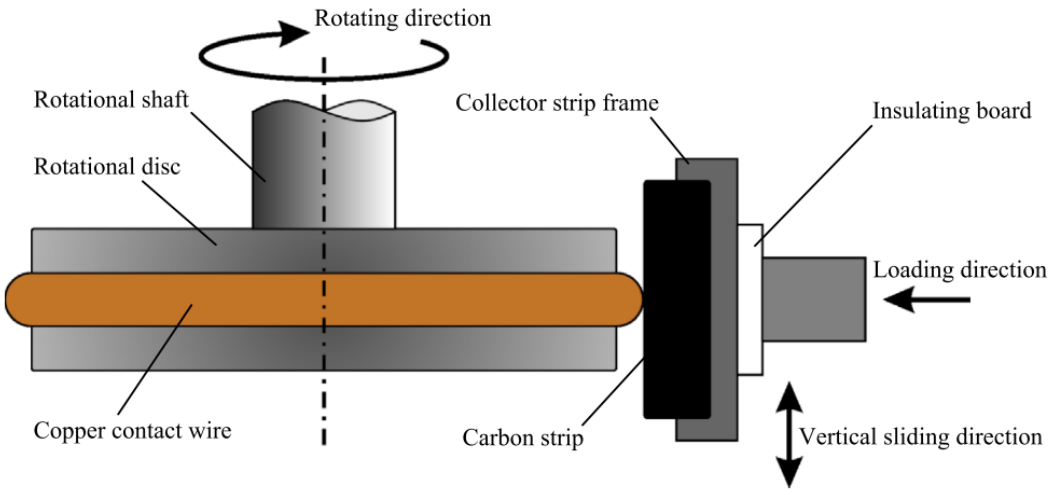


Fig. 2.35 Schematic of the experimental setup [137]

2.4 Identification of Current Research Gaps

The literature on the fatigue of OLE contact wires has highlighted that fatigue issue becomes more critical with the increase of the speed in train lines. Due to having a tensioning and bending stress together at the OLE system, new experimental setups were used in order to replicate bending and tensioning stress together rather than using standard fatigue specimens.

Firstly, a factor needs to be highlighted that, although short samples, relative to wire lengths in real installations, are used in the literature fatigue experiments previous test methods still require contact wire specimens in the order of 2-3 metres length.

Furthermore, in all the designs that were used in the literature, single contact and 3-point bending principles were used. Regarding the boundary conditions of real pantograph-catenary systems, pantograph carbon strip does not have a single point contact with contact wire. Therefore, supports provided by rollers and 3-point bending by an actuator are obscure facts that need to be reconsidered.

The fact that arcing issue in OLE, the problem was occasionally considered from the perspective of pantograph carbon strip wear and voltage-current fluctuations. Although it was highlighted that arc discharge could cause severe damage on OLE contact wire, no detailed study has been done to understand arc discharge effects on contact wire's metallurgical and mechanical properties.

However, the rotating disc experimental setup of the arc issue was primarily designed to investigate the carbon strips. A specific length of contact wire was coiled around a rotating disc and exposed to excessive bending and plastic deformation due to the geometry of this

disc. Therefore, this design is impractical to test metallurgical and mechanical properties of contact wire after the arc discharge.

On the other hand, it has been highlighted in the literature that surface defects due to arc discharge can lead to fatigue crack initiation and accelerate the fatigue failures, there is a lack of study to investigate effects of the arc damage on fatigue behaviours of OLE contact wires.

2.5 Summary

These studies provide valuable insight into the causes of OLE interaction problems due to sliding contact and contact breaks between contact wire and pantograph. Two important themes emerge from the studies discussed so far, namely; effects of electrical discharge on contact wire due to zero contact force (loss of contact) and bending stress and its consequences to the fatigue life of overhead contact wire under the condition of repeated pantograph uplifting force.

Fatigue problem of OLE contact wires can play a vital role with the increase of speed in electrified trains. The fatigue of the contact wire is primarily related to topics of pantograph bending, contact wire tension and surface-wear damages.

On the subject of the electrical arc, nearly all of the studies have focused on damages and impacts of electrical arcs on pantograph carbon strips.

In addition to lack of experimental facilities for fatigue testing of OLE contact wires, existing experimental configurations are impractical to test arc problem and its effects on OLE contact wires. Since these studies remain narrow in focus dealing only with electrical arc impacts on pantograph carbon strips. On the other hand, although it has been mentioned many times in the literature that electrical discharge can cause severe damages on the surface of contact wire and trigger fatigue crack initiation, no in-depth study has been done so far.

Chapter 3

Fatigue Life of Overhead Line Contact Wires

3.1 Introduction

The issue of fatigue due to the uplifting force exerted by the pantograph is an important topic for the safety and reliability of the electrified trains. OLE lines are exposed to fluctuating contact forces due to the trains running with high speed. Fatigue life estimations of contact wires are essential to establish predictive maintenance regime in railway electrification systems. Thus, the potential life of the contact wire can be foreseen more accurately by considering the fatigue life of OLE systems.

In this chapter, force and stress analysis of standard OLE designs, modelling of forces driving overhead line contact wires and a new experimental configuration designed to investigate the fatigue life of OLE contact wires and results of the experiments are explained and discussed.

3.2 Materials and Methods

Fig. 3.1 shows the methods followed in conducting experiments for the fatigue life of the contact wire. Initially, existing OLE mainline contact force data in the UK was investigated to identify the contact force range and locations which were likely to generate fatigue problem in the contact wire. This data was helpful to establish a relationship between contact force and stress in the contact wire. To do this, the OLE geometry and contact force data were transferred to finite element software, and FE models were built using existing stiffness data of standard OLE designs. This enabled this study to develop realistic testing conditions. A

tensile test was conducted to generate stress-strain data for the material properties in the FE model. This tensile test was also a quality measurement of the mechanical properties of the contact wire samples. The FE model also enabled us to compare stress in different standard OLE designs in the world using their design parameters.

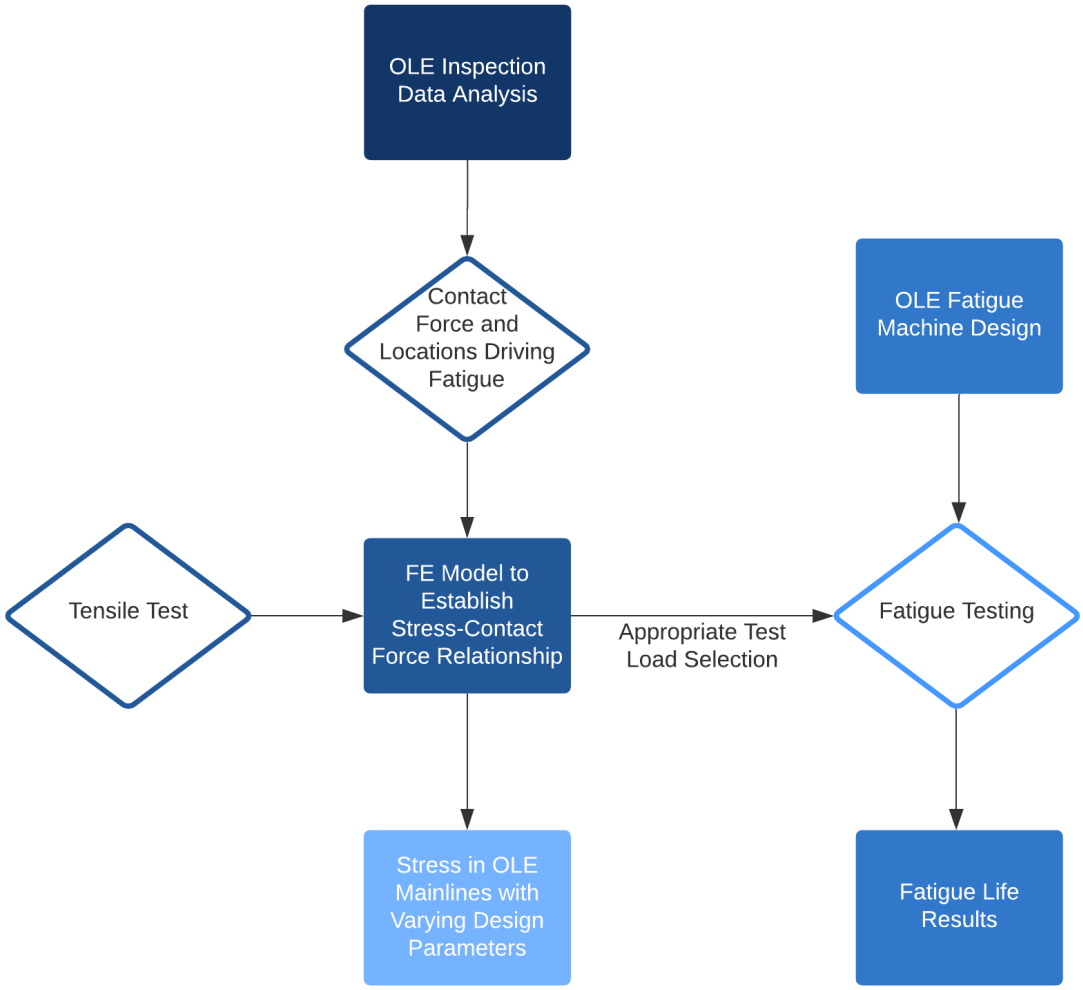


Fig. 3.1 Methods used in testing the fatigue life of the contact wire

A new experimental machine for testing the fatigue life of the contact wire was developed. The appropriate load selection for the experiments was completed based on the same stress range in reality. After conducting the fatigue experiments, the fatigue life results were expressed with strain life approach, and fracture surfaces and behaviours were investigated.

3.2.1 OLE Inspection Data Analysis

Railway electrification has been continuing since 1908 in the UK. Over this period, main lines were subjected to many renovations. These historical developments of the electrification lines in the UK resulted in several varieties in terms of contact wire tension, structures and contact wire type (see Appendix A.1). Initially, in order to investigate contact forces driving the fatigue problem in the contact wire, a newly built electrification line in Great Western Main Line (GWML) was investigated in detail. GWML is a mainline that is operated between London Paddington and Bristol Temple Meads, and the installation has been continuing on the route to Wales. The first stage of the electrification of this route was completed between London Paddington and Stockley in 1996. The route was operated with 25 kV 50Hz AC. However, in this route copper cadmium and hard drawn contact wires with a diameter of 12.3 mm (107 mm^2) were used [185]. This route has been upgraded with new regulations over the time based on Mk3B (Mark 3B Maintenance Parameters [186]. Thus, this part of the GWML between London Paddington and Stockley was difficult to transfer into a finite element model. On the other hand, a new electrification scheme of GWML named Series 1 was completed between Reading and Bristol. This route allowed us to work with consistent and more accurate design parameters to establish the relationship between the contact force and the stress in the contact wire. Table 3.1 shows the system design parameters of Great Western Series 1 [14].

Table 3.1 System parameters of Great Western Series 1

System Parameters		**Standard**
Max Speed		140 mph
Contact Wire	Cross Sectional Area	120 mm^2
	Material	CuAg
	Tension	16.5 kN
Catenary	Cross Sectional Area	65 mm^2
	Material	Bzll
	Tension	13 kN
General Arrangement	Max Span Lengths	65 m
	Max. Wire Run Lengths	1500 m
	Max. Ambient Temperature	-18 $^\circ C$ - +40 $^\circ C$
	Max. Wire Temperature	+70 $^\circ C$

The major advantage of investigating Series I was that the design parameters and structural properties of the mainline were consistent throughout the electrification line. Fig. 3.2 shows

Great Western Electrification Line. Routes of Bristol Parkway, Swindon, Didcot and Reading, were investigated to analyse the contact force variations in the mainline. The maximum contact forces of 21 measurements from two different inspection trains were analysed to find out prospective locations that were repetitively exposed to peak contact forces.

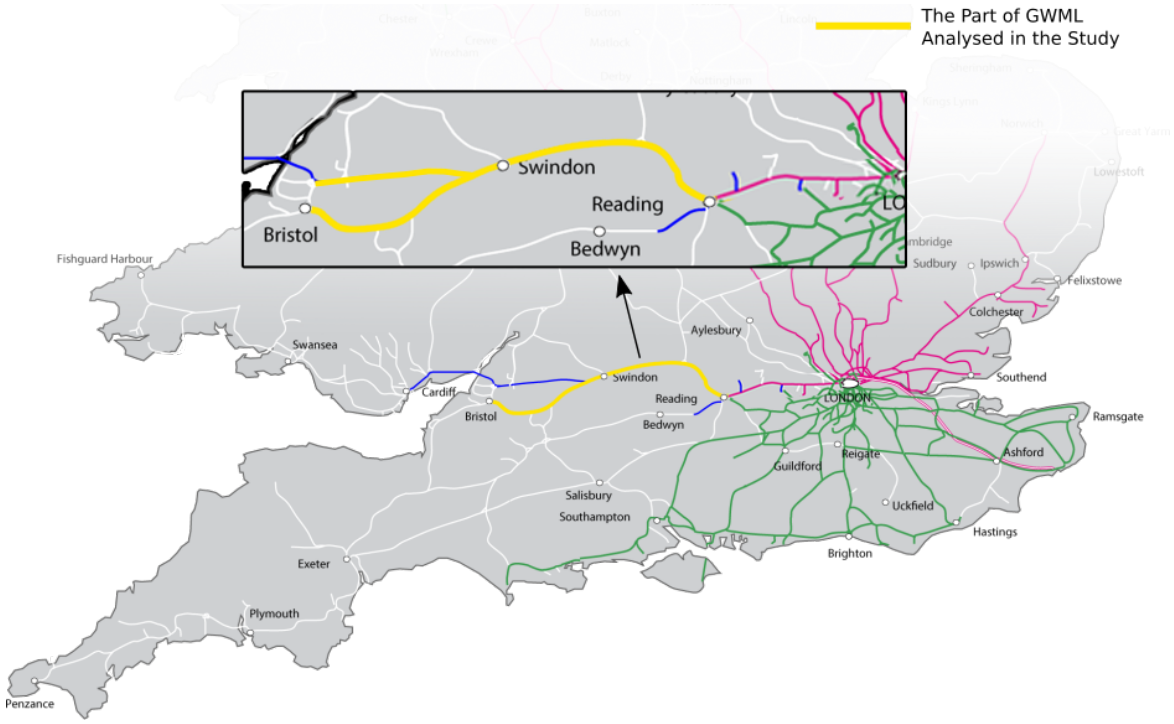


Fig. 3.2 Electrification map of Great Britain

Repetitive Contact Force and Locations in GWML

Initially, measured data from overhead wire inspection was analysed. This data helped to develop a better understanding of the contact force measured in a real OLE mainline. Table 3.2 presents the the maximum contact forces and corresponded locations obtained from GWML. Approximate locations and train directions are also shown in a map in Fig. 3.3. One of the most interesting findings in this table and the figure that the maximum contact forces occurred in specific locations. The highest peak forces which were from 270 to 320 N were measured between the locations of Didcot and Swindon. In the same direction, also between Swindon and Bristol Parkway, peak forces in the range of 280 and 300 N were observed. However, in the reverse direction, the maximum contact force was measured merely to be 200 N at two specific locations of Bristol-Swindon and Swindon-Didcot.

Table 3.2 Maximum contact forces measured in GWML

From	To	km	Force (N)	Speed (km/h)
Reading	**Swindon**	22.4	280	200
		20.6	300	200
		22.55	300	200
		26.3	270	200
		29.6	280	199
		32.9	270	199
		34.2	300	199
Reading	**Grove**	19.6	270	199
		34.4	290	177
		36.6	290	187
		37.4	290	192
		38.5	320	194
Newbury	**Swindon**	59.2	270	192
		54.1	280	190
Swindon	**Bristol Parkway**	16.2	280	186
		17.55	290	194
		21.5	280	200
		26.4	300	200
Bristol	**Didcot**	25.4	200	192
		71.2	200	200



Fig. 3.3 Peak force in GWML

3.2.2 Modelling of Overhead Contact Lines

Investigation of Design Features of Overhead Line Contact Lines

A number of different overhead contact line designs have been used in the world. Although the equipment show similarities, span lengths, contact wire types, pretension and stitch wire connections differ between these designs. Before establishing the finite element model for the design of Series 1 (explained in Section 3.2.1), other designs in Europe, namely, Sicat S1.0, Sicat H1.0, Re250 and EAC 350, were reviewed and span stiffness profiles were compared.

Apart from Series 1, other designs of EAC 350, Sicat S1.0, Sicat H1.0 and Re250 in Europe contain stitch wire. The main reasons for not using stitch wires in Series 1 can be explained with the difficulties during the installation and maintenance of the OLE system. It has been known that the parameters of pretension, contact wire type, span lengths and stitch wires were the critical elements in OLE dynamics. Therefore, the geometries of the OLE designs were modelled in FE software, and identical contact wire stiffness profiles were created with respect to the existing stiffness data shown in Fig. 3.4. The geometry and properties of OLE designs are shown in Fig. 3.5.

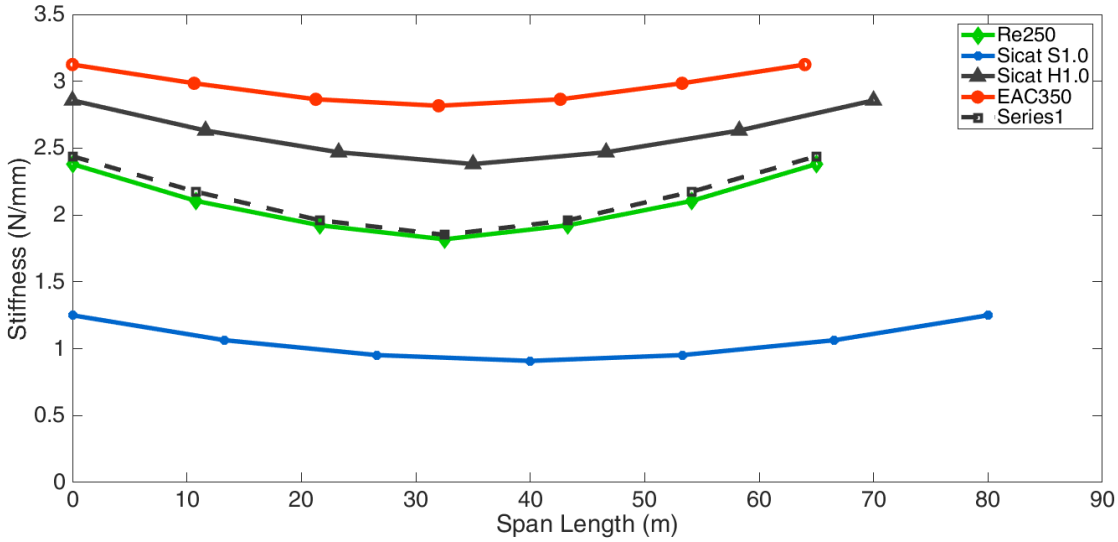
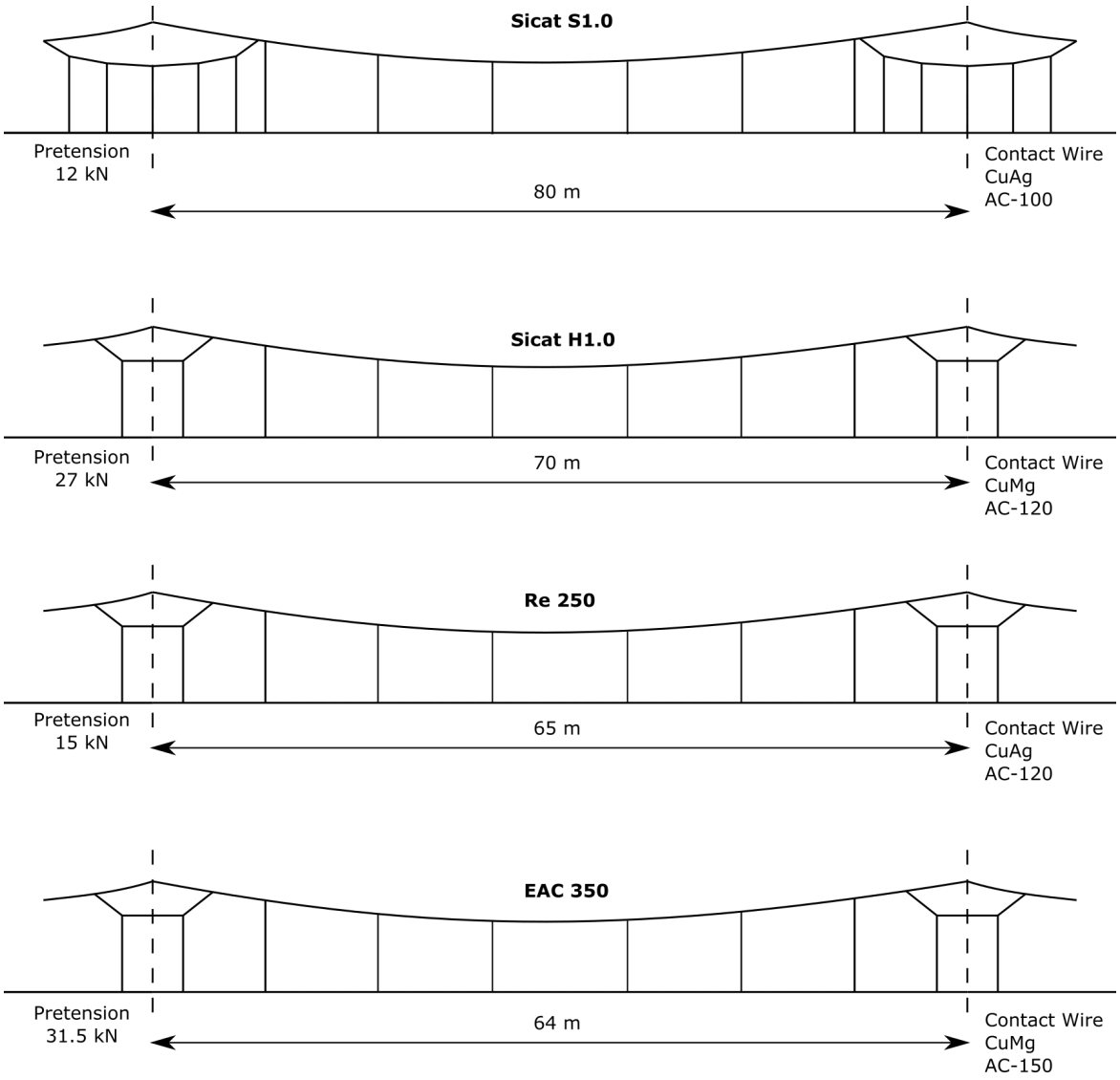
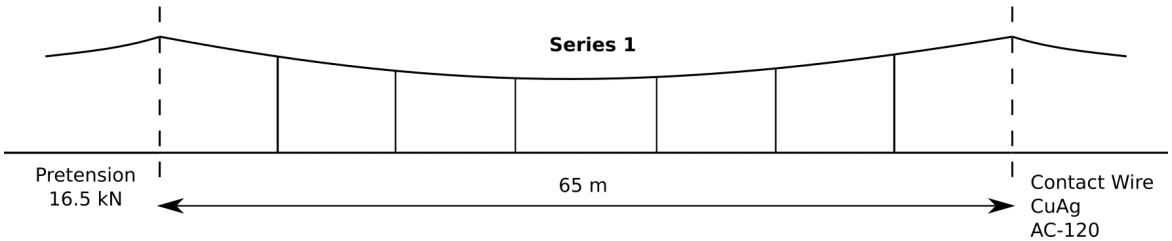


Fig. 3.4 Stiffness profiles of standard overhead contact lines [10]



(a) OLE designs used with stitch wires in Europe

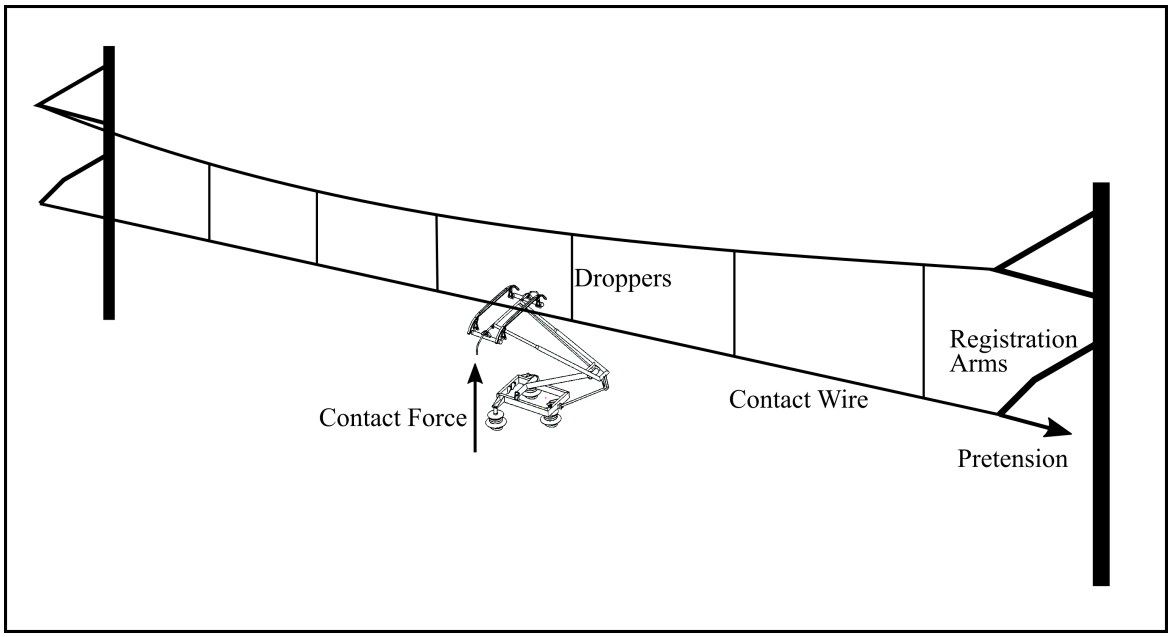


(b) Series 1 used in UK GWML without stitch wire

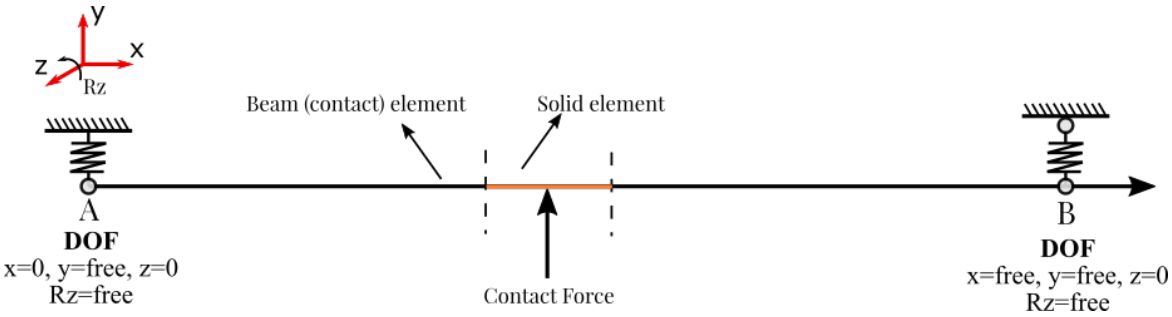
Fig. 3.5 General features of OLE designs in Europe and the UK

Finite Element Model for Contact Force and Fatigue Bending Stress Relationship

An FE model was developed based on the boundary conditions in a span length of the contact wire (Fig. 3.6a). The model was designed as a 3D contact wire, and it was vertically and horizontally supported from the registration arms. The registration arms restrict vertical movement of the contact wire; however, they also have the flexibility to tolerate uplifting pantograph force. This vertical allowance was defined to the registration arms with spring connections, and a stiffness value was set by using the literature data explained in Section 3.2.2. For the lateral and rotational boundary conditions, the model was free to rotate around z-axis at the points of A and B. In order to give lateral movement flexibility (as simply supported beam), the point B was also free to move in x-axis. Fig. 3.6b shows the boundary conditions of the FE model of the contact wire.



(a) Overview of a span of the contact wire system



(b) Boundary conditions of the finite element model of a span-length of the contact wire

Fig. 3.6 Schematic of boundary conditions of a span length of contact wire

Droppers are used to prevent sagging and keep the contact wire in a flat position. Because the contact wire was subjected to uplifting, the droppers were not restricting the vertical movement. It was known that the droppers are essential for dynamic analysis of the contact wire; however, this was only a static model. Therefore, the dropper connections were not taken into consideration in the model. The uplifting force was applied from the middle of the spans, and the maximum stress was expected to be in the centre. In order to minimise the solving time, a-metre length of the contact wire was connected to the registration arm connections with beam(contact) elements.

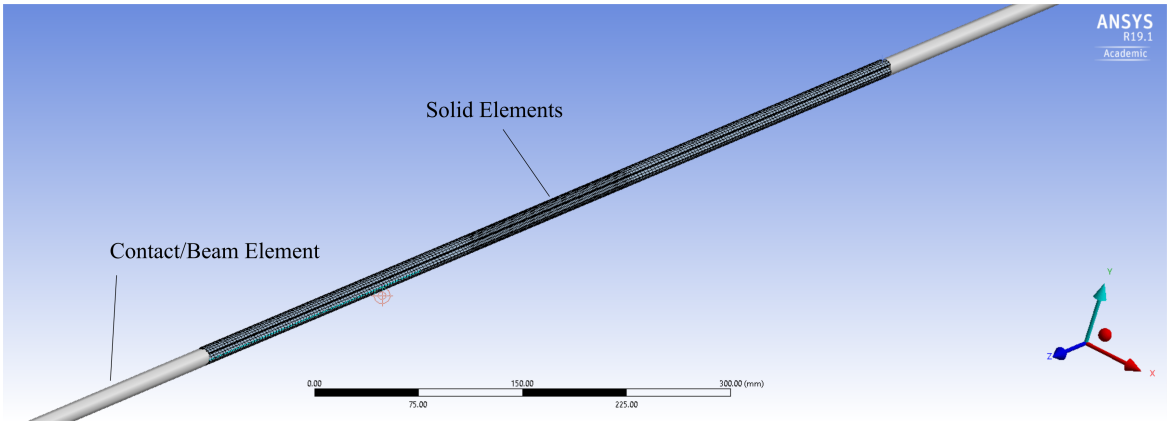


Fig. 3.7 Finite element model with the mesh and beam connections

Fig. 3.7 shows the finite element model developed to investigate the relationship between contact force and stress in the contact wire. The model was divided into three regions for meshing, namely; coarse, fine and very fine. Mesh sizing of the model was finer from the sides to the centre of mid-span since maximum stress was expecting here. A growth ratio of 1.2 was used between the regions. Table 3.3 shows the convergence analysis of the simplified model with mesh size, the number of elements, changes in strain and mesh quality. The % change in strain in each iteration was calculated related to the strain at the first iteration.

Fig. 3.8 also shows the change in mesh quality with an increasing number of elements. Mesh quality checks showed that the quality of the mesh became very stable at iteration number 9. Increasing the number of elements did not significantly contribute to the mesh quality from this point on. Therefore, the mesh size was set to be 1, 1.2 and 1.4 mm for the regions of very fine, fine and coarse, respectively. According to the standard designs explained in Section 3.5, reference tensile properties of copper silver and copper magnesium contact wire with the cross-section of 100 mm^2, 120 mm^2 and 150 mm^2 were used. These properties are explained in Section 3.2.3.

Since the design parameters for each type of overhead line electrification were different, the FE model was run individually with corresponding parameters shown in Table 3.4.

Table 3.3 Mesh parameters used in convergence analysis

Iteration Number	Mesh Size (mm)			Number of Elements	Change in Strain	Mesh Quality
	Very fine	Fine	Coarse		%	%
1	3	3.6	4.32	609004	-	65.03
2	2.75	3.3	3.96	322691	2.22	67.80
3	2.5	3	3.6	193255	2.39	69.53
4	2.25	2.7	3.24	134261	3.58	71.92
5	2	2.4	2.88	98524	2.71	73.77
6	1.75	2.1	2.52	77145	5.71	76.11
7	1.5	1.8	2.16	60356	5.12	77.84
8	1.25	1.5	1.8	50117	8.26	78.90
9	1	1.2	1.44	39906	9.51	80.01
10	0.75	0.9	1.08	34019	9.36	80.66

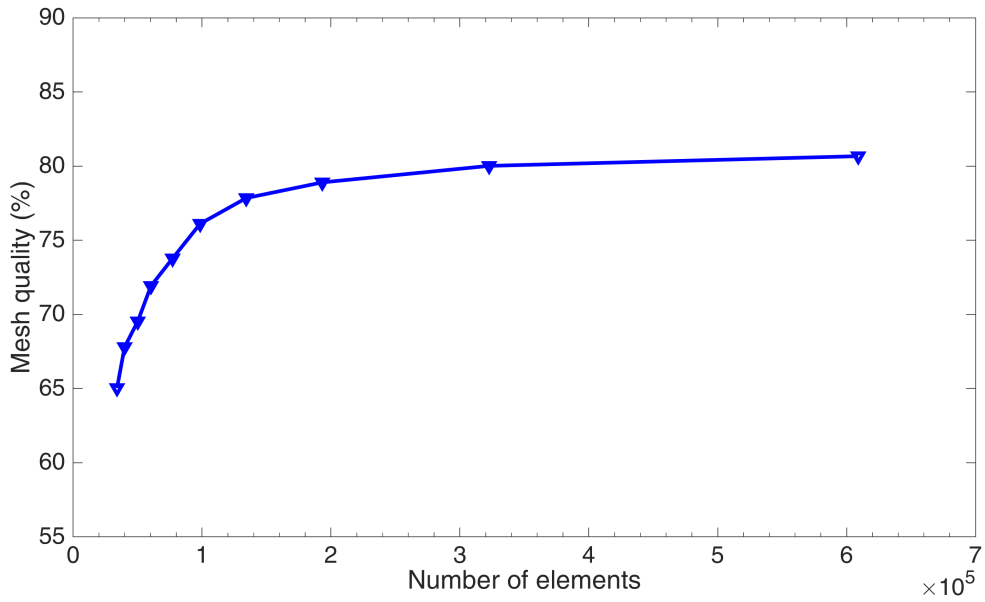


Fig. 3.8 Convergence analysis of the simplified FE model

Table 3.4 Varying parameters in finite element model

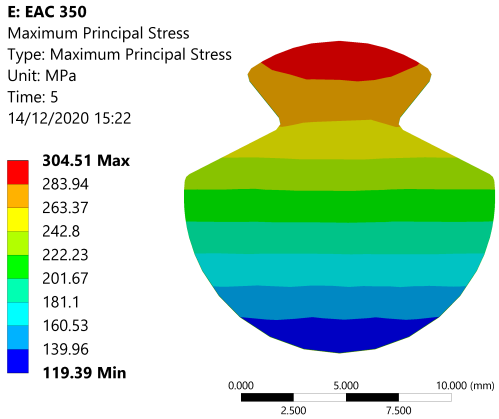
Design Name	Parameters				
	Pretension (kN)	Span Length (m)	Mid Span Stiffness (N/mm)	Contact Wire	
				Type	Material
Sicat S1.0	12	80	0.90	AC-100	CuAg
Sicat H1.0	27	70	2.38	AC-120	CuMg
Re 250	15	65	1.81	AC-120	CuAg
EAC 350	31.5	64	2.81	AC-150	CuMg
Series 1	16.5	65	1.85	AC-120	CuAg

Contact Wire Stress and Strain in Main Lines

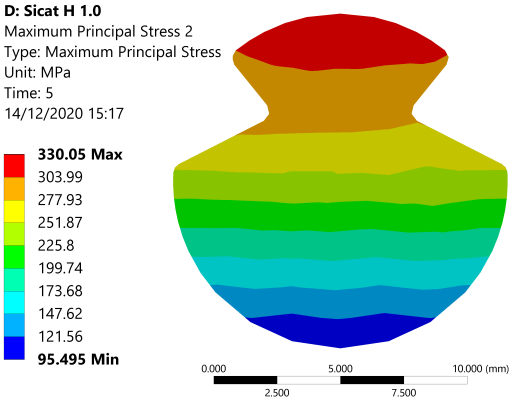
In order to understand the correlation between the contact force and the maximum stress in overhead contact wires, contact forces found in Section 3.2.1 were analysed using the FE models developed for OLE designs (Section 3.2.2). Since OLE mainlines investigated in this study were consisted of different parameters of contact wire geometry, wire tension and span length, this analysis helped to compare these design parameters under the same contact force. In the FE analysis of the standard designs, experimental tensile test results were used for copper-silver contact wire. However, for contact wires other than copper silver grade, literature data was practised.

Fig. 3.9 shows the maximum stress in the middle section of the contact wire and Fig. 3.10 shows the change in the maximum stress range with the increasing contact force from 100N to 300N. Sicat H1.0 and EAC350 initially were subjected to higher stress than other three designs of Sicat S1.0, Re250 and Series 1 under 100 N contact force. The main reason for this was because Sicat H1.0 and EAC350 worked higher pretensions which were 27 kN and 31.5 kN, respectively. Further analysis of the relationship of the contact force and the maximum stress showed that maximum stress in all of the designs rose against increased contact force. However, the designs of Sicat H1.0 and EAC 350 contained the two highest stress levels with just below 350 MPa and 300 MPa. The rest of the designs, Sicat S1.0, Re 250 and Series 1, showed very similar behaviour to one another and rose from just over 180 MPa to in the order of 250 MPa in between the contact force range of 100-300 N.

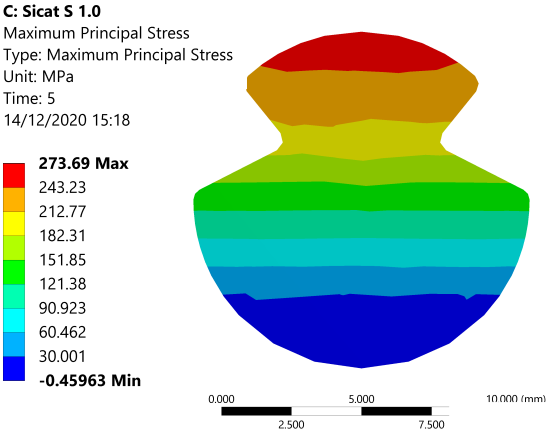
Additionally, the maximum strain in the contact wire was analysed. The relationship between the contact force and contact wire strain is shown in Fig. 3.11. The designs containing copper-magnesium grades of contact wire, Sicat H1.0 and EAC 350, were subjected to the highest strain. However, the most significant increase in the strain was seen in the designs



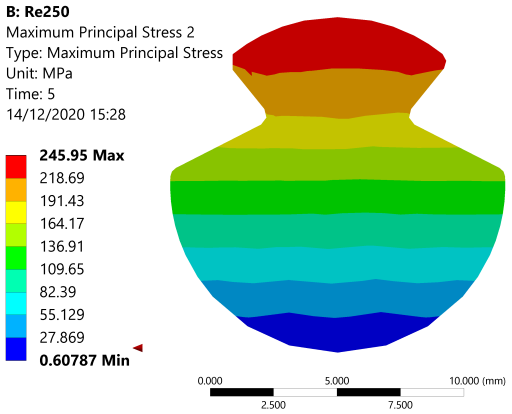
(a) EAC 350



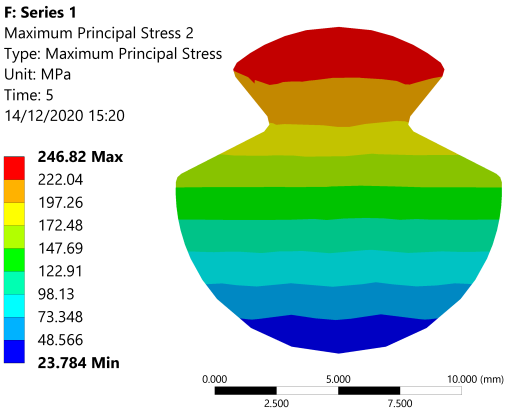
(b) Sicat H1.0



(c) Sicat S1.0



(d) Re 250



(e) Series 1

Fig. 3.9 The maximum stress in the middle section of the contact wire at 350 N contact force

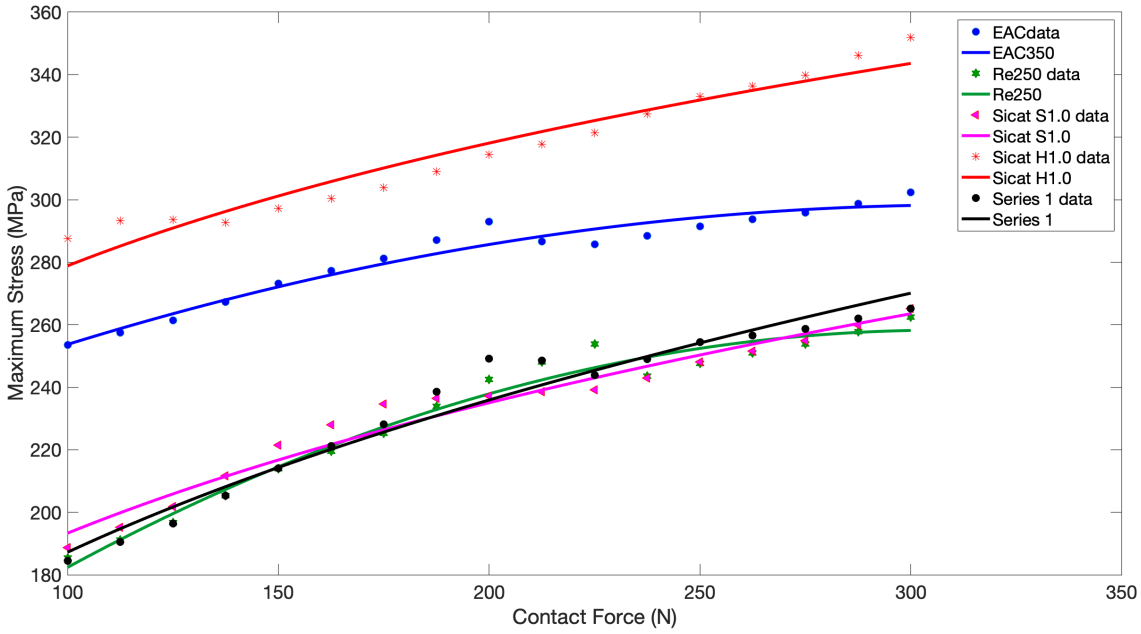


Fig. 3.10 Relationship between contact force and maximum stress for different overhead line designs

containing copper-silver grade contact wires, Sicat S1.0, Re250 and Series 1, as to be in the order of 50 %, while it was just over 20 % and 30 % for main lines of EAC350 and Sicat H1.0 which were equipped with copper-magnesium contact wire. One of the main reasons why the most significant increase was seen in the copper-silver based contact lines can be explained by lower Young's modulus of copper-silver material rather than copper-magnesium grade. Results obtained from the FE analysis was summarised in Table 3.5.

Table 3.5 Increase in stress and strain values in OLE main lines between 100 N and 300 N contact force.

	Stress (MPa)		%	Strain (10^3 mm/mm)		%
	at 100 N	at 300 N		at 100 N	at 300 N	
EAC 350	253.51	304.51	19.26	1.79	2.23	24.30
Sicat H1.0	287.56	330.05	22.37	1.98	2.64	33.37
Sicat S1.0	188.66	273.69	40.52	1.45	2.13	46.51
Re250	185.34	245.95	41.59	1.42	2.09	46.81
Series 1	184.5	246.82	43.70	1.46	2.13	45.72

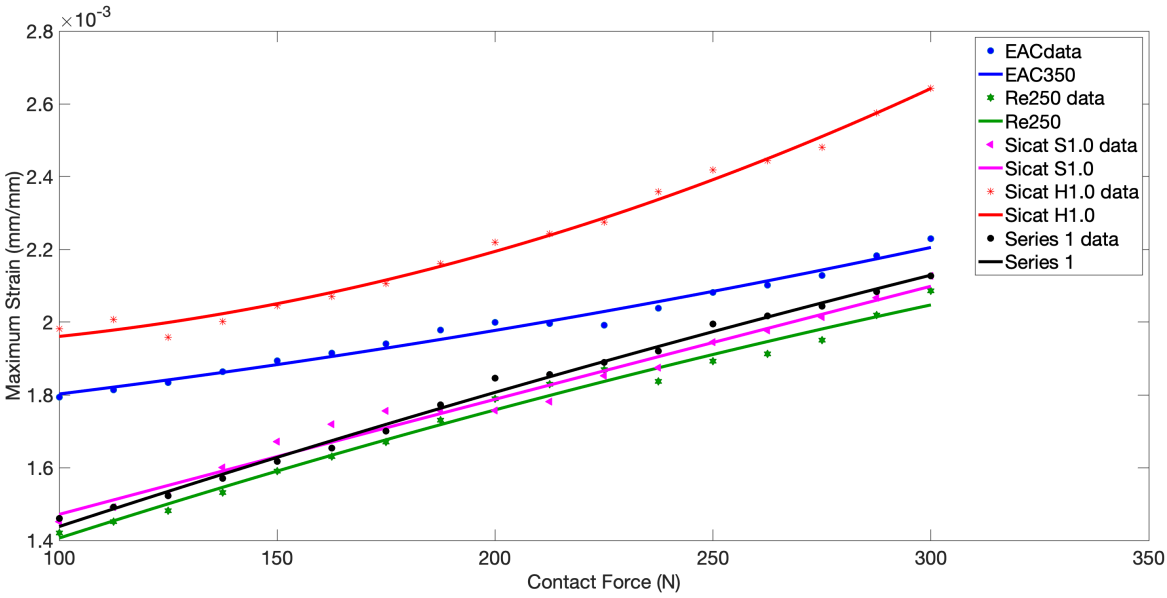


Fig. 3.11 Relationship between contact force and maximum strain for different overhead line designs

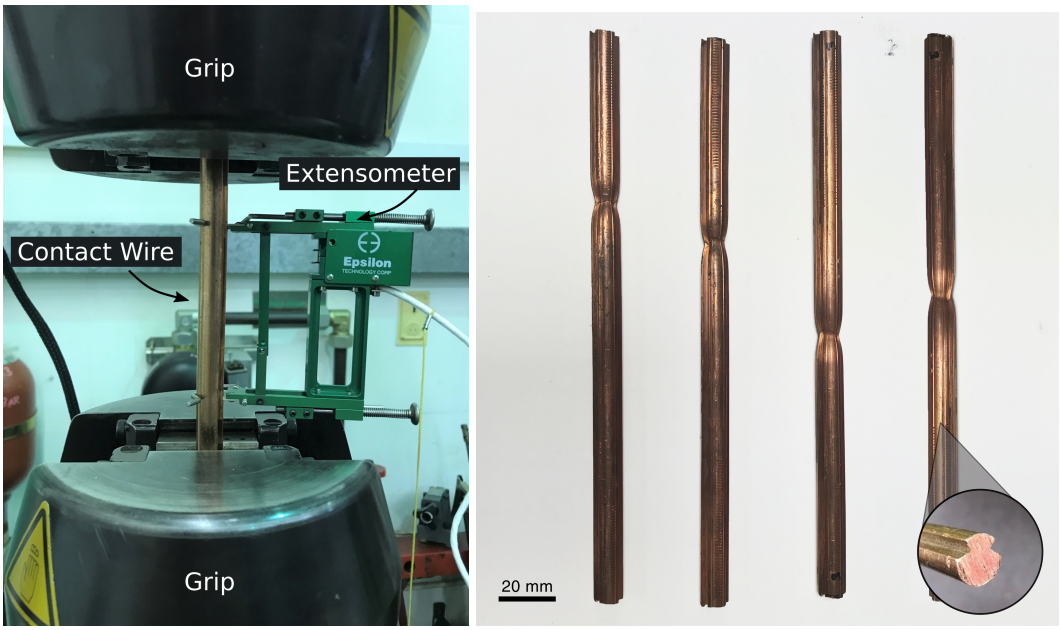
3.2.3 Tensile Testing

In order to understand and obtain data about stress-strain behaviours of copper-silver contact wire, a series of tensile tests were applied to the contact wire specimens prepared for a uniaxial tensioning machine. A capacity of 100kN hydraulic test machine equipped with manual mechanical grips to attach the samples was used. Fig. 3.12a shows the tensile testing configuration.

Copper silver grade (AC120) contact wires were cut to be 250 mm and its natural shape was kept. Displacement control tests were performed with a displacement rate of 0.05 mm/min, and the force was recorded. Strain data was measured by an 80-mm-gage-length extensometer. Tests were repeated with four samples since one of the samples broke from the grip connections. Stress conversions were carried out by dividing the axial force into the cross-section of the contact wire, which was 120 mm^2. Tensile test results of the copper-silver AC120 contact wire were compared with literature data of different alloys of contact wire to verify the test results.

Since ductile materials do not show a certain yield point, it was difficult to identify a yield strength for copper-silver contact wire. Thus, the stress corresponding to offset value at 0.01 % strain was used as 0.01 % proof strength ($R_{p0.01}$) which is accepted the end of the elasticity [187].

Fig. 3.12b shows necking and failure on the contact wire samples after tensile testing. Since unmachined contact wire samples were used, the tensile tests repeated four times to



(a) Tensile testing machine (b) Contact wire samples after tensile testing

Fig. 3.12 Tensile test

verify the test results. An average value of these four tests was obtained for tensile strength of the copper-silver contact wire material. The detailed analysis of tensile test results is shown in Table 3.6.

Table 3.6 Copper-silver contact wire tensile test results

Test Number	Breaking Force (kN)	Tensile Strength (MPa)	Deviation (%)
Test 1	44.7	372.50	0.83
Test 2	45.15	376.25	-0.16
Test 3	45.25	377.08	-0.39
Test4	45.2	376.60	-0.28
Average	45.075	375.625	0

Fig. 3.13 shows the average of the stress-strain curve of the tested copper silver contact wire samples. From this graph, it can be seen that the tensile stress of the contact wire was about 375 MPa which was slightly higher than the standard tensile strength of CuAg0.1 defined in BS EN 50149. Since the copper-silver grade does not show a clear yield point from the tensile test, 0.01% offset yield strength, $R_{p0.01}$ was technically accepted as to be the end of the elastic region. According to this assumption, $R_{p0.01}$ and $\varepsilon_{p0.01}$ were 260 MPa and 2.501x10^{-3} mm/mm, respectively.

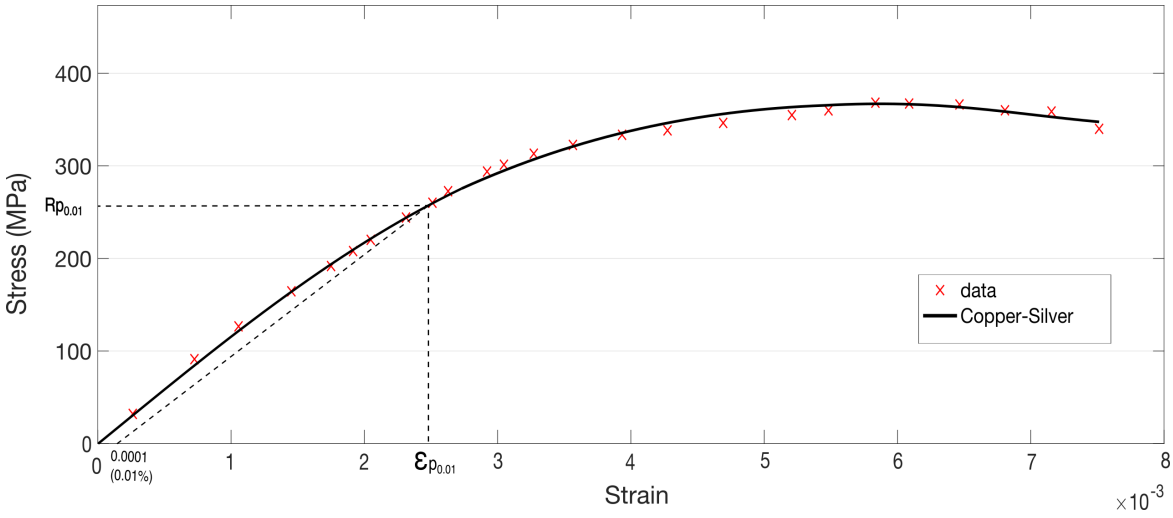


Fig. 3.13 Stress-strain behaviour of copper silver contact wire

The tensile stress of copper-silver contact wire was also compared with copper-magnesium and pure copper contact wires in the literature. Fig. 3.14 shows the graph of stress-strain behaviours of three different contact wire alloys. It can be understood from the graph that copper-magnesium-grade contact wire could satisfy the demand for high-stress levels in the overhead contact lines with the tensile strength of 558 MPa, while that was average of 400 MPa and 375 MPa for pure copper and copper-silver contact wires, respectively. Tensile strength, Young's modulus and elastic stress limit $R_{p0.01}$ from the tensile test of copper-silver contact wire, and literature data of copper magnesium and pure copper contact wire were summarised in Table 3.7.

Table 3.7 Mechanical properties of CuAg contact wire and comparison with other grades in literature

	CuMg [93]	Pure Copper [110]	CuAg
Young's Modulus (GPa)	140	134	120
Tensile Strength (MPa)	558	400	375
$R_{p0.01}$ (MPa)	370	300	260

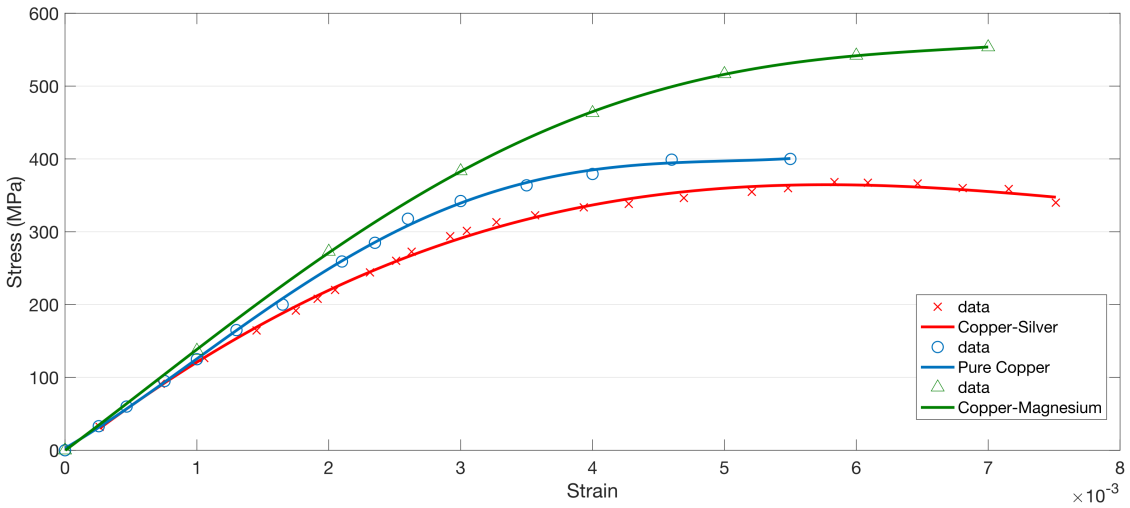
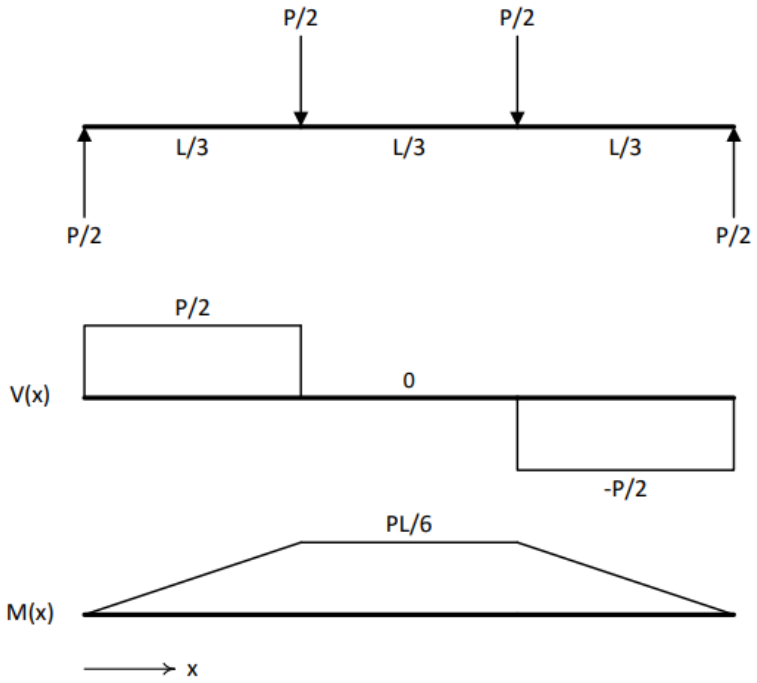


Fig. 3.14 Comparison of stress-strain curves of tested copper-silver contact wire and different grade wires in the literature, magnesium grade [93] and pure copper [110]

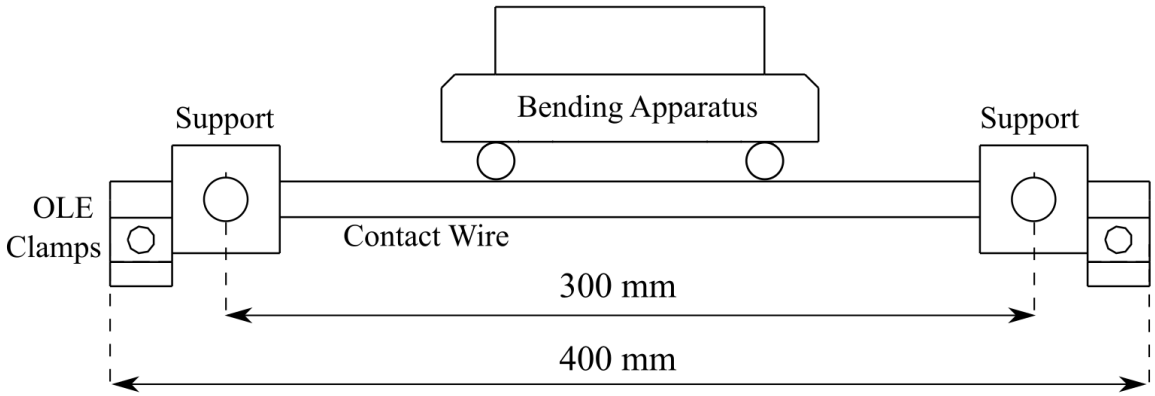
3.2.4 The Design of OLE Fatigue Rig

Span lengths in the mainlines investigated in this study are designed as between 60-80 metres. However, in most recent studies, the dynamic behaviours of OLE contact wire have been tested with 3-4 metres length samples. In this study a new experimental machine was designed and developed. The configuration used for the experimental tests described in this work was capable of testing of 400mm-length contact wire samples. The main reason why a 400mm-length contact wire used was that according to the method of four-point the standard of ASTM D6272-10 [188], the testing sample is divided into three equal lengths (Fig. 3.15a). The vertical bending force was applied from two equally separated points. This was because four-point bending provides a uniform moment distribution across the middle span of the contact wire sample rather than a single high-peak point in three-point bending. Therefore, the sample length in between the left support and right support was considered to be 300 mm. However, the contact wire sample was subjected to axial tension, and it was needed to be supported laterally to prevent the sample from being displaced. Thus, OLE connection clamps were used to connect the contact samples to the supporting ends of the experimental configuration. These additional connections increased contact wire sample length from 300 mm to 400 mm. However, the actual length of the specimen which was subjected to bending stress remained the same because there was not any bending moment beyond the supports. Fig. 3.15b schematically shows the mechanism used in fatigue testing of OLE contact wires.

Beside the four-bending, the contact wire works under pretension, and it was needed to replicate both bending and tensioning effect together. Therefore, the method of four-point



(a) Four-point bending moment and shear diagram according to design of ASTM D6272-10]



(b) Implication of four-point bending to the experimental design for fatigue testing of OLE contact wires

Fig. 3.15 The four-point bending mechanism used in the experimental design

bending was combined with a contact wire tensioning apparatus to ensure a constant pulling force. The entire test configuration designed in this study is shown schematically in Fig. 3.16. Regarding this design, the contact wire sample was held by two rotational bearings. These housings gave rotational freedom to the contact wire sample. A pillow type bearing was selected to provide endurance for long term fatigue tests. A tensioning weight applied the pretension to the contact wire at the far-left end of the apparatus. The tensioning arm provided a 1:10 force ratio. This ratio provided the practice of considerable pretension for the contact wire by using small size weights. The wire was held using standard OLE equipment clamps, connecting it to the bearing supports. Linear guides placed on the tensioning side (left of Fig. 3.16) allowed lateral movement of the contact wire, ensuring it was not over-constrained. Thanks to a mechanism designed to accommodate the bearings on the linear guide, the left-end support was free to both rotate and move laterally while the right-end rotated on the axis of pretension.

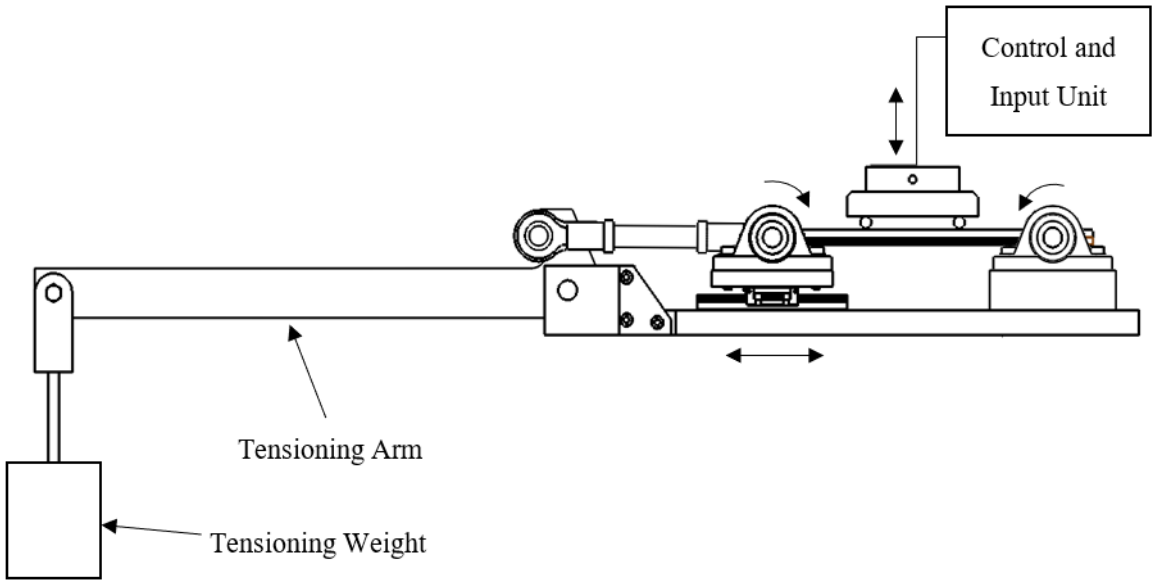


Fig. 3.16 Schematic of movement of the components

The sample mounting fixture was designed to fit within a hydraulic test machine which supplies the actuator and control system for vertical movement. The test would be driven by a sine wave motion or more complex load-time histories from field data or modelling predictions. The vertical load was measured by using a load cell with 500 kg capacity (RLT0500, RDP Group) installed between the actuator and four-point bending apparatus.

Fig. 3.17 shows the OLE fatigue apparatus designed to investigate fatigue properties of OLE contact wire. Standard linear guides and carriages were chosen to provide minimum frictional lateral movement to the tensioning side of supports.

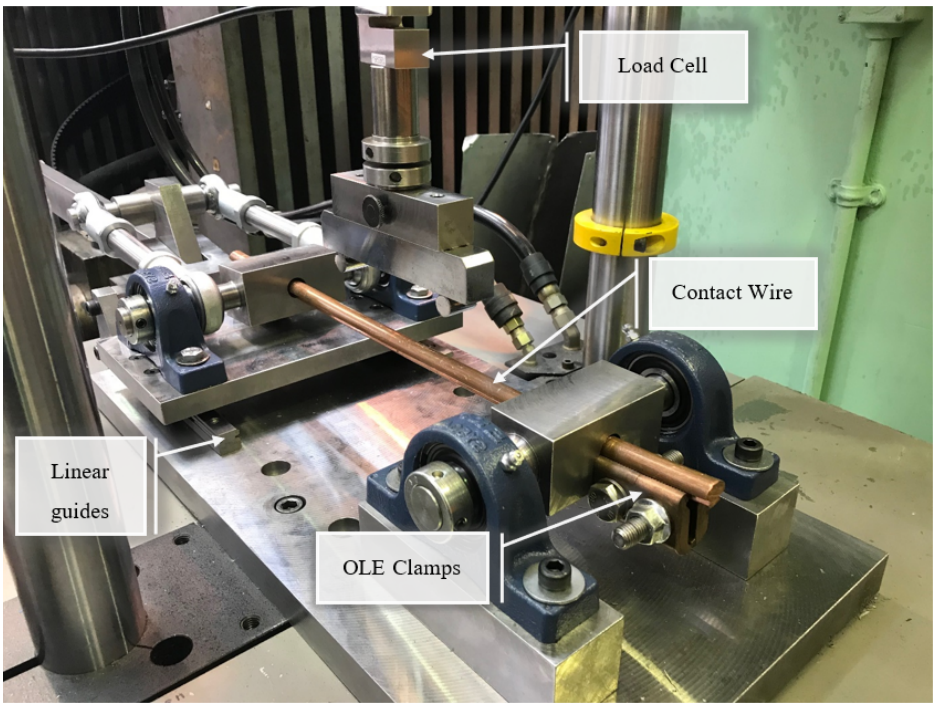


Fig. 3.17 Components of OLE fatigue apparatus

Fig. 3.18 shows the pretension mechanism of OLE fatigue apparatus. This part of the experimental configuration consisted of a lever unit which was holding the weights. The lever was manufactured from a steel material and connected to the end of the support having free lateral movement so that it could transfer the pulling effect to the contact wire. The unit carrying the weights was manufactured by a light material of aluminium (2.3 kg). This aluminium unit was connected to the lever arm by screw type of connections. The pretension of the contact wire was applied by loading the weights onto the holding unit. While selecting the appropriate load for tensioning, the weight of the holding unit was also taken into account.

Load and displacement in the tests were monitored and controlled using a MOOG modular test controller (Fig. 3.19). Force data collected by the load-cell connection was transferred to the monitoring system during the experiments. The sensitivity of the load-cell and displacement was calibrated before starting a new experiment. The experiment was automatically terminated when the loadcell detected zero vertical bending force due to the contact wire failure.

3.2.5 Specimen Preparation

A number of specimen designs can be found in the standards for general fatigue testing, such as; ASTM E8-08 [189], ASTM E466-07 [101] and ASTM D6272-10 [190]. Although it

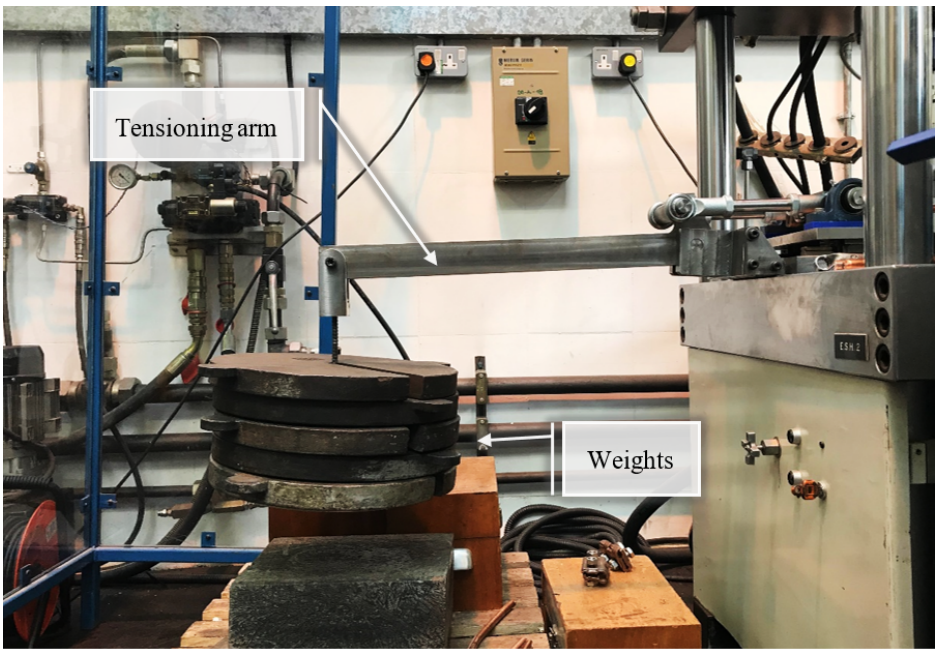


Fig. 3.18 Tensioning mechanism of OLE fatigue apparatus

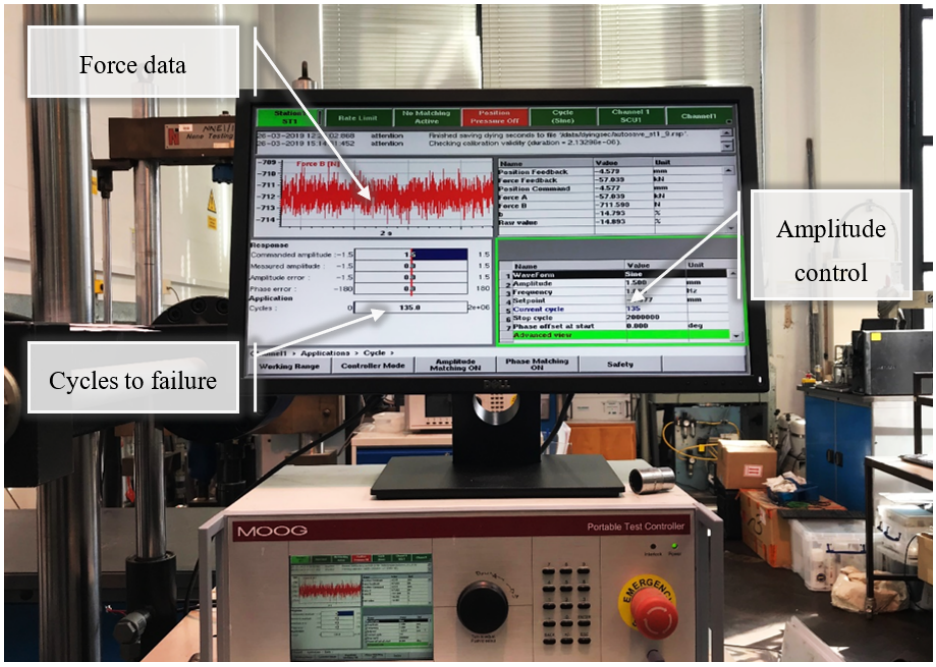
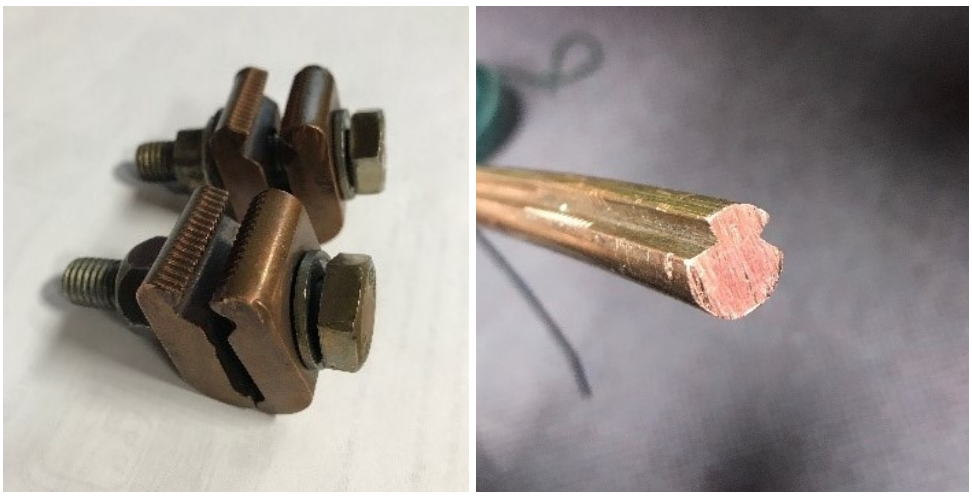


Fig. 3.19 Monitoring of the fatigue experiments

would be possible to prepare a standard fatigue test sample from a contact wire, the aim in the new facility was to test contact wire in its natural form. The preparation was to slice 400-mm-length of wire, although it was also important that the wire was straight and free from surface scratches or handling damage unless such pre-damage was a focus of the tests.

The contact wires were manufactured with continuous casting; therefore, they were supplied as rolled in coils. The first step was starting with uncoiling the supplied overhead contact wires. This operation was good practice for replicating the real installation process of the contact wire. Because during the construction of OLE systems, contact wires are supplied in coils and installed by uncoiling operation. The second step of the specimen preparation was that samples were marked and sawed manually to obtain short-length contact wires. The samples were mounted to the test apparatus by using standard OLE clamps (Fig. 3.20a) that fit into the grooves on the contact wire (Fig 3.20b).



(a) OLE clamps (b) Contact Wire

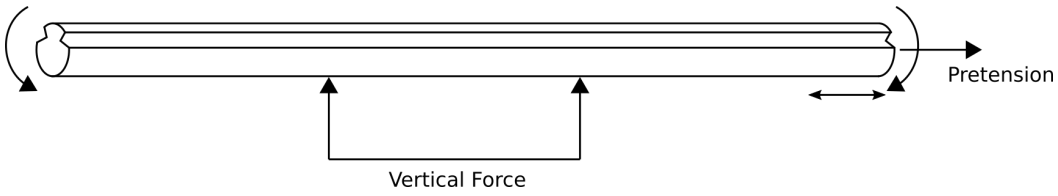
Fig. 3.20 Clamps and the contact wire used in fatigue experiments

Brand new contact wires were used for experiments. Therefore, there was no surface damage and wear on the samples. Besides, specimens were prepared attentively so that no initial crack occurred on the surface of wires during the sawing operation. Once the sample was fitted the fatigue apparatus, the position of the tensioning arm was adjusted as horizontal to the contact wire to apply 1:10 moment ratio. On completion of sample mounting, the process of pretension was carried out by loading weights to the tensioning arm.

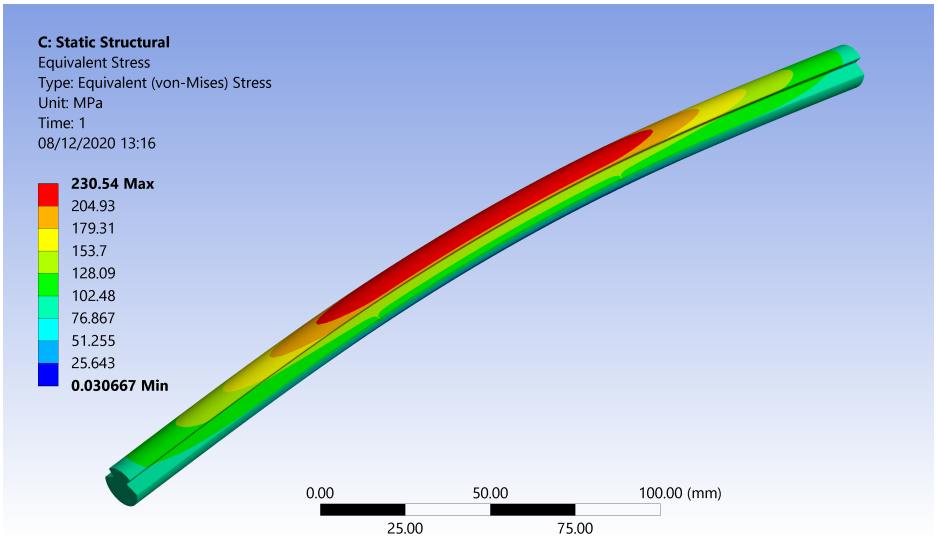
3.3 Fatigue Testing

3.3.1 Appropriate Test Load Selection

Bending fatigue testing was conducted using the experimental apparatus explained in Section 3.2.4. Since the fatigue testing was using a short-length contact wire samples, it was unable to use the pantograph contact force measured in OLE main lines, directly as to be the testing force in the fatigue experiments. The pantograph contact force needed to be optimised to use in short-length contact wire testing. Therefore, the vertical load used in fatigue testing was determined by a strain-vertical bending force relationship. For this reason, static nonlinear analysis was conducted using an FE model with the contact wire under pretension. In the FE model, the boundary condition of the contact wire was a simply supported beam with the combination of axial pretension. The stress-strain curve obtained from a tensile test (Section 3.2.3) was used for defining material properties. Fig.3.21a shows schematically the boundary condition of the finite element model.



(a) Boundary conditions of contact wire sample under pretension and vertical loading



(b) Finite element model for selecting the appropriate test load

Fig. 3.21 Clamps and the contact wire used in fatigue experiments

This FE model helped to develop a correlation between vertical testing load and the maximum strain values. Because the contact wire sample was also subjected to strain in the

condition of zero vertical loadings caused by pretension applied to the contact wire, it was essential to include the effect of tensioning of the wire.

A convergence analysis was applied to the FE model to determine the optimum number of elements. Regarding convergence analysis, the difference in the maximum stress was analysed over the increase in the number of elements. The convergence point in which the maximum stress became flatten and steady in the graph was selected to be the optimum element size. Fig. 5.5 shows the convergence results.

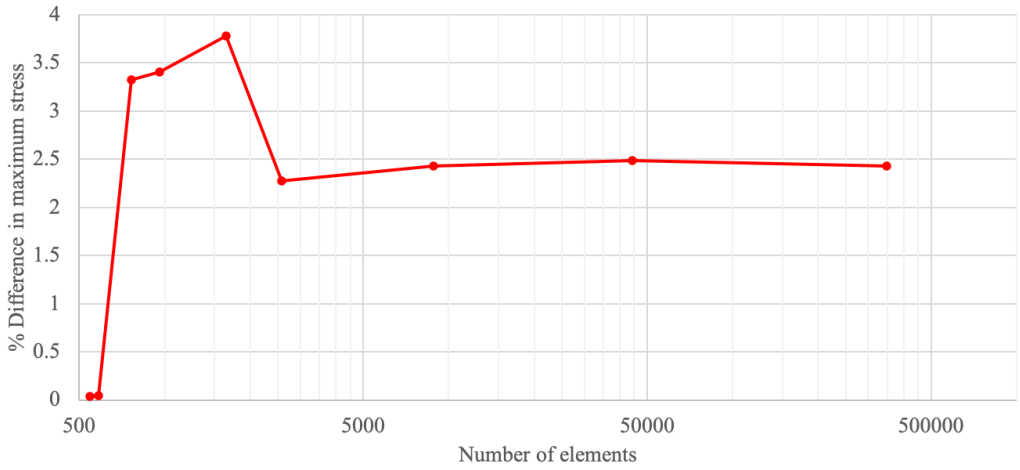


Fig. 3.22 Convergence analysis of FE model in log scale

Furthermore, a number of element quality checks were conducted to asses the accuracy of the model. Table 3.8 presents the measurements results of the element quality of the FE model.

Table 3.8 Element quality assessments of the FE model developed to determine fatigue test loads

	Maximum	Minimum	Average	Standard Deviation
Aspect Ratio	13.5	1.16	1.87	0.46
Jacobian Ratio	1	-1	0.98	$7.6\text{x}10^{-2}$
Skewness	0.97	$4.3\text{x}10^{-5}$	0.24	0.13

*for a perfect tetrahedral element; Aspect ratio: 1 [191],
Jacobian Ratio :1, Skewness : 0.5 [192]

Table 3.9 presents the results obtained from FE analysis (Section 3.3.1) to select appropriate loads for fatigue testing of OLE contact wire specimens under tensioning. Therefore, the stress and strain results in the table also contain axial tension from the tensioning mechanism

of the testing apparatus. Individual tests were carried out in order of the selected loads. These loads were decided to be the maximum test load for each fatigue sample.

Table 3.9 Load selection for fatigue testing

Displacement (mm)	Vertical Force (N)	Strain (mm/mm) 10^{-3}	Stress (MPa)
1.56	1500	2.028	230
2.05	1750	2.470	248
2.66	2000	3.027	280
3.96	2500	4.253	324
5.22	3000	5.553	347
6.25	3400	6.664	365

3.3.2 Loading Conditions

Although a zero-based vertical cycling loading, which varied between zero and positive region, was applied to the contact wire sample, a pre-existed uniaxial stress, which was due to the constant tension in the wire, altered the zero-based cycling loading to alternating loading condition where the stress ratio was positive. This phenomenon was schematically explained in Fig. 3.23. The additional stress due to the contact wire tension increased the maximum and minimum stress in the same proportion. This also increased the mean stress, and the contact wire sample became more vulnerable to the stress alternations.

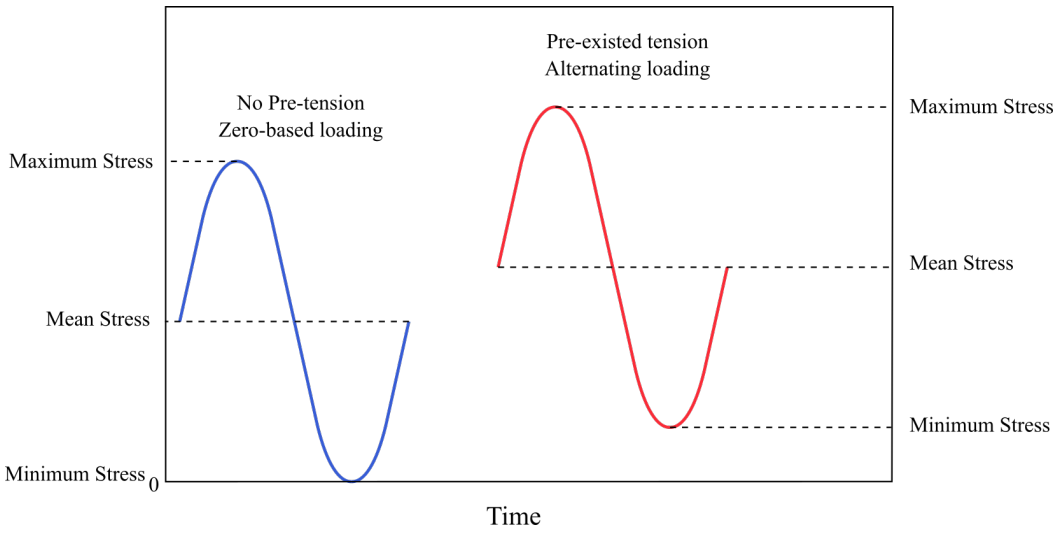


Fig. 3.23 The effect of the contact wire tension on the fatigue loading condition

3.4 Results

Fatigue testing of contact wire samples was conducted with a displacement controlled hydraulic machine equipped with the fatigue apparatus designed in Section 3.2.4. The displacement and the vertical test load was monitored during the experiments. Strain conversation was applied using the parameters found in Section 3.3.1. Table 3.10 shows the fatigue life (cycle to failure) results of overhead contact wires with the loading conditions under pretension. Results were explained with the combination of strain caused by uniaxial tensioning and vertical bending loading. Regarding the plastic strain in the table, corresponding strain value to the 0.01 % offset yield strength was selected as to be plastic strain starting point (in Section 3.2.3). The maximum and minimum stress loading values were calculated by the FE model developed in Section 3.3.1. According to these results, it is clear that the fatigue life of the contact wire became shorter when the maximum strain was increased.

Table 3.10 Fatigue test results

Test Number	Min Strain (10^{-3})	Max Strain (10^{-3})	Plastic Strain (10^{-3})	Fatigue Life (N_f)
1	0.79	2.470	0	6588432
2				7010955
3	0.79	3.027	0.526	1286928
4				1424516
5				1650211
6	0.79	4.253	1.752	480655
7				410951
8				427888
9	0.79	5.553	3.052	210896
10				228444
11	0.79	6.664	4.163	70708
12				73528

Since the copper grade is not a ferrous metal, it is not possible to identify a fatigue limit [193]. It is expected that the fatigue life of the contact wire will become shorter when the maximum strain is increased. To estimate the fatigue life of the contact wire, a strain-life graph was plotted in Fig. 3.24 using the data obtained from the experiments. A second-order exponential curve fitting was applied to the test points in the graph. The curve for the maximum strain against cycle to failure showed a typical strain-life curve characteristic with a tendency to bend towards a more horizontal direction when the elastic strain predominated.

Experiments were not conducted with a constant stress ratio. The main reason for this was that the samples were subjected to constant tension and the stress ratio became more substantial with the increase in vertical testing load. Therefore, the stress ratio was varied between 0.32 and 0.12.

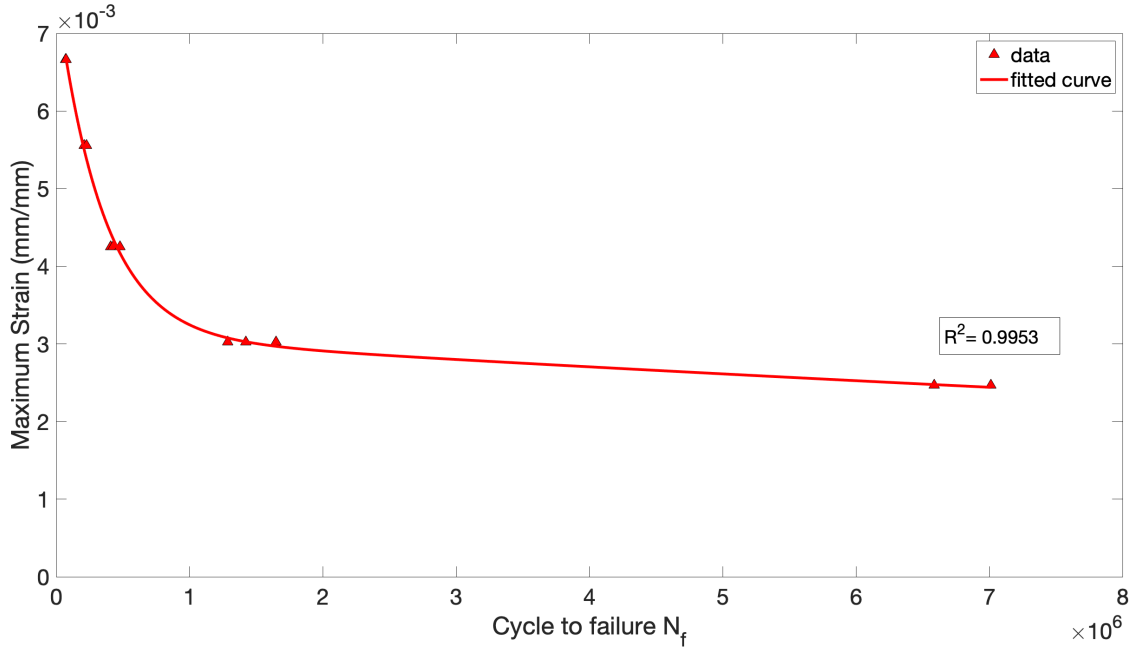
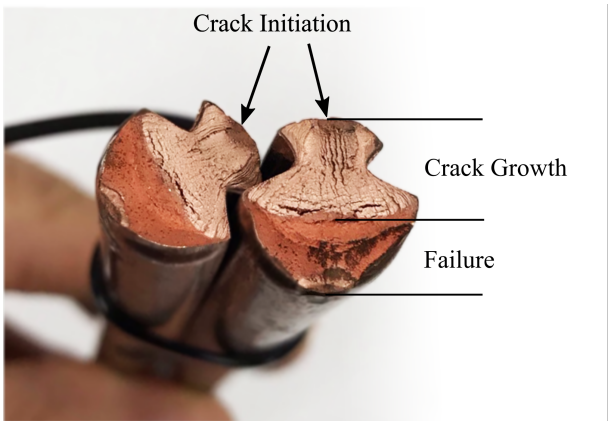


Fig. 3.24 Strain-life curve of the tested contact wire samples

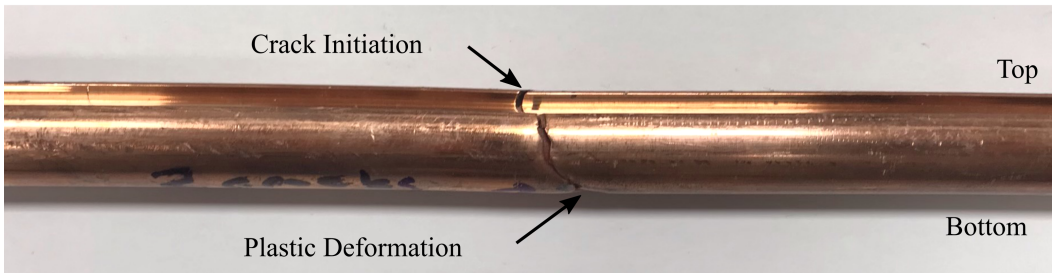
The macroscopic fracture inspection was conducted after the fatigue failure of the contact wire samples. It was seen that all of the samples showed similar fracture behaviours such that a crack initiated at the top of the contact wire and the sample broke from the bottom with plastic deformation seen in Fig. 3.25a and Fig. 3.25b. Since the top surface of the contact wire sample was subjected to maximum tensioning stress, and this developed a crack opening effect. In between the initiation point and the bottom of the contact wire, striations were distributed towards the crack propagation directions. It was also observed a plastic deformation prior to the failure (Fig. 3.25d and Fig. 3.25c). One of the main reasons for this was that the cross-sectional area of the contact wire sample reduced due to the crack propagation. Thus, reduced cross-sectional area was unable to withstand the pretension, and the contact wire samples broke when the crack reached to a critical length.



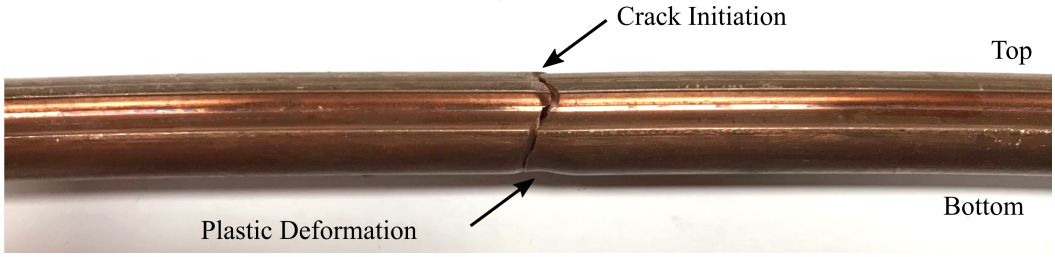
(a) Fracture surface in Test 5



(b) Fracture surface in Test 9



(c) Crack direction and necking after the fatigue in Test 5



(d) Crack direction and necking after the fatigue in Test 9

Fig. 3.25 Fracture surface and crack directions of the samples in Test 5 and Test 9

3.5 Discussion

Results from analysis of real OLE contact wires, completed with the contact force range between 100 N and 300 N, showed that the maximum strain in the contact wire could reach at the very high end of the elastic limit of the material. Considering the increase in the speed of trains, this could elevate the strain (and stress) to higher levels. This will eventually result in plastic deformation in OLE contact wires. Therefore, the strain-life method, which predominantly investigates low cycle fatigue, was essential to predict the fatigue life of the contact wire. Furthermore, the strain-fatigue life curve developed with a range of test loads including the varying level of plastic deformation and full elastic deformation can be used for extrapolating a trend for further high cycle fatigue life results of the contact wire.

In real life, every cycle in the fatigue tests corresponds to a single pantograph passage. Considering the heavy traffic in the highspeed mainlines, it has been known that some OLE mainlines are subjected to maximum of 220000 and average of 150000 pantograph passage (cycle) in a year [21]. Therefore, under the selected loading conditions in this study, while the maximum fatigue life is still around the wear life of the contact wire (approx. 50 years), the minimum fatigue life can be less than a year. Although this short fatigue life is considered a very rapid and extreme condition, it is still a representative test condition. Because it has been already known from Network Rail's technical report [113] that a fatigue associated incident occurred just two years after the installation of the contact wire.

Contrary to standard fatigue tests, it was not possible to perform the fatigue experiments at frequencies higher than 5 Hz with an apparatus designed in this study. Since the fatigue apparatus, which was designed for a real scale fatigue testing of the contact wire, was equipped with a tensioning arm carrying heavyweights. All these weights considered, in order to minimise health and safety issues, experiments were run below 5 Hz.

The fatigue life results of the contact wire in this chapter were used as reference results to compare with those after the arc damage (in Chapter 6). The fatigue apparatus testing the real-scale contact wires also allowed us to investigate the fatigue life of contact wires after surface damage due to electrical arcing, which is not possible to test with standard fatigue tests. The four point bending method was intentionally selected so that fatigue experiments of arc-affected contact wire samples in Chapter 6 can be also conducted without creating additional shear stress or point contact on the surface of the arc location which was located in the middle of the sample.

3.6 Conclusions

This study set out with the aim of understanding fatigue behaviours of overhead contact samples under a constant pretension. Initial analysis of the test data of GWML provided by Network Rail and Furrer+Frey was important to examine the pantograph-contact wire interaction and determine locations subjected to large contact forces. Findings of this analysis showed that contact wires could be exposed to repetitive contact force at specific locations during the pantograph's journey. A finite element model which was capable of analysing standard OLE designs both in Europe and the UK was developed. The analysis of real OLE designs undertaken here has extended our knowledge of contact force-stress relationship. Findings of real OLE system analysis contributed to appropriate and realistic load selection for the fatigue tests. The experimental setup developed for this study may be applied to other fatigue studies of OLE contact wire which cannot be conducted with standard fatigue tests.

The work showed that for an undamaged contact wire fatigue testing is in the order of 70000 cycles at the tests numbers of 11 and 12 was a rapid but still accurate and representative test condition. This and other test parameters in this chapter will be used as a benchmark for the work investigating fatigue life of the contact wires after arc damage in Chapter 6.

Chapter 4

Effects of Arcing on the Contact Wires

Railway overhead line electrification systems transmit energy to trains through a high-speed sliding interface which presents a challenging tribological system. Mechanical wear and electrical transmission at this interface both impact component life. Momentary loss of contact between a pantograph and the overhead contact wire produces arcs and consequent extreme local heating in contact wires.

This chapter investigates the cause of arc damage and then potential mitigation of the damage mechanism with experimental tests. Initially, a machine designed to quantify the effects of arc(s) on overhead railway lines is explained, and the first results are reported. Effects of arcing are discussed using the results obtained from micro-hardness tests, metallography, voltage-current and temperature measurements.

4.1 Arcing in Overhead Line Electrification

Trains collect power from overhead lines using a device named pantograph. The pantograph is a rather complex device equipped with springs, arms, pneumatic system, electrical parts and various mechanical components. However, the sliding contact surface of the pantograph, named carbon strips, is the element which is subjected to mechanical and electrical contact with the contact wire. Although the pantograph is designed to provide constant current collection quality, a range of issues can cause breaks in the circuit of pantograph contact wire pair. Common reasons for the break in the circuit are pantograph dynamics due to the increase in train speed, OLE fitting components and circuit breakers (section insulators or neutral sections). The pantograph is designed to apply a constant uplifting to the contact wire by a spring tension mechanism. Because this mechanism is not an active control, this causes loss of contact between the pan and the contact wire during the train journey, in particular at a higher speed. Although the loss of contact is momentary, this often causes electrical arcs

between pantograph current collection surface (collector strip) and the contact wire. The arcs generate heat exposure on the surface of both collector strip and contact wire. This type of arcing is named "Pantograph Arcing". However, arcs are seen not only as pantograph arcing but also as "Flashover". Because OLE is a complicated structure that can have small electrical clearance when the system includes bridges, overpasses or tunnels. Small electrical clearance can result in flashover arcing between OLE live wires and supporting or external structures (bridges, tunnel or overpass).

One of the main reasons for arcing is that ionised air between components that conducts the electrical current. Current conducting capacity of the air varies depending on the air gap, voltage difference between the conductors and environmental conditions. In this chapter, the arcing problem is studied under the titles of pantograph arcing and flashover.

4.1.1 Pantograph Arcing

Pantograph arcing can be observed in overhead electrification lines due to loss of contact between pantograph and contact wire. Because in operation, contact wire and pantograph surface carbon strips are exposed to staggering, sliding friction, joule heating and surface problems that make the mechanical and electrical contact complicated. This type of arcing can occur as repeating or single arcing. The repeating arcs can be seen in specific locations, such as; neutral sections, OLE fittings, section insulator or droppers in which contact wire misalignment combined with the dynamics of the pantograph cause the electric circuit breaks, for example. Separately, less repeatable arcing in line of the contact wire appears with the increase of train speed that causes more loss of contact between pantograph and contact wire.



(a) Arcing at a section insulator (b) Arcing due to a high speed train journey

Fig. 4.1 Pantograph arcing

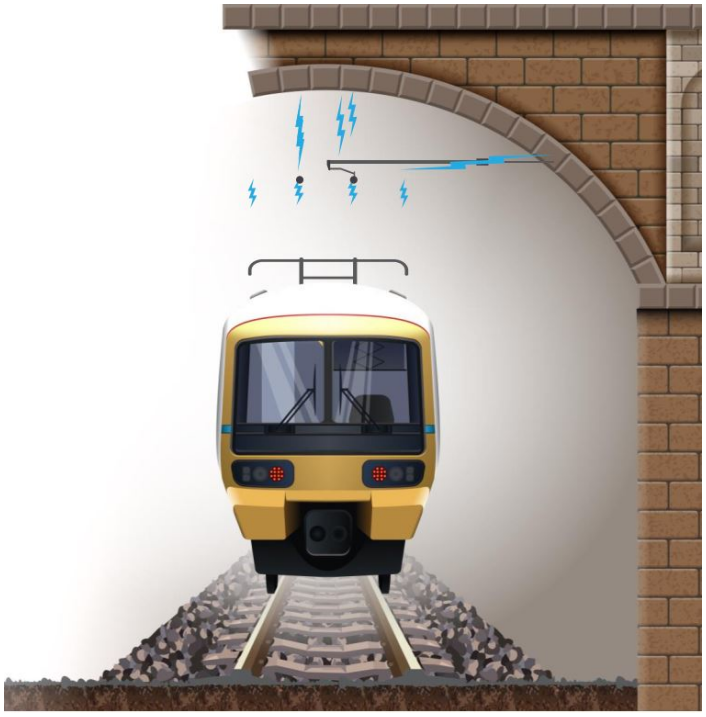
Fig. 4.1 shows pantograph arcing in OLE systems. Neutral sections and section insulators are devices installed in OLE for electrical separation of two electrical feeds while allowing

for the passage of the pantograph. Particularly, train movement from 25 kV to an insulated section generates arcs due to their circuit break properties and arcs tend to attach to contact wire while the pantograph passes through these structures.

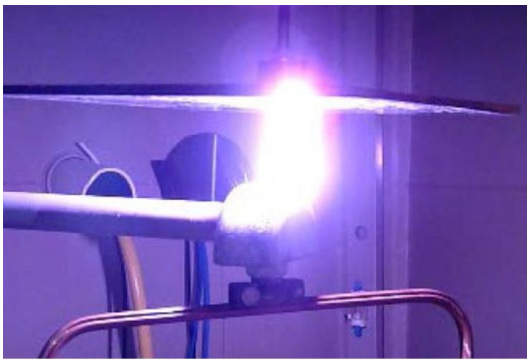
4.1.2 Flashover

Electrical clearance is regulated by standards to keep live OLE wires a safe distance from civil structures [194–197]. Nevertheless, narrow tunnels, low ceiling overpasses and short metal bridges cause limitations to the clearance for OLE structures. This is especially the case where OLE is retro-fitted to an existing railway, so there are lots of cases of this in the UK and worldwide. With the combination of the uplifting of the contact wire while the pantograph passage, arcing between civil structures and live OLE wires is likely to occur. To overcome this problem and avoid civil structures from being damaged, structures are bonded and flashover plates or copper strips placed at the location where the arc is likely to attach to the structure. These plates or strips prevent the unacceptable flow of traction current from being transferred to a third party system/structure. Fig. 4.2 shows the flashover issue between civil structures and live OLE wires.

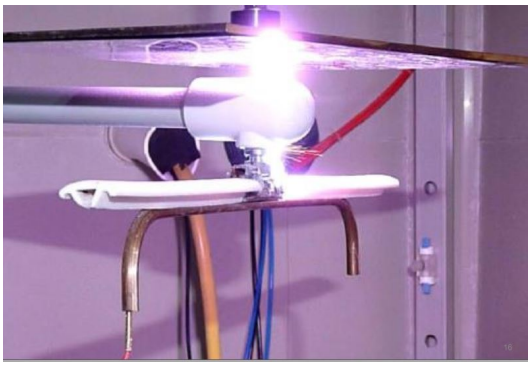
The less well-recognised problem is that the flashover issue also damages to OLE live wires from spots where the electrical discharge occurs. Although the duration of arcing lasts less than a second, the temperature of the contact wire may be elevated to melting temperature. This phenomenon results in burn marks and arc spots on the surface of the contact wire.



(a) Clearance problem between live wires and structures



(b) Arcing between registration arm and flashover plate



(c) Arcing between contact wire and flashover plate through a registration arm

Fig. 4.2 Flashover between structures and OLE live wires [198]

4.2 Materials and Methods

Initially, CuAg0.1 contact wire samples extracted from Milton Keynes was visually inspected and significant arc location were detected on the contact wire surface. Detailed analysis of these arc spots were completed using metallurgical and microhardness examinations. However, in this investigation, parameters of current, duration and number of arcs were unknown. Thus, in this study, for an in-depth analysis, a number of experimental studies were conducted to identify the effects of the arcs on mechanical and metallurgical properties of contact wire with different parameters of current, number of arcs and current type. To conduct arc experiments in the laboratory conditions, an OLE arc machine, SOLARC, was developed. This allowed more control over conditions than would be possible just by observing wires removed from service track. After arc testing, optical microscope, microhardness and grain size measurements of samples were carried out. In these experiments, CuAg0.1 (copper-silver) contact wire (AC120), widely-preferred contact wire type in the UK mainlines, was used. Fig. 4.3 shows the methods followed during the investigation of the effects of arcs on mechanical and metallurgical properties of the contact wire.

In addition to the experiments with copper silver contact wire, a range of experiments were also conducted with oxygen-free copper material for mitigation of severe damage of arcs. To the author knowledge, there was no study about oxygen-free contact wire related to the arcing problem in the OLE systems. However, some studies indicate that oxygen-free copper material can prevent the material from internal defects which would occur in rapid heating-cooling circumstances. Therefore, the role of the oxygen concentration in the microstructural damage was also investigated. However, it was not possible to obtain a contact wire form of oxygen-free copper (OFC) since it had not been widely commercialised yet. Instead, an oxygen-free copper bar was used in the experiments. Because the mechanical properties of these materials are slightly different, only the interior damage and defects were compared.

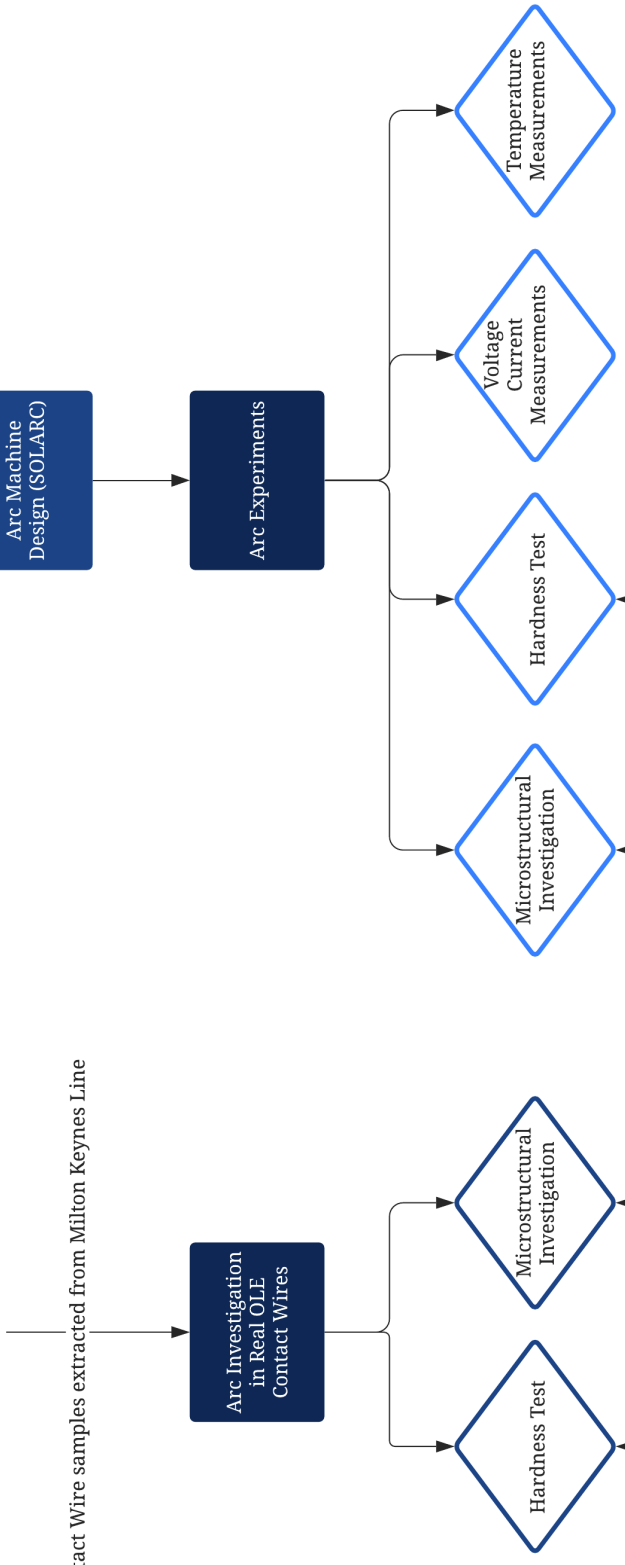


Fig. 4.3 Methods used for investigation of the arc damage to the contact wire

4.2.1 Arc Investigation in Real OLE Contact Wire

Contact wire samples located nearby neutral section connection were extracted from London Euston-Crewe mainline to explore the possibility that arcs form an initiation process for larger-scale damage. One metre-length contact wire was cut off from the arc affected region and prepared for microstructural investigation. Microstructural changes and the effects of the thermal heating on grain and mechanical properties of the contact wire were examined. Fig. 4.4 presents burn marks on a contact wire sample that was extracted from Milton Keynes OLE mainline (location at 58m 32ch between London Euston and Crewe Line).

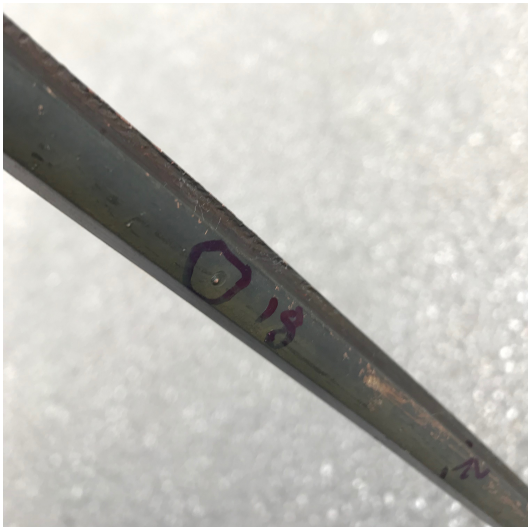


(a) Sample 3

(b) Sample 12



(c) Sample 15



(d) Sample 18

Fig. 4.4 Flashover arc exposed contact wire samples

4.2.2 Overhead Line Arc Machine

Design of the Arc Machine

Several experimental configurations currently exist for testing studies about the issue of the arcing [137, 149, 153, 155, 156, 176–181]. They were mainly designed to investigate arc damage to the collector strip. The effect of arcs on collector surface is immediate, severe and visible at first looking, and this prompted the studies to gather around arc and collector strip damage. In this research, arcing in OLE was investigated from the perspective of arc damage to the contact wire, which would cause long term problems that do not appear for several years.

Because the experimental systems in the literature are not capable of doing an in-depth study on OLE contact wires, a new experimental approach was developed to help understand how the contact strip and flashover arcs affect to metallurgical and mechanical properties of the OLE contact wire. In this research, a new experimental overhead arc configuration, Sheffield Overhead Line Arc Machine (SOLARC), was designed that can accommodate any railway contact wire cross-section. The schematic of the SOLARC machine was shown in Fig 4.5.

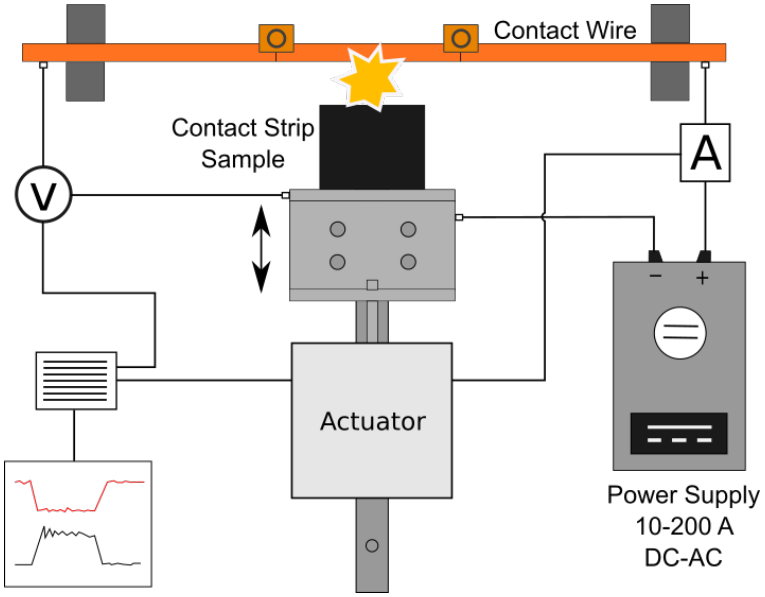


Fig. 4.5 Schematic of OLE arc rig

Mainly, SOLARC machine was equipped with AC and DC power supplies so that arcs in different voltage systems could be investigated. Besides, the machine was equipped with several configurations which could control duration, air-gap and number of arcs. However, in this research, only the parameters of the current type and number of arcs were investigated.

Configuration of the SOLARC Machine

SOLARC was set up to generate arcs with both direct and alternating current. Fig. 4.6 shows the equipment used in the SOLARC machine. A *contact strip sample* material cut from a pantograph strip was used in the experimental setup. Contact and break motions of the strip sample were driven by an *actuator (linear solenoid)*. The contact strip sample was connected to an aluminium *strip holder* that was housed by a *linear guide*. Adjustable *power supply* running from laboratory 230 V AC mains, provides either direct or alternating current with the maximum voltage of 80 V DC and $\pm$ 80 V AC and a current configurable from 10-200 A for DC and $\pm$ 200 A for AC. The voltage is representative of those measured across arcs in overhead line electrification installations but is not the full system voltage which is typically 25kV for AC systems or 750-1500 V for DC systems [10, 13]. Because it was difficult to conduct the experiments with very high voltage in the laboratory conditions. Studies in the literature showed that representative voltage can be used in pantograph arc experiments [153]. The configuration can represent three stages, namely; approaching, full contact (close to zero voltage across the carbon to contact wire, large current flowing), and drawing (80 V between the components and large current flowing).

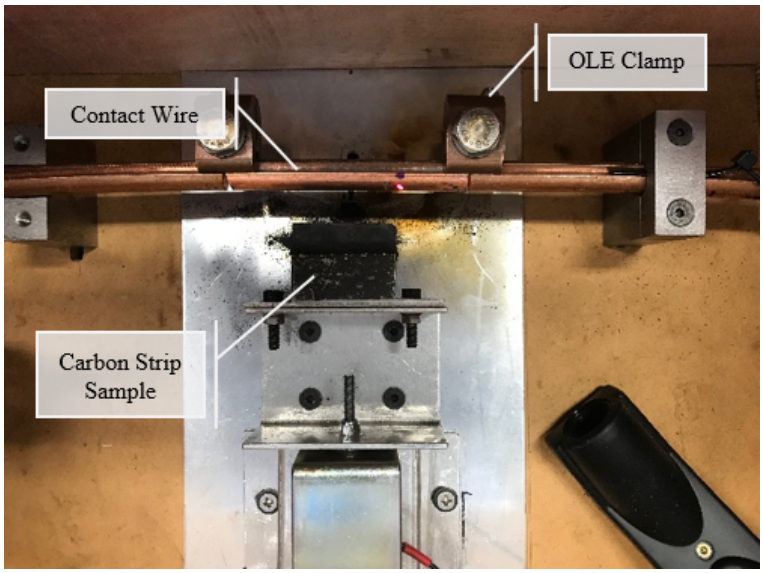


Fig. 4.6 Configuration of SOLARC Machine

Duration, interval time and the number of arcs were controlled by a programmable *microcontroller*. This controller conducted the actuation of a linear solenoid that attached to the contact strip sample. Due to the fact that arcs generated massive flash at the location where we want to photograph, the conventional methods to record the position of the contact strip sample was difficult. Therefore a high-speed camera system (see Appendix B.1.1) was

used for determining the position and the movement of the contact strip sample attached to an actuator during the arcing experiments. Fig. 4.7 shows the position of the actuator during a single arc. The contact strip sample attached to the actuator approached to the contact wire sample, stayed 150 ms in contact and moved back to its starting position. During this period, approaching and drawing arcs were observed.

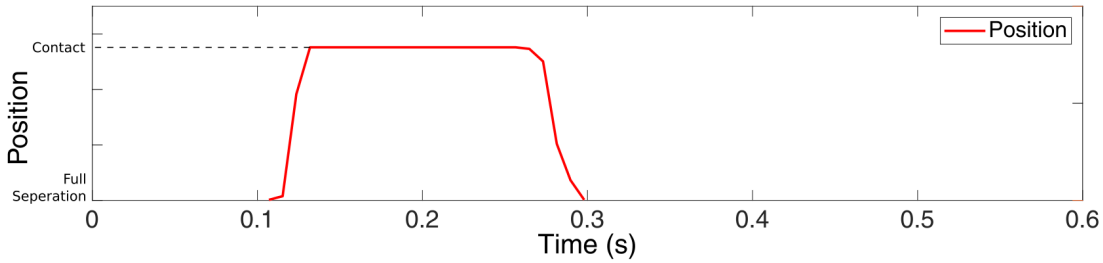


Fig. 4.7 Actuator position recorded with the highspeed camera measurement

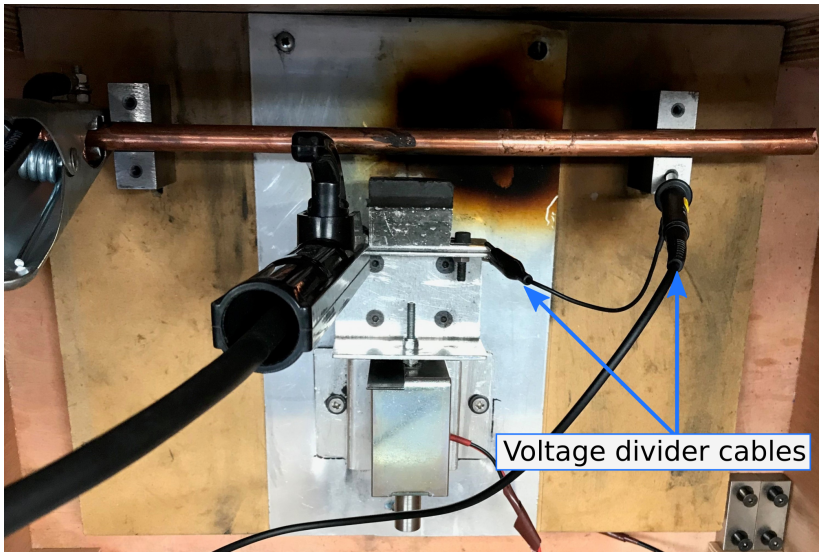
Fig. 4.8 shows the equipment used in measuring the voltage-current during the experiments. A *current probe* was attached to the positive cable of power supply and the contact strip sample, and the contact wire was interconnected with a *voltmeter* with a voltage divider to monitor the current and voltage data during the experiments. Processing of the signals from the current probe and voltmeter was established by a *digital oscilloscope*.

The machine can accommodate specimens up to 400 mm long, but a standard test specimen of 100 mm length was used during tests, this being sufficient to expose the surface to an arc without any influence from the supports or clamps. This small specimen length avoids large amounts of material from being wasted. This method is particularly useful in studying overhead contact wires because the wires keep their neutral flat form during the experiments and are not exposed to roll around coils as it is in the literature studies.

SOLARC machine was built in an enclosed environment with interlocking switches to prevent human access during the experiments. The setup was equipped with an extractor fan to remove fume occurred due to arcing. Sliding interaction between pantograph carbon and contact wire was not present in the tests.



(a) Current Probe



(b) Voltage measurement

Fig. 4.8 Equipment used in voltage-current measurements

4.2.3 Sample Preparation for Experiments

Majority of the experiments were completed by using the copper-silver type of contact wire. Additionally, some tests were repeated with a low-oxygen-content copper material (oxygen-free) to investigate the contribution of oxygen content to the arc damage. The typical electrical resistance of copper-silver overhead line contact wire with a nominal content of 0.1 % Ag and 0.04 % oxygen by weight is given by standard EN 50149 [20] as 0.122 Ω/km and its manufactured hardness as 120HV. Because oxygen-free material was not manufactured as specifically overhead line contact wire, it was difficult to compare mechanical properties with standard copper-silver contact wire. Only the oxygen concentration of OFC can be pointed out as to be 0.0005 % [199, 200, 168].

The specimen preparation process was carried out carefully to prevent the wires from presenting any imperfection (roughness, inclusion and cracks) that significantly affects metallographic inspections. In order to check that there was no pre-damage in the microstructure due to the surface quality, control samples with no arc exposure were prepared for metallography and examined under the microscope. Following the surface quality control checks, newly manufactured contact wires (free of the oxide layer and worn-free) and OFC were used in the experiments.

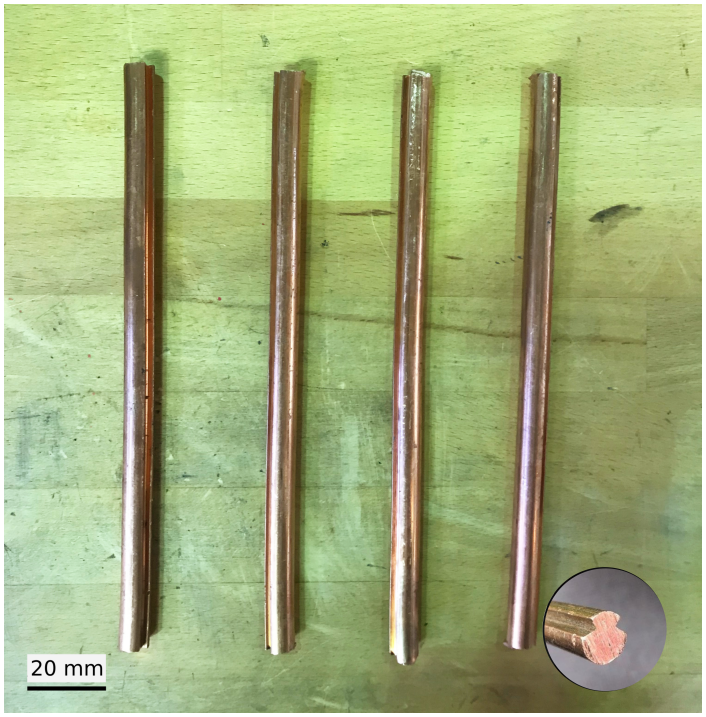


Fig. 4.9 Contact wire samples in arc experiments

4.2.4 Arc Experiments

In the experiments, copper-silver contact wires were used for understanding the damage mechanism of arcing to the microstructural and mechanical properties of railway overhead contact wires. The specimens were subjected to arcing in the SOLARC machine. The duration of contact time was limited to about 150 ms $\pm$ 20 ms and tests were conducted with currents of 100A-200A AC and DC. This variation was due to the arc being sustained for very slightly different durations even when the actuator was operated in the same way. All tests began with the contact wire and carbon strip out of contact, and they moved into contact with the possibility of an approaching arc. For multiple arcs, the time between the arcs was chosen to be 2 minutes to prevent unrealistic heating of the surface of the contact wire and to represent a typical high-capacity railway line.

Furthermore, findings from the preliminary investigation (Section 4.2.1) lead this study to investigate the defects in the microstructure of the contact wire. It has been already known that the oxygen content of the material can play an important role in void formations during the heating process (Section 2.3.5). Thus, additional tests were conducted with OFC. However, since OFC is not a contact wire form (limitation of supplying oxygen-free contact wire), only the void formation and its mitigation were examined by reducing the oxygen contact in the material. All tests took place under indoor laboratory conditions. Table 4.1 shows the parameters used in the arc experiments. The current parameter indicates the limit of current adjusted on the power supply.

Table 4.1 Parameters used in the arc experiments

Test ID	Current [A]	Number of Arcs	Time Between Arcs	Test Repeat	Power Supply
T1	100	1	-	4	DC
T2	100	10	2 min	4	DC
T3	200	1	-	4	DC
T4	200	10	2 min	8	DC
T5	200	2	3.6 sec	4	DC
T6	200	1	-	6	AC
T7	200	10	2 min	6	AC
T8-OFC	200	10	2 min	4	DC
T9	Thermal processed with annealing 2 hours at 450 C				

For DC experiments, T1 and T3 demonstrated a single arc with different currents of 100A and 200A. T2 and T4 considered repetitive arc problem in the specific locations, such as; neutral sections, section insulators where the arc was likely to happen on multiple occasions and attach to the contact wire. The time between the arcs was chosen to be 2 min when

considered trains run at 2 min interval in a high capacity OLE line. T5 represented arcing from both front and rear pantographs of a double pantograph train. In this test, two flashes were seen after the train passed from a specific location. In this test, the interval between arcs was set based on a 125-metre pantograph separation for a train travelling at 125km/h. Therefore, the time between the arcs was expected to be 3.6 seconds.

AC power supply was used in test number T6 and T7. In these tests, single and multiple arcing were investigated with 200 A AC and compared with those of DC tests.

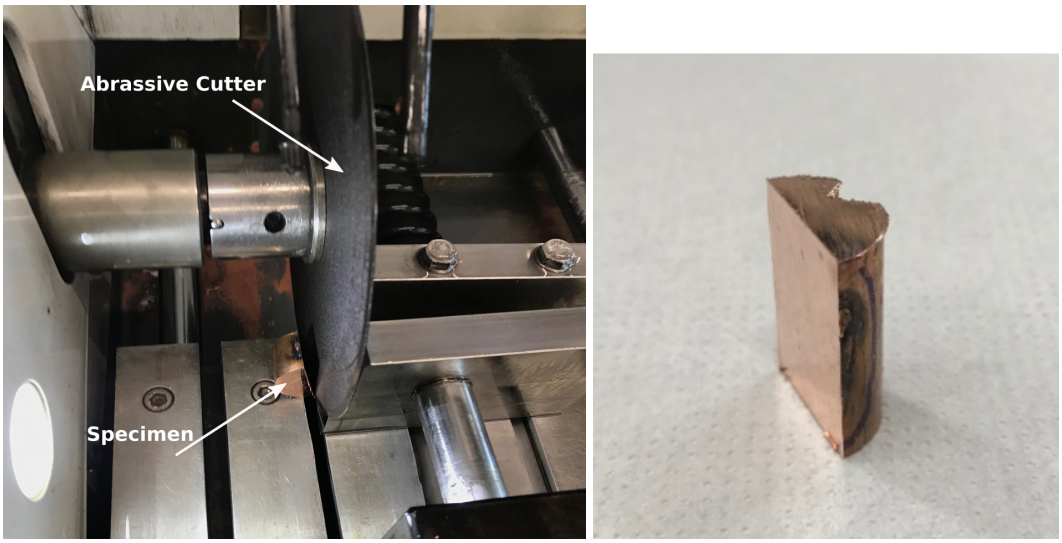
Test number T8 investigated the effects of the copper purity on void formation in the material. Therefore this test was conducted with OFC material, and a repetitive arc exposure with 200 A DC was considered. The approximate grain size of pure copper and its hardness reduction after annealing have already explained in the literature (2.2.4). However, To understand how the grain sizes changed and how thermal path modifies cold-formed grains in the contact wire, in test T9, an arc free of hard-drawn contact wire was annealed at $450°C$ for 2 hours. The recrystallisation temperature of pure copper was just over 250° C. However, silver element elevated recrystallisation temperature of the contact wire to 450° C. Grain size of contact wire material were investigated under an optical microscope according to the standard of ASTM E112-13 [201].

4.2.5 Specimen Preparation for Metallography

Metallurgical examination methods were chosen to gain a detailed understanding of the effect of arc(s) on the contact wire, both at the surface and internally. Contact wire specimens were prepared for metallography following the stages of sectioning, mounting, grinding-polishing and etching. All the metallurgical preparations, experiments and tests were conducted by the thesis author.

Sectioning

Although the test samples were small enough for optical microscopy, sectioning was essential to obtain the same standard quality for all of the contact wire samples. Therefore, following experimental testing contact wire samples were prepared for examination by cutting parallel to the longitudinal axis to reveal the internal cross-section. These examinations (microscopy, micro or nano-indentation and hardness testing) allowed us to investigate the contact wire from the contact surface to the interior. An appropriate SiC-based abrasive cutting disc was used to minimise the surface damage due to sectioning [202]. Fig. 4.10 shows sectioning stage of the contact wire sample with an abrasive cutter.

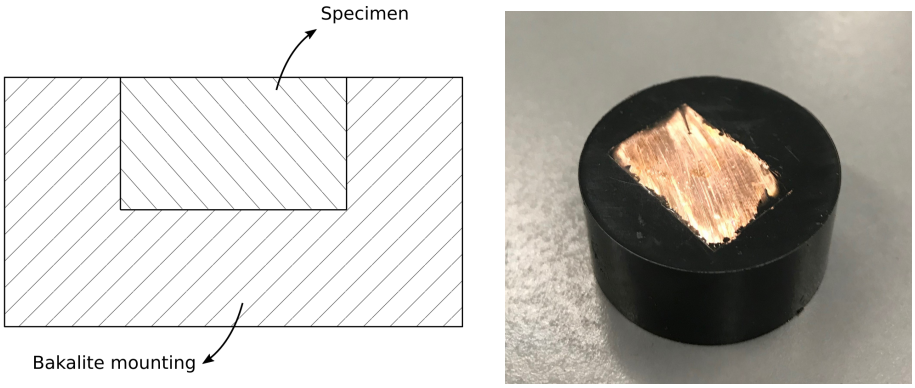


(a) Sectioning stage with an abrasive cutter (b) A sectioned contact wire sample

Fig. 4.10 Longitudinal sectioning of the contact wire

Mounting

After sectioning of samples to minimise the specimen size, a process named *mounting* was applied. The mounting provided a better surface quality for automatic polishing devices. The standard mounted specimen was circular with 35 mm in diameters. Because the contact wire samples were only subjected to optical microscope investigation, only powder of Bakelite (thermosetting phenolics) was used for mounting [203].



(a) Schematic of cross section of a mounted specimen (b) An example of copper specimen mounted in Bakalite

Fig. 4.11 Mounted specimens for optical metallurgy

Fig. 4.11 shows the details of a circular mounted specimen in Bakelite. Mounting stage involved a sequence of processes that started from placing the sectioned specimen into a

mould, then the mould was filled with powder mounting material (Bakelite) and heated under pressure in the order of 15 minutes [204]. Fig. 4.11b shows a specimen after the mounting process. It can be seen that scratches and debris from both sectioning and mounting remained at the surface. These defects need to be removed by grinding and polishing stage to obtain a good sample for microstructural inspection.

Grinding-Polishing

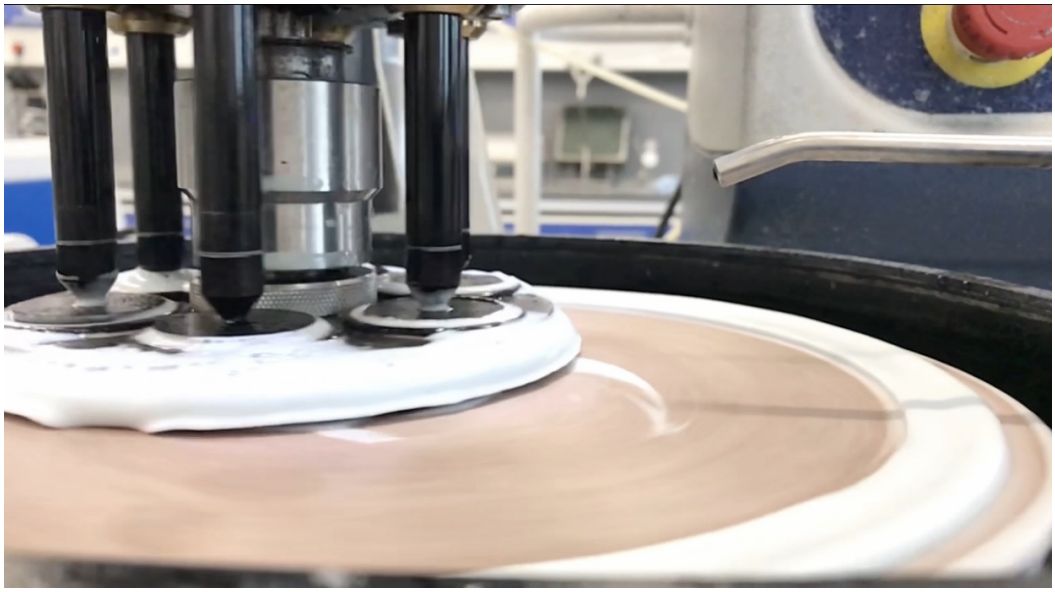
Grinding-polishing was essential for optical metallography. This process was based on abrasion of specimens by using grinding papers, polishing cloths and solutions with different surface roughness. In general, while grinding removes saw marks and uneven surfaces, polishing wipes out the artefacts of grinding [205].

Since copper was subjected to deep scratches against abrasive particles, a low vertical force for grinding of copper material was recommended as to be 22N[206]. Fig. 4.12b shows the surface quality of a copper specimen after grinding and polishing. The surface quality improvements were completed using an automatic grinding-polishing machine shown in Fig. 4.12a.

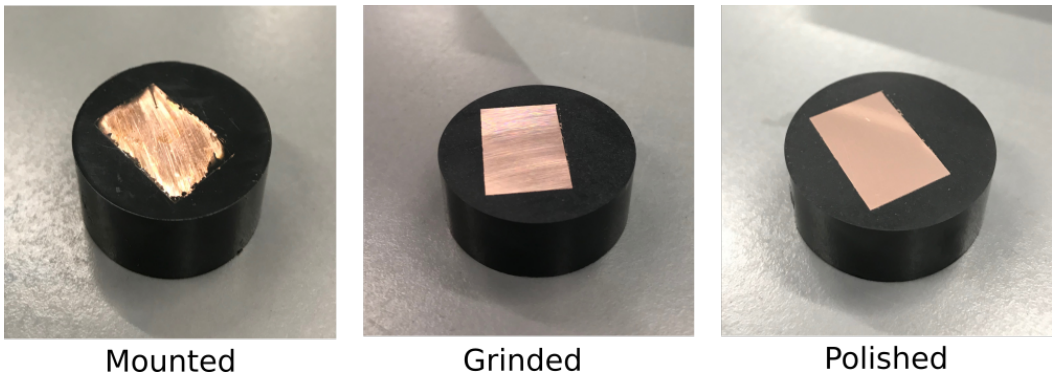
Parameters used in grinding and polishing of contact wire samples were tabulated in Table 4.2. Grinding papers were expressed with *grid numbers*, and particle size in micron was used in polishing solutions. A reference study was used for determining the rotational speed of the machine head and the duration of each process [207].

Table 4.2 Traditional grinding and polishing parameters for copper alloys

Step	Abrasive	RPM	Direction	Load [N]	Time [minutes]
1	120 Grit	240-300	Comp.	22	until flat
2	240 Grit	240-300	Comp.	22	1
3	320 Grit	240-300	Comp.	22	1
4	400	240-300	Comp.	22	1
5	600	240-300	Comp.	22	1
6	6 micron diamond	120-150	Comp.	22	2
7	1 micron diamond	120-150	Comp.	22	2
8	0.06 micron silica	120-150	Comp.	22	2



(a) Polishing of mounted samples with the automatic grinding-polishing machine



(b) Surface quality of the samples after grinding and polishing

Fig. 4.12 Surface improvement of specimens with grinding and polishing

Etching

Although specimens were finished with fine mirror surfaces, it was not possible to observe some of the microstructural properties, such as; grains, grain boundaries, twins, phase boundaries. Therefore, a chemical process named *etching* were used for revealing such features of the materials. Studies in the literature showed that acid solutions of *Ferric Chloride* ($FeCl_3$) dissolved in alcohol gave better contrast for grain size investigations of pure copper and copper alloys [208, 209]. Therefore, specimens were etched with a solution of 5 g $FeCl_3$, 96 ml Industrial Methylated Spirit (IMS) and 2 ml HCl. The etchant attacked at grain boundaries or different rates areas and due to the surface irregularities that etchant causes, the light coming from the device (mostly microscope) reflected the different directions and produces contrast, colouration and polarization [203]. Not only the etchant but also etching time played an essential role in the success of the etching process. Because etching was a chemical reaction that continuously attacked the specimen until it was rinsed and appropriately cleaned to remove all the etchant remains. Etching time was set to be approximately 11 seconds to avoid over-etching of the samples. Fig. 4.13 shows the etching process of the sample preparation.

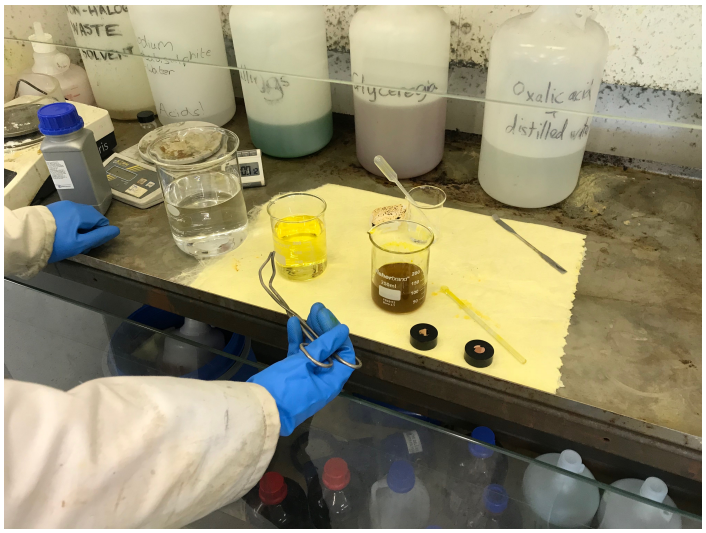


Fig. 4.13 Etching process of contact wire samples

Since grain properties showed differences in between contact surface and interior of the material care was taken not over-etch the heat-affected region which reacted faster to the etchant.

4.2.6 Metallurgical and Mechanical Investigations

A sequence of methods were applied to the contact wire samples after the samples prepared for metallography. Initially, polished and etched contact wire samples were examined to reveal grain properties under the optical microscope. Fig. 4.14 shows the equipment used in contact wire microstructure investigation. After the grain size investigation, to show interior defects, contact wire samples were also examined with 3D surface topology equipment (Alicona).



Fig. 4.14 Optical microscope used in microstructural investigations

Hardness tests were applied to both extracted contact wires from the OLE mainline and samples tested with SOLARC machine. Microhardness tests were performed for each of the samples with more than 40 indents, and three arc tests were conducted for each condition to verify the results. Average results within the same depth from repeated tests were calculated. A hardness survey of the samples after arcing was plotted. Fig. 4.15 shows schematically the method followed to measure hardness distribution of the sectioned surface of tested samples. The depth of the sample showed upwards. This was done to match the microstructure graphs and also the typical alignment of OLE which would get contract strip arc from below.

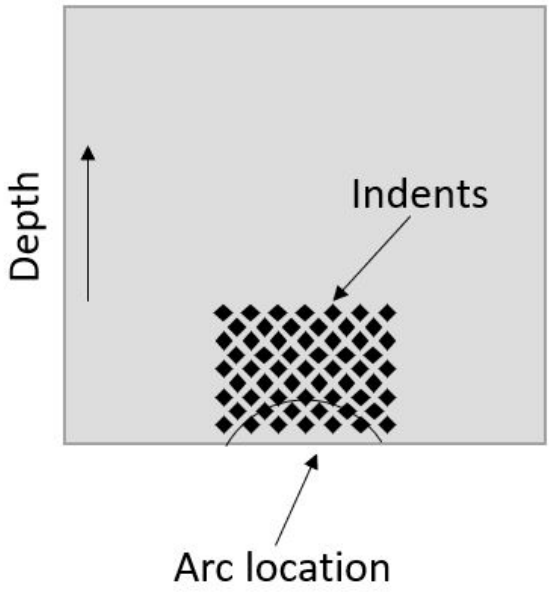


Fig. 4.15 Schematic of micro hardness indentation of sectioned contact wire samples

4.3 Results

4.3.1 Arc Damage and Microstructure

Real OLE Contact Wires

Significant burn marks and arc spots were detected on the one-metre-length sample of the contact wire that was extracted from Milton Keynes electrification line. Twenty-six arcing locations were observed and marked to cut off and analyse metallurgically.

Prior to examining arc damaged locations, arc-free control samples were cut off from the worn contact wire. These samples were taken from two different locations where the contact wire was worn 0.5 and 1 mm. Their microstructural examination was conducted with an optical microscope, and hardness survey was compared with those taken from arc-affected regions. Fig. 4.16 shows a typical microstructural image of a control sample which has no arc damage.

Since the bottom surface had been worn during use, no significant evidence was found in terms of arcing. The bottom surface is likely subjected to many arcs, but the smooth wear surface makes it very difficult to determine the location of arc spots. However, arcing spots found on the top and side surfaces of the contact wire suggest flashover arcing between OLE contact wire and other structures. The investigated arcing spots, numbers of 2,3,24 and 25, were shown in Fig. 4.17a.

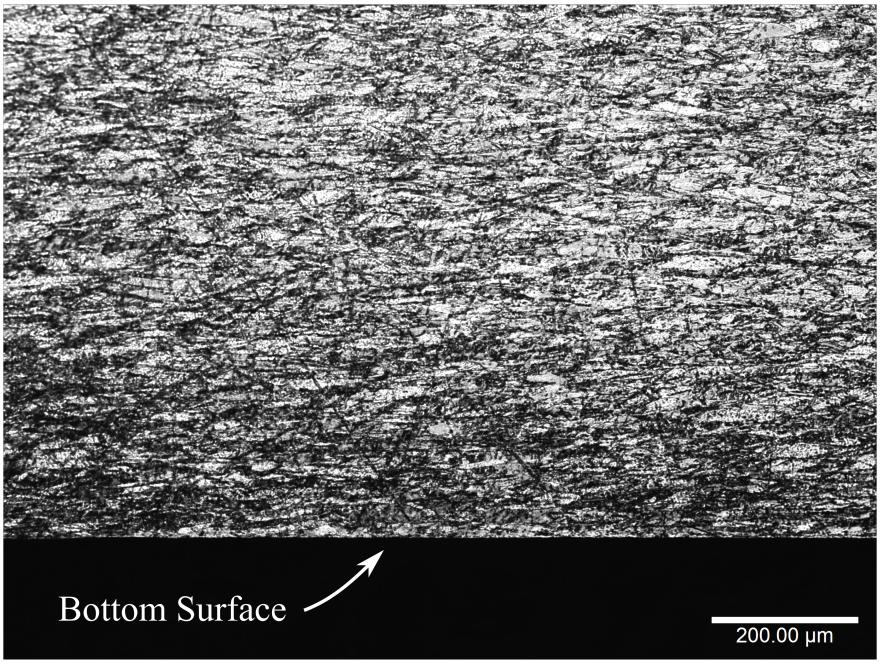
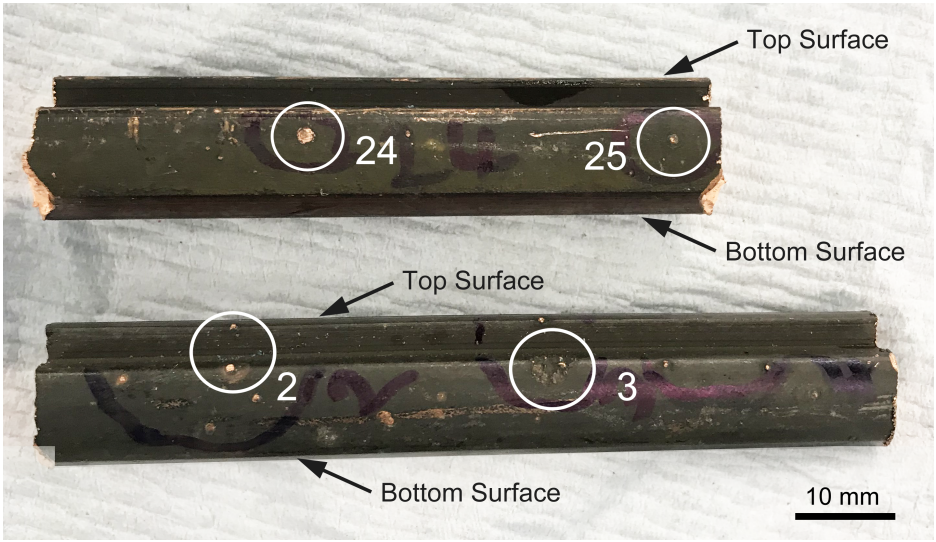
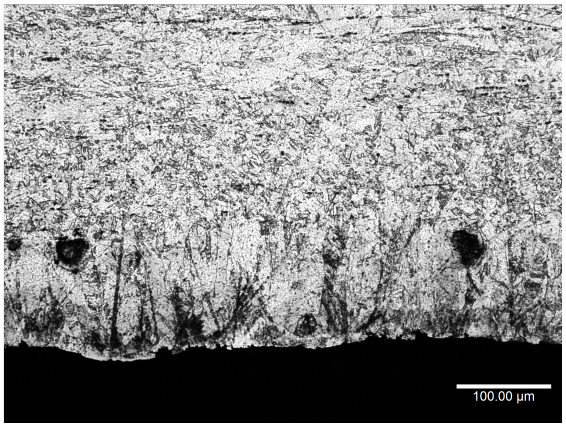


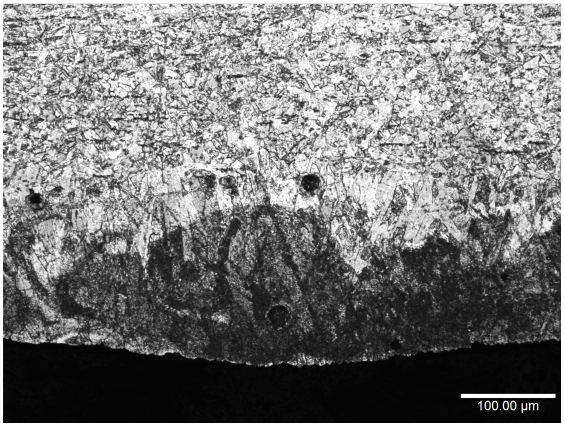
Fig. 4.16 Microstructure of a control sample with no arc damage



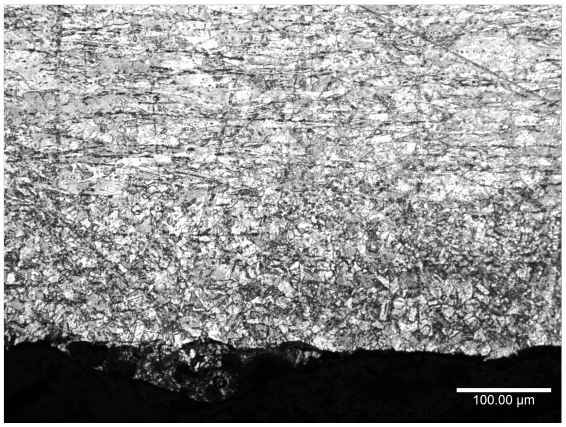
(a) Burn marks and arc spots on the extracted contact wire



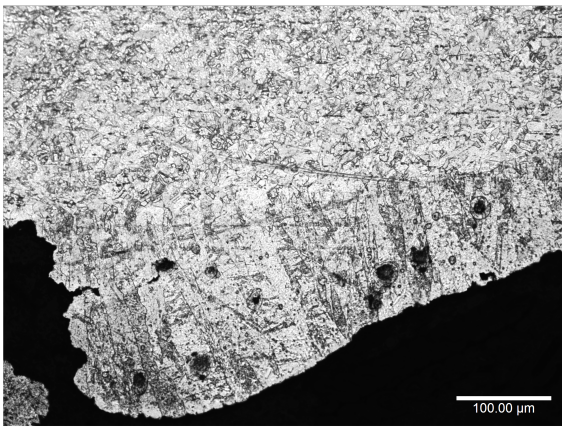
(b) Sample 24



(c) Sample 25



(d) Sample 2



(e) Sample 3

Fig. 4.17 Microstructure of flashover samples

Following sectioning these arcing spots by cutting parallel to the longitudinal axis, different grain properties and severely damaged zone were observed. Fig. 4.17 shows the microstructure of investigated samples. It was seen from the figure that grains that were elongated longitudinal due to being manufactured drawing process were annealed and reformed at the location where the arc attached. Additionally, the arc damage left voids in the material in the samples of 25, 24 and 3 (visible as black spots/regions). In Fig. 4.17d, grain sizes showed an increasing trend from the interior to the arc spot. Also, in Fig. 4.17c, Fig. 4.17e and Fig. 4.17b arc affected to a larger area and formed voids due to the effects of local heating.

Fig. 4.18 shows hardness analysis of arc spots and, 0.5 and 1 mm-worn contact wires. The indents were carried out from the arc surface to the interior through the cross-section of the material. Two control samples with 0.5 and 1 mm wear, were also analysed from the worn surface to the interior of the material to understand whether pantograph wear affected to the material hardness.

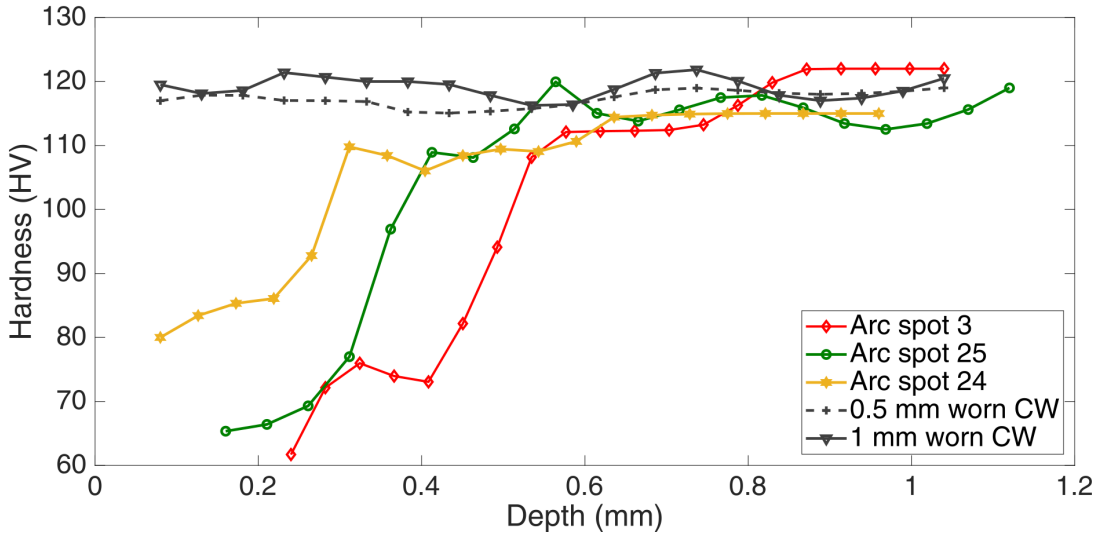


Fig. 4.18 Hardness analysis of arc spots extracted from OLE main line

From the hardness tests, no hardness reduction was found in the samples with 0.5, and 1 mm wear. However, a significant hardness decrease up to 60 % was observed in arc-affected samples. The details of arcs affecting these field samples (current, number of arcs and duration) were unknown; therefore it was difficult to explain the mechanism by which it resulted in the decrease in hardness. However, all the arc spots showed a typical hardness reduction pattern across the sectional area of the material.

Arc Experiments

DC Arcing was tested with different parameters of number of arcs and current. Fig. 4.19 shows a typical drawn arc from DC test T3. Strong arc discharge was detected with both parameters of 100A and 200A DC. After the carbon strip moved away from the contact wire, the arc lasted approximately 300 ms before self-extinguishing. Fig 4.20 shows the burn marks on the contact wire surface from which it can be seen that multiple arcs affected to a broader area. The size of the burn mark of a single arc was measured to cover an average of 2.2 mm along the wire length. It was seen that multiple arcs affected a wider area than single arcs, with the burn area extended longitudinally in the test numbers of T2 and T4.



Fig. 4.19 DC Arc presence during the experiments

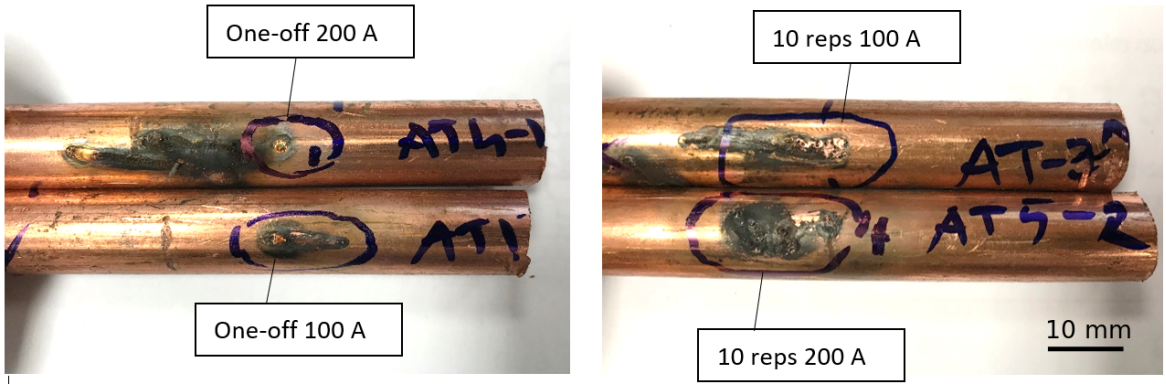


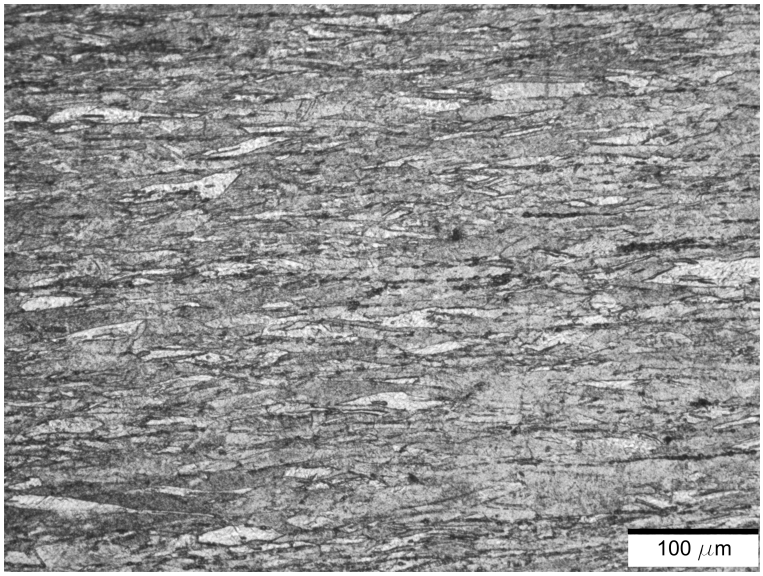
Fig. 4.20 Burn marks on the surface of contact wire samples

Since the first arc modifies the wire surface, it is to be expected that subsequent arcs may move to different areas of the nominal contact between the surfaces. The surface modification inherent in the process means subsequent arcs between the same samples frequently affect a slightly different location across the nominal contact area than the first arc. Tilting the carbon to present a more definite single point of contact would eliminate this issue, but at the expense of reducing how realistic the apparatus was in replicating the pantograph-wire contact. This tilted carbon approach was therefore not adopted.

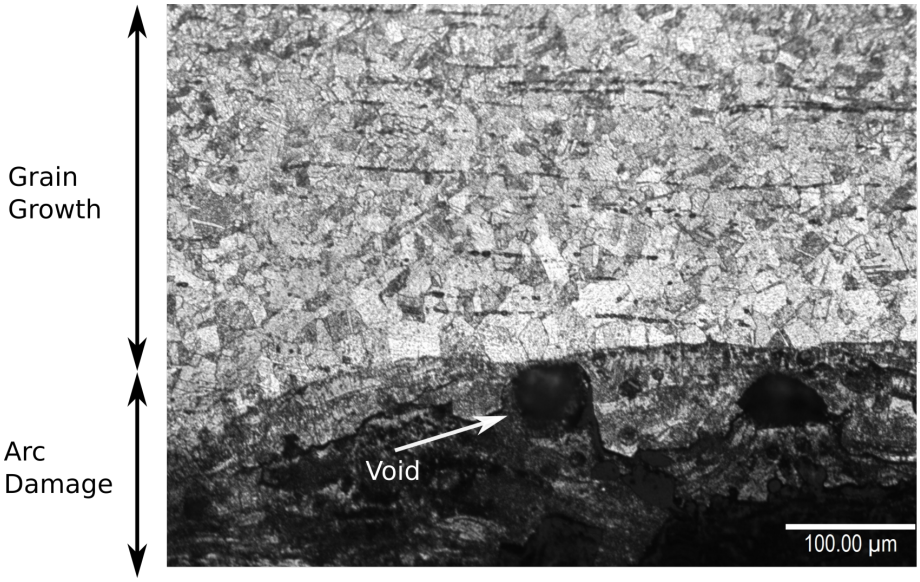
Fig. 4.21a shows the microstructure and grain directions of a control sample with no arc. Considering the initial microstructure of the contact wires tested grains were elongated the parallel to the longitudinal axis of the contact wire, i.e. have a high aspect ratio. After arcing, grain modifications and voids were seen in the material. The grains in the visibly heat-affected zone (HAZ) had an aspect ratio closer to unity and showed growth region due to the thermal annealing impact of arc energy input. Fig. 4.21b shows the voids and the grain growth in the material after repeating arcing with 200 A DC (Test T4).

The severity of damage from the surface to the interior of the contact wire varied depending on the current and number of arcs. Further analysis of the microstructure showed that new grain forms were seen in all tested samples. There was also a significant positive correlation between the arc current and the depth of transition between the visible HAZ and parent material. Fig. 4.22 presents the microstructure of samples tested with DC single and ten repeated arcs (T1, T2, T3 and T4). Hardness measurements (Section 4.3.4) indicated that grain modifications in the material reached deeper than this visible transition.

Another considered condition was double pantograph arcing that occurred at the 3.6-second interval. Fig. 4.23 shows the microstructure of test number T5 that was tested with 200 A DC and double arcing. Similarly, voids in the arc damage zone and grain growths were observed.

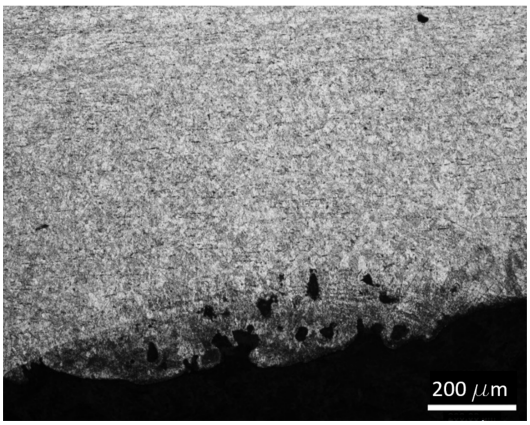


(a) Grain directions of hard-drawn contact wire

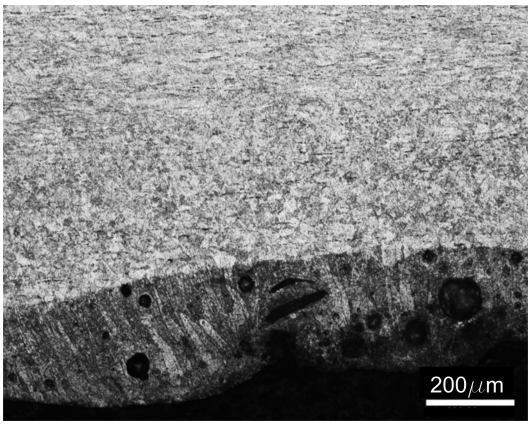


(b) Grain growth and void formation in the material revealed on longitudinal cross section after polishing and etching

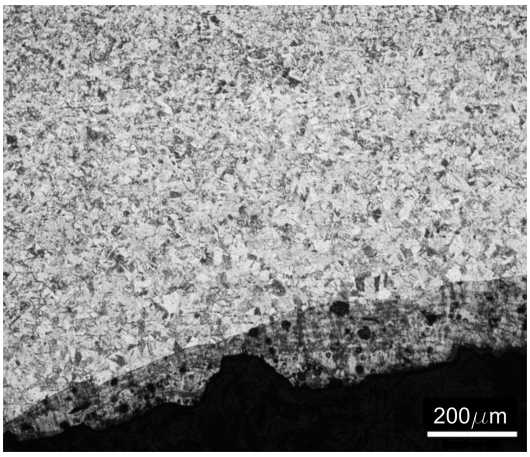
Fig. 4.21 Microstructure of the contact wire before and after arcing



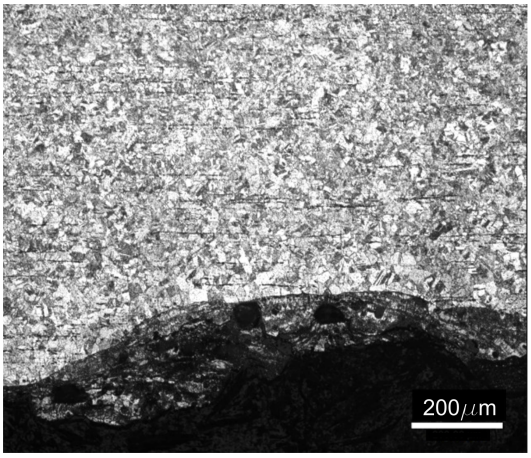
(a) 100 A- Single Arc (T1)



(b) 100 A- 10 repeated arcs (T2)



(c) 200 A- Single Arc (T3)



(d) 200 A- 10 repeated arcs (T4)

Fig. 4.22 Microstructures of the contact wire samples

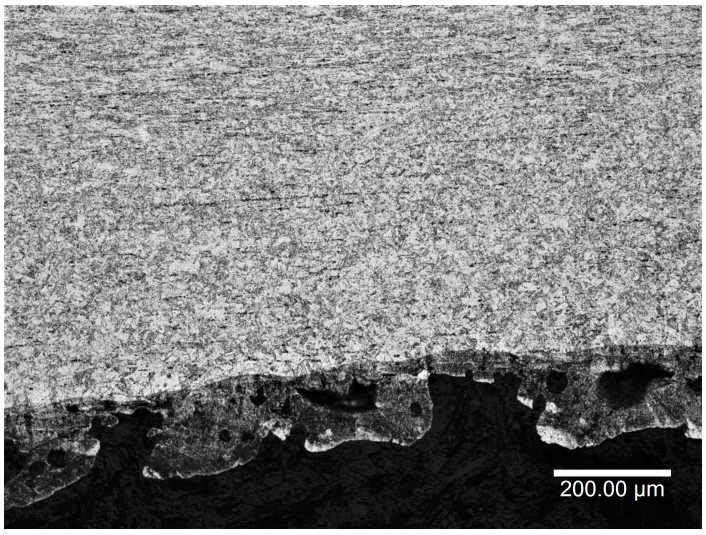


Fig. 4.23 Microstructure of T5 (double arcing)

AC arcing was tested with single and multiple arc conditions (Test number T6 and T7). It was observed that the extinguishing time of the AC arcs was shorter than that of DC arcs. Arcs in AC were more forms of little sparks lasting a relatively short period while it was more severe in DC. It is to be expected because the AC voltage has zero voltage-current points, and this caused arc plasma to interrupt.

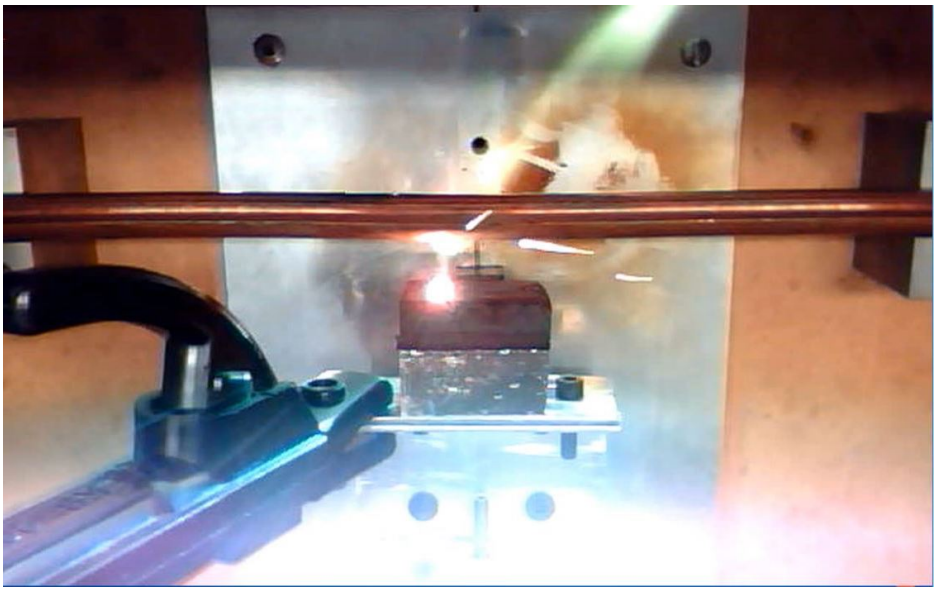
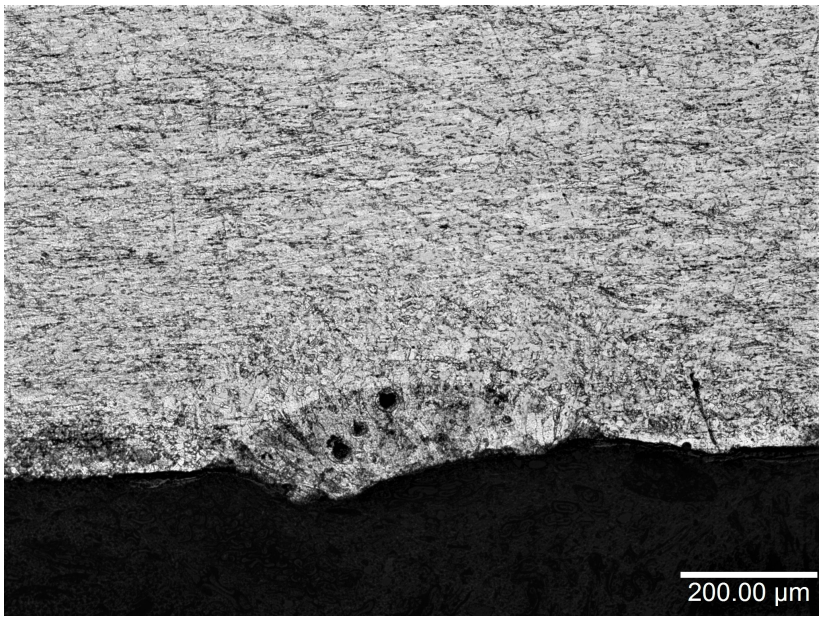
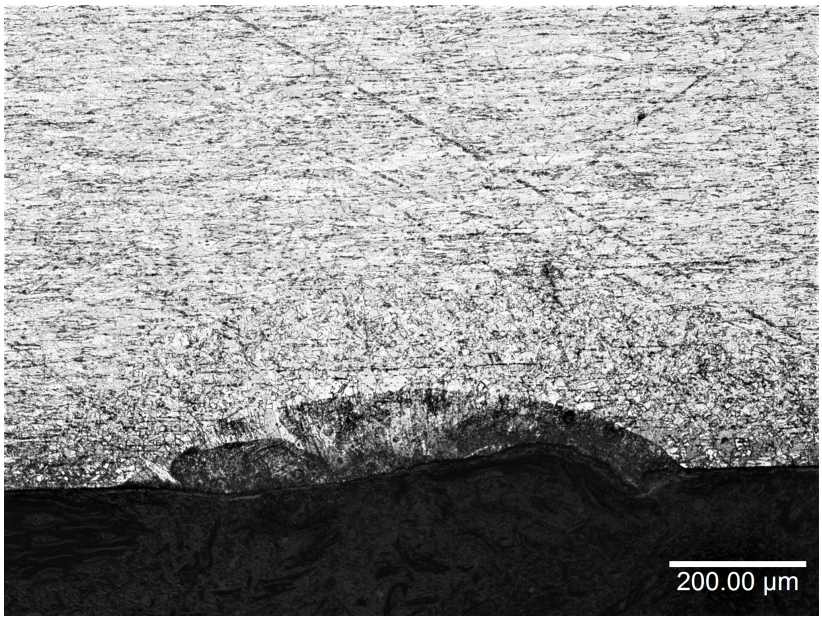


Fig. 4.24 AC Arc presence during the experiments

Metallurgical examination of the samples from the AC tests (Fig.4.25) showed that the microstructural damages existed after arcing regardless of the current type. Also, voids forms were seen both in the tests of single and multiple arcs. After testing with AC, the damage in the microstructure showed similar features to that for DC. In comparing tests (for equal current and number of arcs) the HAZ for AC was in the order of 30 % of the size for DC, as would be expected given the reduced arc duration.



(a) 200 A- Single Arc (T6)



(b) 200 A- 10 repeted arcs (T7)

Fig. 4.25 Microstructures of the contact wire samples tested with AC

Detailed Examination of Voids

Copper-Silver Wire After arcing, it was found the grain structure was modified, and voids were seen from the surface to the interior of the material. Depending on test condition the contact wire was modified in a depth of 100-200 μm in AC and 200-300 μm in DC experiments from the surface severely and voids were seen in this damaged zone. Fig. 4.26 shows the voids in the damaged zone after the test with 200 A DC and ten repeated arcs.

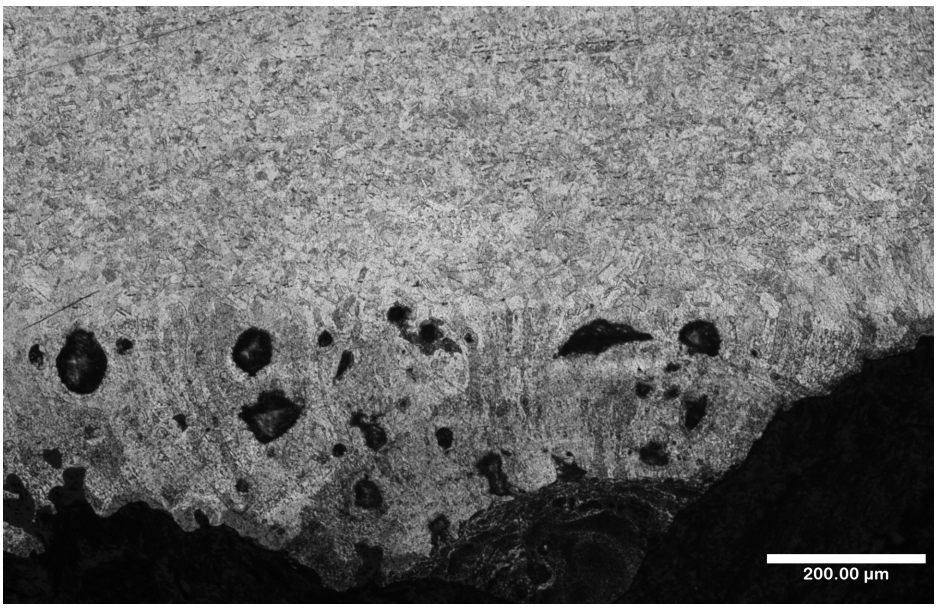
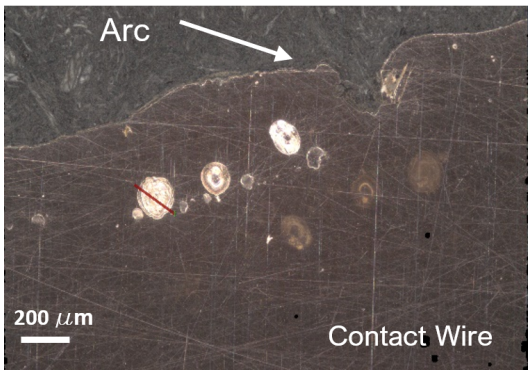
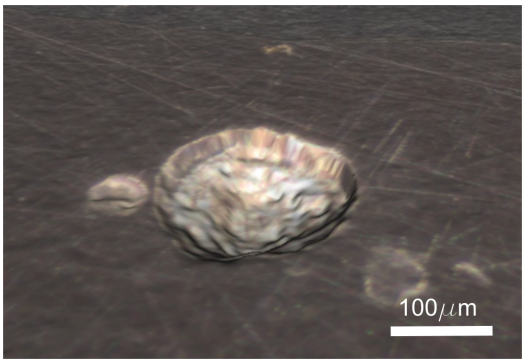


Fig. 4.26 Voids in the microstructure after arcing with 200A and repeated arc

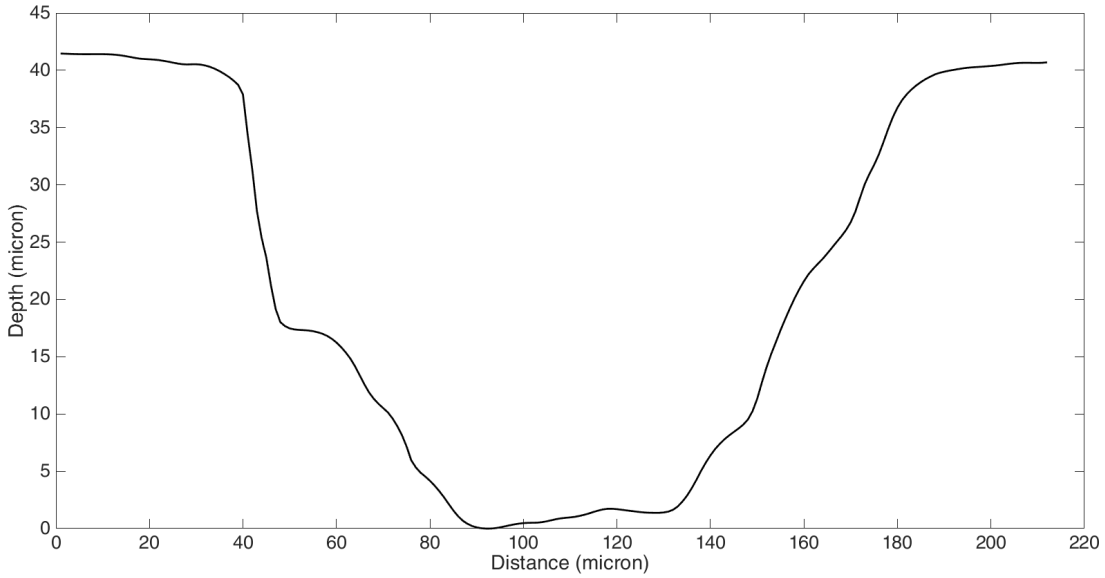
A detailed 3D surface mapping was carried out for the sample of test T4 to understand the profile of the voids that were found in microstructural inspections. Fig. 4.27 shows microstructure, the surface profile of voids in test T4. 3D surface mapping showed that voids had a smooth interior surface with a depth of 40 μm in the damaged region.



(a) The measured void for 3D surface profile



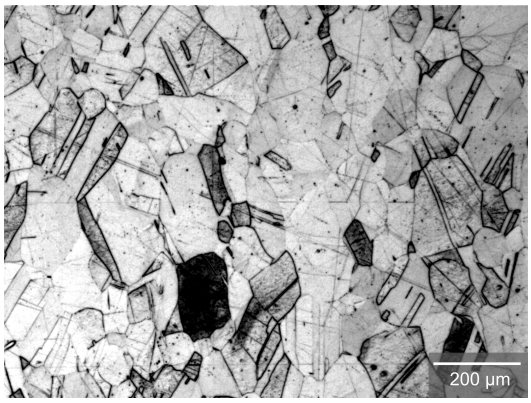
(b) 3D view of the void



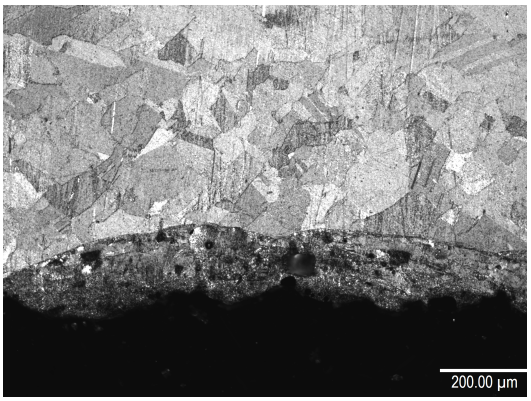
(c) Surface profile across the void

Fig. 4.27 3D surface mapping of void forms

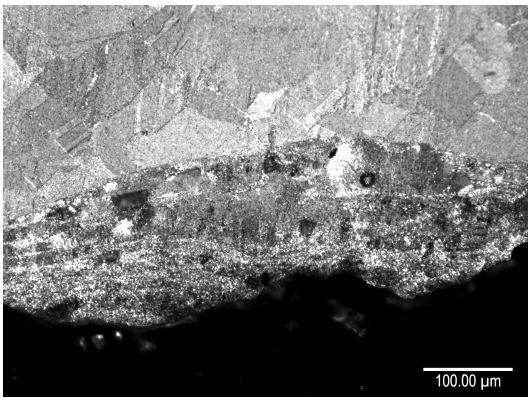
Oxygen-free Copper The microstructure of OFC tested with 200 A DC repeating arc (Test T8-OFC) was investigated under a microscope. Fig. 4.28 shows the microstructure of the OFC control sample with no arc and OFC sample after arc damage with two different magnifications. Although the arcing damaged approximately 200 µm layer of the contact wire, there was a significant improvement relative to the conventional contact wire material in terms of preventing large void formation in the damaged area. When the microstructure of the arc affected samples and the control sample was compared, there was not a significant grain size modification in the vicinity of the region severely affected by arcs.



(a) Control sample with no arc



(b) 10x



(c) 20x

Fig. 4.28 Arc damage in oxygen free copper with different magnifications

Hardness tests were also applied to the OFC samples starting from the bottom surface edge where the arc affected to the sample, to the core of the sample. Because OFC used in the experiments was not a contact wire, its hardness results were explained separately in this section. Fig. 4.29 presents the average hardness results of OFC samples tested with parameters in test number T8-OFC. It can be seen from the graph that the core hardness of OFC was just over 100 HV. However, it decreased to in the order of 70 HV in the vicinity

of the end of a severely damaged layer (0.24 mm from the bottom edge). In other words, although there was no visible internal defect in that region, the material lost 30 % of its hardness.

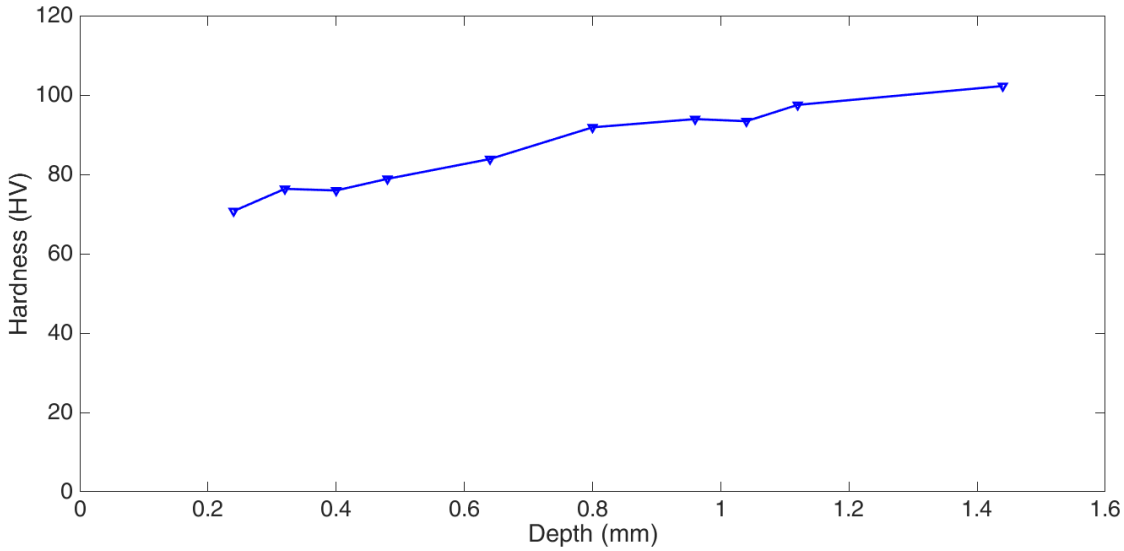
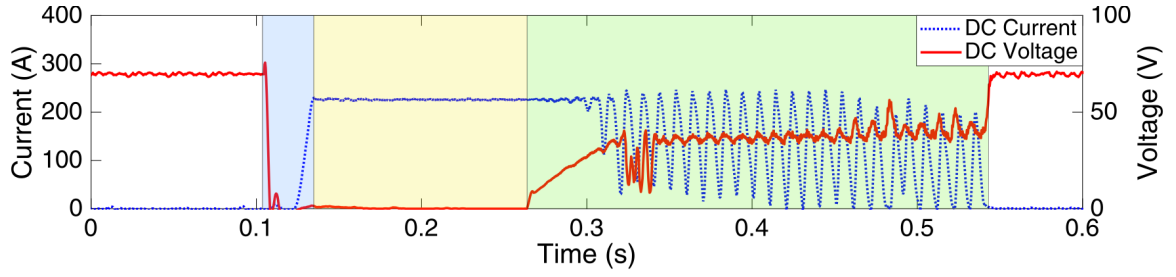


Fig. 4.29 Hardness survey of arc affected OFC

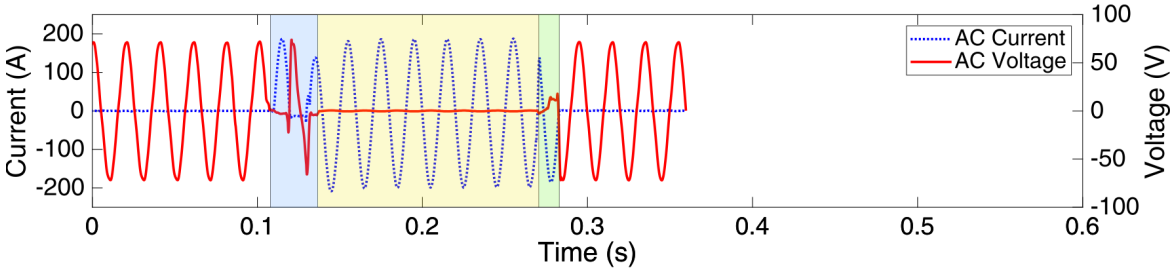
4.3.2 Voltage-Current Measurements

Fig. 4.30 shows the typical current and voltage variations of a single arc during tests of DC and AC, and the corresponding position of the contact strip sample over time. It can be seen that the graphs were divided into three stages, namely; approaching arc (I), full contact (II) and drawn arc (III). Fig. 4.30a shows the voltage-current measurements with 200 A DC (Test number T3). In stage I, the contact strip sample moved towards contact wire, the voltage between them dropped sharply to zero as the contact was made and current rose to just over 200 A. Once mechanical contact was established current remained at just over 200A and voltage remained very close to zero in stage II during which good contact was maintained. In stage III, a drawn arc developed when mechanical contact broke. The uni-directional current was maintained throughout from the DC supply, but significant current fluctuation was measured between zero and 200A, with an average current of 132.6 A and voltage 40 V in the typical test Fig. 4.30a. The drawn arc lasted for an average of 300 ms across the tests. After stage III, the contact wire and contact strip sample pair was fully separated, and the voltage across the contact rose to a maximum of 70 V with no current flow.

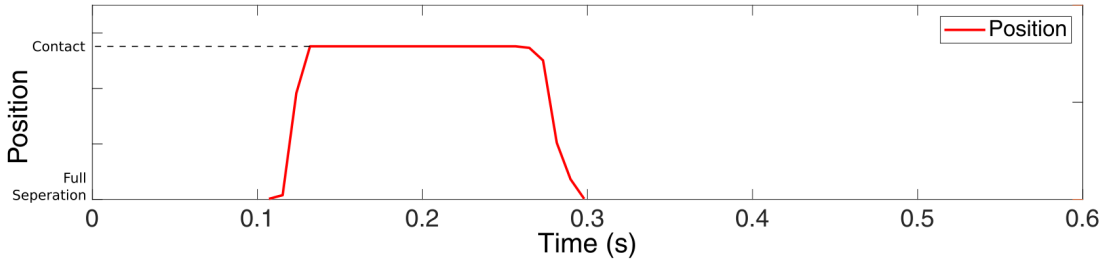
In the AC system, due to voltage and current alternating in polarity, "Root Mean Square (RMS)" reading was applied to the data collected from a digital oscilloscope. Since the



(a) DC



(b) AC



(c) Carbon collector position

Fig. 4.30 Current and voltage measurements with corresponding carbon collector position during the arc experiment

waveform showed sinusoidal behaviour, RMS values of current and voltage were calculated as follows [210];

$$V_{RMS} = V_{peak} \frac{1}{\sqrt{2}} \tag{4.1}$$

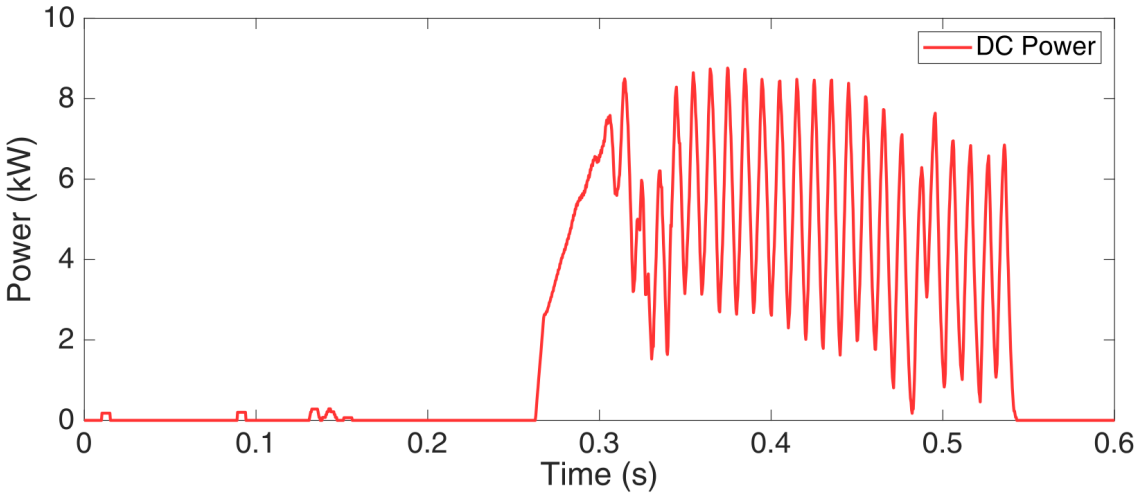
The motion command of the collector strip was unchanged for the ac experiments, but arc durations were significantly reduced. Fig. 4.30b shows a typical voltage and current graph of test number T6. Open circuit peak voltage (V_{peak}) was around 70 V, and RMS voltage (V_{RMS}) was 49 V.

In stage I of the AC test, an approaching arc was observed in the period of 30 ms. Peak current (I_{peak}) was just below 200 A. In stage II, mechanical contact between the collector strip, and contact wire was established, and the voltage between them remained zero throughout the period. Peak current (I_{peak}) fell slightly to 185 A. In stage III, as the contact strip sample moved away from contact wire a drawn arc was produced, lasting for 20 ms. During this period, the voltage increased slightly from zero to 17 V.

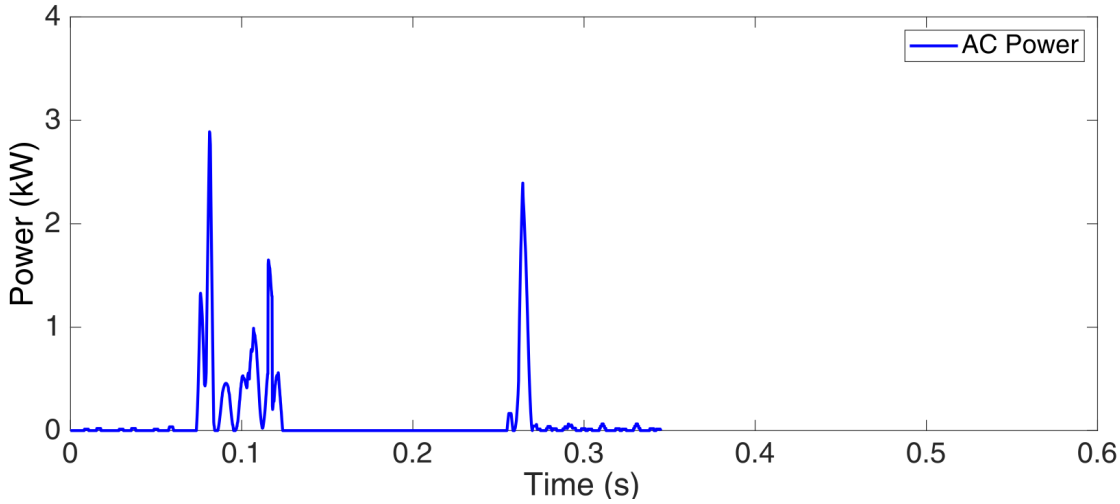
Power graphs were plotted by using voltage and current data of DC and AC arcing to calculate the energy inputs during the tests. Fig. 4.31 show the power generated by arcing during pantograph arcing. Also, the accumulated energies for both AC and DC arcing were generated from the area under the curves (Section 4.3.4).

The movement of the collector strip was identical for both AC and DC tests; however, the duration of the arcs varied. In particular, the drawn arcs in the DC tests lasted longer than those in AC tests. Since the thermal conductivity of the contact strip sample material was considerably smaller than that of the contact wire (398 W/mK contact wire, 6 W/mK pantograph carbon material) [173], energy dissipated by the contact strip sample was neglected. As would be expected, the input energy was nearly zero in the regions of good contact and full separation stages due to zero voltage or current values. The results provided a means to correlate damage observed by microstructural examination (Section 4.3.1) with the Joule heating law.

The average energy input was calculated from the area under voltage and current graphs. The energy input for a single arc was 1.59 kJ for test number T3 (200A DC) while it was only 0.03 for test number T6 (200A AC). The current-voltage measurements showed that the accumulated energy was nearly zero in the regions of full contact and full separation due to zero voltage and current values. These results provided valuable insights into the thermal damage from the effect of Joule heating during arcing.



(a) DC arcing



(b) AC arcing

Fig. 4.31 Power generated by arcing

4.3.3 Temperature Measurements

An infrared thermometer device was used for temperature measurements of the contact wires during the arc experiments with the current of 200 A AC and 200 A DC. Room temperatures were 18 ° C and 19 ° C for AC and DC experiments, respectively and the samples were thermodynamically stable. Due to the arc flashing caused a large amount of light exposure at the arc location, the infrared thermometer was unable to measure directly at this location. Therefore, the infrared point was directed to the closest location that was able to measure the temperature reliably. The location of points was adjusted to be 5 mm away from the arc location to prevent the temperature results from being affected by flashes and flames. Fig. 4.32 shows the experimental setup used to measure temperatures of contact wires during the experiments.

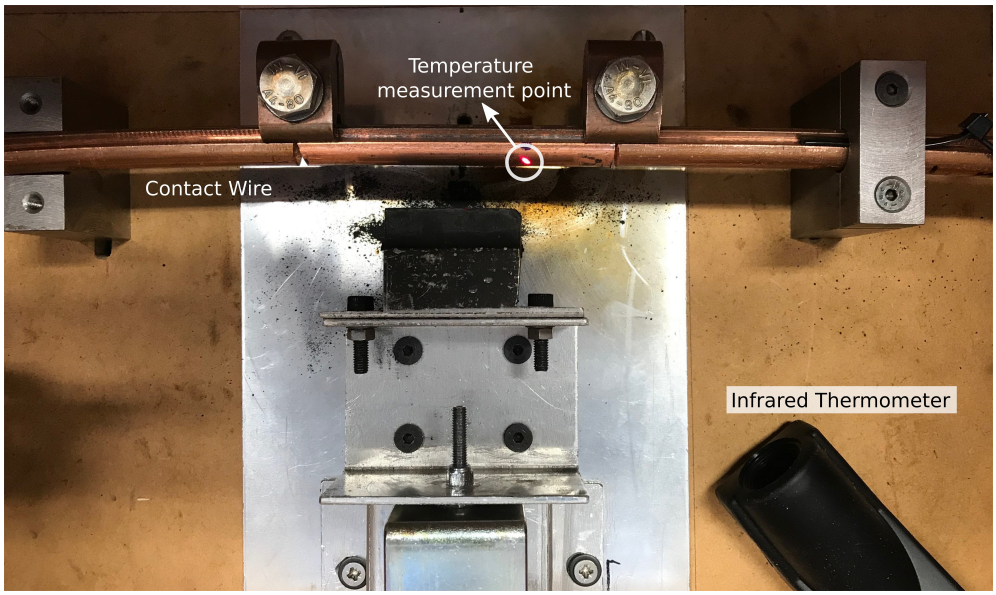
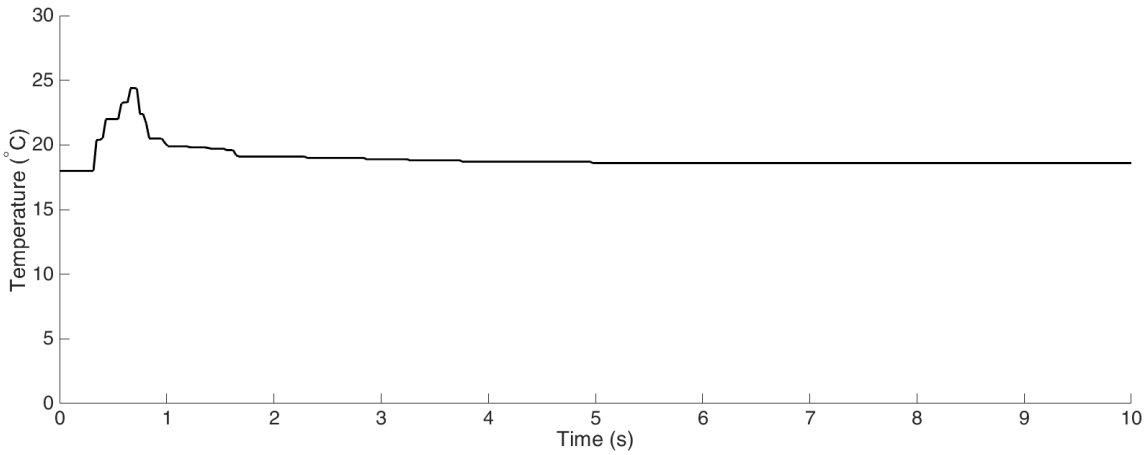


Fig. 4.32 Setup used to measure temperature variations of contact wires during the experiments

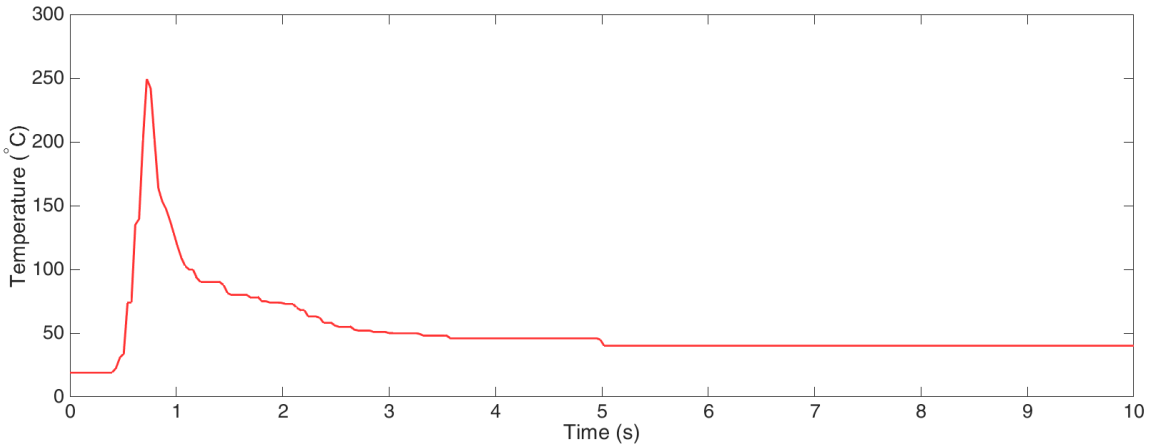
Fig. 4.33 presents the temperature measurement data of the location over the time during the arcing experiments with the parameters of 200 A AC and 200 A DC with a single arc. From the figure, it can be seen that both tests showed that the temperature of measured location increased in both cases. However, while in DC arcing, the temperature of the remote point rose to 250 ° C, it was merely 25 ° C in AC arcing. After reaching the maximum, both samples were entirely cooled down after 2 minutes.

Considering the standard temperature limits for material mechanical properties, according to EN 50119 [47], over 200 ° C is expected to reduce the strength of the copper-silver contact

wire. In particular, the material at the arcing location is likely to reach melting points. Thus, the strength reduction in the arc location can be more severe.



(a) 200 A AC arcing



(b) 200 A DC arcing

Fig. 4.33 Maximum temperature of measured points over the time

The results obtained from temperature measurements in this section were used in verification of the finite element model developed in Chapter 5, which was an in-depth temperature analysis of contact wire during the arcing stage.

4.3.4 Hardness

For samples with voids or severely damaged surface, hardness measurements were started from the border of the severely damaged layer (0.24 mm from the surface) running to the interior of the contact wire due to avoid making unreliable measurements close to these

internal defects. Fig. 4.34 depicts the hardness of the specimen for test number T4. Wires tested under the other conditions examined had similar characteristics. In addition to regions of grain growth and recrystallised material (the visible HAZ) already discussed in this chapter, there was also a region of softened material, labelled 'tempered zone' with no visible distinction from the unaffected interior material. There was a clear trend of hardness decreasing from the interior towards the heat-affected zone. The hardness of the grain growth region was significantly affected by the annealing effect of arcing. Although no grain growth was observed in the tempered zone, arcing still reduced the material hardness with a reduction in the order of 10 % from the parent material.

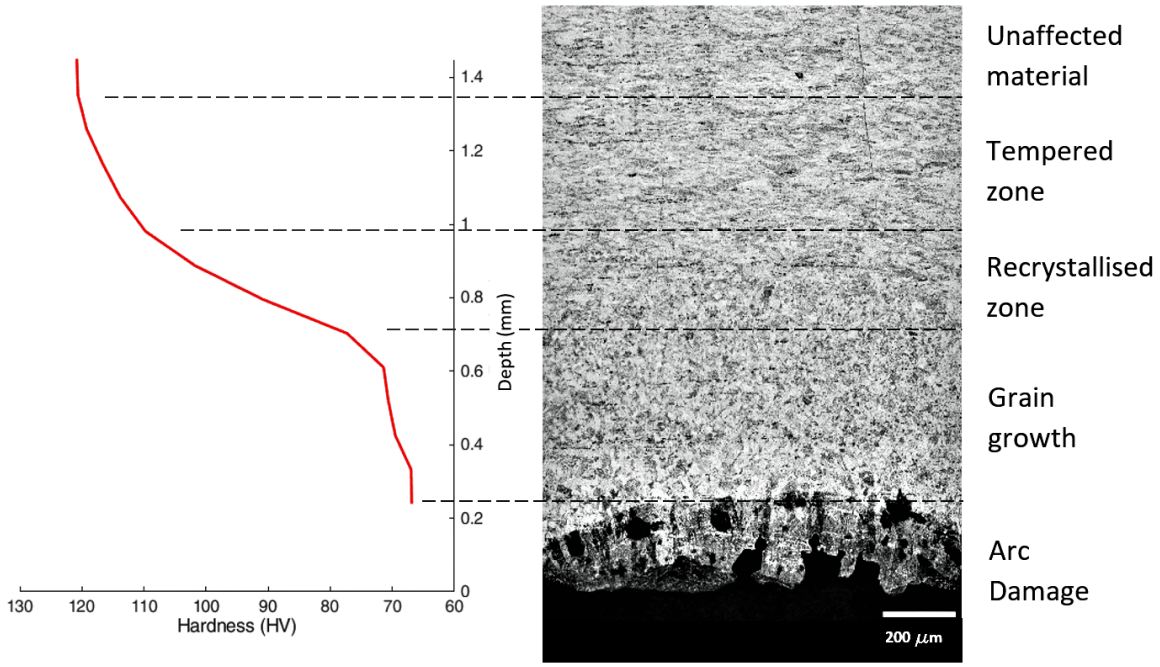


Fig. 4.34 Hardness reduction of the sample of T4 (200 A- Multiple arc)

The variation of hardness with the depth for all the samples after arcing is shown in Fig. 4.35. To quantify the comparison of the hardness results, the depth at which hardness was reduced to 80 % of its core value is tabulated in Table 4.3. Using the intercept of the hardness plot with the 80 % core value is useful to indicate a depth of hardening, while also avoiding trying to define this point on the rapidly varying hardness very near the wire surface. This is similar to the concept of using proof stress to define the yield point in materials without a clearly defined elastic limit. A similar softening pattern was seen for all of the samples with differences correlated with test conditions.

Samples tested with DC had greater penetration depth of hardness reduction than samples tested with AC. Particularly, 200A DC samples were more than 40 % softer than samples

with no arc for first 0.7 mm of their depth, while this level of softening ran to a depth of the 0.5 mm for 100A DC samples. It can also be seen from the hardness graph of the tested samples with 200 A DC and 100 A DC that the heat-affected zone extended 1.4 mm and 1 mm into specimens, respectively. The test condition of having two pantographs on the train resulted in double arcing in a short time (3.6 seconds for a train travelling at 200 km/h) stayed between the test of single arc and ten arcs.

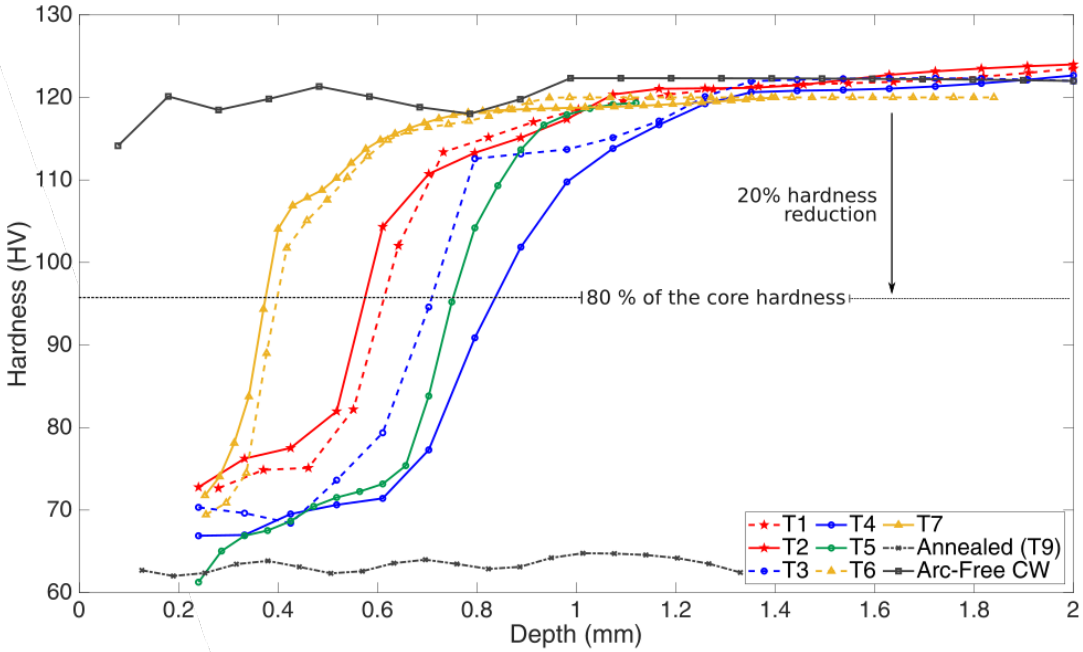


Fig. 4.35 Hardness variation of tested samples

Interior of the material was changed less significantly with AC tests compared to those of DC. Although the hardness of the material dropped to 70 HV close to the area where was damaged due to arcing, it took only 0.6 mm to reach its core hardness.

When the consequences of single and multiple arcs were compared, no significant difference in the reduction of the near-surface hardness was found, with single and multiple arcs affected samples almost identically. The depth of softening was marginally higher for repeated arc tests than the corresponding single arc tests, but the overall finding was that a single arc could generate the majority of the damage and softening. Test number of T5 representing two pantographs on a single train producing rapid repetition of arcing generated similar hardness change to the other tests.

In order to compare all the results with better understanding, hardness measurements of an arc free sample and an annealed sample were added to the hardness survey of the

experimental results, and 80 % of the core hardness (96 HV) was lined in the Fig. 4.35. In that condition, minimum hardness reduction was seen in the tests with AC 200A. They were softened 20 % within the depth of 0.38 mm while DC 100 A (single and multiple arcs), DC 200 A single arc, DC 200 A double pantograph and DC 200 A multiple arcs were 0.58 mm, 0.7 mm, 0.75 and 0.82 mm, respectively.

Table 4.3 shows the hardness reduction at the closest point to the damaged area (0.24 mm depth) to reach 80 % of core hardness. On the surface, arc damage can cause a local hardness reduction of up to 50 %. It can also be seen that the severity of DC arc damage was stronger than the one of AC and caused significant hardness reduction within the depth of 0.82 mm of the contact wire. Also, the combination of hardness results with energy input obtained from voltage-current measurements showed that there was a correlation between the depth affected by the decrease in hardness % and the energy input. For equal current and number of arcs, the depth for DC tests in which the material lost its hardness up to 20 % was 50 % larger than that for AC tests. The higher energy input in DC can be the reason of affecting the reduction in hardness to a deeper area.

Table 4.3 Hardness reduction and input energy due to arcing

Test ID	**Current [A]**	**Number of Arcs**	**Energy Input for Single Arc [kJ]**	**Hardness Reduction (at 0.24 mm depth) [%]**	**Depth for 80% of core hardness [mm]**
T1	100 DC	1	1.35	39	0.61
T2	100 DC	10	1.3	39	0.58
T3	200 DC	1	1.56	41	0.75
T4	200 DC	10	1.59	44	0.82
T5	200 DC	2	–	49	0.75
T6	200 AC	1	0.03	43	0.39
T7	200 AC	10	0.03	41	0.37

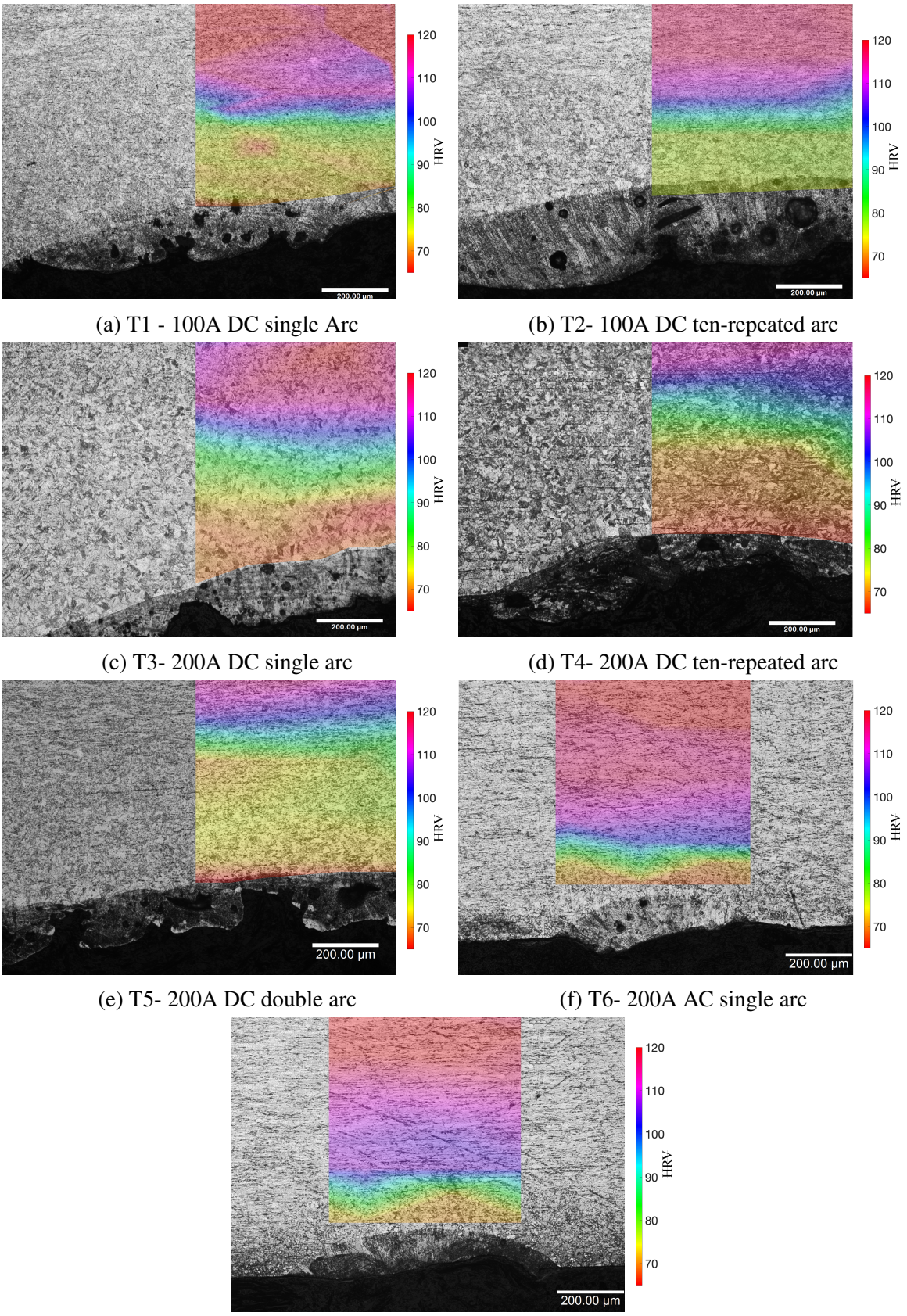
4.3.5 Hardness Map with Microstructure

It was apparent from the hardness results that the microstructural modification due to the increased temperature in the contact wire was a cause of softening of the material. Therefore, results from the optical microscope and microhardness tests were expressed together in this section to understand better the contact wire softening. This also helped to compare hardness reduction patterns in contact wire samples obtained by experiments and real OLE contact wire investigations. Fig. 4.36 shows the change in the hardness of the contact wire depending on its microstructural properties. The colour scale of the figures was set to be in the same

range, in between 65 and 120 HRV, to compare the results appropriately. The coloured area was restricted by the microhardness measured area.

In the same vein with the hardness survey of the samples shown in Fig. 4.35, the depth of the material subjected to grain size modification became larger with increase in the current. Although, the surface damage in AC arcs (Fig. 4.36f and Fig. 4.36g) was very similar to the DC ones ((Fig. 4.36c and Fig. 4.36d) , for the same testing parameters, the depth resulted in grain growth and severe hardness reduction was almost half of that in DC experiments.

Fig. 4.37 shows the hardness map of the interior of the contact wire samples extracted from OLE mainline. The mainline investigated in this study was running with the AC feeding system. Therefore, when the hardness results of real OLE contact wires (Fig. 4.37a and Fig. 4.37b) compared with those obtained from AC experiments (Fig. 4.36f and Fig. 4.36g), very similar microstructural and hardness behaviours were seen. This meant a very high hardness reduction by the arc damage region and a narrow transition zone. In the AC experiments and real contact wire investigations, the layer where the contact wire lost up to its 80 % of its hardness affected by the hardness reduction was just below 0.4 mm. This also shows that the experiments developed in this study are representative of the arc problem in real life.



(a) T1 - 100A DC single Arc

(b) T2- 100A DC ten-repeated arc

(c) T3- 200A DC single arc

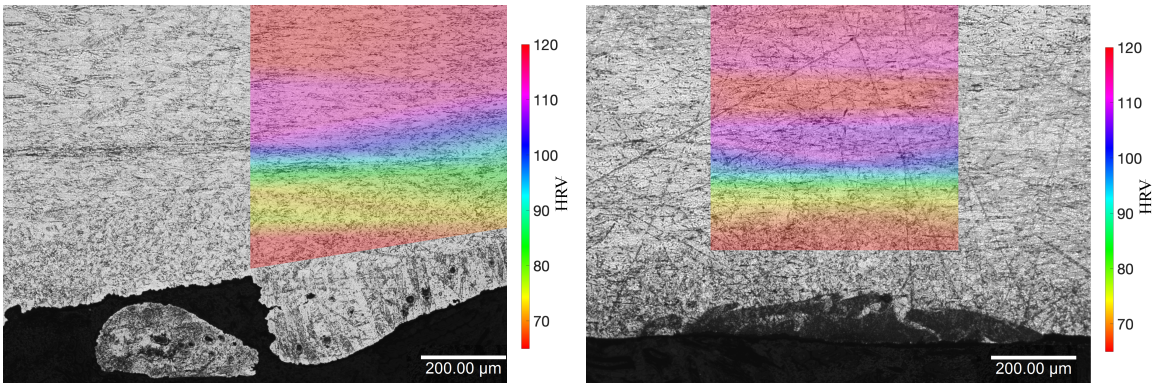
(d) T4- 200A DC ten-repeated arc

(e) T5- 200A DC double arc

(f) T6- 200A AC single arc

(g) T7- 200A AC ten-repeated arc

Fig. 4.36 Hardness map of the samples from experiments with microstructure



(a) Sample 3 (b) Sample 25

Fig. 4.37 Hardness map of the samples from OLE main lines with microstructure

4.3.6 Tempering Effects of Arcing

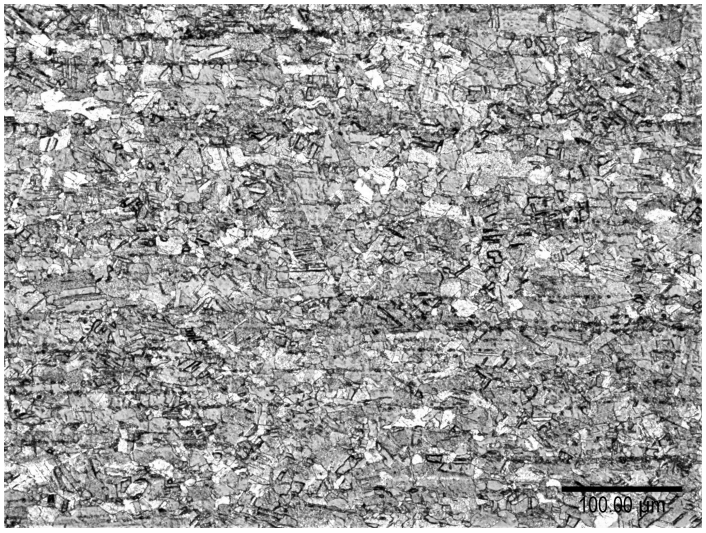
Copper-silver contact wire was annealed at 450° C for 2 hours to understand why the grain sizes changed and how to compare grain size with those of arc experiments. Recrystallisation temperature of copper-silver contact wire is elevated to 450° C due to the effect of the silver element while the recrystallisation temperature of pure copper (T_{RE}) is just over 250° C [40]. Grain sizes were investigated with an optical microscope according to the standard of ASTM E112-13 [211]. An equation from the standard was used to calculate grain sizes as follows;

$$N_{AE} = 2^{G-1} \tag{4.2}$$

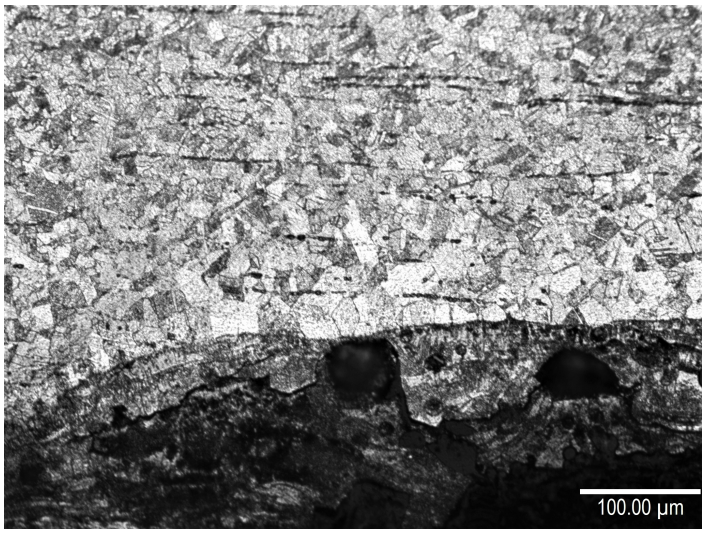
where G is ASTM grain size number and N_{AE} is the number of grains per square inch.

Fig. 4.38 shows the grains after annealing process and heating effect from arcing. The results showed that grain shapes and sizes after arcing presented similar results. Following the microhardness test of tempered contact wire samples, the average hardness was found to be just over 60 HV. When considering that hardness reductions of all tested samples varied from 120 HV to 60 HV, the hardness of the tempered sample showed strong evidence that grain growth phenomena contributed to the hardness reduction after arcing issue.

Table 4.4 provides the grain size results obtained from optical microscopy with the ASTM method. It was found that DC experiments resulted in bigger grains compared to those of AC experiments. Also, the maximum grain size was measured as 19.5 μm in the test of DC with 200 A, and multiple arcs that was the maximum hardness reduction was seen. The largest grain size was observed to be 20.2 μm in the tempered samples.



(a) 2 hours annealing at 450° C



(b) Multiple arcing with 200A DC

Fig. 4.38 Grain sizes after tempering and arcing of the copper samples

Table 4.4 The maximum grain size of samples after arcing and tempering

Test ID	Current Type	Current-Arc Number	ASTM (G)	Grain Size (μm)
T1	DC	100A-1	9.4	13.8
T2	DC	100A-10	9	15.9
T3	DC	200A-1	7.8 (50x)	12.0
T4	DC	200A-10	6.5 (50x)	19.5
T5	DC	200A-2	9.6	13.0
T6	AC	200A-1	10.5	9.4
T7	AC	200A-10	9.7	12.5
T8	Oxygen-free copper only investigated for voiding			
T9	-	-	8.3	20.2

4.4 Discussion

The methods and the experimental works described in this chapter indicate that importance of arcing in determining non-tribological damage in OLE contact wires. Notably, findings from the contact wire samples extracted from the OLE mainline the importance of analysing of effects of arcing on contact wire material. The preliminary investigation was conducted with contact wire samples extracted from a real OLE line in Milton Keynes. Although the parameters of arcs (duration, current, number of arcs) caused damage on the contact wire surface was unknown, severe interior damage and grain modification in the contact wire was observed. Additionally, these arc spots were seen not only at the lower surface (facing towards the pantograph collector strip) but also on the upper and side surfaces of the contact wire. This is significant evidence of flashover arcs which occurs between the contact wire and OLE structure.

In order to understand the role of arc parameters in the contact wire damage, a number of experiments were conducted with SOLARC machine. The primary findings from the microstructural investigation of the tested samples showed that;

- Significant grain growth was observed in all samples local to the arc exposed area of each sample
- A recrystallised zone with completely revised grain shapes and an annealed zone (original grains but much softer) formed between the region of surface damage and unaffected base material.
- Voids formed within 200-300 μm of the surface in DC and AC experiments.

- The duration of drawn arcs was higher for DC than AC under otherwise identical conditions.

The hardness and microstructural results from the experiments match those observed in the investigation real OLE contact wire extracted from Milton Keynes. Particularly, void forms, grain modifications and reduction in the hardness across the cross-section of the contact wire showed very similar behaviours in both analyses.

It has been known from the literature that DC systems do not have zero voltage and current points, thus, in DC it is expected to sustain arcs for a longer time with higher temperature comparing to AC systems [172, 171]. In the same vein, this study also confirms that contact wires are exposed to more severe damage and burn marks due to DC arcing. In particular, increasing current from 100 A DC to 200 A DC resulted in more softened surface and microstructure properties. Also, the time between arcs played a vital role to modify grains and heat-affected layers of the contact wire. When the time was 3.6 seconds between the arcs (double pantograph), because the material was unable to cool down after the first arc, the second arc contributed to enlarge the softening area and damaged the contact wire surface more severe compared to single arc condition. However, in the tests with ten repeated arcs and 2 minute time between the arcs, there was no clear correlation between the number of arcs and softening of the material. In these tests, the majority of the damage appeared after the first arc.

Another important finding in the microstructure after the arc damage was void forms. Some studies in the literature [166, 168, 212] indicated that voids and defects are found in the heat affected area of copper materials during the studies about weldability. This issue was already discussed in the literature review (Chapter 2), which is named "hydrogen embrittlement". We also know that electrical arcs in the OLE system can be considered as "electrical welding" [48]. Therefore, a possible explanation of void formation in the heat affected area may be hydrogen embrittlement. A comprehensive explanation of this is that the oxygen concentration in the material and high-pressure steam that is a product of hydrogen diffusion and reaction with carbides and oxides at elevated temperatures results in oxide depletion and holes at the heat affected region [213, 166, 214, 212, 167]. Thus, a number of additional tests were conducted with OFC material. Using OFC in the arc experiments showed a significant improvement in preventing large voids in the damaged area, this may offer a route to avoid void formations in the contact wires. Due to the limitation of obtaining OFC in contact wire form, because OFC contact wire has not been a widely industrialised product, experiments were conducted with OFC bar material. It is difficult to compare the mechanical behaviours of OFC and copper-silver contact wire material. Thus, further work is required to fully understand the potential for this material when combined with

the manufacturing process for overhead line wire. Besides, its mechanical wear behaviour and performance under combine both sliding and electrical contact will require further investigation before deployment.

Additionally, voids are very close to the surface of the contact wire, and this arises a question whether these defects influence mechanical behaviours of the contact wire. Line tension combined with uplift and bending of the contact wire (Section 2.3) can reach at very high levels and results in plastic deformation (Section 3.2.1) in the contact wire. Voids under high stress in line can play an important role in the service life of the contact wire. It has been known that fatigue-related cracks can initiate near the micro-voids [215, 216]. More interestingly, some studies also mention that the crack initiation occurs not only on the contact surface but also inside the material below the surface [217, 218]. Studies in the past found that critical void diameters for crack initiation can vary between 20 and 70 μm for different materials [219, 220]. Considering this, the diameter of the voids observed in this research can be up to 150 μm, which is rather larger than that in the literature. The line tension together with voids observed close to the arc affected surface of contact wire, is capable of driving fatigue crack initiation, eventually leading to sudden contact line failure. Therefore, arcing must be avoided when considered pantograph applies repeating bending force to the contact wire. Given that the growth of a fatigue crack is difficult to stop once it begins in a line under tension, the question also arises of whether its initiation through void formation can be prevented.

Returning briefly to softening of contact wire after arc damage, this is also a potential for accelerated wear in areas that have undergone softening, following Archard's relationship showing inverse proportionality of wear and hardness [52]. While wear could reduce the life of the wire, it is a surface phenomenon so can be easily monitored by visual inspection. Moreover, the regions of arc softened material is small relative to the cross-section of the wire and the pantograph collector strip contact area, so surrounding unaffected material will mitigate the development of locally severe wear spots. Although arcing is a momentary phenomenon, there are circumstances that the contact wire can be subjected to longer arcs and result in breakage while it is in a standstill position. Wada et al. showed in their study that particularly in the insulated overlaps, arc spots in the contact wire occurred in a current range of 30-300A can lead to necking and eventually the breakage of the contact wire is inevitable [221]. Therefore, the arc problem itself can be significantly serious in the estimation of the contact wire life as well as its combination of the other interaction problems; such as fatigue and wear.

Further research of the effects of voids and arc spots on fatigue life of OLE contact wire with different loading conditions was conducted in Chapter 6.

4.5 Conclusions

This study set out to investigate the identification of arc damage, its potential effects on mechanical and metallurgical properties of the contact wire, and mitigation of consequences of arc damage using OFC material. Analysis of contact wires from OLE main lines was in a good agreement with the results from the experiments. Therefore, the findings from experiments support the hypothesis of the arcing problem that would modify the microstructure and reduce the strength of the contact wire due to local heating.

From the experiments, it was found that arc damage occurred after only one event and consisted of voids near the surface, a significant depth of soft material, and zones of larger grains. The higher current caused the softening to spread deeper into the specimen, but the effect of the increasing number of arcs was not significant. However, the application of oxygen-free copper material to the overhead line electrification may be a solution in restricting void forms which are likely to trigger fatigue crack initiation mechanism.

Together with real OLE contact wire analysis, the present study extended our knowledge that flashover arcs can play an important role in the service life of the contact wire as well as pantograph arcs. This new understanding should help to improve predictions of potential effects of arcs on contact wires.

Chapter 5

Thermal Modelling of Arc Affected Contact Wire

Investigating the causes and results of the problem of arcing is a continuing concern within the railway electrification systems. Mainly, the evidence found in Chapter 4 shows that temperature plays an essential role in the metallurgical and mechanical properties of contact wires during the arcing process. However, due to high difficulty of measuring the temperature variation of the arc spot over the time of arcing (Chapter 4), another method is necessary to understand temperature distribution in the contact wire. In this chapter, an in-depth temperature analysis is carried out by using FE solutions to make the link between the temperature of the arc affected material and that adjacent to but just outside the arc exposed region. The temperature of this adjacent material is much more measured. Several significant contributions to research on arc damage to contact wires are completed.

5.1 Hypotheses Used in the Model

Arcing between the contact wire and the pantograph is a complex process depending on various factors, such as; the gap between the contact wire and pantograph, the current type of the system, the resistance of the material and mechanical wear. Arc plasma involves electrical, magnetic and thermal field. Therefore, simulations in the literature were designed based on these three criteria in order to investigate the characteristics of arcing. However, simulations by Gao et al. [141] showed that electromagnetic force could be neglected in the event of low currents between 0 and 200 A. This is important evidence that thermal field is the predominant mechanism during the arcing process. The thermal field can be explained by Joule heating in which the rate of heat generation per unit volume is proportional to the

square of the current density [222]. Because current transmitted through the arc between pantograph and contact during arcing generates heating in the contact wire.

In this study, a contact wire based thermal model was aimed to investigate the temperature distribution of the contact wire during a single arc. This work was not a CFD model simulating arc plasma. It was a further analysis of experimental outcomes (voltage and current measurements found in Chapter 4) with a thermal FE model..

Experimental findings showed that in the DC system, although current and voltage graphs fluctuated over the arcing process, no zero-crossing regions were observed. However, in the AC system, due to the alternating current in a range between plus and minus values, the electrical discharge is subjected to interruptions and zero energy points. Therefore, these two circumstances need to be investigated separately. The duration of arcs (energy input) was set as the same as it was in the experiments ($\approx$ 300 ms).

In parallel with the experiments done in Chapter 4, the following hypotheses were developed to investigate the thermal distribution in the contact wire due to electrical arcing:

1. Joule heating and its effects on the contact wire was considered
2. Thermal radiation and magnetic field were neglected
3. A constant environment convection was applied to all models
4. Input power of pantograph arcing was obtained from the arc voltage and current.
5. Verification of the results was done with the temperature measurements during the experiments in Chapter 4.

The main reason why the thermal cooling due to radiation was neglected is that energy per unit area lost by radiation was minor compared to that went into the contact wire. This can be explained by the thermal radiation calculation also known as Stefan-Boltzmann Law as follows [223];

$$q = \lambda \alpha A (T_i - T_0)^4 \tag{5.1}$$

where q is heat transfer per unit time (W), λ is emissivity coefficient of object ($0 < \lambda < 1$), α is the Stefan-Boltzmann constant ($5.6703\ 10^8 Wm^{-2}K^{-4}$), T_i and T_0 are object and ambient temperatures, respectively.

According to the thermal radiation calculations, the heat per unit time lost by radiation in the contact wire was in the order of one in a thousand of that went into the wire through

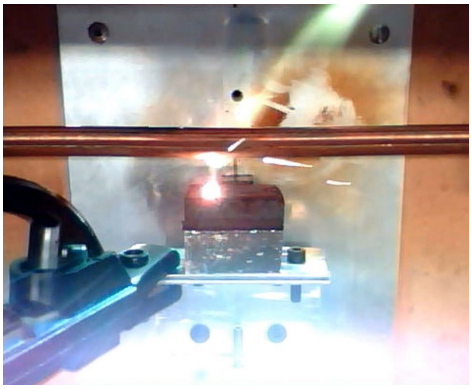
joule heating (Appendix C.1.1). One of the main reasons for this was because the area affected by extensive heating on the contact wire surface was minimal (approximately 20 mm^2). Also, the heat dissipated to a bigger surface in the vicinity of this local area reduced absolute temperature (T_i - T_0) and resulted in minor thermal radiation.

5.2 Understanding the Mechanism of Arcing

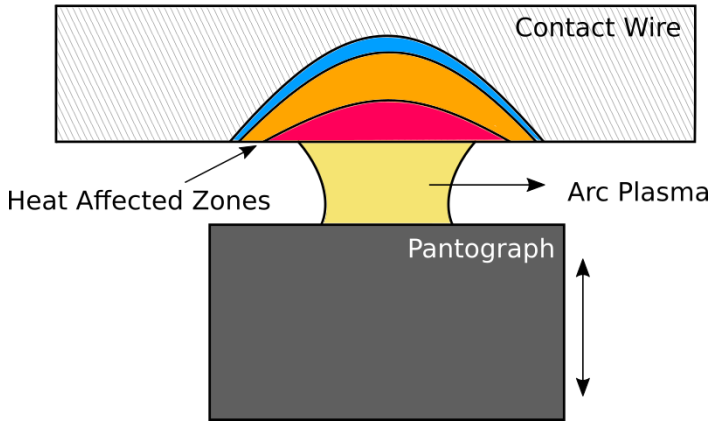
Arcing is considered one of the main issues influencing the current collection quality. When the mechanical contact is lost, the power is not transmitted continuously, voltage or current drops or losses. This means that arcing occurs between the pantograph and the contact wire.



(a) Pantograph-contact wire arc



(b) Arc plasma during arcing



(c) Schematic of pantograph contract wire arc

Fig. 5.1 Geometry and model of pantograph-contact wire system

Fig. 5.1 shows the pantograph-contact wire arc and schematic of the arc plasma. Once the mechanical contact between the conductors breaks, an arc occurs, and conductivity is maintained by an electrical discharge through the air. When arc discharge is taking place,

voltage and current variations play an important role to determine the characteristic of arcs, and approaching and drawn arcs can be understood from the voltage-current graphs. Therefore, accumulated energy is calculated by using joule heating formulation as follows;

$$E_a = \int_{t_1}^{t_2} U_{arc}(t) I_{arc}(t) dt \tag{5.2}$$

where E_a is accumulated energy between the time range of t_1 and t_2, $U_{arc}(t)$ is arc voltage and $I_{arc}(t)$ is arc current.

Although the duration of arcs is in milliseconds, it is enough to elevate the temperature of the contact wire to the melting point. Chapter 4 showed that it could be over 200 $^{\circ}C$, but small scale melting indicates that it must reach the melting temperature, typically copper-silver alloys used in OLE contact wire.

The extensive heat generated by arcing dissipates into the contact wire and the air. However, findings of the experimental work in Chapter 4 showed that arcs could cause modifications and different zones in the microstructure of the material. Hence, the temperature distribution in the material caused by arcing is essential for determining the different heat-affected zones formed in the contact wire (Fig. 5.1c).

5.3 Thermal Effects of Arcing between the Pantograph and Contact Wire

5.3.1 Properties of Contact Wire in the Thermal Model

To investigate thermal distribution due to arcing an FE model was developed, and simulations were analysed by using transient thermal analysis in Ansys Workbench. Since OLE is a complicated system containing different variables and actual length of contact wires in the main lines are in the order of 500-600 metres, only a partial configuration that affects the arcing issue was considered. Given that arcing is a local event, and conduction of thermal energy only produces a significant temperature rise over 5 mm from the arc, this is sufficient to represent the event. AC120, copper-silver 13.2mm-diameter contact wire was geometrically modelled as described in the standard of BS EN 50119.

A sub modelling technique was used to reduce the solving time. The dimensions of the arc spot were chosen from the experimental data in Chapter 4 and the energy was transferred from this location to the contact wire. The power graphs generated from voltage-current measurements were used to determine the heat input over time. The radiation from arcing

was neglected, and temperature-depended thermal conductivity properties [224] (Appendix C) were used to consider the influence of heating to the conductivity of the contact wire.

The surface affected by the arc energy input was selected based on the measurements done on the contact wire surface. Burn marks on the contact wire were investigated and the diameter of the marks was measured. Three tested contact wire samples with the same arcing parameters were analysed and their average burn mark diameters were selected to be average of 1.8 mm (ϕd_{AC}) and 5 mm (ϕd_{DC}) for AC and DC models, respectively (Fig 5.2)

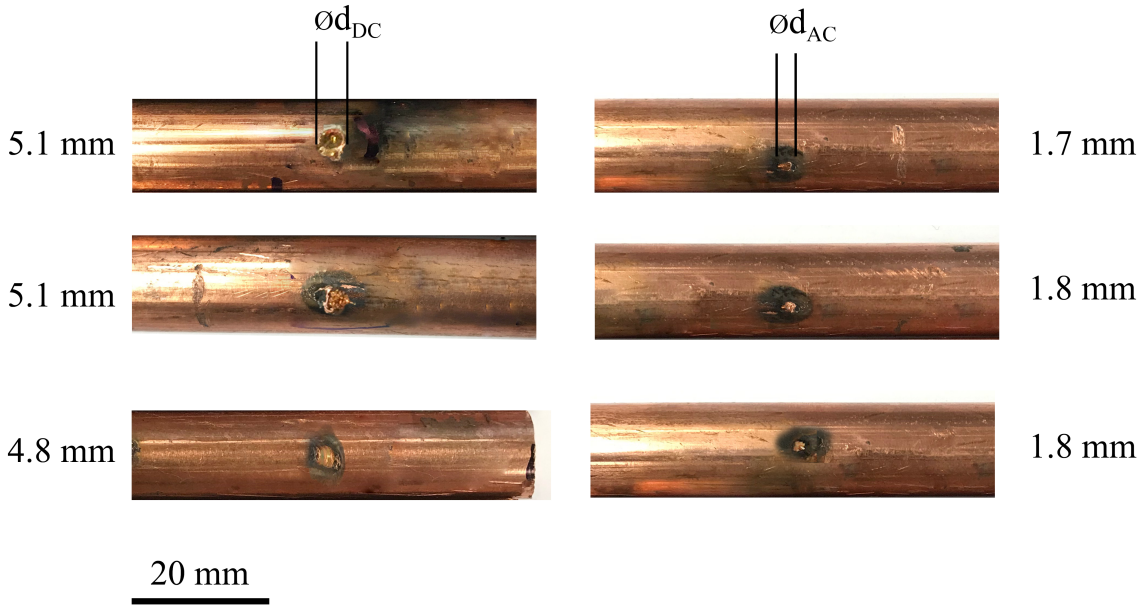
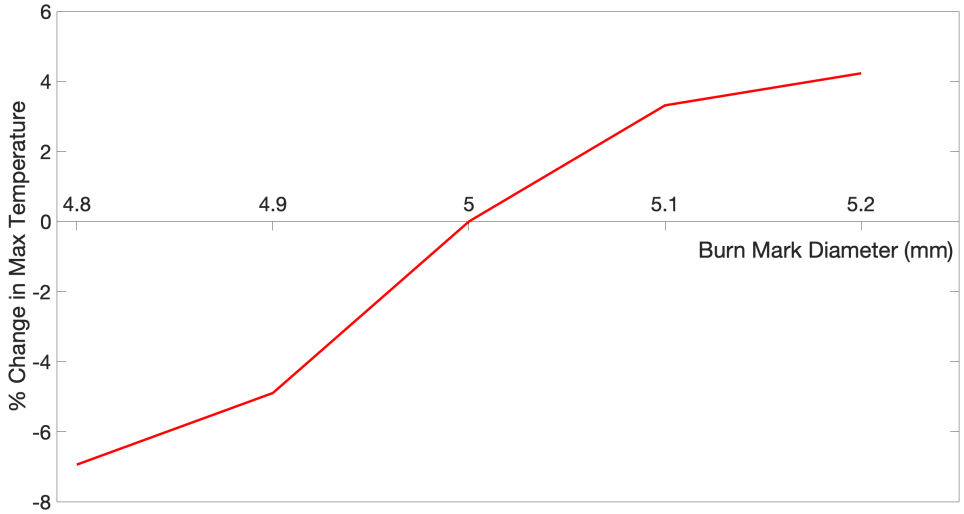


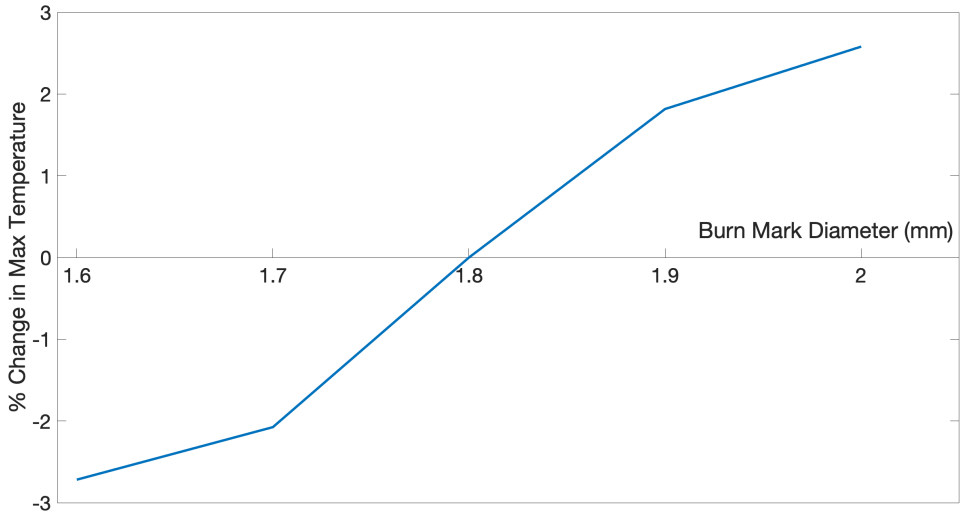
Fig. 5.2 Burn marks measured after the experiments with AC and DC

The sensitivity analysis of the effect of the burn mark size on the maximum temperature of the model was also controlled prior to completing the FE models. Fig. 5.3 shows the sensitivity analysis of how the burn mark diameter affect to the maximum temperature in the contact wire.

Regarding the material properties of the model, the specific heat and thermal conductivity were essential parameters for a realistic solution. Due to the fact that the wire was expected to reach elevated temperatures, it was necessary to use temperature-depended thermal properties for the model. Thus, reference values of specific heat and thermal conductivity parameters for copper material in the literature were used for defining the material properties of the FE model. Graphs of the variation of this reference data with temperature are shown in Appendix C.



(a) DC



(b) AC

Fig. 5.3 Sensitivity analysis of the burn mark diameter

Besides, the heat convected by open-air was an important determinant of cooling of the contact wire material. Therefore, another experimental reference data in the literature [225] developed for convection cooling of overhead power lines was defined to the FE model. The material properties of the model were tabulated in Table 5.1.

Table 5.1 Material properties used in FE modelling

Material Properties	Contact Wire
Density (kg/m^3)	8890
Melting Temperature (°C)	1080
Young's Modulus (MPa)	120000
Thermal Conductivity	Appendix C
Specific heat	Appendix C
Convection (W/m^2K)	45.76

5.3.2 The Quality of Finite Element Models and Meshes

The arcing problem was investigated with 3D finite element modelling. Contact wire was a circular material containing grooves by the sides. Therefore, in terms of fitting better the complex geometry, a tetrahedral element was chosen to build a mesh structure of the model. Prior to finite element analysis, a sequence of mesh quality measurements was conducted.

Initially, a convergence analysis was applied to the FE models. The models were divided into three mesh sizing regions, namely; very coarse, coarse and fine. A ratio between the mesh sizes in the regions was used to be 0.5. Fig. 5.4 shows the regions divided for the mesh refinement.

Although the model of DC arcing seemed very similar to that of AC, the surface area of the burn mark in AC was in the order of 1.8 mm which was relatively smaller than that in DC (5 mm). Therefore, individual models and meshing were used for both DC and AC situations. Element sizes and the number of elements used in convergence analysis were tabulated in Table 5.2.

Following determining the element size parameters, convergence analysis with nine iterations was conducted for both the models of AC and DC. Fig. 5.5 shows the change in maximum temperature depending on the number of elements. The difference in the maximum temperature was recorded and compared at each iteration number. Both models showed that the difference in the maximum temperature compared to the previous iteration dropped below 0.5 % at the iteration number of seven. The parameters in the further iterations did not significantly contribute to the increase in maximum temperature. Therefore, element size

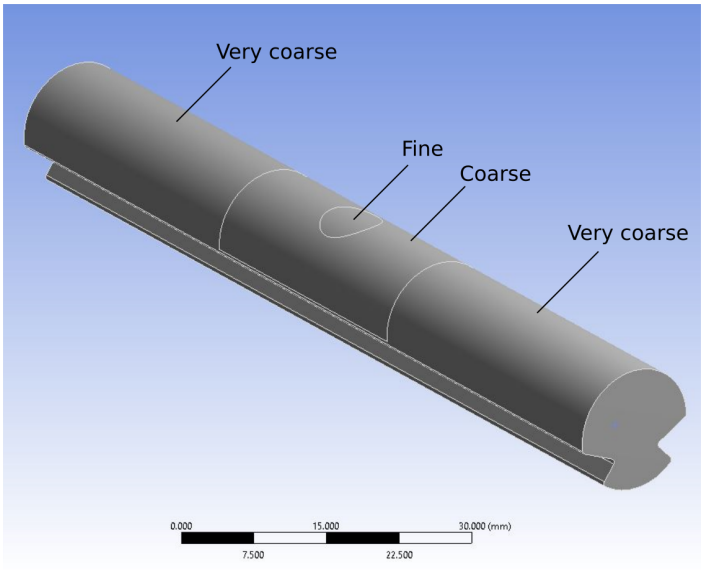


Fig. 5.4 Mesh sizing regions used in finite element models

Table 5.2 Element sizes and corresponded number of elements used in convergence analysis

Iteration	Element Size (mm)			Number of Elements	
Number	Very Coarse	Coarse	Fine	DC Model	AC Model
1	3.5	1.75	0.875	116707	77449
2	3	1.5	0.75	117571	79096
3	2.5	1.25	0.625	120747	81263
4	2	1	0.5	125946	86004
5	1.5	0.75	0.375	140398	98663
6	1	0.5	0.25	192521	147149
7	0.5	0.25	0.125	620974	501551
8	0.4	0.2	0.1	1022723	810415
9	0.3	0.15	0.075	1902262	1499135

optimisation was terminated at the iteration number of seven, and corresponding parameters were used for mesh refinement for both AC and DC models.

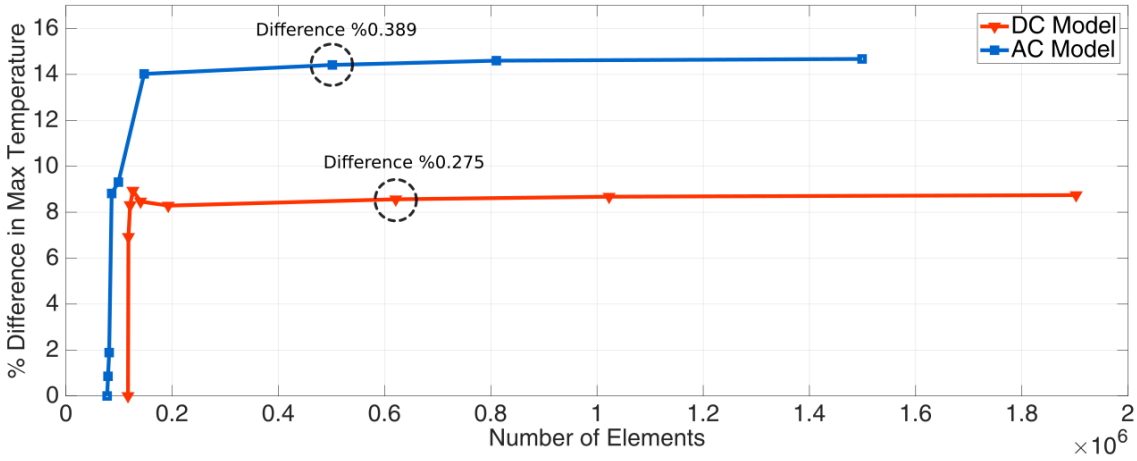


Fig. 5.5 Convergence analysis of FE models of DC and AC

Other meshing quality techniques, aspect quality, volume-length quality (the Jacobian) and angular measure of element quality (Skewness) were applied to models. Table 5.3 shows quality check results applied to AC and DC models, separately. The results of quality checks showed that element size and method used to develop finite element models for arcing simulations were in a good agreement with the reference limit values described in the table.

Table 5.3 Measures of element quality

Method	Maximum		Minimum		Average		SD	
	DC	AC	DC	AC	DC	AC	DC	AC
Aspect Ratio	7.28	4.29	1.16	1.16	1.84	1.86	0.43	0.42
Jacobian Ratio	1	1	-1	1	0.99	1	0.01	0
Skewness	0.96	0.84	0	0	0.23	0.24	0.12	0.12

Reference values for a perfect model
Aspect ratio: 1 [191], Jacobian Ratio :1, Skewness <0.5 [192]

5.3.3 Boundary Conditions

A thermal transition analysis was used for developing 3D finite element models. Although a small size sample was chosen to reduce the solving time of the analysis, infinite thermal conduction was applied across the longitudinal direction of the contact wire in order to

provide natural cooling to the model. For the heat taken away by airflow, convection was defined to all surfaces. Boundary conditions of the finite element models were schematically shown in Fig. 5.6.

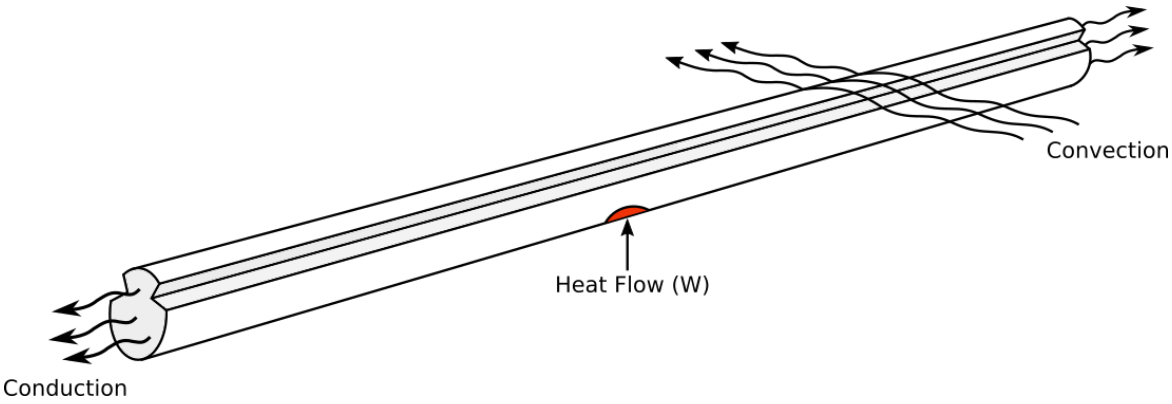


Fig. 5.6 Boundary conditions of the FE model

Regarding the heat input used to demonstrate the energy exposed by arcing, voltage-current data measured in the experiments (Section 6) converted into graphs with energy per unit time using Joule heating law. This data was tabulated in Table 5.4 and the amount of Joule heating energy of a single arc was shown at the bottom row of the table for AC and DC arcing. Initial temperatures of the models were decided based on the measurements during the experimental work described in Chapter 4. Eventually, it was applied to be 18 ° C and 19 ° C for AC and DC models, respectively.

5.4 Results

The first set of analyses examined the verification of the models by comparing with the results obtained from experimental measurements. Due to the lack of a temperature measuring technique of the contact wires in the arc-exposed spot during the arcing, it was not possible to obtain the temperature of the arc location and interior of the material. Therefore a nearby location was determined and marked on the wire and temperature variation there was recorded during the arcing experiments (see Section 4.3.3). The same locations were chosen in the FE models, and temperature variations were compared with those in experimental findings for verification.

Secondly, the temperature distributions were simulated for both under AC and DC arcing with 200 A, and zones affected by temperature increase were identified.

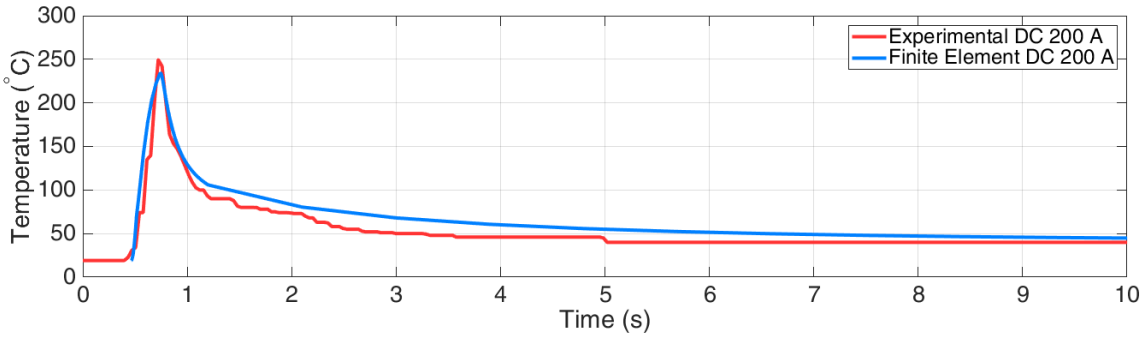
Table 5.4 Heat input converted from voltage-current measurements

AC		DC	
Time (s)	Heat Flow (W)	Time (s)	Heat Flow (W)
0	0	0	0
0.1103	0	0.2626	0
0.1211	990	0.2682	2619
0.1262	27	0.29	5545
0.1296	1650	0.3052	7585
0.1395	0	0.3101	5595
0.2658	0	0.3147	8494
0.27	143	0.3304	1527
0.2733	0	0.3426	6154
0.2782	2393	0.5382	3719
0.2836	0	0.5428	0
1	0	1	0
10	0	10	0
Total Energy	0.0375 kJ	Total Energy	1.48 kJ

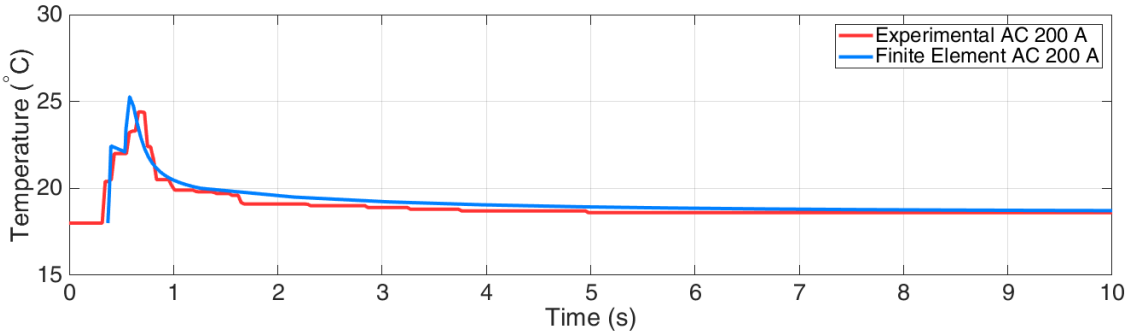
5.4.1 Comparing Temperature Results with Experimental Measurements

The temperature results from the measured points in the experiments and the finite element analysis are shown in Fig. 5.7. These results showed the nodal solutions of the FE models in the same location where the temperature was measured during the experiments.

Fig. 5.8 shows the verification of the maximum temperature in FE models in percentage compared to those in the experimental measurements. It can be seen from the figure that the models show the maximum surface temperature just after the arc with around 4 % and 6 % difference for AC and DC, respectively. In the cooling process, the same reference data about convection and conduction of OLE cables was used for both AC and DC models. However, the energy generated during the arcing was relatively more extensive in the DC feeding system compared to the one in AC; therefore the difference in between real temperature measurements and the FE solution was larger in the DC model which was just below 12 %.



(a) DC with 200 A



(b) AC with 200 A

Fig. 5.7 Verification of FEM results by comparing the temperature variation of selected points

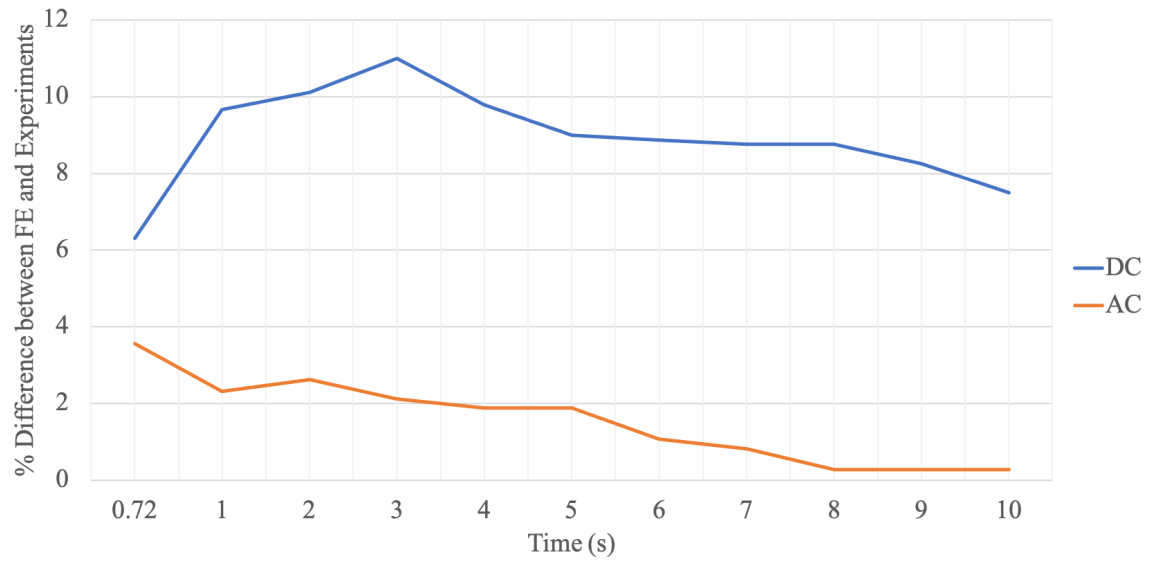
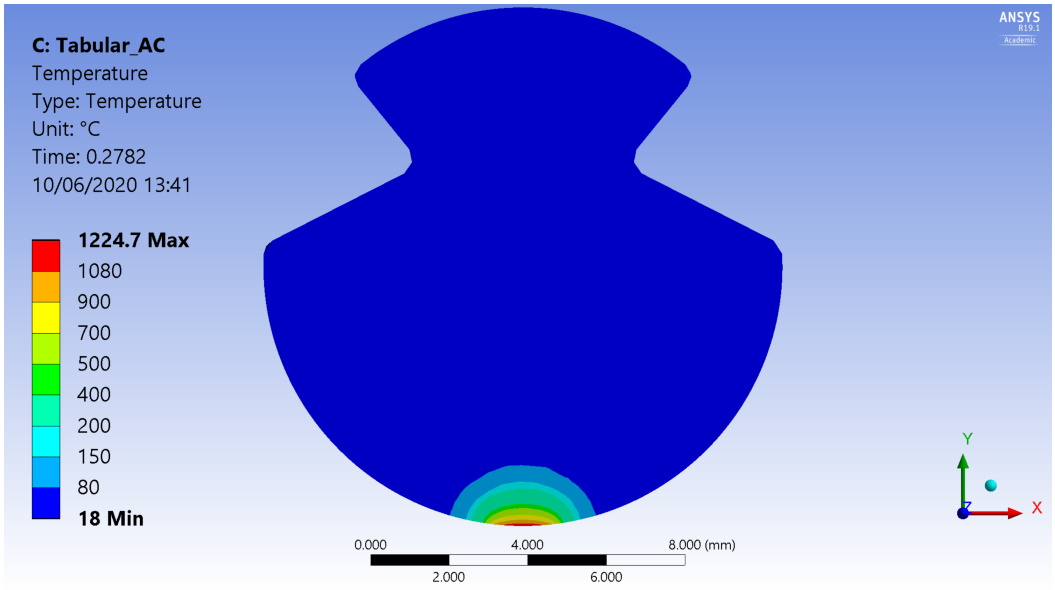


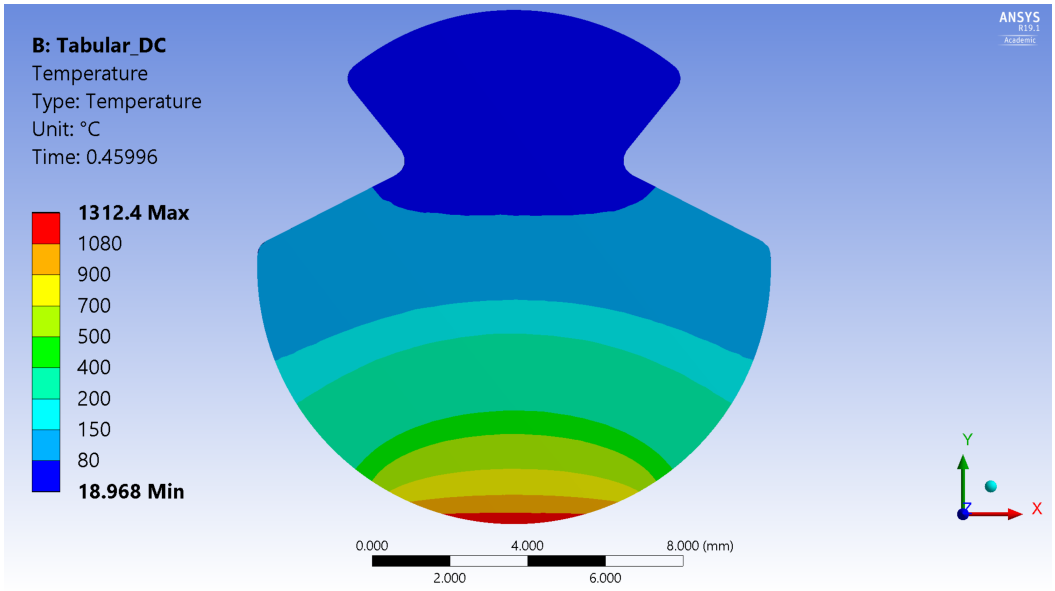
Fig. 5.8 The difference in the maximum temperature between FE model solutions and experimental findings

5.4.2 Thermal Distribution in OLE Contact Wire

The transient thermal analysis of the contact wire was carried out with 3D finite element models for AC and DC arcing. Temperature distribution in the cross-section of the contact wire is shown in Fig. 5.9. Temperature above the melting point of the material was indicated to be red colour. Red melting zone and its dissipation over the bottom surface of the contact wire are shown in Fig. 5.10.

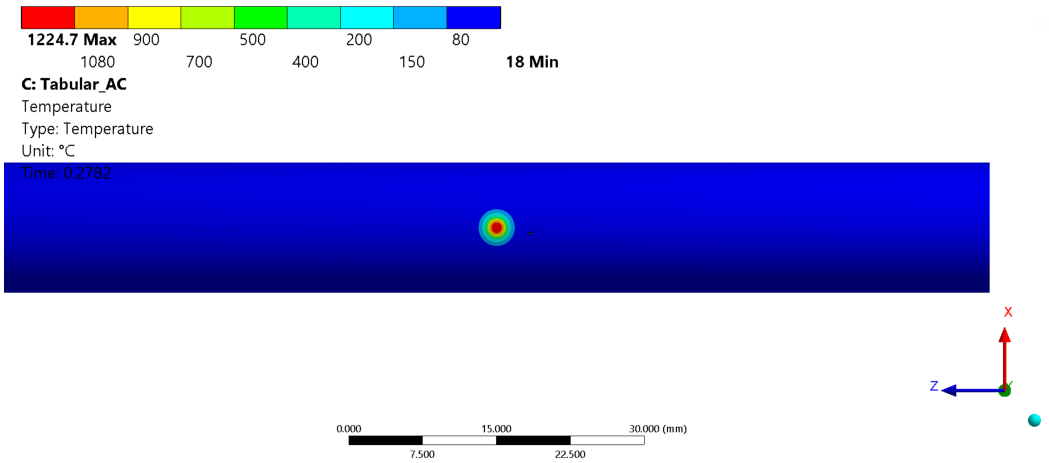


(a) AC with 200 A

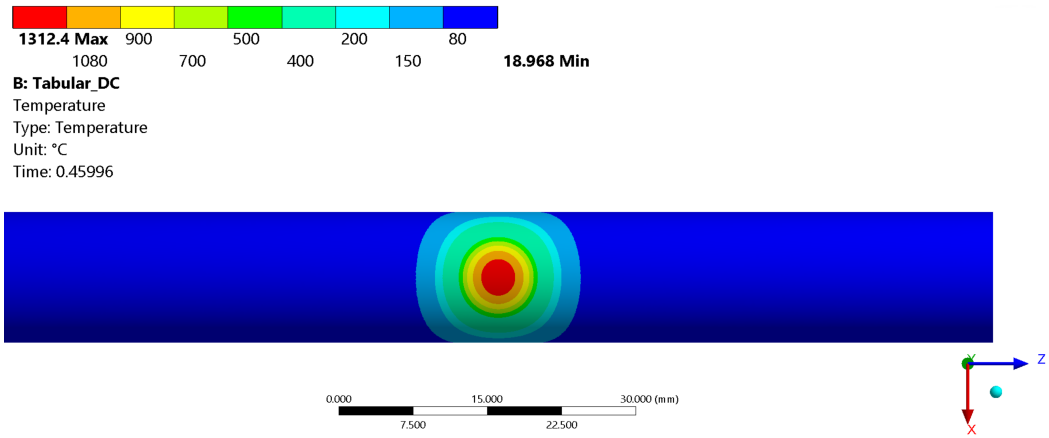


(b) DC with 200 A

Fig. 5.9 Maximum temperature distribution in the cross section of the contact wire model



(a) AC with 200 A



(b) DC with 200 A

Fig. 5.10 Maximum temperature distribution at bottom surface of the contact wire

The maximum temperatures were just over 1200 and 1300 ° C for AC and DC models, respectively. It was also clearly seen that the heat-affected area in the DC model was more extensive than that in the AC model. To clearly understand how the heat distributes throughout the cross-section of the wire, a path, shown in Fig. 5.11, was analysed.

Further analysis of the heat-affected layers of the contact wire models showed that the depth in which the temperature increased above the melting point of the material was 0.3 mm in DC model while it was only 0.1 mm in AC model. Another temperature which warranted attention was recrystallisation temperature of contact wire material. It was already explained in Section 4.3.6 this is in the order of 250 ° C for pure copper and 450 ° C for a copper-silver alloy. In the AC model, the depth affected by the temperature above 450 ° C was just over 0.5 mm; however, it was 2.7 mm, almost more than five times, in the DC model.

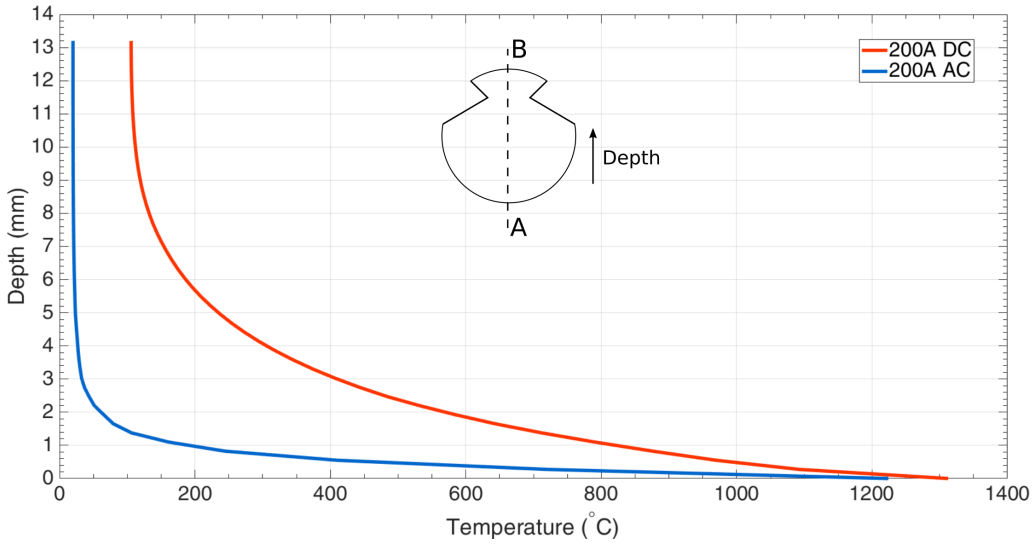


Fig. 5.11 Temperature distribution from A to B across the cross section of the contact wire

To investigate the cooling process of the contact wire, time-depended results of the temperature distribution from A to B were post-processed. The cooling stages of the contact wire section were plotted until the temperature spread evenly across the cross-section of the model. Fig. 5.12 and Fig. 5.13 show the cooling process of the models over the time for AC and DC arcing, respectively. It was seen from the figure that the time needed to cool down and dissipate the increase in the temperature to the section evenly in DC arcing was ten times more than that in AC.

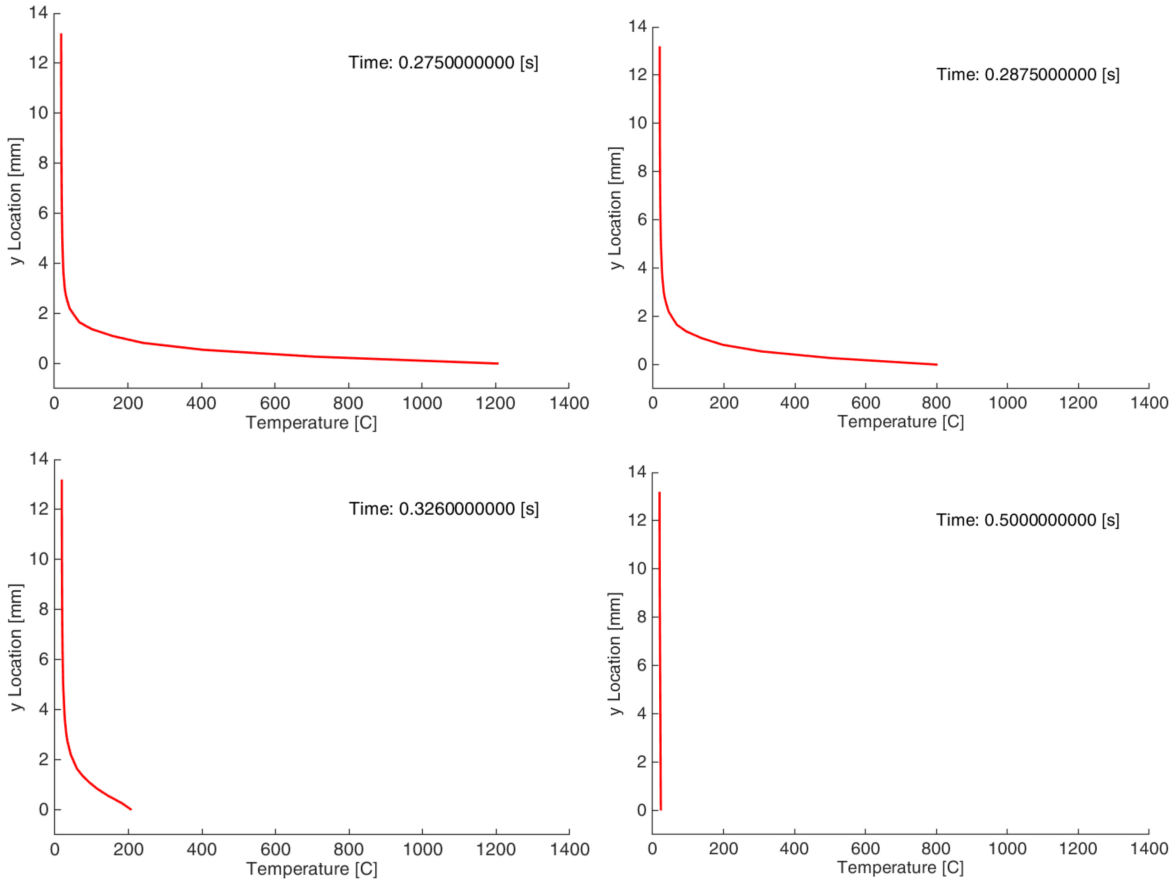


Fig. 5.12 Cooling stages of contact wire from A to B after reaching at maximum temperature with 200 AC

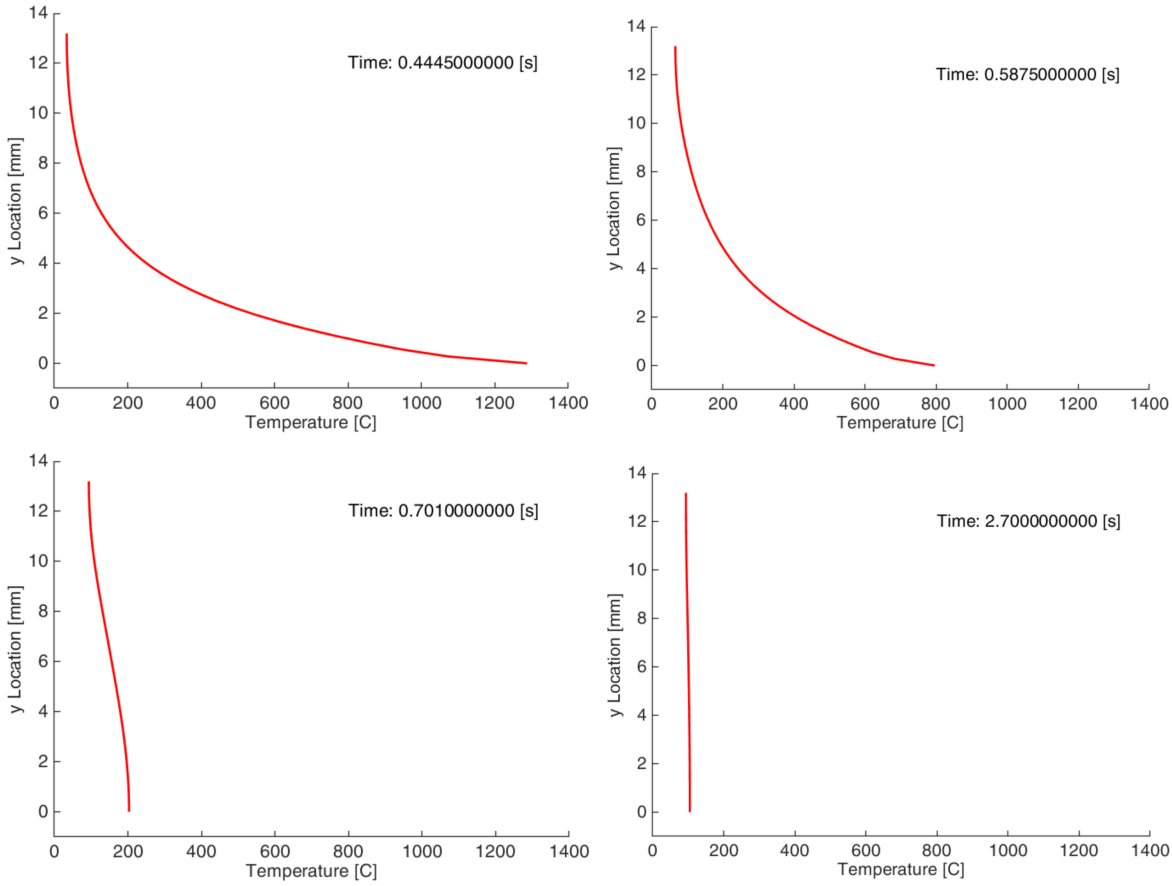


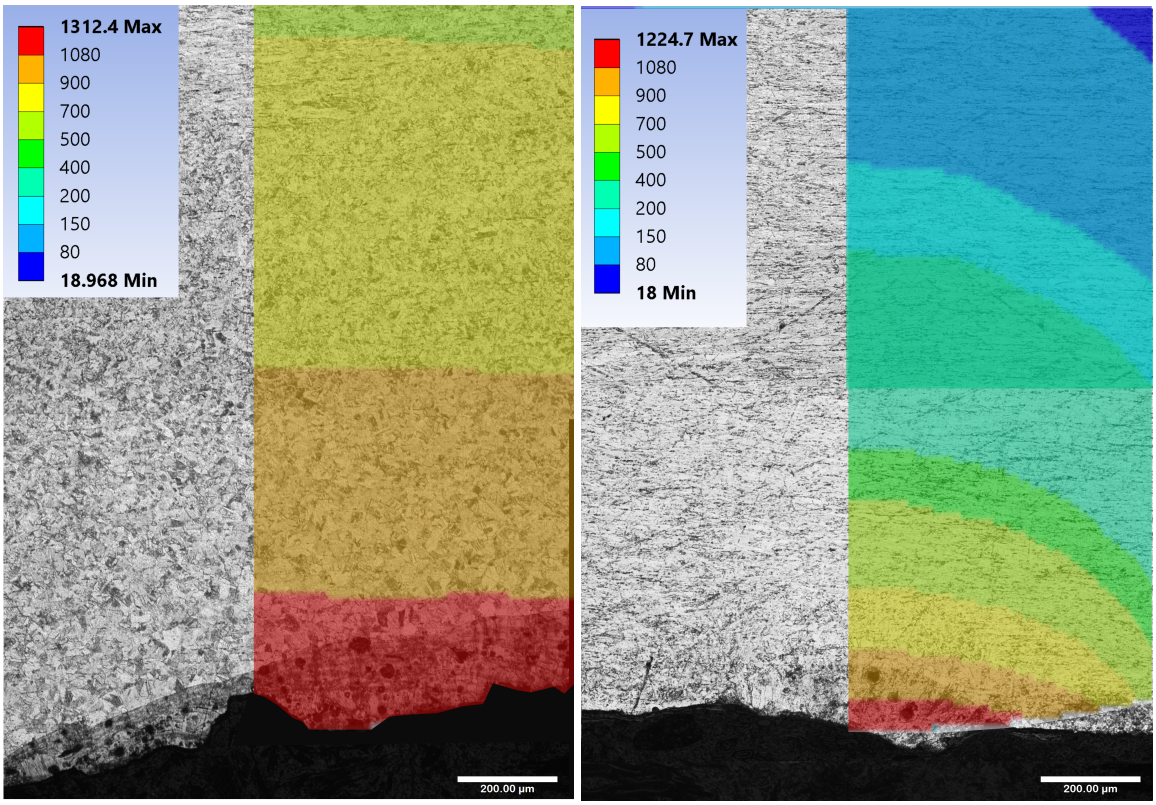
Fig. 5.13 Cooling stages of contact wire from A to B after reaching at maximum temperature with 200 DC

5.5 Discussion

The present study was designed to determine the increase in the maximum surface and interior temperature of the contact wire caused by arcing with AC and DC. The most prominent finding from the analysis is that a melting layer exists in the contact wire, and the thickness of this is firmly related to the current type used for generating the arc. The depth of this melting layer in DC arcing can be three times larger than that in AC arcing. Also, the maximum layer of the contact wire that reached above the recrystallisation temperature of copper-silver grade contact wire material can be in the order of 2.7 mm in DC arcing. However, recrystallisation of a material is not only a function of temperature but also time. Therefore, although the temperature of the contact wire reached elevating temperatures, the model showed that the cooling process of the wire is rapid. The length of the time for cooling the model was in the order of 0.2-0.3 s, being at the middle to the higher end of this range for DC as it had more significant energy input. Duration of the annealing time (below a second) can be seen very low compared to actual annealing procedure which is usually between half an hour and 2 hours. In general, for 2 hours annealing time, the recrystallisation temperature of the CuAg0.1 material is known to be just above 450 ° C. Nevertheless, studies in the literature show that the annealing process ican be very rapid, below a second, it can result in recrystallisation or grain growth with elevated temperature over 1000 ° C for copper materials [226, 227]. The recrystallisation layer and modifications in the grain shapes had been already observed in the experimental work in Section 4.3.4. In order to understand the details of grain modification and temperature distribution in the contact wire, the interior temperature distribution found in this chapter can be presented together with the microstructural findings from Chapter 4. Fig. 5.14 shows the interior temperature of the contact wire after arcing combined with the microstructural properties.

Although the layer exposed to recrystallisation temperature (450 ° C) was 2.7 mm in the finite element analysis of DC arcing, this layer was just below 1 mm in the microstructural investigations and hardness tests of the experimental work in Chapter 4. One of the main reasons why the layer affected by the increase in temperature in the physical tests was thinner than that in finite element analyses could be explained with the very rapid cooling of the material which was in milliseconds. Although the temperature was very high, there was no time for the material to grow larger grains. It has been known from the literature that annealing of materials consists of three stages, namely; dislocation release, recrystallisation and grain growth [228]. Besides temperature and time, there are other parameters which influence recrystallisation kinetics, such as; deformation degree, deformation rate or impurities [229]. As the contact wire was manufactured by the drawing process, it is a highly deformed material which has longitudinal grains. Thus, the dislocation concentration of the material

was very high, and this can also be another reason why the recrystallisation layer was thinner in reality.



(a) DC with 200 A (b) AC with 200 A

Fig. 5.14 Combination of the optical microstructure images and FE temperature solutions

5.6 Conclusions

This chapter explains the cause of modifications in the grains of the contact wire found in the in Chapter 4 by investigating the maximum temperature and temperature distribution in the contact wire with finite element modelling. The model was validated with experimental findings of real temperature measurements of the location, which was a little away from the arc spot. Before this study, it was difficult to make predictions about the maximum temperature caused by arcing and how it distributes across the section of wire over time. These results provide valuable insights into the details of the arcing process and its thermal effects in the contact wire for the current types of AC and DC. The method of modelling with FE used for this study is helpful to identify the consequences of arcing occurred in milliseconds which is challenging to observe in physical tests.

Findings from this study show that the maximum surface temperature is not the only parameter to understand the severity of arcing but also is interior temperature distribution. Although both DC and AC arcs generate similar maximum surface temperatures, temperature distribution over the lower surface and across the cross-section of the wire in DC was larger than that in AC.

Particularly for plastically deformed materials, annealing leads to a decrease in hardness, and it is expected that the crack propagation rate becomes faster. Therefore, this study can help to understand the maximum depth of the contact wire of which mechanical properties are affected by arcing.

Together, these findings suggest an important role not only for temperature but also for the cooling time in the thermal layer occurrence identified as grain growth, recrystallised and tempered zones in Chapter 4.

§

Chapter 6

Effects of Arcing on the Fatigue Life of Contact Wires

6.1 Introduction

The issue of fatigue and arcing in OLE contact wires have received considerable attention in the past decade. Existing studies of this combination were not identified by the literature review. To the author's knowledge, the possible consequences of arcing that influence mechanical or metallurgical properties of contact wires were not investigated in the literature. However, the research in Chapter 4 has consistently shown that the contact wire can be severely damaged due to single or repeating arcs. These arc spots can subjected to compression or tension stress depending on the contact wire and the pantograph interaction. The detailed analysis of the contact wire showed that material microstructure could be subjected to grain size modification and voiding. Since the surface of the contact wire is left pitted due to arcing, these locations can behave crack initiation points.

Findings from Chapter 4 indicated a need to understand whether surface damage caused by arcing can trigger fatigue crack initiation and affect the fatigue life of the contact wire. Thus, in this chapter, an experimental programme was developed, and results were explained to understand the effects of arcing on fatigue life of overhead contact wires.

6.2 Materials and Methods

In this chapter, the techniques developed in Chapter 3 and Chapter 4 were combined. Both SOLARC machine (Section 4.2.2) and overhead line fatigue apparatus (Section 3.2.4) were used without any configurational difference. The contact wire samples whose fatigue be-

haviours were to be tested after arcing were prepared in the same way (avoiding surface damage, same size and unrolling the coils) in the tests of fatigue life of OLE contact wires (Chapter 3). Fig. 6.1 shows the methods followed to test the fatigue of arc affected contact wires.

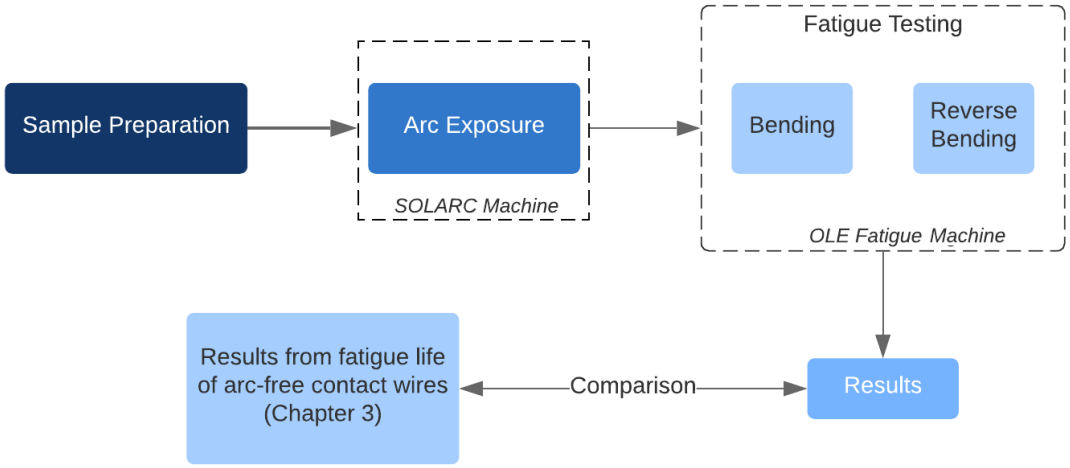


Fig. 6.1 Flow chart of the methods applied for assessing effects of arcing on fatigue life of OLE contact wires

6.2.1 Arc Exposure

Findings from Chapter 4 prompted this research to investigate the potential effect of surface deterioration on fatigue life of overhead contact wires. Initially, results in Chapter 4 was studied detailed again. According to results in Chapter 4, the surface damage resulted in void forms and microcracks in the microstructural scale. It was clear that the surface quality of the materials can play an important role in determining the fatigue characteristics. Additionally, the effects of micro-cracks found in the cross-section of the contact-wire were essential to be investigated. Therefore, before fatigue testing, 12 contact wire samples were exposed to 10 repeated arcs with 200 A DC.

The SOLARC machine (Section 4.2.2) was used to arc-affected contact wire samples. OLE clamps had been used to connect short sample contact wire samples in Chapter 4, in contrast, no clamp connection was used for placing the contact wire sample in this study. Since the length of contact wires (400 mm) was large enough to be accommodated by steel blocks in the SOLARC machine. Fig. 6.2 presents the configuration of the SOLARC machine and the connection of the contact wire to the machine. Arcs were generated between the

contact strip sample and the contact wire with a DC power supply as a consequence of the motion of the linear solenoid. When the mechanical contact broke between the contact wire and the contact strip sample, the electrical contact sustained a certain time until the gap reached a level that broke the electrical contact of these two materials.

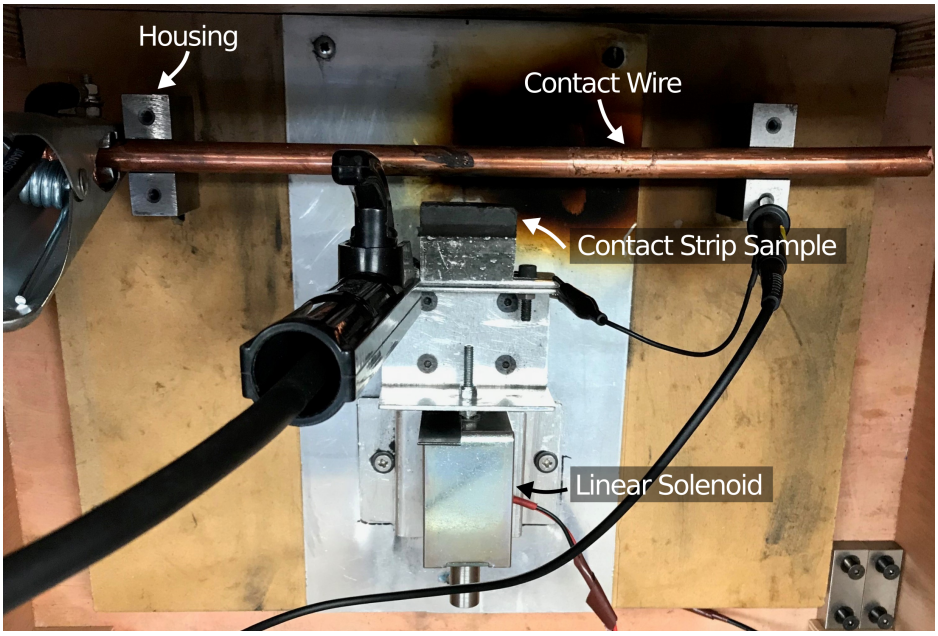


Fig. 6.2 SOLARC machine setup used in arc exposure of contact wire samples

6.2.2 Fatigue Testing

An apparatus designed in Chapter 3 was used for conducting the fatigue testing of arc affected contact wire samples. The arc location of the contact wire was centred on being in the middle of the vertical loading location. Since the setup was designed to work with the four-point bending principle, this generated a uniform bending moment with free of shear stress along the arc damaged surface of the contact wire. Same loading parameters as in Chapter 3 were used for performing the fatigue testing. The results were analysed using the strain-life method and compared with arc-free contact wire samples. Vertical load-strain conversation was completed based on the analysis in Section 3.3.1. Fig. 6.3 represents the test configuration of a typical fatigue testing for contact wire samples after arc exposure. The contact wire samples can be accommodated in this apparatus, either the arc affected side upper or lower position.

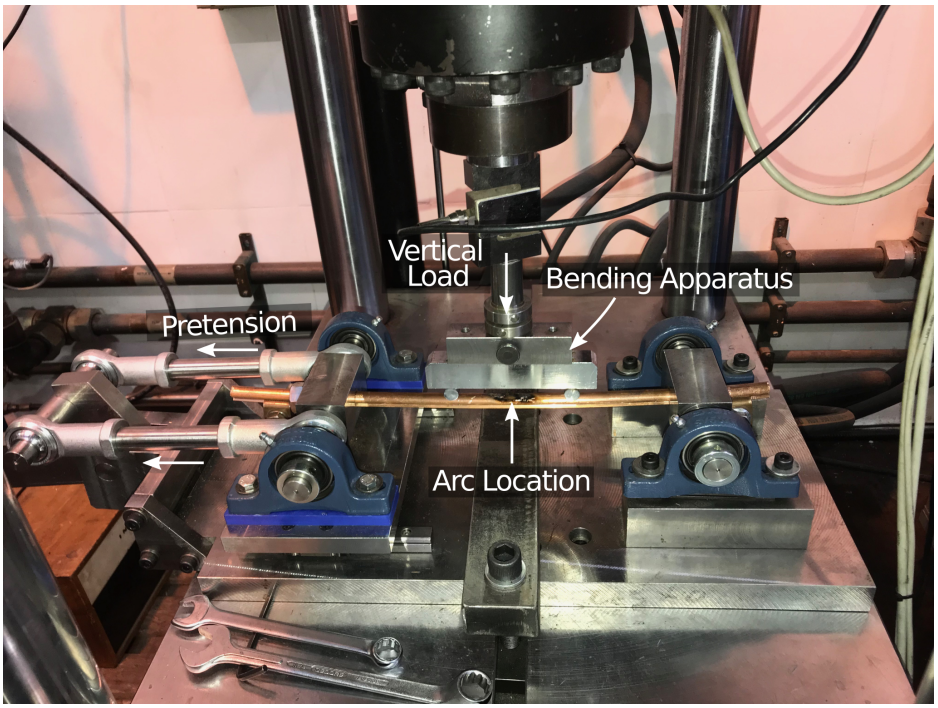


Fig. 6.3 Fatigue testing of arc affected contact wire samples

Loading Conditions

In this study, to assess whether and how the arc damage on the surface affects fatigue behaviours of the contact wire, two sample orientations were concerned.

The first loading condition was normal bending condition which the arc location was subjected to compression stress due to the bending of the contact wire by the pantograph (Fig. 6.4). This is a very common case which occurs due the exerted uplifting force by the pantograph.

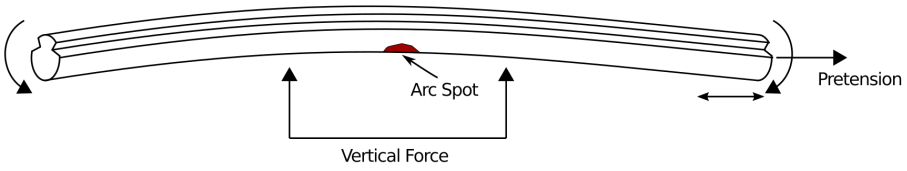


Fig. 6.4 Arc-affected contact wire sample loading with bending

The second loading condition was selected to present a reverse bending situation which often occurs when the contact wire is connected with OLE fittings (claws, clamps or droppers). Particularly, few centimetres before and after of OLE fittings were reported to be highly critical to initiate fatigue cracks from the bottom surface of the contact wire in the literature

[90]. Similarly, some cases were observed in the studies of risk analysis of fatigue crack initiation in the contact wires [21, 111]. In this case, because the OLE fittings have high stiffness and high mass, points before and after the junction claw/OLE fittings are reversely bent and exposed to tension stress due to the reverse bending during the pantograph passage. Therefore, the second loading condition was selected to present tension stress on the bottom surface of the contact wire combined with the arc damage (Fig. 6.5).

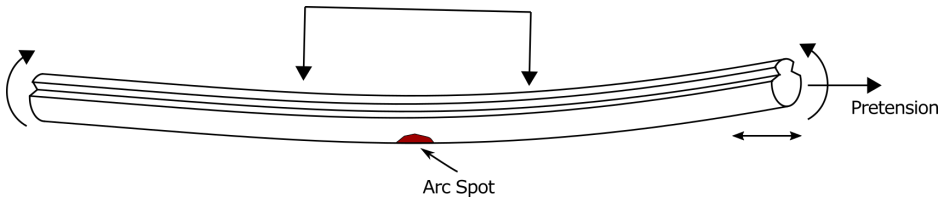


Fig. 6.5 Arc-affected contact wire sample loading with reverse bending

Multiple contact wire samples were prepared for each loading conditions, and the experiments were conducted in a range from highly plastic bending/reverse bending to elastic bending/reverse bending. Together with the fatigue life tests in Chapter 3 all parameters of the experiments can be summarised as in Table 6.1 and Table 6.2.

Table 6.1 Fatigue testing parameters in bending condition

Test Number		Minimum Strain 10^{-3}	Maximum Strain 10^{-3}	Plastic Strain 10^{-3}
Bending (Arc affected)	Bending (No arc)			
TA1 TA2	T1 T2	0.79	2.470	0
TA3 TA4 TA5	T3 T4 T5	0.79	3.027	0.5260
TA6 TA7 TA8	T6 T7 T8	0.79	4.253	1.752
TA9 TA10	T9 T10	0.79	5.553	3.052
TA11 TA12	T11 T12	0.79	6.664	4.163

Table 6.2 Fatigue testing parameters in reverse bending condition

Test Number Reverse Bending (Arc affected)	Min Strain 10^{-3}	Maximum Strain 10^{-3}	Plastic Strain 10^{-3}
TAR1 TAR2 TAR3 TAR4	0.79	2.028	0
TAR5 TAR6 TAR7	0.79	3.027	0.526
TAR8 TAR9 TAR10	0.79	4.253	1.752
TAR11 TAR12	0.79	5.553	3.052
TAR13 TAR14	0.79	6.664	4.163

6.3 Results

6.3.1 Fatigue Results

The first set of experiments with undamaged contact wire was already carried out in Chapter 3. The fatigue tests of arc affected contact wire samples were conducted in the same way using the fatigue apparatus in Section 3.2.4. The results of arc affected contact wires were presented with those of arc-free (undamaged) contact wires in Table 6.3. This helped to compare the results obtained from fatigue experiments of arc-free contact wires and arc-affected contact wires together. From the table, it can be seen that test parameters containing plastic deformation were identical for all three experiments of arc-free bending, arc-affected bending and arc-affected reverse bending. However, the strain parameters with no plastic deformation in arc-affected reverse bending tests (TAR1-2-3-4) were lower than those in arc-free bending and arc-affected bending tests (TA1-2, T1-2). This was intentionally set to keep the fatigue life of the contact wire below 10^7 cycles. Because under reverse bending condition, the fatigue life of arc-affected contact wire was significantly reduced, and it was necessary to perform tests with no plastic deformation at lower maximum strain values. Eventually, the fatigue life curves of three loading conditions were plotted in a close range

without the need for extrapolation. Second-degree exponential curve fitting method was applied to the test results, and the strain-life curve was plotted. Fig. 6.6 shows the fatigue life behaviours of the contact wire from the experiments of arc-free bending, arc-affected bending and arc-affected reverse bending. From the figure, it can be seen that the arc affected contact wire in reverse bending case, where the arc damage was on the tension surface of the contact wire, showed the lowest cycle to fatigue failure. On the other hand, the fatigue life of the samples involving arc damage on the compression surface were almost the similar to fatigue life behaviours of those without arc.

Speaking about the difference in the fatigue life of three different experimental studies, at high strain ($4.23\text{x}10^{-3}$), for the same testing parameters, in reverse bending condition the fatigue life of arc-affected contact wire was half of those in bending and bending with no arc conditions. However, for a lower strain, life can drop dramatically. Considering the strain around $2.7\text{x}10^{-3}$, while the fatigue life of the contact wire in bending condition was around $7\text{x}10^{6}$ cycles, it was only in the order of $2.5\text{x}10^{6}$ cycles when the arc-affected contact wire was loaded with reverse bending. The effect of the arc being located on the tension surface was significant in the crack initiation. Because all the samples in arc-affected reverse bending experiments broke from the arc location, while there were not any arc-related fatigue failures in arc-affected contact wires samples in bending condition. In order to understand the main contribution of the arc damage on the surface of the contact wire to the reduction in fatigue life, a detailed fracture analysis was carried out in the next section.

Table 6.3 Fatigue life results of arc free and arc affected contact wire samples

Test Number			Min Strain 10^{-3}	Max Strain 10^{-3}	Plastic Strain 10^{-3}	Fatigue Life		
Arc-free Bending	Arc-affected Bending	Arc-affected Reverse Bending				Arc-free Bending	Arc-affected Bending	Arc-affected Reverse Bending
-	-	TAR1	0.79	2.028	0	-	-	7804699
-	-	TAR2	0.79	2.028	0	-	-	8044980
-	-	TAR3	0.79	2.028	0	-	-	8169431
-	-	TAR4	0.79	2.028	0	-	-	9665213
T1	TA1	-	0.79	2.470	0	6588432	6879533	-
T2	TA2	-	0.79	2.470	0	7010955	7339806	-
T3	TA3	TAR5	0.79	3.027	0.5260	1286928	1706759	844070
T4	TA4	TAR6	0.79	3.027	0.5260	1424516	1513488	790453
T5	TA5	TAR7	0.79	3.027	0.5260	1650211	1321397	720594
T6	TA6	TAR8				480655	640938	218513
T7	TA7	TAR9	0.79	4.253	1.752	410951	450653	107813
T8	TA8	TAR10				427888	430582	180193
T9	TA9	TAR11	0.79	5.553	3.052	210896	181546	81311
T10	TA10	TAR12				228444	175654	96028
T11	TA11	TAR13	0.79	6.664	4.163	70708	59698	48642
T12	TA12	TAR14				73528	65785	51366

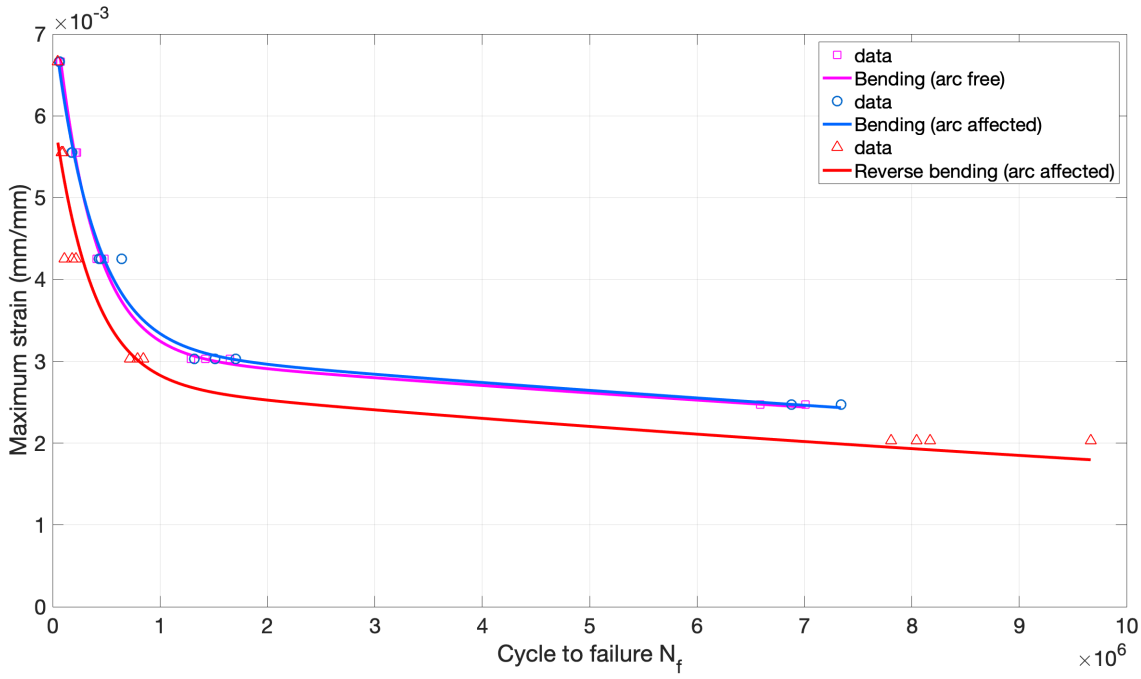
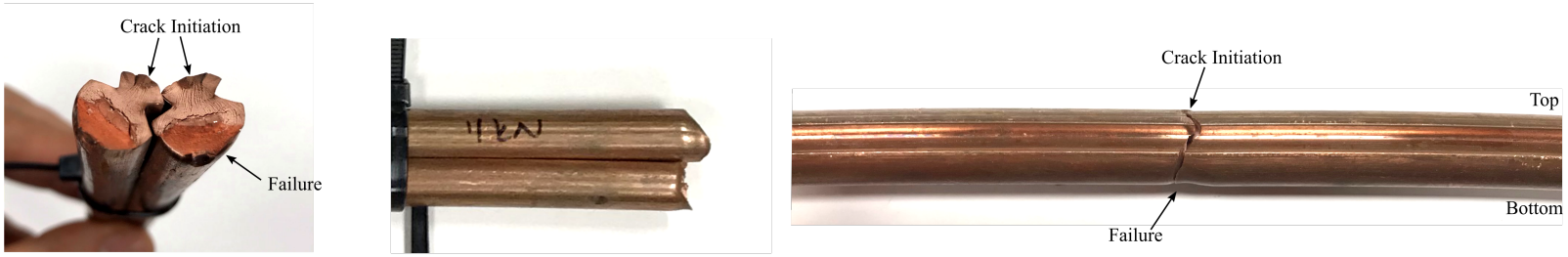


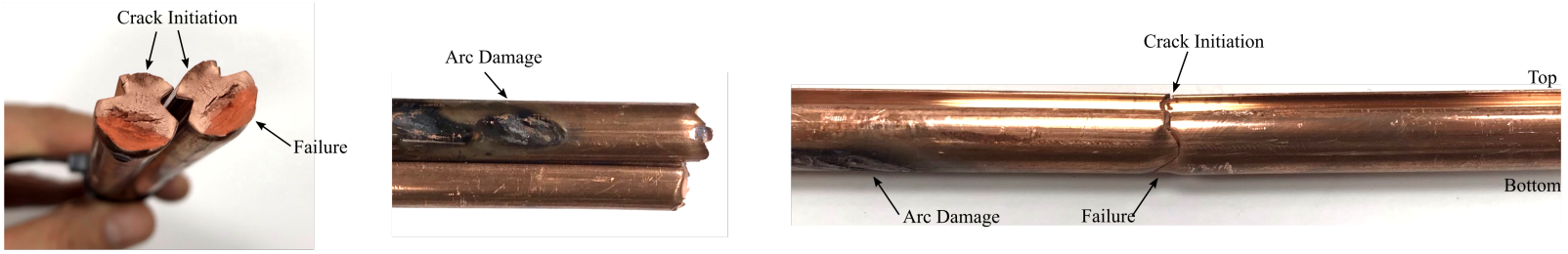
Fig. 6.6 Strain-life curves of the contact wire with arc-free bending, arc-affected bending and arc-affected reverse bending conditions.

6.3.2 Fracture Analysis

Crack initiation, propagation and the failure due to the fatigue loading were seen in the detailed fracture inspection of the tested samples. Fig. 6.7 presents the fracture surface and the crack initiation locations of the samples with three different loading conditions which plastic deformation was predominant. From the results in the figure, it is apparent that the crack started from the top surface of the contact wire for both cases of arc-free and arc affected samples with bending. Since the arc damage was on the compression surface of the wire in Fig. 6.7b, it did not contribute and accelerate the fatigue failure of the contact wire. Therefore, fatigue results from these two cases did not show any significant differences.



(a) Arc-free samples with bending



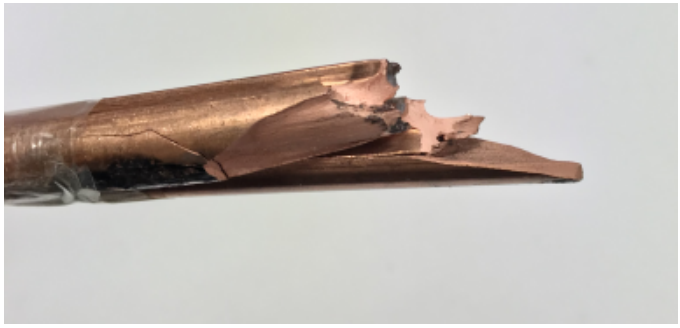
(b) Arc-affected sample with bending



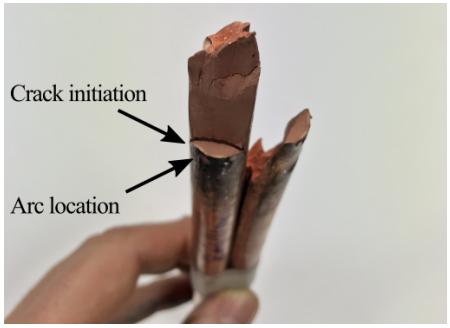
(c) Arc-affected sample with reverse bending

Fig. 6.7 Fracture surface and crack initiation locations of contact wire samples in the fatigue tests loaded with plastic strain

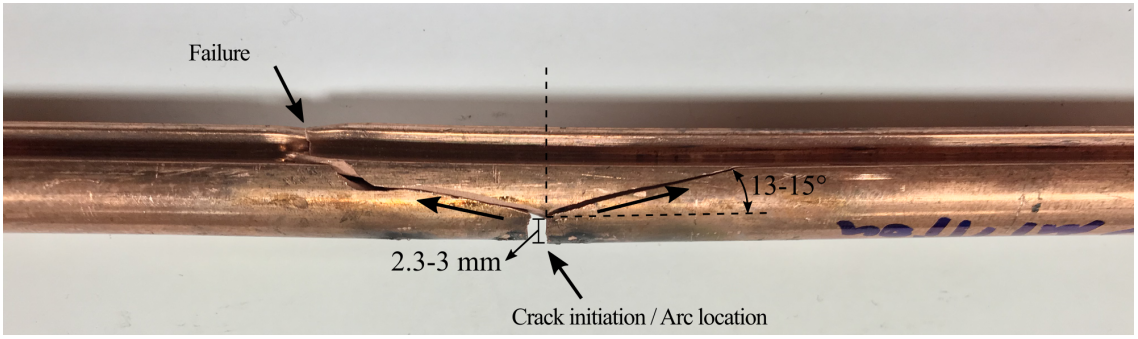
On the other hand, the fatigue life of the arc-affected samples with reverse bending was significantly affected by the arc damage. When the samples were loaded in this configuration, arc damage on the wire surface was exposed to tension stress, all the cracks initiated from here and propagated through the cross-section and resulted in failure. Because the crack initiation was pre-existed, this accelerated the cycle to the failure of the samples with reverse-bending. At high strain, the life of the contact wire was halved since the crack initiation stage was bypassed by the pre-existed arc damage on the surface. It can be said that the proportion of crack initiation in life was close to 50 %. The fatigue life reduced to approximately one in two the total life. In other words, almost 50 % of the total life was spent in initiation for the sample without pre-existed crack. To bypass the crack initiation stage with surface arc damage massively affected the fatigue life of the contact wire.



(a) One half of the sample after the fatigue fracture



(b) The cross section of broken sample



(c) Side view of crack propagation and branching

Fig. 6.8 A typical fatigue fracture after testing the arc-affected contact wire with fully elastic reverse bending condition

Additionally, fracture type and the failure of the arc affected contact wires with reverse bending under elastic strain was a rather interesting outcome. After crack initiated at the arc location, it propagated normal to the surface but then diverted into two directions with an angle. Eventually, one of the crack propagations resulted in a failure, and the fatigue experiment terminated. Measurements from the broken contact wires showed that the normal

distance from the start point of crack branching to the zero surfaces of the contact wire varied between 2.3 and 3 mm and the crack angle was in a range of 13 and 15 degrees. Fig. 6.8 shows a typical fatigue fracture surface and crack propagation direction of an arc exposed sample tested with reverse bending loading condition under elastic strain.

6.4 Discussion

The observed difference of fatigue life of arc exposed contact wires samples with bending and reverse bending loading conditions was significant. The most prominent finding to emerge from the experiments is that all the contact wire samples in reverse bending condition broke from the arc location while no arc-damage-oriented fatigue failure was observed in bending condition. Arc damage on the tension surface of the wire behaved as a pre-existed crack. Therefore, the crack initiation stage was bypassed. Comparing the arc-free and arc-oriented cracks, the proportion of the crack initiation in the total life of the wire was significant. Notably, a strain giving very long life for bending condition resulted in shorter life in reverse bending condition. This can be very significant for determining the design life of the contact wire with the combination of the wear and fatigue life. In reality, the wear life of the contact wire is predominant to its fatigue life; however, the fatigue problem combined with arcing can severely be apparent than its wear life under reverse bending condition. It was shown in Chapter 3 that under the normal bending of the contact wire with arc and without an arc, the fatigue life of the contact wire was around $7x10^6$ cycles and considered safe (Because the wear life is normally less than 50 years.) for in the order of 50 years (based on 150000 pantograph passage in a year [21]). However, for the same strain value, under the reverse bending the fatigue life of the arc-affected contact wire was found in the order of $2.5\ x10^6$ cycles which corresponds to just over 16 years (the one third of fatigue life of normal bending condition) based on the same traffic condition. Therefore, in terms of the effect of the arc damage on the fatigue life of the contact wire, arcs can be even more critical in lower strains.

The arc location in the experiments was representatively selected to be at the bottom surface of the contact wire; however, these results are also valid for the condition which the arc damage is on the top surface of the contact wire.

In this study, the wear between the bottom surface of the contact wire and the pantograph was neglected. It was already found that arcs on the compression surface of the wire do not significantly affect to the fatigue life of the contact wire, however, in the event that bottom surface is a tension side of the wire, arc damages would be worn away due to the sliding wear before it leads to propagating a crack. When considered the strain in the contact wire, it is difficult to estimate whether the arc damage will be worn away due to the sliding contact.

The wear of contact wire is highly depended on the contact force. The more contact force the contact wire is subjected to, the more wear is expected. Therefore, at high strain (high contact force), contact wire wear is likely to be more dominant than arc damage, and vice versa at low strain. However, the bottom of the contact wire is not the only surface exposing arcs. Findings from Chapter 4 showed that arc damage also existed on the top surface of the contact wire due to flashovers. This top surface arcs can be also critical for the fatigue life of the contact wires because they are often subjected to tension stress due to the contact force bending, and there is no sliding interaction on this surface which can result in wear of the wire.

Regarding the fracture analysis of the contact wire, no evidence of crack branching was detected in any experiments with plastic strain. As for elastic strain, a crack branching was only seen in experiments with arc-affected samples under reverse bending condition while there was not in arc-free and arc-affected samples in bending condition. In the reverse bending case, all the cracks initiated at the arc location were split into two. Because the branching was only seen in arc-oriented cracks at low strain (elastic strain), it can be pointed that arc occurrence might have a significant influence on crack propagation behaviours under elastic loadings. When looked at the crack path, the crack was branched after a straight propagation perpendicular to the wire surface. Crack branching is a very complicated phenomenon, and there is a small number of studies in the literature about crack branching, which explained in Section 2.3.4. However, the main reason why a crack branching was seen only in the arc-oriented crack under reverse bending condition can be explained by findings of Ravi-Chandar's study [128] which pointed that crack branching is related to crack propagation speed. According to his explanation, dynamic stress intensity factor changes significantly even for minimal changes in the crack speed. Therefore, the crack does not have to change the speed significantly, and it instead merely has to find a mechanism to break up into two or more cracks and continue to grow at the same speed but with a slightly smaller process zone. The existence of softened layer due to the thermal effect of arcing, found in Chapter 4, which could reduce the hardness of the contact wire up to 50 %, can be influential on the crack propagation speed with parallel to the study done by Mellouli et al. [230] who concluded that the decreases in the hardness of the material lead to increase in the fatigue crack growth rate. Therefore, a possible explanation of crack branching can be that fast-growing straight crack triggered by the softened material property, dissipated the crack growing energy for breaking up into two cracks when it reached to the core material which was not affected by arcs. Furthermore, microstructural investigations in Chapter 4 showed interior voids in the layer affected by the thermal heating. It is challenging to establish substantial evidence between these internal voids and crack branching, but voids might cause

micro-cracks in the material which can lead the straight crack having the high-stress intensity to split into two cracks by meeting micro-cracks.

6.5 Conclusions

Previous studies noted the importance of fatigue in OLE. In reviewing the literature, to the author's knowledge, no data was found on the association between arcing and fatigue in OLE contact wires. The question in this study sought to determine whether the surface damage generated by arcing would behave as a crack initiation point and trigger the fatigue damage. For this purpose, a sequence of process and experimental procedure was applied to test the fatigue life of OLE contact wires after arcing, and the results were compared with those in experiments with arc-free contact wire in Chapter 3. This study emerged that any arc damage on the maximum tension surface of the wire can significantly shorten the fatigue life of the contact wire. Although the fatigue life is considered longer than the wear life in the design stage, under reverse bending with the combination of arcing problem, the fatigue life of the contact wire can be largely shorter than the wear life. Therefore, particularly around the locations where the arcing is likely, the fatigue life of the contact wire should be taken into consideration together with the arcing problem.

These findings contribute in several ways to our understanding of how the arcing problem can affect the service life of OLE contact wires in terms of fatigue problem. Furthermore, the fracture analysis of the broken samples after arcing provided interesting results about behaviours of the crack propagating throughout different mechanical behaviours.

Chapter 7

Conclusions and Future Work

7.1 Conclusions

This PhD study set out to aimed to answer the question of whether arcing is a cause of damage, and then also the potential fatigue mechanism by which it creates that damage and a possible way to mitigate it. To achieve this, existing OLE main lines were analysed for both understanding the fatigue and arcing problem and then a number experiments were conducted for identification of arc damage and its potential effect on fatigue life of the contact wire. Initially, the fatigue of arc-free contact wires was examined. This study identified fatigue behaviours of the contact wire under a pretension by developing a small-scale fatigue testing machine. Contact force data from an existing OLE mainline (Great Western Mainline) was essential to determine the contact force range and potential locations where the repetitive contact force occurred. OLE systems are dynamic, and the contact wire deflects and uplifts; therefore, it was essential to build a model to establish a stress-contact force relationship. The most prominent finding to emerge from this study is that contact wire could reach the elastic limit of the material. When considered the increase in the speed of trains, the stress in the contact line is likely to increase because higher contact forces are expected. The apparatus designed here is useful for fatigue testing of the original form of the contact wire without the need for standard fatigue sample preparing procedure. Findings of this study established reference fatigue results for the copper-silver contact wire.

Subsequently, the visual inspection of contact wire samples extracted from a UK OLE showed severe arc damage on the contact wire. The microstructural investigation urged that significant interior damage existed in the contact wire as well as the surface damage. This study has shown that significant void forms were seen below the contact surface of the contact wire in both the preliminary investigation and the experiments. Also, significant local grain growth was seen in all the test samples in the arc exposed area. A recrystallisation

zone and tempered zone followed this grain growth region from the contact surface to the interior of the material. For the same testing parameters, DC voltage had a more substantial effect on the change in metallurgical and mechanical properties of the contact wire rather than AC voltage. The results of hardness and microstructural examinations also showed that arc damage occurred after only one event and consisted of voids below the contact surface, a significant depth of soft material and zones of larger grains. The higher current caused the softening to spread deeper into the contact wire, but the effect of the increasing number of arcs was not significant.

In terms of mitigation of voids, a range of experiments conducted with oxygen-free copper (OFC) showed that it might be a solution in restricting voids forms which likely to accelerate surface crack initiation mechanism. Findings of this study extended our knowledge that arcs can play an important role in mechanical and metallurgical behaviours of the contact wire. Mainly, together with the investigation of real OLE mainline contact wires, the results generated show that arcs characteristic of flashover to structures can severely damage the contact wire as well as the pantograph arcing.

Results of the identification of arc damage to the contact wire showed that temperature plays a vital role in the metallurgical and mechanical properties of the contact wire during arcing. However, due to the great difficulty of measuring the temperature variation of the arc spot over the time of arcing experiments, another method was necessary to understand temperature distribution in the material. It is also important to mention that the temperature varies in milliseconds, and it is difficult to observe it with experimental techniques. Therefore, the thermal damage process during arcing was modelled with the finite element method. The model was validated with experimental results of real temperature measurements of the location, which was a little away from the arc spot. The results of this investigation showed that although AC and DC generate similar surface temperature, the temperature distribution of the interior of the material is different. In DC, a higher temperature is spread more in-depth into the specimen compared to those in AC. Particularly for materials manufactured by plastic deformation (cold forming, drawing or forging), annealing leads to a decrease in hardness, and it is expected that the crack propagation rate becomes faster. Therefore this study can help to understand the severity of arc damage and the potential depth of the contact wire of which mechanical properties are affected by arcing.

Findings from fatigue test of arc-free contact samples and identification of arc damage to the contact wire indicated a need to understand whether surface damage caused by arcing could accelerate fatigue crack initiation and affect the fatigue life of the contact wire. Both SOLARC machine and OLE fatigue apparatus were used without any configurational difference. In these tests, two-sample orientation was considered, namely; fatigue life of the

arc-affected contact wires under bending and reverse bending conditions by exposing the arc location to tension and compression stress. Initially, findings from the study showed that arc-affected contact wires under reverse bending (tension stress) could lead to accelerate the crack initiation stage and have significantly short fatigue life compare to those tested with bending condition. Secondly, all of the contact wires broke from the arc affected areas under reverse bending loading, however, in the tests in which arcs on the compression surface of the contact wire, the damage from arcs was not involved in the fatigue fracture under the bending condition. The main reason for having short fatigue life of arc-affected contact wires tested with reverse bending is that the crack initiation stage was bypassed due to the pre-existed surface (arc) damage/crack. In particular, a severe reduction in fatigue life was seen in the arc-affected samples tested with reverse bending. For the same loading parameters, the fatigue life of arc-affected contact wire sample under reverse bending was more than half of the that under normal bending. Having short fatigue life can be very significant for determining the design life of the contact wire, because it is normally considered that the wear life is predominant to the fatigue life. However, this study showed that the reverse bending issue combined with arcs can be more critical than the wear life. Additionally, very interesting crack branching was observed in tests with arc occurrence on tension surface at low strain loading (fully elastic) while none was seen in other tests and loading conditions. It is a very complicated phenomenon and difficult to explain it with either fast-growing straight crack triggered by softened material property or internal voids that might cause micro-cracks in the material.

This thesis has provided a more in-depth insight into both the arcing and fatigue problem in overhead line electrification. Findings from microstructural modification of the contact wire after arc exposure shed new light on the importance of arcs in OLE. The insights gained from using OFC material in this study may be assistance in restricting internal defects (voids) after arcing. Oxygen-free material is rather costly compared to standard copper-silver contact wires. However, it can be used in specific locations in which the arcs are likely to occur and damage to the contact wire. The methods developed for determining fatigue life of the copper-silver contact wire can be applied to other types of contact wires elsewhere in the world.

Overall, the fatigue of the contact wire combined with the arc problem makes several contributions to the current literature. Firstly, the fatigue test of the small-length of contact wires under a pretension is novel in this study. This approach is also useful for fatigue testing of contact wires with arc damage or any surface defects as well as for defect-free contact wires. Secondly, this study showed that the potential risk of fatigue of the contact wires combined with arcs could be very high. This research successfully identifies the potential

consequences of arcs to the contact wire mechanical and metallurgical properties and predicts the fatigue life of the contact wire before and after the arc exposure. Strain-fatigue life curves developed from the experimental results can be used for extrapolating a trend for further high cycle fatigue problems of the contact wire.

This study did not conduct experiments for the contact wire system (containing all the structures of OLE). It tested only the contact wire under sinusoidal loading with constant conditions throughout each test. The real system will have a number of different dynamic effects and changes in the temperature. Besides, it was limited by the absence of the sliding interaction between the contact wire and the collector strip. However, notwithstanding the limitations, the findings of this research are still useful for answering the question of whether arcs could be a cause of damage and potential for reduction in the fatigue life of the contact wire.

7.2 Future Work

This study consists of a combined work of a real-world problem and academic research. Future work for extending our knowledge about the mechanism damaging the contact wire by arcs and its mitigation with different material content is essential. However, the application of experimental findings of this research to the industry is also important. Therefore, the future studies of this research will be explained under the titles of academic and application next steps.

7.2.1 Academic Next Steps

Findings from arc experiments of copper-silver contact wire urged this study to investigate the cause of void forms in the material after arcing. However, the contact wire manufactured with OFC has not been widely commercialised, and the experiments for mitigation of void formation was not conducted with contact wire form of OFC. Further experiments and investigations are needed with oxygen-free contact wire to determine whether the contact wire form of oxygen-free material shows better resistance to the void occurrence and reduction in mechanical properties.

As for the fatigue fracture of arc-affected contact wires, crack branching was a complicated phenomenon to explain with current findings of this research. It was not clear that the reason for the branching was either the change in crack propagation speed or pre-existed microcracks in the vicinity of arc damaged region. In order to clarify the reason of crack branching, additional tests are necessary with a combination of crack propagation speed mea-

surements. Besides, microcrack occurrence can be analysed after arcing. Non-destructive tests can be applied to the contact wire after arcing, such as liquid penetrant inspection. This method will help to indicate the microcracks formed in the material. Also, it is a non-destructive test; therefore, the fatigue tests still can be applied to the same samples afterwards.

In the event that voids play an essential role in the crack propagation direction, this study can be supported by finite element or boundary element models. It has been already known that FE and BE solutions are capable of solving the dynamic stress intensity problems. Void forms combined with dynamic stress intensity can help to develop an in-depth analysis of crack behaviours in arc-affected contact wire materials.

7.2.2 Application Next Steps

The application of findings of this research to the real world is important as well as the theoretical and academic findings. Prior to suggesting a solution for more reliable OLE systems, several steps are necessary to be completed.

The work done about the identification of arc damage and its mitigation with experiments can be transferred to a test track area. In this test track, particular attention can be paid to repetitive arc locations such as neutral sections, section insulators or OLE fittings. A specific length of contact wire can be replaced by oxygen-free contact wire, and arc damage in the contact wire and its mechanical and metallurgical properties can be compared with those of copper-silver contact wire under the same traffic conditions.

On the subject of fatigue life of the contact wires, the locations subjected to repetitively high contact forces were already determined in this study and contact force, and stress in the contact wire conversion was completed a simplified FE model. However, it was difficult to determine the exact location of the pantograph from the inspection data used in the study, because a span length was relatively short considering the length of the mainline. Therefore, the locations where the maximum contact force was selected to the point where the maximum moment affected a span-length of the contact wire. In reality, a real-time contact force or vertical displacement of the contact wire can be used to determine the stress in the contact wire. This real-time stress and displacement monitoring of the contact wire can be done by a device developed in NeTIRail project [231]. This device is an accelerometer sensor which is clipped in the contact wire side grooves. Photovoltaic cells placed on the upper surface provide energy to the sensor. These sensors are capable of real-time monitoring of the contact force, and this can be converted into stress in the line. Thanks to this, potential locations which are likely to have high repetitive stress can be monitored. The real-world application of contact wire stress monitoring will help to conduct contact-force and stress

conversion accurately and determine whether the contact wire is subjected to extensive stress which can result in fatigue failure in the long term.

References

[1] F. Birol, "The Future of Rail Franchising," tech. rep., International Energy Agency, France, 2019.

[2] N. Regis, M. T. E. Heinrich, and F. Kelch, "Electrification of the Transport System: Studies and Reports," *Renewable and Sustainable Energy Reviews*, vol. 10, no. 6, pp. 1–49, 2017.

[3] S. V. GmbH, "New Study: Railway Electrification Continues to Grow in 2018," Tech. Rep. April, SCI Verkehr GmbH, Germany, 2018.

[4] Mersen, "Current Collection Technical Guide," tech. rep., Amiens-France, 2016.

[5] N. Rail, "Challange-Statements for Smarter Electrification," tech. rep., London, 2019.

[6] ORR, "Rail infrastructure, assets and environmental: Quality and Methodology Report," Tech. Rep. October, London, 2018.

[7] N. Rail, "Network RUS: Electrification Strategy (Draft for Consultation)," tech. rep., 2009.

[8] L. Butcher, "Rail Electrification - Briefing Paper," Tech. Rep. July, 2017.

[9] S. Frey, *Railway Electrification Systems and Engineering*. White Word Publications, first edit ed., 2012.

[10] F. Kiessling, P. Rainer, A. Schmieder, and S. E, *Contact Lines for Electric Railways*. Siemens, second edi ed., 2009.

[11] G. Zhen, Y. S. Kim, S. W. Hong, H. C. Li, J. M. Koo, C. S. Seok, K. W. Lee, and S. Y. Kwon, "Fatigue life estimation of cold drawn contact wire," *International Journal of Precision Engineering and Manufacturing*, vol. 15, no. 11, pp. 2291–2299, 2014.

[12] P. Grey, *A History of Travel in 50 Vehicles*. Tilbury House Publishers, 2016.

[13] G. Keenor, "Railway Eleftrification- Power Engineering Handbook: Introduction to Overhead Line Electrification," Tech. Rep. August, Scott Wilson Railways, 2008.

[14] Furrer+Frey, "Series 1 The Great Western Railway Electrification Project Technical Report," tech. rep., Bern, 2014.

[15] G. Keenor, "Overhead Line Electrification for Railways," *Book*, p. 64, 2018.

[16] Y. H. Cho, K. Lee, Y. Park, B. Kang, and K. N. Kim, "Influence of contact wire pre-sag on the dynamics of pantographrailway catenary," *International Journal of Mechanical Sciences*, vol. 52, no. 11, pp. 1471–1490, 2010.

[17] BSI, "BS EN 50318 : Railway applications - Current collection systems - Validation of simulation of the dynamic interaction between pantograph and overhead contact line," vol. 3, p. 20, 2012.

[18] G. Mei, W. Zhang, H. Zhao, and L. Zhang, "A hybrid method to simulate the interaction of pantograph and catenary on overlap span," *Vehicle System Dynamics*, vol. 44, no. SUPPL. 1, pp. 571–580, 2006.

[19] N. Zhou and W. Zhang, "Investigation on dynamic performance and parameter optimization design of pantograph and catenary system," *Finite Elements in Analysis and Design*, vol. 47, no. 3, pp. 288–295, 2011.

[20] BSI, "BS EN 50149: Railway applications — Fixed installations — Electric traction — Copper and copper alloy grooved contact wires," Tech. Rep. October, 2012.

[21] Nguyen-Tajan, Mai S H, Massat J P, A. S. (, Banting J, J. P. Bianchi, and Maitournam H, "Fatigue crack initiation risk analysis and crack propagation modelling in the catenary contact wire of high speed lines," (Sydney, Australia), World Congress on Railway Research (WCRR) 2013,, 2013.

[22] A. Vinogradov, M. Maruyama, Y. Kaneko, and S. Hashimoto, "Effect of dislocation hardening on monotonic and cyclic strength of severely deformed copper," *Philosophical Magazine*, vol. 92, no. 6, pp. 666–689, 2012.

[23] P. Coddet, C. Verdy, C. Coddet, and F. Debray, "On the mechanical and electrical properties of copper-silver and copper-silver-zirconium alloys deposits manufactured by cold spray," *Materials Science and Engineering A*, vol. 662, pp. 72–79, 2016.

[24] P. R. Subramanian and J. H. Perepezko, "The ag-cu (silver-copper) system," *Journal of Phase Equilibria*, vol. 14, pp. 62–75, feb 1993.

[25] M. Hansen, K. Anderko, and H. W. Salzberg, *Constitution of Binary Alloys*, vol. 105. New York, Toronto, London: McGraw-Hill Book Company, second ed., 1958.

[26] G. Zhang, *Wear Experiments on Railway Overhead Line and Pantographs*. Msc thesis, The University of Sheffield, 2010.

[27] L. Hadron and C. Project, "Residual Resistivity Ratio (RRR) Measurements of LHC Superconducting NbTi Cable Strands .," Tech. Rep. September 2005, European Laboratory for Particle Physics, European Organization for Nuclear Research, CERN,Geneva-Switzerland, 2006.

[28] P. Li, L. Ye, J. Jiang, and T. Shen, "RRR and thermal conductivity of Ag and Ag0 . 2wt % Mg alloy in Ag / Bi-2212 wires," in *20th Cryogenic Engineering Conference and International Cryogenic Materials Conference*, (Tucson, AZ), pp. 1–7, IOP Conf.Ser.Mater.Sci.Eng., 2015.

[29] C. H. Yin, Z. H. Gan, S. H. Wang, D. L. Liu, and L. M. Qiu, "The Measurement of RRR and Resistance for Aluminum Alloy Based on a Cryocooler," in *Cryocoolers 19*, (Boulder), pp. 605–612, International Cryocooler Conference, 2016.

[30] A. International, "Standard Specification for Bronze Trolley Wire 1," Tech. Rep. Reapproved, 2017.

[31] T. Chandler and J. Corrado, "Copper Trolley Wire And A Method Of Manufacturing Copper Trolley Wire," 2000.

[32] J. Shea, *Microstructural characterization of materials [Book Reveiw]*, vol. 16. 2005.

[33] J. Smith, William F.; Hashemi, *Foundations of material science and engineering(4th edition)*. 2001.

[34] D. Zipperian, *Metallographic Handbook*, vol. 1. Tucson, Arizona USA: PACE Technologies, 2011.

[35] C. S. Obayi, R. Tolouei, A. Mostavan, C. Paternoster, S. Turgeon, B. A. Okorie, D. O. Obikwelu, and D. Mantovani, "Effect of grain sizes on mechanical properties and biodegradation behavior of pure iron for cardiovascular stent application," *Biomatter*, vol. 6, no. 1, p. e959874, 2016.

[36] E. O. Hall, "The deformation and ageing of mild steel: II Characteristics of the Lüders deformation," *Proceedings of the Physical Society. Section B*, vol. 64, no. 9, pp. 742–747, 1951.

[37] S. Lefebvre, B. Devincre, and T. Hoc, "Simulation of the Hall-Petch effect in ultra-fine grained copper," *Materials Science and Engineering A*, vol. 400-401, no. 1-2 SUPPL., pp. 150–153, 2005.

[38] X. H. Dong, X. T. Hong, F. Chen, B. R. Sang, W. Yu, and X. P. Zhang, "Effects of specimen and grain sizes on compression strength of annealed wrought copper alloy at room temperature," *Materials and Design*, vol. 64, pp. 400–406, 2014.

[39] T. A. Kals and R. Eckstein, "Miniaturization in sheet metal working," *Journal of Materials Processing Technology*, vol. 103, no. 1, pp. 95–101, 2000.

[40] G. E. Totten and D. S. Mackenzie, "Annealing and Recrystallization of Coppers," in *ASM Handbook,* (G. E. Totten and D. S. Mackenzie, eds.), vol. 4E, ch. Heat Treat, pp. 325–334, 2018.

[41] G. E. Totten and D. S. Mackenzie, "Principles of Heat Treating of Nonferrous Alloys," in *ASM Handbook Heat Treating of Nonferrous Alloys*, vol. 4, pp. 3–31, ASM International, 2018.

[42] J. Yu, G. Wang, and Y. Rong, "Experimental Study on the Surface Integrity and Chip Formation in the Micro Cutting Process," *Procedia Manufacturing*, vol. 1, no. January 2016, pp. 655–662, 2015.

[43] G. Reiss, J. Vancea, and H. Hoffmann, "Grain-Boundary Resistance in Polycrystalline Metals," *Physical Review Letters*, vol. 56, pp. 2100–2103, may 1986.

[44] A. Ma, C. Zhu, J. Chen, J. Jiang, D. Song, S. Ni, and Q. He, "Grain Refinement and High-Performance of Equal-Channel Angular Pressed Cu-Mg Alloy for Electrical Contact Wire," *Metals*, vol. 4, no. 4, pp. 586–596, 2014.

[45] Beuhler, *A Guide to Materials Preparation and Analysis*. Buehler, second edi ed., 2013.

[46] "NEK EN 50206-1:2010 Railway applications - Rolling stock - Pantographs : Characteristics and tests - Part 1 : Pantographs for main line vehicles," 2010.

[47] "BSI Standards Publication Railway applications — Fixed installations — Electric traction overhead contact lines BS EN 50119," tech. rep., The British Standards Institution, 2009.

[48] D. Hai He, R. R. Manory, and N. Grady, "Wear of railway contact wires against current collector materials," *Wear*, vol. 215, no. 1-2, pp. 146–155, 1998.

[49] A.-D. Y. Riyadh A., Al-samara.i, Haftirman., Ahmad Khairel Rafezi., "Effect of Load and Sliding Speed on Wear and Friction of," *International Journal of Scientific and Research Publications*, vol. 2, no. 3, pp. 3–6, 2012.

[50] R. G. Bayer, *Mechanical Wear Fundamentals and Testing*. New York-Basel: Marcel Dekker Inc, second edi ed., 2004.

[51] I. Hutchings and P. Shipway, *Tribology: Friction and wear of engineering materials: Second Edition*. second ed., 2017.

[52] J. F. Archard, "Contact and rubbing of flat surfaces," *Journal of Applied Physics*, vol. 24, no. 8, pp. 981–988, 1953.

[53] G. Straffelini, *Friction and Wear: Methodologies for Design and Control*. 2015.

[54] G. Bucca and A. Collina, "A procedure for the wear prediction of collector strip and contact wire in pantograph-catenary system," *Wear*, 2009.

[55] A. Bouchoucha, S. Chekroud, and D. Paulmier, "Influence of the electrical sliding speed on friction and wear processes in an electrical contact copper-stainless steel," *Applied Surface Science*, vol. 223, no. 4, pp. 330–342, 2004.

[56] T. Ding, G.-X. Chen, Y.-M. Li, Q.-D. He, and W.-J. Xuan, "Friction and Wear Behavior of Pantograph Strips Sliding Against Copper Contact Wire with Electric Current," *AASRI Procedia*, vol. 2, pp. 288–292, 2012.

[57] H. Zhang, L. Sun, Y. Zhang, and B. Shangguan, "The Study of Arc Rate, Friction, and Wear Performance of C/C Composites in Pantograph–Catenary System," *Tribology Transactions*, vol. 57, no. 6, pp. 1157–1163, 2014.

[58] C.-f. Ocoleanu, I. Popa, G. Manolea, and A.-i. Dolan, "Temperature investigation in contact pantograph - AC contact line," *International Journal Of Circuits, Systems And Signal Processing*, vol. 3, no. 3, pp. 154–163, 2009.

[59] H. J. Yang, G. X. Chen, G. Q. Gao, G. N. Wu, and W. H. Zhang, "Experimental research on the friction and wear properties of a contact strip of a pantograph-catenary system at the sliding speed of 350km/h with electric current," *Wear*, vol. 332-333, pp. 949–955, 2015.

[60] N. Zhou, W.-h. Zhang, and R.-p. Li, "Dynamic performance of a pantograph-catenary system with the consideration of the appearance characteristics of contact surfaces," *Journal of Zhejiang University SCIENCE A*, vol. 12, no. 12, pp. 913–920, 2011.

[61] S. NAGASAKA and M. ABOSHI, "Measurement and Estimation of Contact Wire Unevenness," *Quarterly Report of RTRI*, vol. 45, no. 2, pp. 86–91, 2005.

[62] A. Collina, F. Fossati, M. Papi, and F. Resta, "Impact of overhead line irregularity on current collection and diagnostics based on the measurement of pantograph dynamics," *Proceedings of the Institution of Mechanical Engineers, Part F: Journal of Rail and Rapid Transit*, vol. 221, no. 4, pp. 547–559, 2007.

[63] M. Aboshi, I. Nakai, and S. Makino, "Research for Contact Loss Reduction Method by Damping Catenary Vibration," *IEEJ Transactions on Industry Applications*, vol. 117, no. 9, pp. 1154–1161, 2011.

[64] O. V. Van, J. P. Massat, C. Laurent, and E. Balmes, "Introduction of variability into pantograph-catenary dynamic simulations," *Vehicle System Dynamics*, vol. 52, no. 10, pp. 1254–1269, 2014.

[65] W. Zhang, G. Mei, X. Wu, and Z. Shen, "Hybrid Simulation of Dynamics for the Pantograph-Catenary System," *Vehicle System Dynamics*, vol. 38, no. 6, pp. 393–414, 2003.

[66] R. H. Huan, G. F. Pan, and W. Q. Zhu, "Dynamics of pantograph-catenary system considering local singularities of contact wire with critical wavelengths," *Lecture Notes in Electrical Engineering*, vol. 147 LNEE, no. VOL. 1, pp. 319–333, 2012.

[67] S. Suresh, *Fatigue of Materials*. Cambridge: Cambridge University Press, 1998.

[68] C. Bathias and A. Pineau, "Fatigue of Materials and Structures: Fundamentals," *Fatigue of Materials and Structures: Fundamentals*, no. January 2010, 2013.

[69] A. Wöhler, "Versuche liber die Festigkeit der Eisenbahnwagenachsen. Zeitschrift fur Bauwesen," *Zeitschrift fur Bauwesen*, 1860.

[70] A. Wöhler, "Bericht über die Versuche, welche auf der Königl. Niederschlesisch-Märkischen Eisenbahn mit Apparaten zum Messen der Biegung und Verdrehung von Eisenbahnwagen-Achsen während der Fahrt angestellt wurden," *Zeitschrift für Bauwesen*, vol. 8, no. 1858, pp. 641–652, 1858.

[71] A. Wöhler, "Über die Versuche zur Ermittlung der Festigkeit von Achsen, welche in den Werkstätten der Niederschlesisch-Märkischen Eisenbahn zu Frankfurt adO angestellt sind," *Zeitschrift für Bauwesen*, vol. 13, pp. 233–258, 1863.

[72] A. Wöhler, *Über die festigkeitsversuche mit eisen und stahl*. Ernst \& Korn, 1870.

[73] G. SAATÇI and N. TAHRALI, "Birikimli hasar teorileri ve hareket iletim elemanina uygulanmasi," *Havacilik ve Uzay Teknolojileri Dergisi*, vol. 1, no. 2, pp. 21–30, 2003.

[74] J. A. Ewing and J. C. W. Humfrey, "The Fracture of Metals under Repeated Alternations of Stress," *Philosophical Transactions of the Royal Society A: Mathematical, Physical and Engineering Sciences*, vol. 200, pp. 241–250, jan 1903.

[75] L. Spangenberg, *Über das verhalten der metalle bei wiederholten anstrengungen, etc.* Ernst \& Korn, 1875.

[76] W. Kloth and T. Stroppel, "Kriftel, Beanspruchungen und Sicherheiten in den Landmaschinen," *Z-VDI g0*, pp. 85–92, 1936.

[77] W. Callister, *Materials science and engineering: An introduction (2nd edition)*, vol. 12. 1991.

[78] V. I. Shabalin, "On the Discontinuity in Fatigue Curves of Duralumin," in *Soviet Physics Doklady*, vol. 3, p. 1022, 1958.

[79] L. Pook, *Why Metal Fatigue Matters*. Springer, 2007.

[80] G. Z. Libertiny, "Short-life fatigue under combined stresses," *The Journal of Strain Analysis for Engineering Design*, vol. 2, no. 1, pp. 91–95, 1967.

[81] O. H. Basquin, "An energy based approach to the simulation of fatigue crack initiation in metal forming tools," in *Proc. ASTM*, vol. 10, pp. 625–630, 1910.

[82] S. S. Manson, *Behavior of materials under conditions of thermal stress*, vol. 2933. National Advisory Committee for Aeronautics, 1953.

[83] L. F. Coffin, "The Problem of Thermal Stress Fatigue in Austenitic Steels at Elevated Temperatures," *Symposium on Effect of Cyclic Heating and Stressing on Metals at Elevated Temperatures*, pp. 31–31–22, 1954.

[84] F. Campbell, *Fatigue and Fracture: Understanding the Basics*, vol. 53. 2012.

[85] R. G. Sell, G. E. Prince, and D. Twine, "an Experimental Study of the Overhead Contact," *Proceedings of the Institution of Mechanical Engineers*, vol. 179, no. 1, pp. 765–781, 1964.

[86] T. Wu, "Study of current collection from catenary-pantograph at high speed by simulation," *The Journal of China Railway Society*, pp. 55–61, 1996.

[87] M. K, "Periodical dynamic stabilities of a catenary pantograph system," tech. rep., Quarterly Report of RTRI 35 112-117, 1994.

[88] T. X. Wu and M. J. Brennan, "Analytical Study of Pantograph-Catenary System Dynamics," 1997.

[89] Y. Kim, K. Lee, Y. H. Cho, Z. Guo, J. M. Koo, and C. S. Seok, "Fatigue safety evaluation of newly developed contact wire for eco-friendly high speed electric railway system considering wear," *International Journal of Precision Engineering and Manufacturing - Green Technology*, vol. 3, no. 4, pp. 353–358, 2016.

[90] J. Bianchi, E. Balmes, and M.-L. Nguyen-Tajan, "Dynamic stress prediction in catenary wires for fatigue analysis," *The Dynamics of Vehicles on Roads and Tracks - Proceedings of the 24th Symposium of the International Association for Vehicle System Dynamics, IAVSD 2015*, no. October, 2016.

[91] A. Sugahara, C. Yamashita, and T. Usuki, "Applicability of Rain Flow Method to Fatigue Life Span Estimation of Overhead Contact Wire," *Quarterly Report of RTRI*, vol. 51, no. 4, pp. 176–181, 2010.

[92] M. N. Mai, S.H., "Simulation of Fatigue Crack Growth of a Contact Wire," *Proceedings of the Eleventh International Conference on Computational Structures Technology,*, no. 128, 2012.

[93] G. Zhen, Y. Kim, L. Haochuang, J. M. Koo, C. S. Seok, K. Lee, and S. Y. Kwon, "Bending fatigue life evaluation of Cu-Mg alloy contact wire," *International Journal of Precision Engineering and Manufacturing*, vol. 15, no. 7, pp. 1331–1335, 2014.

[94] C. Yamashita and A. Sugahara, "Influence of Mean Stress on Contact Wire Fatigue," *Quarterly Report of RTRI*, vol. 47, no. 1, pp. 46–51, 2006.

[95] S. H. Mai and M. L. Nguyen-tajan, "Prediction of fatigue crack growth of the contact wire in the railway catenary using XFEM simulation," no. Wccm Xi, p. 2014, 2014.

[96] P. Hu, J. Liang, and W. Fan, "Dynamic fatigue reliability of contact wires based on dynamic simulation of high-speed pantograph-catenary," vol. 020152, no. May, p. 020152, 2017.

[97] A. Beagles, D. Fletcher, M. Peffers, P. Mak, and C. Lowe, "Validation of a new model for railway overhead line dynamics," vol. 169, no. TR5, pp. 339–349, 2016.

[98] Y. Song, H. Ouyang, Z. Liu, G. Mei, H. Wang, and X. Lu, "Active control of contact force for high-speed railway pantograph-catenary based on multi-body pantograph model," *Mechanism and Machine Theory*, vol. 115, pp. 35–59, 2017.

[99] K. Smith, T. H. Topper, and P. Watson, "A stress-strain function for the fatigue of metals(Stress-strain function for metal fatigue including mean stress effect)," *Journal of materials*, vol. 5, no. January 1970, pp. 767–778, 1970.

[100] H. E. Boyer, "Atlas of Fatigue Curves," in *ASTM International-*, ch. Fatigue Te, p. 518, 1986.

[101] ASTM, "E466- Standard Practice for Conducting Force Controlled Constant Amplitude Axial Fatigue Tests of Metallic Materials," tech. rep., ASTM International.

[102] ASTM, "Standard Practice for Presentation of Constant Amplitude Fatigue Test Results for," *Current*, vol. 90, no. Reapproved, pp. 1–6, 2004.

[103] ASTM, "Standard Test Method for Strain-Controlled Fatigue Testing," *E606/E606M-12*, vol. 96, no. 2004, pp. 1–16, 2004.

[104] L.-c. F. Testing, "Standard Practice for Statistical Analysis of Linear or Linearized Stress-Life (," *Statistical Analysis of Fatigue Data*, vol. 10, no. Reapproved 2015, pp. 129–129–9, 2009.

[105] ASTM, "Standard practice for verification of testing frame and specimen alignment under tensile and compressive axial force application.," *E1012 - 14*, vol. i, pp. 1–18, 2013.

[106] E1049, "Standard practices for cycle counting in fatigue analysis," *ASTM Standard*, vol. 85, no. Reapproved 2017, pp. 1–10, 2017.

[107] E1283, "Standard Terminology Relating to Fatigue and Fracture Testing," *ASTM International*, vol. 03, no. Discontinued, pp. 1–22, 1998.

[108] *Fatigue*. Ohio, USA: International, ASM, 2008.

[109] T. G. Labo, R. A. Tory, and O. F. The, "Repeated-stress (fatigue) testing machines used in the materials," *University of Illinois Bulletin*, vol. XXXI, no. 30, 1934.

[110] Y. Kim, K. Lee, H. Li, C.-S. Seok, J.-M. Koo, S.-Y. Kwon, and Y. H. Cho, "Fatigue life prediction method for contact wire using maximum local stress," *Journal of Mechanical Science and Technology*, vol. 29, no. 1, pp. 67–70, 2015.

[111] J. P. Massat, T. M. L. Nguyen-Tajan, H. Maitournam, E. Balmès, A. Bobillot, and J.-P. Massat, "Fatigue analysis of catenary contact wires for high speed trains," in *9th Word Congress on Railway Research WCRR*, (Lille,France), 2011.

[112] A. Sugahara, C. Yamashita, T. Usuki, and T. Mitsumoji, "Improvement of Anti-fatigue Property of Contact Wire by Modifying Cross-section Shape," *Quarterly Report of RTRI*, vol. 54, no. 1, pp. 30—-38, 2013.

[113] R. Stainton, "Network Rail Safety Bulletin Arthur Flury Single Rod Neutral Section Installations – Risk of uncontrolled release of Contact Wire tension, Technical Report IGS 301," tech. rep., London, 2013.

[114] N. E. Dowling, C. A. Calhoun, and A. Arcari, "Mean stress effects in stress-life fatigue and the Walker equation," *Fatigue and Fracture of Engineering Materials and Structures*, vol. 32, no. 3, pp. 163–179, 2009.

[115] M. Janssen, J. Zuidema, and R. Wanhill, *Fracture mechanics*. Spon Press, second edi ed., 2002.

[116] T. Anderson, *Fracture Mechanics*. CRC Press, third edit ed., mar 2017.

[117] G. R. Irwin, J. M. Kraft, P. C. Paris, and A. A. Wells, "Basic Aspects of Crack Growth and Fracture," *Naval Research Labaratory*, pp. 1–74, 1967.

[118] G. R. Irwin, "Fracture mode transition for a crack traversing a plate," *Journal of Fluids Engineering, Transactions of the ASME*, vol. 82, no. 2, pp. 417–423, 1960.

[119] E. W. BROWN, "Review of developments in plane strain fracture toughness testing," 1970.

[120] C. Feddersen, "Evaluation and Prediction of the Residual Strength of Center Cracked Tension Panels," *ASTM Special Technical Publication*, pp. 50–78, 1971.

[121] Dr.ir. P.J.G. Schreurs, *Fracture Mechanics*. PhD thesis, Eindhoven University of Technology Department of Mechanical Engineering, 2004.

[122] W. F. Stuhrke, J. L. Carpenter, N. Moya, and G. Mandel, "Fracture toughness testing data: A technology survey and bibliography," Tech. Rep. January 1975, NASA, Orlando, Florida, 1975.

[123] E399, "Standard Test Method for Linear-Elastic Plane-Strain Fracture Toughness K Ic of," *ASTM Standards*, pp. 1–35, 2010.

[124] E1820-18ae1, "Standard Test Method for Measurement of Fracture Toughness," *ASTM Standards*, pp. E 1820 – 01, 2019.

[125] X. K. Zhu and J. A. Joyce, "Review of fracture toughness (G, K, J, CTOD, CTOA) testing and standardization," *Engineering Fracture Mechanics*, vol. 85, pp. 1–46, 2012.

[126] A. Kobayashi and B. Wade, "Fracture Dynamics of Homolite-100," in *Deformation and Fracture of High Polymers*, pp. 487–500, Boston, MA: Springer, 1973.

[127] E. H. . Yoffe, "LXXV. The moving griffith crack," *The London, Edinburgh, and Dublin Philosophical Magazine and Journal of Science*, vol. 42, no. 330, pp. 739–750, 1951.

[128] K. Ravi-Chandar, *Physical Aspects of Dynamic Fracture*. 2004.

[129] D. Hull, "The effect of mixed mode I / III on crack evolution in brittle solids," *International Journal of Fracture*, vol. 70, pp. 59–79, 1995.

[130] F. Erdogan and G. C. Sih, "On the Crack Extension in Plates Under Plane Loading and Transverse Shear," vol. 9, 1963.

[131] M. Ramulu and A. Kobayashi, "Dynamic crack curving—A photoelastic evaluation," *Experimental Mechanics*, vol. 23, no. 1, pp. 1–9, 1983.

[132] R. Ritchie, "Fatigue of Brittle Materials," in *Comprehensive Structural Integrity*, pp. 359–388, Elsevier, 2003.

[133] P. Paris and F. Erdogan, "A critical analysis of crack propagation laws," *Journal of Basic Engineering*, pp. 528–534.

[134] S. Midya, D. Bormann, T. Schütte, and R. Thottappillil, "DC component from pantograph arcing in AC traction system-influencing parameters, impact, and mitigation techniques," *IEEE Transactions on Electromagnetic Compatibility*, vol. 53, no. 1, pp. 18–27, 2011.

[135] J. J. Shea and X. Zhou, "Contact material and arc current effect on post-current zero contact surface temperature," *IEEE Transactions on Components and Packaging Technologies*, vol. 29, no. 2, pp. 286–293, 2006.

[136] J. Poza and J. M. Canales, "Mayr's Equation-Based Model for Pantograph Arc of High-Speed Railway Traction System," *IEEE Transactions on Power Delivery*, vol. 25, no. 2, pp. 586–588, 2010.

[137] Z. Yang, Y. Zhang, F. Zhao, and B. Shangguan, "Dynamic variation of arc discharge during current-carrying sliding and its effect on directional erosion," *Tribology International*, vol. 94, pp. 71–76, 2016.

[138] I. Aydin, S. B. Celebi, S. Barmada, and M. Tucci, "Fuzzy integral-based multi-sensor fusion for arc detection in the pantograph-catenary system," *Proceedings of the Institution of Mechanical Engineers, Part F: Journal of Rail and Rapid Transit*, vol. 232, no. 1, pp. 159–170, 2018.

[139] S. Barmada, M. Tucci, M. Menci, and F. Romano, "Clustering techniques applied to a high-speed train pantograph-catenary subsystem for electric arc detection and classification," *Proceedings of the Institution of Mechanical Engineers, Part F: Journal of Rail and Rapid Transit*, vol. 230, no. 1, pp. 85–96, 2016.

[140] X. Yu and H. Su, "Design and Simulation for Optical Acquisition of Pantograph-catenary Arcing Detection System of Electrified Railway," *IOP Conference Series: Materials Science and Engineering*, vol. 439, no. 5, pp. 3–8, 2018.

[141] G. Gao, J. Hao, W. Wei, H. Hu, G. Zhu, and G. Wu, "Dynamics of Pantograph-Catenary Arc during the Pantograph Lowering Process," *IEEE Transactions on Plasma Science*, vol. PP, no. 99, pp. 2715–2723, 2016.

[142] S. Midya and R. Thottappillil, "An overview of electromagnetic compatibility challenges in European Rail Traffic Management System," *Transportation Research Part C: Emerging Technologies*, vol. 16, no. 5, pp. 515–534, 2008.

[143] G. Wu, Y. Zhou, G. Gao, J. Wu, and W. Wei, "Arc Erosion Characteristics of Cu-Impregnated Carbon Materials Used for Current Collection in High-Speed Railways," *IEEE Transactions on Components, Packaging and Manufacturing Technology*, vol. 8, no. 6, pp. 1014–1023, 2018.

[144] S. Midya, D. Bormann, T. Schutte, and R. Thottappillil, "Pantograph Arcing in Electrified Railways-Mechanism and Influence of Various Parameters-Part I: With DC Traction Power Supply," *IEEE Transactions on Power Delivery*, vol. 24, no. 4, pp. 1940–1950, 2009.

[145] L. Heyun, G. Xiaosong, and T. Wenbi, "Icing and Anti-Icing of Railway Contact Wires," *Reliability and Safety in Railway*, 2012.

[146] S. Kubo and K. Kato, "Effect of arc discharge on wear rate of Cu-impregnated carbon strip in unlubricated sliding against Cu trolley under electric current," *Wear*, vol. 216, no. 2, pp. 172–178, 1998.

[147] F. J. Gonzalez, J. A. Chover, B. Suarez, and M. Vazquez, "Dynamic analysis using finite elements to calculate the critical wear section of the contact wire in suburban railway overhead conductor rails," *Proceedings of the Institution of Mechanical Engineers, Part F: Journal of Rail and Rapid Transit*, vol. 222, no. 2, pp. 145–157, 2008.

[148] G. Bucca and A. Collina, "Electromechanical interaction between carbon-based pantograph strip and copper contact wire: A heuristic wear model," *Tribology International*, vol. 92, pp. 47–56, 2015.

[149] G. X. Chen, H. J. Yang, W. H. Zhang, X. Wang, S. D. Zhang, and Z. R. Zhou, "Experimental study on arc ablation occurring in a contact strip rubbing against a contact wire with electrical current," *Tribology International*, vol. 61, pp. 88–94, 2013.

[150] W. Wang, G. Wu, G. Gao, B. Wang, L. Zhou, Y. Cui, and D. Liu, "Experimental study of electrical characteristics on pantograph arcing," *2011 1st International Conference on Electric Power Equipment - Switching Technology, ICEPE2011 - Proceedings*, pp. 602–607, 2011.

[151] A. Shimanovsky, V. Yakubovich, and I. Kapliuk, "Modeling of the Pantograph-Catenary Wire Contact Interaction," *Procedia Engineering*, vol. 134, pp. 284–290, 2016.

[152] Y. Wang, Z. Liu, X. Mu, K. Huang, H. Wang, and S. Gao, "An Extended Habedank's Equation-Based EMTP Model of Pantograph Arcing Considering Pantograph-Catenary Interactions and Train Speeds," *IEEE Transactions on Power Delivery*, vol. 31, no. 3, pp. 1186–1194, 2016.

[153] W. Wei, J. Wu, G. Gao, Z. Gu, X. Liu, G. Zhu, and G. Wu, "Study on Pantograph Arcing in a Laboratory Simulation System by High-Speed Photography," *IEEE Transactions on Plasma Science*, vol. PP, no. 99, pp. 2438–2445, 2016.

[154] F. Ren, S. Jia, G. Zhou, P. Liu, B. Tian, and M. Zheng, "Sliding wear behavior of copper alloy contact wire against copper-based strip for high-speed electrified railways," *Wear*, vol. 262, no. 7-8, pp. 772–777, 2006.

[155] H. J. Yang, G. X. Chen, G. Q. Gao, G. N. Wu, and W. H. Zhang, "Experimental research on the friction and wear properties of a contact strip of a pantograph-catenary system at the sliding speed of 350km/h with electric current," *Wear*, vol. 332-333, pp. 949–955, 2015.

[156] S. Kubo and K. Kato, "Effect of arc discharge on the wear rate and wear mode transition of a copper-impregnated metallized carbon contact strip sliding against a copper disk," *Tribology International*, vol. 32, no. 7, pp. 367–378, 1999.

[157] A. von Meier, *Electric Power Systems: A Conceptual Introduction*. Wiley survival guides in engineering and science, Wiley, 2006.

[158] S. Midya, D. Bormann, T. Schutte, and R. Thottappillil, "Pantograph Arcing in Electrified Railways- Mechanism and Influence of Various Parameters-Part II: With AC Traction Power Supply," *IEEE Transactions on Power Delivery*, vol. 24, no. 4, pp. 1940–1950, 2009.

[159] D. H. He, "Test Method of Arcing Behaviour for Railway Current Collection System," *Proc. of the Wold Congress on Railway Research*, no. poster 300, 2001.

[160] R. Holm, *Electric Contacts*. Berlin, Heidelberg: Springer Berlin Heidelberg, 4 ed., 1967.

[161] . Slade Paul G., *Electrical contacts : principles and applications*. New York : Marcel Dekker, 1999.

[162] E. I. Shobert, "Carbon, graphite and contacts," *IEEE Trans. Parts, Hy- brids, Packag.*, vol. vol. PHP-1, no. 6, pp. 62–74, 1976.

[163] S. Midya, D. Bormann, A. Larsson, T. Schutte, and R. Thottappillil, "Understanding pantograph arcing in electrified railways-influence of various parameters," *IEEE International Symposium on Electromagnetic Compatibility*, vol. 2008-Janua, 2018.

[164] D. Bormann, S. Midya, and R. Thottappillil, "DC components in pantograph arcing: Mechanisms and influence of various parameters," *Proceedings of the 18th International Zurich Symposium on Electromagnetic Compatibility, EMC*, pp. 369–372, 2007.

[165] S. Midya, D. Bormann, T. Schütte, and R. Thottappillil, "Pantograph arcing in electrified railways-mechanism and influence of various parameters - Part II: With AC traction power supply," *IEEE Transactions on Power Delivery*, vol. 24, no. 4, pp. 1940–1950, 2009.

[166] I. Zedin and S. Mnushkin, "Effect of oxygen on the susceptibility of copper to "hydrogen sickness"," *Metal Science and Heat Treatment*, vol. 10, no. 3, pp. 184–185, 1968.

[167] P. K. Nagata, "Hydrogen Embrittlement of Tough Pitch Copper by Brazing," 1975.

[168] J. Helavirta, "Oxygen-Free Copper for Industrial Applications," tech. rep., Luvata, Pori, Finland, 2019.

[169] M. R. L. Jr, "Hydrogen Embrittlement of Metals : A Primer for the Failure Analyst," *Journal of Failure Analysis and Prevention*, vol. 8, no. 3, pp. 289–307, 2008.

[170] M. Farzaneh and J. Zhan, "Modelling of DC arc discharge on ice surface," *IEEE Poceedings-Generation, Transmission and Distribution*, vol. 147, no. 2, pp. 81–86, 2000.

[171] A. Xiao, S. M. Rowland, J. C. Whitehead, and X. Tu, "Comparison of the temperature of low-current AC/DC discharge," *Annual Report - Conference on Electrical Insulation and Dielectric Phenomena, CEIDP*, pp. 1066–1069, 2013.

[172] Y. J. Kim and H. Kim, "DC arc characteristics according to source voltage and load power level," *7th International IEEE Conference on Renewable Energy Research and Applications, ICRERA 2018*, vol. 5, pp. 205–208, 2018.

[173] G.-y. Zhu, G.-q. Gao, G.-n. Wu, Z. Gu, J. Wu, and J. Hao, "Modeling pantograph-catenary arcing," *Proceedings of the Institution of Mechanical Engineers, Part F: Journal of Rail and Rapid Transit*, vol. 230, no. 7, pp. 1687–1697, 2016.

[174] T. Ding, G. X. Chen, J. Bu, and W. H. Zhang, "Effect of temperature and arc discharge on friction and wear behaviours of carbon strip/copper contact wire in pantograph-catenary systems," *Wear*, vol. 271, no. 9-10, pp. 1629–1636, 2011.

[175] T. Ding, G. X. Chen, Y. M. Li, H. J. Yang, and Q. D. He, "Arc erosive characteristics of a carbon strip sliding against a copper contact wire in a high-speed electrified railway," *Tribology International*, vol. 79, pp. 8–15, 2014.

[176] Y. Feng, M. Zhang, and Y. Xu, "Effect of the electric current on the friction and wear properties of the CNT-Ag-G composites," *Carbon*, vol. 43, no. 13, pp. 2685–2692, 2005.

[177] G. X. Chen, Y. Hu, B. J. Dong, H. J. Yang, G. Q. Gao, G. N. Wu, W. H. Zhang, and Z. R. Zhou, "Experimental study on the temperature of the contact strip in sliding electric contact," *Proceedings of the Institution of Mechanical Engineers, Part J: Journal of Engineering Tribology*, vol. 231, no. 10, pp. 1268–1275, 2017.

[178] H. Nagasawa and K. Kato, "Wear mechanism of copper alloy wire sliding against iron-base strip under electric current," *Wear*, vol. 216, no. 2, pp. 179–183, 1998.

[179] A. Dong, G. Wu, G. Gao, L. Zhou, W. Wang, B. Wang, Y. Cui, and M. Yang, "Simulation system of pantograph arcing," in *2011 1st International Conference on Electric Power Equipment - Switching Technology, ICEPE2011 - Proceedings*, (Xi'an-China), pp. 637–641, 2011 1st International Conference on Electric Power Equipment – Switching Technology, 2011.

[180] C. Tu, Z. H. Chen, and J. Xia, "Thermal wear and electrical sliding wear behaviors of the polyimide modified polymer-matrix pantograph contact strip," *Tribology International*, vol. 42, no. 6, pp. 995–1003, 2009.

[181] H. Zhao, G. C. Barber, and J. Liu, "Friction and wear in high speed sliding with and without electrical current," *Wear*, vol. 249, no. 5-6, pp. 409–414, 2001.

[182] O. Bruno, A. Landi, M. Papi, and L. Sani, "Phototube sensor for monitoring the quality of current collection on overhead electrified railways," *Proc Instn Mech Engrs Vol*, no. November 2000, pp. 231–241, 2001.

[183] Y. Park, K. Lee, S. Y. Kwon, C. Park, J. K. Kim, and W. S. Choi, "Analysis of percentage of arcing between pantograph and overhead contact line as a function of duration of arc," *Transactions of the Korean Institute of Electrical Engineers*, vol. 63, no. 6, pp. 855–859, 2014.

[184] G. Gao, T. Zhang, W. Wei, Y. Hu, G. Wu, and N. Zhou, "A pantograph arcing model for electrified railways with different speeds," *Proceedings of the Institution of Mechanical Engineers, Part F: Journal of Rail and Rapid Transit*, vol. 232, no. 6, pp. 1731–1740, 2018.

[185] "NR / L2 / ELP / 21088 Module 08 – Mark 3D Maintenance Parameters Contents 1 Scope 2 Definitions 3 Equipment Design Definition 4 Equipment Design Variations 5 Equipment Design Designations 6 Environmental Conditions 7 Maximum Pantograph Operational Speeds," tech. rep., Network Rail, London, 2015.

[186] N. Rail, "NR / L2 / ELP / 21088 Module 06 – Mark 3B Maintenance Parameters Contents 1 Scope 2 Definitions 3 Equipment Design 4 Equipment Design Variations 5 Equipment Design Designations 6 Environmental Conditions 7 Maximum Pantograph Operational Speeds 8 Continuou," tech. rep., Network Rail, London, 2015.

[187] M. Yüksel and C. Meran, *Malzeme Bilgisine Giris*. Denizli/Turkey: MMO, first ed., 2010.

[188] "ASTM D6272-10, Standard Test Method for Flexural Properties of Unreinforced and Reinforced Plastics and Electrical Insulating Materials by Four-Point Bending, ASTM International,," tech. rep., ASTM International, 2017.

[189] "ASTM E8/E8M - 08 Standard Test Methods for Tension Testing of Metallic Materials," tech. rep., American Association Stat.

[190] "ASTM D672-10-Standard Test Method for Flexural Properties of Unreinforced and Reinforced Plastics and Electrical Insulating Materials by Four-Point Bending," Tech. Rep. Reapproved 2012, 2010.

[191] P. Kurowski, *Finite Element Analysis for Design Engineers*, vol. 53. Warrendale, USA: SAE International, second ed., 2017.

[192] E. J. Myers, "Finite Element Modeling (FEM) of Porous Additively Manufactured Ferromagnetic Shape Memory Alloy Using Scanning Electron Micrograph (SEM) Based Geometries," no. May, 2017.

[193] R. Hughes, *Fatigue of Structures and Materials*, vol. 53. Dordrecht: Springer Netherlands, 2009.

[194] N. Rail, "Earthing and Bonding for AC Electrification Schemes applying Common Bonding: Project Advice Note," tech. rep., 2019.

[195] D. Benson, "Recommendations for the design of bridges to BS EN 1993," Tech. Rep. 1, Railway Group Standards, London, 2000.

[196] Railway Safety, "GERT8025: Electrical Protective Provisions for Electrified Lines, Issue 1," vol. 1, 2001.

[197] M. Hsiao, "Traction Electrification System Requirements for Grounding and Bonding and Protection against Electric Shock,"

[198] R. Stainton, "AC electrification with DC clearances," tech. rep., Network Rail, London, 2015.

[199] ASTM, "B152- Standard Specification for Copper Sheet , Strip , Plate , and Rolled Bar 1," pp. 1–8, 2011.

[200] Aurubis, "EN CW009A Material Datasheet Cu-OFE," tech. rep., Hamburg, 2018.

[201] ASTM, "ASTM E112-13: Standard test methods for determining average grain size," *ASTM International*, pp. 1–28, 2013.

[202] G. F. Vander Voort, *Metallography Principles and Practice*. USA: ASM International, 1999.

[203] M. R. Louthan and M. Engineering, "Optical Metallography," *ASM Handbook, Volume 10: Materials Characterizations*, vol. 10, pp. 299–308, 1986.

[204] G. Petzow, "Metallography," *ASM International*, 1999.

[205] R. Ltd. and J. Beck, "Grinding and polishing machine," *Journal of Scientific Instruments*, vol. 34, no. 11, pp. 468–469, 1957.

[206] Struers, "Metallographic preparation of aluminium and aluminium alloys Application Notes," p. 6, 2014.

[207] G. F. Vander Voort, "Copper color metallography," *Advanced Materials and Processes*, vol. 158, no. 1, pp. 36–40, 2000.

[208] H. S. Rawdon and M. G. Lorentz, "Metallographic etching reagents; I, for copper," *Scientific Papers of the Bureau of Standards*, vol. 16, p. 641, 1920.

[209] H. S. Rawdor and M. G. Lorentz, "Metallographic etching reagents; II, for copper alloys, nickel, and the alpha alloys of nickel," *Journal of the Franklin Institute*, vol. 194, no. 1, pp. 94–95, 1922.

[210] R. Richard and J. Law, eds., *A Dictionary of Physics*. Oxford: Oxford University Press, jan 2009.

[211] ASTM, "ASTM E112-13: Standard test methods for determining average grain size," *ASTM International*, pp. 1–28, 2013.

[212] D. H. Herring, "Hydrogen Embrittlement," *Fall 2010/Wire Forming Technology International*, vol. 13, no. 4, pp. 2–5, 2010.

[213] S. Nakahara and Y. Okinaka, "The hydrogen effect in copper," *Materials Science and Engineering A*, vol. 101, no. C, pp. 227–230, 1988.

[214] A. H. Caskey, G RDEXTER, M. L. Holzworth, M. R. Louthan, and R. G. Derrick, "The Effect of Oxygen on Hydrogen Transport in Copper," *Corrosion*, vol. 32, no. 9, pp. 370–374, 1976.

[215] Q. G. Wang, D. Apelian, and D. A. Lados, "Fatigue behavior of A356-T6 aluminum cast alloys. Part I. Effect of casting defects," *Journal of Light Metals*, vol. 1, no. 1, pp. 73–84, 2001.

[216] C. Q. Bowles and J. Schijve, "The role of inclusions in fatigue crack initiation in an aluminum alloy," *International Journal of Fracture*, vol. 9, no. 2, pp. 171–179, 1973.

[217] Q. Deng, N. A. Bhatti, X. Yin, and M. Abdel Wahab, "The effect of a critical microvoid defect on fretting fatigue crack initiation in heterogeneous material using a multiscale approach," *Tribology International*, vol. 141, no. May 2019, p. 105909, 2020.

[218] Q. Deng, N. Bhatti, X. Yin, and M. A. Wahab, "Numerical modeling of the effect of randomly distributed inclusions on fretting fatigue-induced stress in metals," *Metals*, vol. 8, no. 10, 2018.

[219] L. C. Chan, X. Z. Lu, and K. M. Yu, "Multiscale approach with RSM for stress-strain behaviour prediction of micro-void-considered metal alloy," *Materials and Design*, vol. 83, pp. 129–137, 2015.

[220] D. A. Lados, "Fatigue crack growth mechanisms in Al-Si-Mg alloys," *Surface Engineering*, vol. 20, no. 6, pp. 416–424, 2004.

[221] S. Wada, K. Ito, and T. Hayasaka, "Current estimation method at the time of a contact-wire breakage during standstill below insulated overlap based on contact-wire necking length," *WIT Transactions on the Built Environment*, vol. 181, no. 1, pp. 25–35, 2018.

[222] Y. Ueda, H. Murakawa, and N. Ma, *Welding Deformation and Residual Stress Prevention*. Elsevier, 2012.

[223] Y. Cengel, *Heat Transfer: A Practical Approach*. McGraw-Hill Book Company, second ed., 2002.

[224] J. G. Hust A. B. Lankford, "Thermal Conductivity of 1 K To the Melting Point," Tech. Rep. June, National Bureau of Standards U.S. Department of Commerce, Boulder, Colorado, 1984.

[225] P. Chatzipanagiotou, M. Felczak, and G. D. E. Mey, "Convection and radiation cooling of overhead power lines - laboratory verification using thermography," *Measurement Automation Monitoring*, vol. 63, no. 03, pp. 107–110, 2017.

[226] D. S. Albin, G. D. Mooney, A. Duda, J. Tuttle, R. Matson, and R. Noufi, "Enhanced grain growth in polycrystalline CuInSe2 using rapid thermal processing," *Solar Cells*, vol. 30, no. 1-4, pp. 47–52, 1991.

[227] L. Lu, N. R. Tao, L. B. Wang, B. Z. Ding, and K. Lu, "Grain growth and strain release in nanocrystalline copper," *Journal of Applied Physics*, vol. 89, no. 11 I, pp. 6408–6414, 2001.

[228] P. R. Rios, F. Siciliano, H. R. Z. Sandim, R. L. Plaut, and A. F. Padilha, "Nucleation and growth during recrystallization," *Materials Research*, vol. 8, no. 3, pp. 225–238, 2005.

[229] S. Ivanov, D. Markovich, L. Stuparevich, and D. Guskovich, "Effect of degree of cold work and annealing temperature on the microstructure and properties of cold drawn copper wires and tubes," *Bulletin of Materials Science*, vol. 19, no. 1, pp. 131–138, 1996.

[230] D. Mellouli, N. Haddar, A. Köster, and H. F. Ayedi, "Hardness effect on thermal fatigue damage of hot-working tool steel," *Engineering Failure Analysis*, vol. 45, pp. 85–95, 2014.

[231] "Data on system damage for different combinations of wire tension, pantograph collector strip material and upload force," Tech. Rep. May, NeTIRail-INFRA H2020-MG-2015-2015 GA-636237, 2018.

[232] H. Street, "Specialist Technical Report OLE Neutral Section Reliability Review - Final Report," vol. 44, no. 0, pp. 1–31, 2014.

[233] C. Cagran, *Thermal Conductivity and Thermal Diffusivity of Liquid Copper*. PhD thesis, Technische Universitat Graz, 2000.

Appendix A

Fatigue Properties of OLE Contact Wires

A.1 UK Electrification History

UK Electrification Build History

19/11/2016

Type	Date		Voltage		Route	Route Designation
	Start	Finish	From	To		
New Build		1908	-	6.7kV 50Hz AC	Lancaster - Morecambe - Heysham	L&YR
New Build		1909	-	6.7kV 50Hz AC	London Victoria - London Bridge via Denmark Hill	LB&SCR
New Build		1911	-	6.7kV 50Hz AC	Battersea Park - Crystal Palace via Streatham Hill	LB&SCR
New Build		1912	-	500V DC	Grimsby (Corporation Bridge) - Immingham Town	Grimsby & Immingham Railway
New Build		1912	-	6.7kV 50Hz AC	Peckham Rye - Streatham Hill; Peckham Rye - Crystal Palace Low Level via Tulse Hill	LB&SCR
New Build		1913	-	500V DC	Immingham Town - Immingham Dock	Grimsby & Immingham Railway
New Build		1913	-	3.5kV DC	Bury - Holcombe Brook	L&YR
New Build		1915	-	500V DC	Immingham Town - Immingham Queens Bridge	Grimsby & Immingham Railway
New Build		1915	-	1.5kV DC	Middridge Sidings - Bowesfield; Shildon Yard - Middridge Sidings; Bowesfield - Erimus Yard	Newport - Shildon Railway
New Build		1916		1.5kV DC	Erimus Yard - Newport East	Newport - Shildon Railway
New Build		1916	-	1.5kV DC	Newport (nr Newcastle) - Shildon	Newport - Shildon Railway
New Build		1925	-	660V DC	Rossall	Blackpool Tram
New Build		1925	-	6.7kV 50Hz AC	Balham - Coulsdon North & Sutton	LB&SCR
New Build		1928	-	6.7kV 50Hz AC	Tulse Hill - Streatham Common	LB&SCR
New Build		1929	-	6.7kV 50Hz AC	Victoria - Sutton & Coulsdon North	LB&SCR
New Build		1931	-	1.5kV DC	Manchester - Altrincham	MSJ&A Line
De-electrification		1935	1.5kV DC	-	All NSR lines	Newport - Shildon Railway
New Build		1949	-	1.5kV DC	London Liverpool Street - Shenfield	GE
New Build		1949	-	1.5kV DC	London Fenchurch St - Bow Jct via Gas Factory Jct	LTS
New Build		1952	-	1.5kV DC	Dunford Bridge - Wath	Woodhead Route
Conversion	1951	1953	6.7kV 50Hz AC	25kV 50Hz AC	Lancaster - Morecambe - Heysham	
New Build		1954	-	1.5kV DC	Manchester London Rd - Sheffield Victoria via Wath	Woodhead Route
New Build		1955	-	1.5kV DC	Darnall Depot - Rotherwood Sidings	Woodhead Route
New Build		1956	-	1.5kV DC	Shenfield - Chelmsford	GE
New Build		1956	-	1.5kV DC	Shenfield – Southend Victoria	
De-electrification	1956	1961	500V DC	-	All G&IR Lines	Grimsby & Immingham Railway
New Build		1958	-	25kV 50Hz AC	Wilmslow - Slade Lane	WCML test scheme
New Build		1959	-	25kV 50Hz AC	Colchester - Clacton & Walton	25kV test scheme
Conversion		1960	1.5kV DC	6.25kV 50Hz AC	London Liverpool St - Southend Victoria	GE
Conversion		1960	1.5kV DC	6.25kV 50Hz AC	Bethnal Green - Chingford, Enfield Town & Cheshunt	GE
New Build		1960	-	6.25kV 50Hz AC	Helensburgh - Glasgow Queen Street - Airdrie; Dalreoch - Balloch; Dalmuir Park - Hyndland via Westerton; Bellgrove - Springburn; Dalmuir Park - Yoker - Parkhead; High Street - Bridgeton	Glasgow suburban lines stage 1A
Conversion		1960	1.5kV DC	6.25kV 50Hz AC	London Fenchurch St - Bow Jct via Gas Factory Jct	LTS
New Build		1960	-	25kV 50Hz AC	Crewe – Manchester	WCML stage 1
New Build		1960	-	25kV 50Hz AC	Cheshunt - Bishops Stortford & Hertford East	
New Build		1961	-	6.25kV 50Hz AC	Glasgow Central - Motherwell via Uddingston; Cathcart Circle; Cathcart - Neilston High	Glasgow suburban lines stage 1B
Conversion		1961	1.5kV DC	6.25kV 50Hz AC	Gas Factory Jn - Shoeburyness; Barking - Pitsea via Grays; Barking - Forest Gate Jn; Upminster - Grays	LTS
New Build		1961	-	25kV 50Hz AC	London Fenchurch St – Southend (via Laindon & Tilbury)	LTS
New Build		1962	-	25kV 50Hz AC	Southend - Shoeburyness	LTS
New Build		1962	-	25kV 50Hz AC	Crewe – Liverpool	WCML stage 2
Conversion		1962	1.5kV DC	25kV 50Hz AC	Shenfield - Chelmsford	
New Build		1963	-	25kV 50Hz AC	Stafford - Crewe	WCML stage 3
New Build		1963	-	25kV 50Hz AC	Lichfield - Stafford	WCML stage 3
New Build		1963	-	25kV 50Hz AC	Chelmsford - Colchester	
New Build		1964	-	25kV 50Hz AC	Nuneaton - Lichfield	WCML stage 3
New Build		1964	-	25kV 50Hz AC	Rugby - Nuneaton	WCML stage 3
New Build		1965	-	1.5kV DC	Woodborn Jct & Darnall West Jct - Tinsley Yard	Woodhead Route
New Build		1965	-	25kV 50Hz AC	Cheadle Hulme - Macclesfield	WCML stage 4
New Build		1965	-	25kV 50Hz AC	London Euston - Rugby inc Northampton Loop	WCML stage 5
New Build		1966	-	25kV 50Hz AC	Wolverhampton - Stafford & Bescot; Portobello Jct - Bushbury Jct	WCML stage 6
New Build		1966	-	25kV 50Hz AC	Camden - Camden Town	WCML stage 7
New Build		1966	-	25kV 50Hz AC	Colwich - Macclesfield via Stone	WCML stage 8
New Build		1966	-	25kV 50Hz AC	Stone - Norton Bridge	WCML stage 8
New Build		1966	-	25kV 50Hz AC	Rugby - Wolverhampton via Birmingham	WCML stage 8
New Build		1966	-	25kV 50Hz AC	Birmingham - Walsall	WCML stage 8
New Build		1966	-	25kV 50Hz AC	Aston - Stechford	WCML stage 8
De-electrification		1966	6.7kV 50Hz AC	-	Lancaster - Morecambe - Heysham	
New Build		1967	-	25kV 50Hz AC	Glasgow - Gourock & Wemyss Bay	Glasgow suburban lines stage 2
New Build		1969	-	25kV 50Hz AC	Clapton Jct - Cheshunt Jct	Lea Valley
Conversion	1968	1971	1.5kV DC	25kV 50Hz AC	Manchester Oxford Rd - Altrincham	MSJ&A Line
New Build		1973	-	25kV 50Hz AC	Weaver Jn - Bamfurlong (Freight Only)	WCML Extension stage 1
New Build		1973	-	25kV 50Hz AC	Bamfurlong - Preston (Freight Only)	WCML Extension stage 2
New Build		1974	-	25kV 50Hz AC	Weaver Jn - Preston (Passenger)	WCML Extension stage 3
New Build		1974	-	25kV 50Hz AC	Preston - Glasgow Central	WCML Extension stage 4
New Build		1974	-	25kV 50Hz AC	Lanark Jct - Lanark	
New Build		1975	-	25kV 50Hz AC	Glasgow West St - Muirhouse Jct	

UK Electrification Build History

19/11/2016

Type	Date		Voltage		Route	Route Designation
	Start	Finish	From	To		
New Build		1976	-	25kV 50Hz AC	Drayton Park - Welwyn Garden City & Hertford North	Great Northern Suburban Stage 1
New Build		1977	-	25kV 50Hz AC	Witham - Braintree	
Conversion		1978	6.25kV 50Hz AC	25kV 50Hz AC	Dalmuir Park - Finnieston via Westerton; Yoker - Jordanhill; Westerton - Milngavie	Glasgow Suburban
New Build		1978	-	25kV 50Hz AC	London Kings Cross - Finsbury Park	Great Northern Suburban Stage 2
New Build		1978	-	25kV 50Hz AC	Welwyn Garden City - Royston	Great Northern Suburban Stage 2
Conversion		1979	6.25kV 50Hz AC	25kV 50Hz AC	Dalmuir Park - Yoker	Glasgow Suburban
Conversion		1979	6.25kV 50Hz AC	25kV 50Hz AC	Finnieston - Parkhead inc Bridgeton branch	Glasgow Suburban
Conversion		1979	6.25kV 50Hz AC	25kV 50Hz AC	Bellgrove - Springburn	Glasgow Suburban
Conversion		1979	6.25kV 50Hz AC	25kV 50Hz AC	Pollokshields East - Cathcart	Glasgow Suburban
New Build		1979	-	25kV 50Hz AC	Hertford North - Stevenage	Great Northern Suburban Stage 2
New Build		1979	-	25kV 50Hz AC	Cornbrook Jct - Trafford Park FLT	
New Build		1979	-	25kV 50Hz AC	Finnieston Jct - Rutherglen	
New Build		1980	-	1.5kV DC	Haymarket - St James, Bank Foot, Heworth & South Shields	Tyne & Wear Metro
Closure		1981	-	-	Hadfield - Sheffield Victoria	Woodhead Route
New Build		1981	-	25kV 50Hz AC	Edgeley - Hazel Grove	
New Build		1981		25kV 50Hz AC	Mossend - Coatbridge FLT	
New Build		1983	-	25kV 50Hz AC	London St Pancras & Moorgate – Bedford	Midland Mainline
Conversion		1983	6.25kV 50Hz AC	25kV 50Hz AC	London Liverpool St - Cheshunt	
Conversion		1983	6.25kV 50Hz AC	25kV 50Hz AC	Hackney - Chingford	
Conversion		1983	6.25kV 50Hz AC	25kV 50Hz AC	Bury Street - Enfield Town	
Conversion		1984	1.5kV DC	25kV 50Hz AC	Manchester - Hadfield	Woodhead Route (truncated)
New Build		1985	-	25kV 50Hz AC	Bishop's Stortford - Cambridge	
New Build		1985	-	25kV 50Hz AC	Freight Terminal Jct - Camden Road East Jct	
New Build		1985	-	25kV 50Hz AC	Navarino Road Jct - Reading Lane Jct	
New Build		1985	-	25kV 50Hz AC	Colchester - Ipswich	
New Build		1986	-	25kV 50Hz AC	Paisley - Ayr	Ayrshire Coast
New Build		1986	-	25kV 50Hz AC	Kilwinning - Ardrossan South Beach; Dubbs Jct - Byrehill Jct	Ayrshire Coast
New Build		1986	-	25kV 50Hz AC	Hitchin - Huntingdon	ECML stage 1
New Build		1986	-	25kV 50Hz AC	Manningtree - Harwich	
New Build		1986	-	25kV 50Hz AC	Ipswich - Stowmarket	
New Build		1986	-	25kV 50Hz AC	Romford - Upminster	
New Build		1986	-	25kV 50Hz AC	Wickford - Southminster	
New Build		1987	-	25kV 50Hz AC	Ardrossan South Beach - Largs & Ardrossan Harbour	Ayrshire Coast
New Build		1987	-	25kV 50Hz AC	Huntingdon - Peterborough	ECML stage 2
New Build		1987	-	25kV 50Hz AC	Stratford - Camden via Dalston	North London Line
New Build		1987	-	25kV 50Hz AC	Stowmarket - Norwich	
New Build		1987	-	25kV 50Hz AC	Bishop's Stortford - Cambridge	
New Build		1987	-	25kV 50Hz AC	Glasgow – Ardrossan & Largs	
New Build		1987	-	25kV 50Hz AC	Canonbury Jct - Finsbury Park	
New Build		1987	-	25kV 50Hz AC	Stratford FLT	
New Build		1987	-	25kV 50Hz AC	Temple Mills Yard	
New Build	1987	1988	-	25kV 50Hz AC	Royston - Shepreth Branch Jct	
New Build	1987	1988	-	25kV 50Hz AC	Watford Junction - St Albans Abbey	
New Build		1989	-	25kV 50Hz AC	Peterborough - Leeds via Doncaster	ECML stage 3
New Build		1989	-	25kV 50Hz AC	Doncaster - York	ECML stage 4
New Build		1989	-	25kV 50Hz AC	Seven Sisters - Tottenham South	
New Build		1989	-	25kV 50Hz AC	Airdrie - Drumgelloch	
New Build		1990	-	25kV 50Hz AC	York - Newcastle	ECML stage 5
New Build		1990	-	25kV 50Hz AC	Stratford - Copper Mill Junction	
New Build		1990	-	25kV 50Hz AC	Stansted Jct - Stansted Airport	
New Build	1990	1991	-	25kV 50Hz AC	Carstairs – Edinburgh	
New Build		1991	-	25kV 50Hz AC	Drem Jct - North Berwick	
New Build	1990	1992	-	25kV 50Hz AC	Lichfield - Birmingham New St; Aston - Redditch	Cross City Line
Conversion		1992	25kV 50Hz AC	750V DC	Manchester - Altrincham	MJS&A; now Metrolink
Conversion		1992	1.2kV DC	750V DC	Manchester - Bury	Metrolink
New Build	1990	1992	-	25kV 50Hz AC	Cambridge – King's Lynn	
New Build		1993	-	25kV 50Hz AC	North Pole Depot	Channel Tunnel
New Build		1993	-	25kV 50Hz AC	Dollands Moor Freight Terminal	Channel Tunnel
New Build		1993	-	25kV 50Hz AC	Manchester Airport North Spur	
New Build		1994		750V DC	Sheffield - Meadowhall, Halfway, Herdings Park, Malin Bridge & Middlewood	Sheffield Supertram
New Build		2000		750V DC	Croydon - New Addington, Wimbledon, Beckenham Jct & Elmers End	Croydon Tramlink
New Build		2004		750V DC	Nottingham - Phoenix Park & Hucknall	Nottingham Express Transit
New Build		1999		750V DC	Birmingham Snow Hill - Wolverhampton	Midland Metro
New Build		1994	-	25kV 50Hz AC	Cheriton - Frethun	Channel Tunnel
New Build	1992	1994	-	25kV 50Hz AC	Leeds - Bradford, Skipton & Ilkley	Leeds North West
New Build	1994	1996	-	25kV 50Hz AC	London Paddington - Heathrow Airport	Heathrow Express
New Build		1996	-	25kV 50Hz AC	Manchester Airport South Spur	
Conversion	1996	1998	750V DC	25kV 50Hz AC	Acton Central - Camden Rd	North London Line
New Build		2000	-	25kV 50Hz AC	Kensal Green Jct - Willesden Jct	
New Build		2001	-	25kV 50Hz AC	Melton Jct - Edwalton	Old Dalby Test Track
New Build	2001	2003	-	±25kV 50Hz AC	Fawkenham Jct - Cheriton	Channel Tunnel Rail Link Section 1

UK Electrification Build History

19/11/2016

Type	Date		Voltage		Route	Route Designation
	Start	Finish	From	To		
New Build		2003	-	25kV 50Hz AC	Crewe - Kidsgrove	WCRM
New Build		2002	-	1.5kV DC	Pelaw Jct - Sunderland	Tyne & Wear Metro
New Build	2003	2005	-	25kV 50Hz AC	Haughhead Junction - Larkhall	
New Build	2003	2007	-	±25kV 50Hz AC	Fawkenham Jct - St Pancras International	Channel Tunnel Rail Link Section 2
New Build		2010	-	25kV 50Hz AC	Shields Jct - Glasgow Airport	Glasgow Airport Scheme (GARL)
New Build	2008	2010	-	25kV 50Hz AC	Airdrie - Haymarket	Airdrie to Bathgate (A2B)
New Build		2014	-	25kV 50Hz AC	Rutherglen - Coatbridge	EGIP
New Build		2015	-	25kV 50Hz AC	Manchester Victoria - Edge Hill	NWEP
New Build	2014	2016	-	±25kV 50Hz AC	Scours Lane - Didcot	GWEP
New Build	2014	*2017*	-	±25kV 50Hz AC	Maidenhead - Stockley	Crossrail/GWEP
Conversion		*2018*	25kV 50Hz AC	±25kV 50Hz AC	Royal Oak - Liverpool St	Crossrail
New Build		*2018*	-	25kV 50Hz AC	Pudding Mill Lane - Abbey Wood	Crossrail
Conversion	2016	*2018*	25kV 50Hz AC	±25kV 50Hz AC	Kensal Green - Stockley	Crossrail/GWEP
New Build	2015	*TBC*	-	±25kV 50Hz AC	Maidenhead - Reading	GWEP
New Build	2015	*TBC*	-	±25kV 50Hz AC	Reading - Scours Lane	GWEP
New Build	2015	*TBC*	-	±25kV 50Hz AC	Didcot - Wootton Bassett	GWEP
New Build	2015	*TBC*	-	±25kV 50Hz AC	Wootton Bassett - Bristol Parkway	GWEP
New Build	2015	*TBC*	-	±25kV 50Hz AC	Bristol Parkway - Cardiff	GWEP
New Build	2016	*TBC*	-	±25kV 50Hz AC	Wootton Bassett - Bristol Temple Meads	GWEP
New Build	TBC	*TBC*	-	±25kV 50Hz AC	Bristol Temple Meads - Bristol Parkway	GWEP
New Build	2015	*TBC*	-	±25kV 50Hz AC	Reading - Newbury	GWEP
New Build	2015	*TBC*	-	±25kV 50Hz AC	Didcot - Oxford	GWEP
New Build		*TBC*	-	25kV 50Hz AC	Edinburgh - Glasgow via Falkirk	EGIP
New Build		*TBC*	-	25kV 50Hz AC	Manchester Victoria - Preston via Bolton	NWEP
New Build		*TBC*	-	25kV 50Hz AC	Preston - Blackpool	NWEP
New Build		*TBC*	-	25kV 50Hz AC	Liverpool - Wigan via St Helens	NWEP
New Build		*TBC*	-	25kV 50Hz AC	Springburn - Cumbernauld	EGIP
New Build		*TBC*	-	25kV 50Hz AC	Stirling - Alloa - Dunblane	EGIP
New Build		*TBC*	-	±25kV 50Hz AC	Bedford - Derby - Sheffield; Tren Junction - Nottingham	MMLE
New Build		*TBC*	-	25kV 50Hz AC	Oxenholme - Windermere	
New Build		*TBC*	-	25kV 50Hz AC	Barnt Green - Bromsgrove	

A.2 OLE Circuit Breaker Components

A.2.1 Neutral Section

Neutral sections are used in phase breaks to help manage of different phases of power supplies. Fig. A.1 shows the design of a typical Arthur Flury neutral section [232].



Fig. A.1 The design of Arthur Flury neutral section [232]

A.2.2 Section Insulator

To allow maintenance to sections of the overhead line without having to turn off the entire system, the overhead line system is broken into electrically separated portions known as sections. A section insulator is shown in Fig. A.2.



Fig. A.2 A typical section insulator used in OLE main lines [9]

Appendix B

Chapter 4

B.1 SOLARC Machine Configuration

B.1.1 High Speed Camera Measurement

The equipment and the configuration used in the high-speed camera measurements of arcing is shown in this chapter.



Fig. B.1 Highspeed camera unit used in measuring movement of current collector

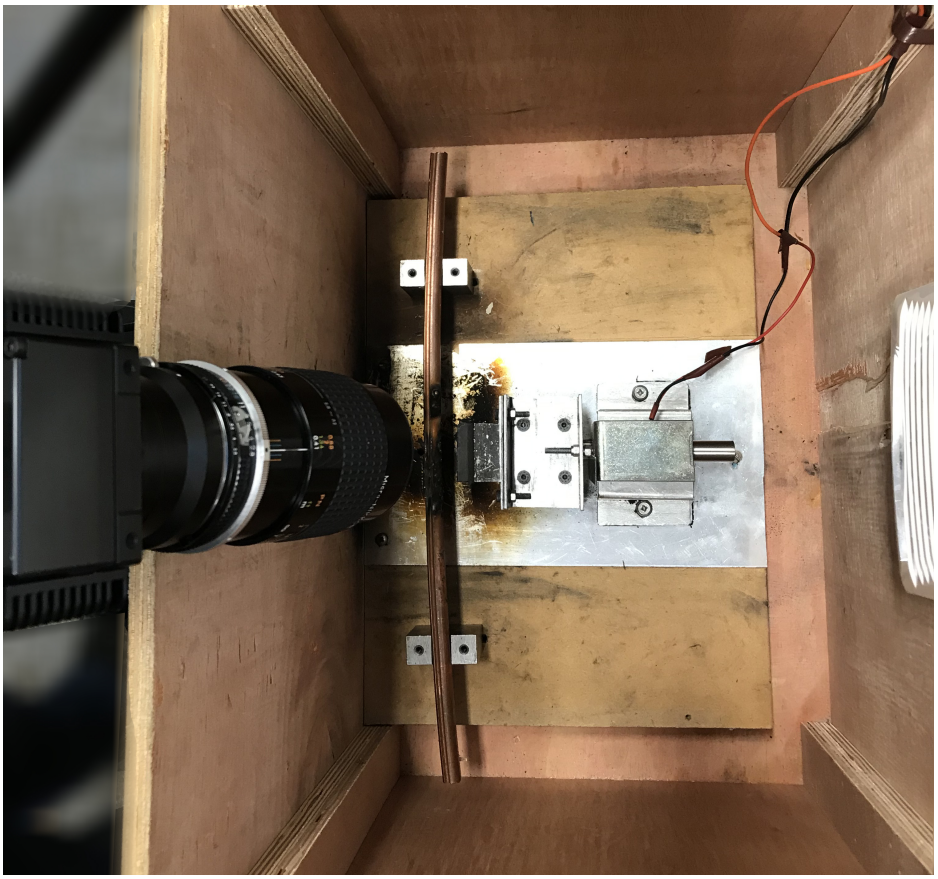


Fig. B.2 Configuration of highspeed camera equipment

Appendix C

Parameters Used in Thermal Modelling

C.1 Hypothesis for Developing the Model

C.1.1 Thermal Cooling due to Radiation

C.2 FE Model Parameters

C.2.1 Specific Heat and Thermal Conductivity

Reference thermal properties of the copper material used in finite element modelling are shown in Fig. C.1, Fig. C.2 and Fig. C.3 and average of the specific heat of solid and liquid form of copper was tabulated in Table C.2.

Table C.1 The energy lost per unit time due to radiation depending on maximum temperature at the ambient temperature of 18 degrees.

Time s	Joule Heat W	Max Local Temperature ° C	Heat Loss by Radiation W
0	0	18.0	0.01
0.2626	0	18.0	0.01
0.2682	2619	161.1	0.03
0.29	5544.9	627.4	0.65
0.3052	7585	1000.4	2.68
0.3101	5595	981.8	2.52
0.3147	8494	1151.7	4.22
0.3304	1527	743.1	1.07
0.3426	6154	985.0	2.55
0.5382	3719	1163.4	4.36
0.5428	0	923.5	2.08
0.6	0	347.7	0.14
1	0	117.9	0.02
10	0	44.7	0.01
120	0	19.4	0.01

Table C.2 Average specific heat of copper in the forms of solid and liquid

The Specific Heat	Copper
$C_{p,solid}$	481 $J.kg^{-1}.K^{-1}$
$C_{p,liquid}$	531 $J.kg^{-1}.K^{-1}$

T (K)	λ(W·m^{-1}·K^{-1}) RRR = 30	RRR = 100	RRR = 300	RRR = 1000	RRR = 3000
1	46	156	471	1574	4726
2	91	312	942	3147	9434
3	137	468	1413	4710	14044
4	183	624	1880	6243	18380
5	228	779	2343	7715	22170
6	274	933	2796	9075	25084
7	319	1085	3232	10260	26834
8	365	1235	3642	11197	27328
9	409	1380	4015	11836	26756
10	454	1520	4343	12172	25496
12	541	1778	4844	12127	22264
14	624	2002	5144	11544	19150
16	703	2186	5267	10725	16398
18	777	2324	5231	9771	13924
20	843	2408	5054	8727	11683
25	960	2381	4215	6135	7271
30	999	2119	3245	4151	4573
35	970	1784	2436	2859	3028
40	900	1467	1841	2047	2122
45	814	1205	1423	1531	1568
50	731	1002	1135	1196	1216
60	597	740	799	824	832
70	513	601	634	647	651
80	465	526	549	557	560
90	437	485	502	508	510
100	421	461	475	480	482
150	396	419	426	429	430
200	391	407	413	414	415
250	388	401	405	407	407
300	386	397	400	401	402
400	383	391	393	394	394
500	379	385	387	388	388
600	374	379	381	381	381
700	368	372	374	374	374
800	362	365	367	367	367
900	356	359	360	360	360
1000	350	352	353	353	354
1100	344	347	347	348	348
1200	339	341	342	342	342
1300	335	337	337	338	338

Fig. C.1 Thermal conductivity of copper from 1 K to the melting point [224]

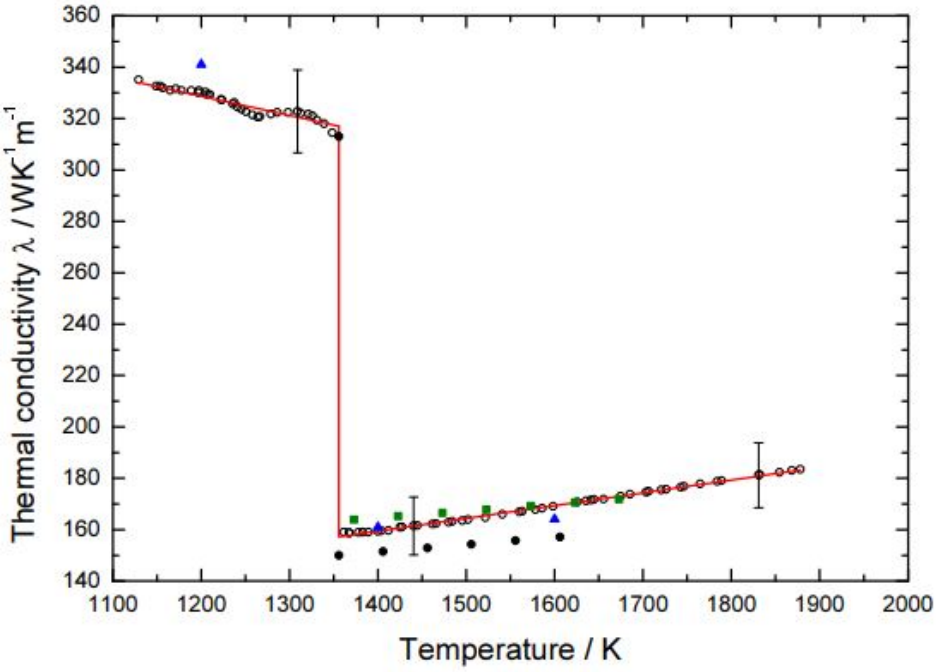


Fig. C.2 Thermal conductivity of copper from the melting point to 1900 K [233]

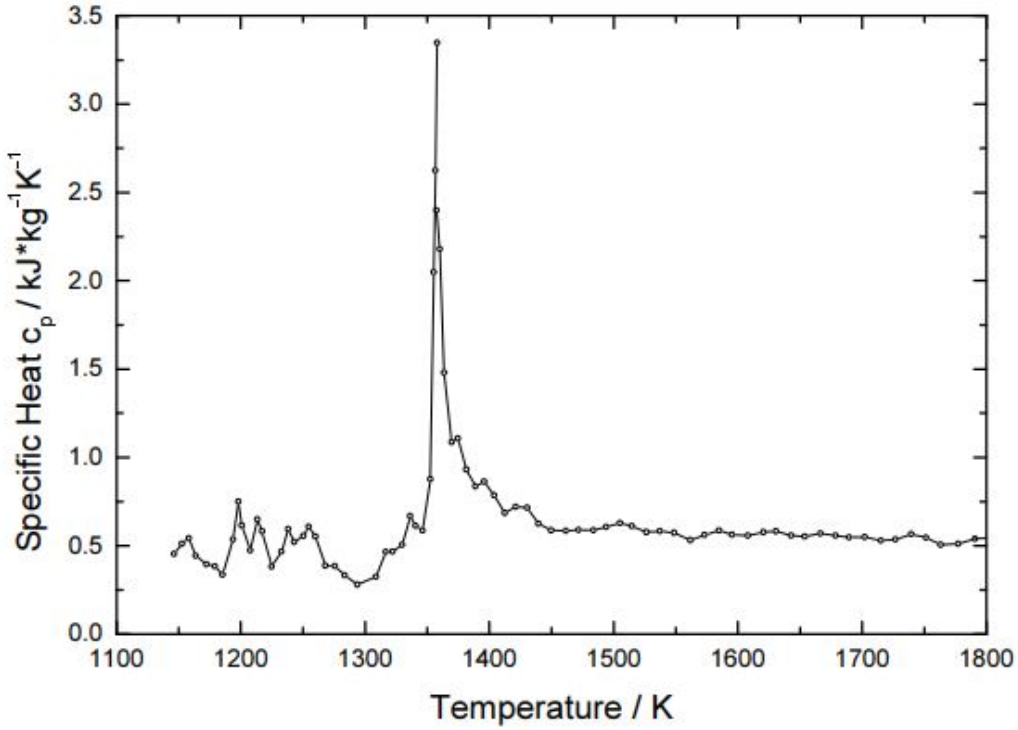


Fig. C.3 Temperature depended specific heat of copper material [233]